Dispersive waves in Earth's outer core

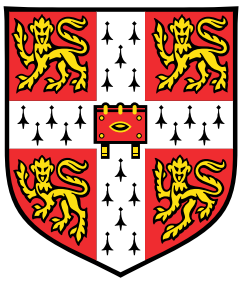

Oliver P Bardsley

Supervisor: Prof. P. A. Davidson

Department of Engineering
University of Cambridge

This dissertation is submitted for the degree of
Doctor of Philosophy

Pembroke College

February 2019

Declaration

I hereby declare that except where specific reference is made to the work of others, the contents of this dissertation are original and have not been submitted in whole or in part for consideration for any other degree or qualification in this, or any other university. This dissertation is my own work and contains nothing which is the outcome of work done in collaboration with others, except as specified in the text and Acknowledgements. This dissertation contains fewer than 65,000 words including appendices, bibliography, footnotes, tables and equations and has fewer than 150 figures.

Oliver P Bardsley
February 2019

Abstract

Dispersive waves in Earth's outer core

Oliver P Bardsley

This thesis addresses the generation and propagation of waves in Earth's fluid outer core, with the objective of better understanding their role in maintaining our planet's magnetic field. The classes of waves studied, which owe their existence both to the rapid rotation of the Earth about its axis and the vibration of magnetic field lines, are united by the fact they are *dispersive* — which is to say, the velocity at which a given wave travels is a function of the spacing and orientation of its wave crests; the behaviour of such waves is remarkably rich and has frequently counter-intuitive consequences.

Our analysis begins at the very smallest scales of the convection which stirs the liquid iron outer core, asking how localised features – such as turbulent eddies or buoyant parcels – might incite oscillatory motions at this fundamental scale. Of particular interest are the mechanisms by which columnar flow structures are established and sustained. We show that, in a situation where the wave source is threaded by a large-scale magnetic field, these processes are managed by a previously-overlooked denomination of oscillations dubbed *inertial-Alfvén waves*.

These objects establish the starting point for an investigation into the journeys embarked upon by packets of waves throughout the outer core, following their progress as global-scale variations in the magnetic field force them to evolve both their spatial structure and propagation velocity. A growing ambient field slows them considerably, even to the point where certain rays are arrested completely and quenched by electromagnetic losses. It is seen that the whole spectrum of small-scale waves influenced by rotation and mean magnetic field have a part to play in this story.

Finally, we study a rather distinct variety of waves: hydrodynamic *quasi-geostrophic Rossby waves*, which rely upon the rapid background rotation and the slope of the core-mantle boundary for their existence. Our interest in these waves is as a possible explanation for the westward drift of the non-dipolar part of the observable magnetic field. As it happens, the crests of these waves invariably progress eastward; however, for a certain subset – corresponding to radially-extended sheet-like flows compatible with the convective driving – they can nevertheless convey energy to the west. This insight raises an intriguing new possibility in the mission to solve this centuries-old puzzle.

Acknowledgements

I would like to take this opportunity to acknowledge a number of people and organisations whose contributions have made this work possible.

Firstly, my supervisor, Peter Davidson, whose vast research experience has been indispensable throughout my studies. I am grateful for the academic freedom he has allowed me, but also for his help and guidance in all matters, from scientific insight to assistance with writing articles to practical advice and counsel. I have thoroughly enjoyed our many technical discussions over the past five years.

I am also grateful to my friends and colleagues in the fluids group who have provided such good comradeship throughout my PhD. In particular, to the geophysical fluids enclave – Jack Atkinson, Avishek Ranjan, and Ben McDermott – who have provided so many helpful contributions in group meetings and casual discussions over the years. Daily coffee breaks and weekly cake mornings with our office neighbours in acoustics – Alastair, Amélie, Andy, Ben, Ed, and Max – have been enriching and enjoyable.

I spent autumn 2017 as a visiting academic in the Earth and Planetary Magnetism group at ETH Zürich, a time during which I made great progress on the latter portion of this thesis. I am grateful to Andrew Jackson for hosting me, and to the students and post-docs of the Departement Erdwissenschaften for making me feel so welcome, in particular office-mates Fabian and Daria.

Financially I am indebted to the Department of Engineering for offering me the Doctoral Training Award, funded by the Engineering and Physical Sciences Research Council, which has supported my studies. I am also grateful to the Department of Applied Mathematics and Theoretical Physics for awarding me the David Crighton Fellowship which made my visit to ETH Zürich possible.

Respite from work has all too often been found in bell ringing — I am sad that the end of my PhD also heralds the close of an eight-year ensconcement with the Cambridge University Guild of Change Ringers, an extraordinary community to which I have given and from which I have taken so much. The opportunities afforded through ringing with the Society of Cambridge Youths over the past few years have also been immensely enjoyable.

I would also like to thank my parents and even my in-laws for their immutable love and support. Last but by no means least, to my wife and best friend Megan, for her continued dedication over four incredibly happy years in this beautiful city.

Table of contents

List of figures

List of tables

Nomenclature

Where appropriate, the approximate values or ranges of physical quantities relating to the outer core of the Earth are given.

Abbreviations

CMB	Core-mantle boundary
DNS	Direct numerical simulation
ICB	Inner core boundary
MC	Magnetic-Coriolis
MHD	Magnetohydrodynamic(s)
ODE	Ordinary differential equation
QG	Quasi-Geostrophic
TC	Tangent Cylinder
TOs	Torsional oscillations
WKB(J)	Wentzel Kramers Brillouin (Jeffreys)

Dimensionless Groups

Λ	Elsasser number	$B^2/\rho\mu\eta\Omega$
Ek	Ekman number	$\nu/\Omega L^2$
Em	Magnetic Ekman number	$\eta/\Omega L^2$
Le	Lehnert number	$\left(B/\sqrt{\rho\mu}\right)/\Omega L$
Pm	Magnetic Prandtl number	ν/η
Pr	Prandtl number	ν/κ
q	Roberts number	κ/η
Ra	Rayleigh number	$\beta_T g\Delta T/\Omega^2 D$
Rm	Magnetic Reynolds number	UL/η

Ro	Rossby number	$U/\Omega L$

Notation

$\hat{\square}$	Fourier transform
$\mathbb{R}\{\square\}$	Real part
$\square_\perp$	Component perpendicular to the rotation axis

Symbols

α	Phase	$\boldsymbol{k}\cdot\boldsymbol{x}-\omega t$
β_T	Thermal expansion coefficient	$\sim 2\times10^{-5}\mathrm{K}^{-1}$ (i)
$\boldsymbol{E}$	Vector electric field	
$\boldsymbol{m}$	Magnetic dipole moment	
$\boldsymbol{x}$	Wave packet location	
$\boldsymbol{\omega}$	Vorticity	$\nabla\times\boldsymbol{u}$
$\boldsymbol{A}$, $\boldsymbol{a}$	Solenoidal magnetic vector potential, and perturbation	$\nabla\times\boldsymbol{A}=\boldsymbol{B}$
$\boldsymbol{B}$, $\boldsymbol{b}$	Vector magnetic field, and perturbation	
$\boldsymbol{c}_g$	Group velocity	
$\boldsymbol{c}_p$	Phase velocity	
$\boldsymbol{F}$	Generic body force	
$\boldsymbol{J}$, $\boldsymbol{j}$	Vector current density, and perturbation	
$\boldsymbol{k}$	Wavenumber vector	
$\boldsymbol{r}$	Position vector	
$\boldsymbol{v}^\pm$	Elsasser variables	$\boldsymbol{v}^\pm=\boldsymbol{u}\pm\frac{\boldsymbol{b}}{\sqrt{\rho\mu}}$
χ	Quasi-geostrophic streamfunction	
ΔT	Superadiabatic temperature contrast across outer core	$\sim 10^{-5}\mathrm{K}$ (i)
$\boldsymbol{e}_\square$	Unit vector associated with a given co-ordinate	
ℓ	Small lengthscale	$\sim 10\mathrm{km}$
η	Magnetic diffusivity	$(\mu\sigma)^{-1}\sim 0.5\mathrm{m}^2\,\mathrm{s}^{-1}$ (iii)
κ	Thermal diffusivity	$\sim 2.5\times10^{-5}\mathrm{m}^2\,\mathrm{s}^{-1}$ (iii)
λ	Wavelength	

$\mathscr{E}$	Energy per unit mass	
$\mathscr{H}$	Helicity density	$\boldsymbol{u}\cdot\boldsymbol{\omega}$
μ	Magnetic permeability	$4\pi\times10^{-7}\mathrm{H\,m^{-1}}$
ν	Kinematic viscosity	$\sim10^{-6}\mathrm{m^2\,s^{-1}}$ (iv)
$\Omega,\boldsymbol{\Omega}$	Background rotation rate	$7.29\times10^{-5}\mathrm{rad\,s^{-1}}$
ϕ	Azimuthal co-ordinate	
ρ	Density	$\sim10^{4}\mathrm{kg\,m^{-3}}$ (i)
σ	Electrical conductivity	$\sim1.5\times10^{6}\Omega^{-1}\,\mathrm{m^{-1}}$ (iii)
τ	Generic timescale	
θ	Spherical polar co-ordinate	
ϖ	Frequency	
A	An area or control surface within a fluid	
c	Relative density perturbation	ρ'/ρ
D	Outer core thickness	$R_o-R_i=2254\mathrm{km}$ (ii)
$g,\boldsymbol{g}$	Gravitational acceleration	$4.3-10.8\mathrm{m\,s^{-2}}$ (ii)
H	Average container half-height in linearised quasi-geostrophic formulation	
h	Half-height of container in quasi-geostrophic formulation	
h'	Container slope in linearised quasi-geostrophic formulation	
i	Imaginary unit	$\sqrt{-1}$
L	Generic lengthscale	
m	Azimuthal wavenumber	
n	Radial wavenumber	
p	Pressure	
R_i	Inner core radius	$1231\mathrm{km}$ (ii)
R_o	Outer core radius	$3485\mathrm{km}$ (ii)
s	Cylindrical radial co-ordinate	
t	Time co-ordinate	
U	Characteristic velocity	$\sim0.4\mathrm{mm\,s^{-1}}$ (i)

$u, \boldsymbol{u}$	Flow speed/velocity
V	A particular volume of fluid
x, y	Co-ordinates perpendicular to rotation axis
z	Co-ordinate aligned with rotation axis

[(i)] Roberts & King (2013)
[(ii)] Henderson & Henderson (2009)
[(iii)] Pozzo et al. (2014)
[(iv)] de Wijs et al. (1998)

Chapter 1

Introduction

The planet Earth, along with many of its neighbours in our solar system, is known to harbour its own magnetic field, a protective sheath around the globe which guards us against harmful cosmic radiation and a guiding light to navigators for centuries (Smith & Needham, 1967; Kivelson & Russell, 1995). In this sense, the geomagnetic field is essential both to the safety of life on Earth as we know it, and to the building of modern civilisation — from primitive naval navigation through to complex satellite systems (Mitchell, 2018), our need to understand the Earth's magnetic field has grown alongside the march of technical progress.

However, the source of our magnetic field, the *geodynamo*, still seems to be holding back more mysteries than it provides answers, despite centuries of endeavour from scientists across many disciplines. It is probably fair to say that no complete explanation for the exact mechanism of magnetic field generation has yet been universally adopted, and so elusive is the geomagnetic field that such a consensus may prove difficult to reach in the near future. All avenues of attack – be they observational, experimental, analytical or numerical – currently each face their own serious barriers to progress. That said, it is hoped that by building a combined picture from these various angles simultaneously the community will be able to approach a plausible, self-consistent physical model.

The focus of this thesis is the importance of waves to the dynamics of Earth's liquid outer core. Particularly, we investigate the properties and behaviour of certain classes of *dispersive travelling waves* — by which we mean, oscillatory motions which convey energy in such a way that the rate of propagation is dependent upon the wavelength of the disturbance. Our principal motivation comes from a theoretical cartoon of dynamo action, originally proposed by Davidson (2014) and reviewed in Davidson & Ranjan (2018*a*), which we refer to as the *helical wave dynamo*; however, the results presented herein possess significance beyond the scope of this one model, since the propagation of waves – and

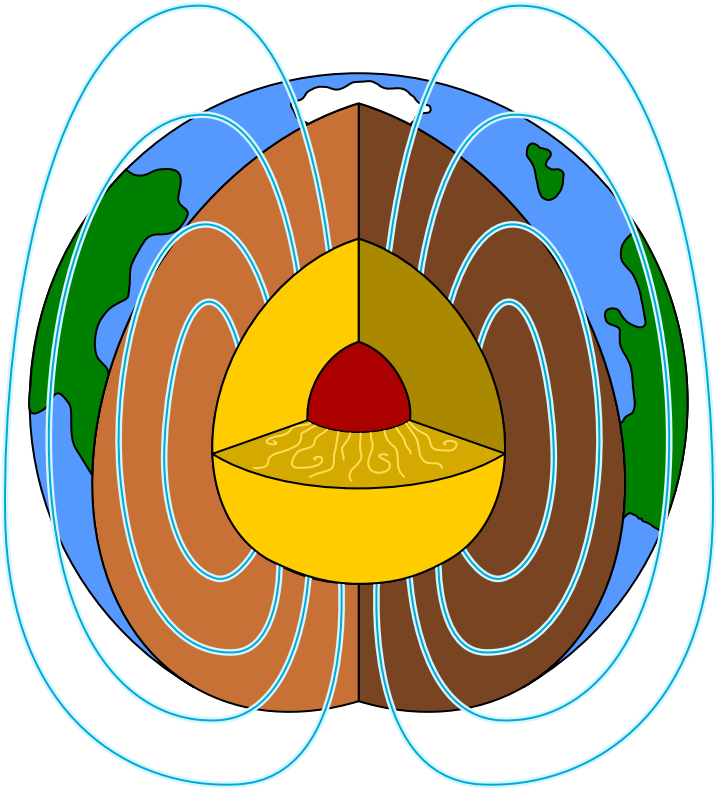

Fig. 1.1.1 Earth's interior, showing mantle (brown), liquid outer core (yellow) and solid inner core (red). Dipolar external magnetic field lines in blue (internal field not shown).

therefore information – throughout the Earth's fluid outer core has a fundamental bearing on its dynamic behaviour regardless of the details of the dynamo's operation.

This first chapter aims to introduce background material which will be of use going forward, with no pretence at offering a comprehensive review of the vast field of geomagnetism and dynamo theory — introductions which are both more detailed and more general can be found by Moffatt (1978); Davidson (2013); Roberts & King (2013); Schubert (2015), and others.

1.1 The outer core and the geodynamo

The outer core of the Earth, occupying the spherical shell 1231–3485km from its centre and situated 2886km beneath our feet, is a vast ocean of liquid iron and nickel – plus a mixture of lighter elements – within which our planet's magnetic field is forged (figure 1.1.1). At its heart, the inner core – a sphere of iron heated intensely during the planet's formation – attempts to shed that thermal energy as it gradually freezes and expands. At its periphery, the molten rock of the mantle provides a stoic barrier both to fluid motion and the internal

electric currents from which the geomagnetic field derives. Because of this, the mantle lives up to its name in cloaking the core from most attempts at detailed observation, although it is possible to map the magnetic field from the core-mantle boundary (CMB) outwards. What is seen is a spatial structure biased towards an axially-oriented dipole, with field lines tending to emerge from the core in the southern hemisphere and re-enter it in the north. Looking beyond this zero-order picture, the geomagnetic field shows significant variations in space and fluctuations in time which hint at a series of much more complicated, chaotic processes underlying its operation.

The root for all of these processes is the cooling and freezing of the solid inner core, which provides a buoyancy flux out towards the mantle as a result of two effects: first, there is simple thermal convection due to the temperature contrast between inner core and mantle; second, during the process of solidification at the inner core boundary (ICB), certain light elements dissolved in the liquid outer core – mainly silicon, sulphur and oxygen – come out of solution, providing a compositional buoyancy flux. This convection is vigorous, with the temperature contrast across the outer core estimated to be $\sim 10^4$ times that required for convective onset (Christensen & Aubert, 2006), but somewhat paradoxically the velocities involved are also rather small, on the order of fractions of millimetres every second. At a pace of $0.2\,\mathrm{mm\,s^{-1}}$, a fluid parcel which left the inner core at the moment of the magnetic field's discovery (Gilbert, 1600) might have arrived at the mantle just in time for the publication of the first plausible physical models of its generation (Parker, 1955) — testament both to the sluggishness of convection and the challenge of the problem.

That *geodynamo problem* asks how the potential energy possessed by the buoyant material is converted into magnetic field, which must be maintained against its natural inclination to decay over time. The solution sought is a *self-excited fluid dynamo* (Larmor, 1919; Elsasser, 1946; Desjardins et al., 2007) in which the convecting flow is constantly re-energising an internally-generated magnetic field, rather than more apparent explanations, such as permanent magnetism (the core temperature is well above the Curie point, so this is impossible) or any primordial trapped field formed during the planet's creation (since the field has been maintained over very many magnetic diffusion times). Schematically, the self-excited fluid dynamo hypothesis answers the question of the origin of the Earth's magnetic field — though extracting the details of how it works has kept many great minds employed for an entire century.

1.1.1 Dominant effects in the outer core

We now discuss which physical phenomena are likely to be most important in the outer core of the Earth; it is possible to make reasonable guesses at this from the available observational

and experimental data, and there is reasonable consensus on the appropriate dynamo equations (Braginsky & Roberts, 1995; Matsui et al., 2016) and target parameter values (Moffatt, 1978; Christensen, 2011). The most important effects are thought to be:

1. **Buoyancy** As the driver for the whole geodynamo system, the buoyancy flux obviously has an important part to play. As mentioned before, it vigorously stirs the molten iron, meaning convective motions are likely to be highly chaotic and stochastic. The buoyancy is typically treated using the Boussinesq approximation, meaning changes in density supply a buoyancy force but do not affect the fluid's inertia.

2. **The Coriolis force** Rotation is king in the outer core — the spinning of the Earth about its axis at an angular rate Ω of approximately 2π radians per day far outstrips the pace of any other processes within the core. In a reference frame rotating with the Earth, conservation of angular momentum for fluid particles manifests itself as a fictitious force known as the Coriolis force, which always acts perpendicular to the direction of material motion and therefore can do no work on the fluid (it may only alter the *direction* of motion, not the energy). That is not to say it is impotent; the Coriolis force must play an incredibly important role in organising flow structures with this outer core, as how else would the geomagnetic field know to be so eminently dipolar and axially-aligned?

3. **Magnetic induction** The process by which the kinetic energy of convection is converted into magnetic field is know as *magnetic induction*; the fluid has the ability to drag magnetic field lines with it as it moves, stretching and twisting them in such a way that the total magnetic energy is amplified (Moffatt, 1978).

4. **The Lorentz force** Whilst the velocity field is acting on magnetic field lines through the process of induction, the field lines are also responding through the action of the Lorentz force; in schematic terms, this is represented by a tension possessed by magnetic field lines which resists any attempts to stretch or bend them out of position.

5. **Magnetic diffusion** Earth's magnetic field is constantly dissipating energy through the process of Ohmic heating, or magnetic diffusion, thanks to the finite conductivity of liquid iron. It is against this constant sapping of energy that the geodynamo must be maintained. If it were left to its own devices without this renewal process, the field would decay in a time of the order $R_o^2/\eta \sim 10^5$yr, where R_o is the outer core radius and $\eta \sim 0.5\mathrm{m}^2\,\mathrm{s}^{-1}$ (Pozzo et al., 2014) the magnetic diffusivity. This is of interest for two reasons: first, it is much shorter than the known history of magnetism on Earth (Gubbins & Herrero-Bervera, 2007), creating a need for some form of self-excited

dynamo; second, it is considerably longer than timescales over which the field is known to undergo substantial changes — including the so-called *secular variation* (10-100yr, see Jackson & Finlay (2015)) and dipole reversal or excursion events (10^3-10^4yr, see Clement (2004)). Hence, these effects must be a result of other processes than the simple decay of the magnetic field over time, although the importance of magnetic diffusion in quenching internal motions is paramount.

6. **Inertia** This is probably the most controversial term in the equations governing the geodynamo. As mentioned above, fluid velocities (in excess of the background rotation) are thought to be very small, and the observed temporal evolution of the magnetic field occurs over long timescales compared to (say) the background rotation rate, so it is tempting to neglect the inertia of the fluid entirely. This is likely to be acceptable for the non-linear advection term $\boldsymbol{u}\cdot\nabla\boldsymbol{u} \sim U^2/L$, since the characteristic velocity U is small and lengthscale L is large, but is not so clean-cut for the acceleration $\partial\boldsymbol{u}/\partial t$, since neglecting it requires prescribing a timescale to the dynamics. Indeed, attempting to remove this term, which reduces conservation of momentum to a diagnostic equation for the fluid velocity as a function of the magnetic field, results in some very oddly-behaved systems (Taylor, 1963; Walker et al., 1998). In this thesis, our interest is in waves across all timescales of motion within the core, but particularly the fast dynamics, meaning it will be necessary to retain $\partial\boldsymbol{u}/\partial t$ in all we do.

A notable absentee from this list is the fluid's viscosity. This is because the kinematic velocity of iron at the Earth's core conditions is though to be little different from that of water, i.e. a value $\nu \sim 10^{-6}\mathrm{m}^2\,\mathrm{s}^{-1}$, and therefore approximately six orders of magnitude smaller than the magnetic diffusivity; it seems that in any realistic dynamo, the Ohmic losses must greatly outweigh viscous ones.

To quantify the relative importance of the above effects, and in particular the dominance of rotation, we estimate some key dimensionless parameters (all with rotation rate in the denominator) in table 1.1.2, which uses the estimates for physical values in table 1.1.1. The fact that these are all less than unity – most of them significantly so – is compelling evidence that outer core dynamics are rotationally-dominated. The one possible exception is the Elsasser number (usually denoted Λ), which gauges the comparative magnitudes of the Lorentz and Coriolis forces. This turns out to be of order one in Earth's outer core, which is suggestive of a leading order equilibrium between these two forces, the so-called *magnetostrophic balance* (Malkus & Proctor, 1975; Soderlund et al., 2015). If buoyancy ('Archimedian') effects are included as well, the resulting balance – termed *Magnetic-Archimedian-Coriolis (MAC)* – is an attractive proposition for outer core conditions. However, this argument does not take into account the fact that the vast majority of the Coriolis force may in fact be balanced

Quantity	Symbol	Exact or estimated magnitude
Density	ρ	$\sim 10^4 \mathrm{kg\,m^{-3}}$
Kinematic viscosity	ν	$\sim 10^{-6} \mathrm{m^2\,s^{-1}}$
Background rotation	Ω	$7.29 \times 10^{-5} \mathrm{rad\,s^{-1}}$
Large lengthscale	L	$\sim R_o = 3.49 \times 10^6 \mathrm{m}$
Fluid velocity	U	$\sim 4 \times 10^{-4} \mathrm{m\,s^{-1}}$
Magnetic field strength at CMB	B	$\gtrsim 4 \times 10^{-4} \mathrm{T}$
Magnetic diffusivity	η	$\sim 0.5 \mathrm{m^2\,s^{-1}}$

Table 1.1.1 Some salient physical quantities for determining the dominant force balance. (For references see nomenclature.)

Dimensionless Number	Physical Quantity	Definition	Force Balance	Order of magnitude
Rossby	Inertia	$\frac{U}{\Omega L}$	$\frac{\lvert\boldsymbol{u}\cdot\nabla\boldsymbol{u}\rvert}{\lvert 2\boldsymbol{\Omega}\times\boldsymbol{u}\rvert}$	10^{-6}
Elsasser	Lorentz force	$\frac{B^2/\rho\mu}{\eta\Omega}$	$\frac{\lvert\rho^{-1}\boldsymbol{J}\times\boldsymbol{B}\rvert}{\lvert 2\boldsymbol{\Omega}\times\boldsymbol{u}\rvert}$	0.3
Ekman	Viscosity	$\frac{\nu}{\Omega L^2}$	$\frac{\lvert\nu\nabla^2\boldsymbol{u}\rvert}{\lvert 2\boldsymbol{\Omega}\times\boldsymbol{u}\rvert}$	10^{-15}
Magnetic Ekman	Magnetic diffusivity	$\frac{\eta}{\Omega L^2}$	-	10^{-9}
Lehnert	Magnetic oscillations	$\frac{B/\sqrt{\rho\mu}}{\Omega L}$	-	10^{-5}

Table 1.1.2 Dimensionless measures of the importance of key physical processes compared to the background rotation rate. Estimates use values from table 1.1.1.

by pressure (so-called *geostrophic* balance), and it is only the remaining rotational portion which is left to equilibrate with the Lorentz force (Davidson, 2014) — a situation which is not so trivially quantified (Dormy, 2016). Furthermore, although the Elsasser number is found to be of order unity for Earth, it varies widely across other dynamo-harbouring planets and therefore the universal significance of $\Lambda \sim 1$ is somewhat questionable, a point to which we return in section 1.1.5. Finally, note that the common definition of Λ here implicitly uses the velocity scale η/L rather than U; making this change reduces the quantity by a factor 10^3 (i.e. $\Lambda \sim 10^{-4}$), almost as small as the other dimensionless quantities.

There are another couple of subtleties hidden by table 1.1.2. First, the characteristic lengthscale used is the very largest one possible, the outer core radius R_o, and therefore the orders of magnitude pertain to global balances. One might expect the more meaningful lengthscale of the vigorously-forced convection to be a factor of 100, or even 1000, less than the outer core radius, and this could have a big effect on the dimensionless measures of table 1.1.2. For example, using $L = 0.01 R_o$ increases the magnetic Ekman number by a factor

of 10^4; this, combined with the possibility of using a larger turbulent diffusivity instead of η (Gubbins, 2001), makes magnetic diffusion effects more potent than the 10^{-9} value in table 1.1.2 suggests.

Second, in estimating the Rossby number, we were careful to use the advective derivative $\boldsymbol{u}\cdot\nabla\boldsymbol{u}$ rather than the flow acceleration $\partial\boldsymbol{u}/\partial t$ (or total derivative $\mathrm{d}\boldsymbol{u}/\mathrm{d}t$). This is because rapid oscillations – comparable in frequency to the rotation rate – have a significant time derivative despite the associated fluid velocities being very small; such oscillations are studied at length in chapters 2 and 3.

1.1.2 The significance of rotation

As evidenced by the fact that the geomagnetic poles are closely aligned with the geographic ones, and as inferred from the dimensionless measures of table 1.1.2, the background rotation of the Earth must be a powerful arbitrator of its internal dynamics. It is worthwhile, therefore, asking what rapidly-rotating flows tend to look like.

The answer, in broadest terms, is that the rapid rotation tends to constrain motions in the plane perpendicular to the rotation axis, leading to tall, columnar flow structures. In the rotating frame, any fluid parcel which moves with a component of its velocity perpendicular to the rotation vector $\boldsymbol{\Omega}$ will experience a Coriolis force $2\boldsymbol{u}\times\boldsymbol{\Omega}$ perpendicular to its trajectory, and therefore if a particle is disturbed, it will tend to follow a circular path in the neighbourhood of its original position rather than travel to a different region of the fluid entirely. The same does not apply to particles moving axially (i.e. parallel to $\boldsymbol{\Omega}$), since they experience no Coriolis force. Because of this, the flow will attempt to organise itself in a strongly anisotropic manner, with structures tending to be greatly elongated along the rotation axis.

This claim is well-supported by a wealth of experimental, analytical and numerical findings, both within the context of Earth's outer core and not. Such examples can be found in Greenspan (1968); Pouquet & Mininni (2010); Davidson (2013); Aurnou et al. (2015), including the striking simulation result of figure 1.1.2, in which intense columnar vortices dominate in a rapidly-rotating periodic cube of turbulent fluid. Numerical dynamos, as we shall see in section 1.1.4, are also inclined to migrate toward this axially-elongated state; the mechanisms by which this occurs, and consequences of the result, will be a recurrent theme throughout this thesis.

[(i)] Credit to Annick Pouquet: https://sites.google.com/site/pouquetannick/some-figures

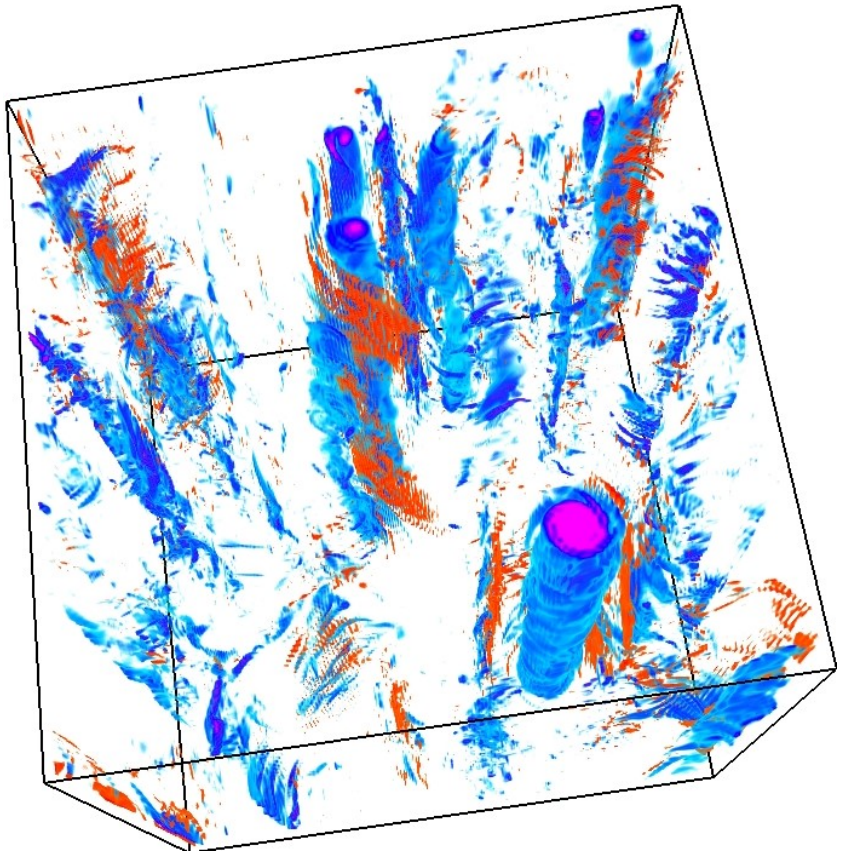

Fig. 1.1.2 Columnar structures in rapidly-rotating turbulence, visualised by helicity[(i)].

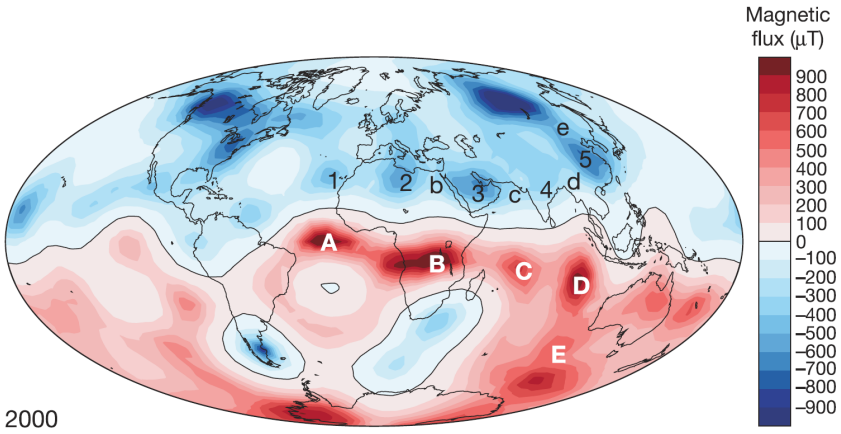

Fig. 1.1.3 Radial magnetic field at the CMB in the year 2000, from Jackson (2003).

1.1.3 Observational evidence

We now proceed to review the available evidence which may help us in our quest to better understand the geodynamo, treating observations in this section and numerical simulations in the next.

Unfortunately, a defining feature of geodynamo research is the sparsity of available observational evidence. Modern satellite missions and ground observatories are able to monitor the vector magnetic field with impressive accuracy (Finlay et al., 2016), and since there are minimal electric currents in the intervening space between said observers and the core, it is possible to extrapolate the magnetic field as a potential field down to the CMB — such a map is shown in figure 1.1.3, taken from Jackson (2003). The general dipolarity is clear – magnetic flux tends to leave the core in the southern hemisphere and re-enter it in the north – but so too are significant variations with space, most notably a region of weakened field called the *south Atlantic anomaly* (Pavón-Carrasco & De Santis, 2016), and the strong equatorial flux patches labelled in figure 1.1.3. What should also be evident is a lack of resolution; one might expect a field spawned from convective plume to have spatial scale comparable with that convection, maybe down to one-hundredth or one-thousandth of the core size. Instead, what is plotted is significantly under-resolved — this is because permanent magnetism within the crust contaminates the data below a certain spatial scale (harmonic degree 13, corresponding to features of size ~ 1000km at the CMB or 1500km at the surface), the so-called *magnetic curtain* (Olsen & Mandea, 2008; Roberts & King, 2013). Observation of the internally-generated potential field is sadly curtailed at this lengthscale — and what's more, the spectral energy shows little sign of decreasing with harmonic degree (Holme et al., 2011), meaning much of the energetic content of the field is likely being hidden from view.

Perhaps even worse is the fact that the internal components of the magnetic field are not merely filtered, but utterly invisible to direct measurement. In particular, the toroidal component is strictly confined to the core. Because the mantle is to a good approximation electrically insulating, the electric currents which maintain the geodynamo must be contained within the core. The toroidal field must pass through poloidal current loops by Ampère's law — but as these currents may not pass through the CMB, the toroidal field must also go to zero at the core's periphery, rendering it unavailable to observation. Indirect measurements from oscillations of the field are available (e.g. Gillet et al., 2010), but require a large number of assumptions working with reasonably meagre data.

The time-dependence of the magnetic field is perhaps the richest mine of information, however. Owing to the magnetic field's utility for navigation, useful data exists right back to 1590 (Jackson et al., 2000), and particularly high-quality vector field measurement from satellites are available for the past couple of decades (Finlay et al., 2016) — variations of the magnetic field over these timescales is known as the *secular variation*. (Though use of the word secular is anachronistic, these changes are in fact amongst the fastest internal variations observed.) The secular variation exhibits a diverse range of phenomena, which

have been extensively analysed in an attempt to learn more about the outer core. For example, decadal oscillations thought to be linked to torsional magnetic waves (Gillet et al., 2010), abrupt changes in field known as geomagnetic jerks (Brown et al., 2013), and gradual westward drift of flux patches (Finlay & Jackson, 2003). Study of wave dynamics in the outer core seems to come hand-in-hand with attempts to better understand this secular variation, and this thesis is no exception; the waves studied in chapter 3 have, since publication in Bardsley & Davidson (2016), been linked to events such as geomagnetic jerks (Aubert & Finlay, 2019) — and chapter 5 is devoted to the relationship between certain classes of waves and the westward drift.

1.1.4 Evidence from the numerical dynamos

Since the advent of the first self-consistent numerical dynamo simulations (Glatzmaier & Roberts, 1995), computational models of Earth's magnetic field have been a cornerstone of the campaign to understand the geodynamo — and as our processing resources have increased, the simulation fidelity has inevitably improved. There is a constant push to try and drive the numerics as close as possible to Earth's core conditions, an aspiration which has proved immensely hard to realise. Recent investigations have been able to break new ground in terms of the accessible parameter regimes (Schaeffer et al., 2017; Aubert, 2018; Sheyko et al., 2018), though are unavoidably still significantly over-viscous (as measured by the Ekman number $Ek = \nu/\Omega L^2$, of order 10^{-15} for the outer core, but at least 10^{-7} in simulations) and under-forced (as measured by the Rayleigh number $Ra = \beta_T g \Delta T/\Omega^2 D$, which is $\sim 10^4$ times its critical value in the Earth, but only ~ 100 times in simulations (Christensen, 2011)). Furthermore, the Roberts and magnetic Prandtl numbers ($q = \kappa/\eta$ and $Pm = \nu/\eta$), ratios of key diffusivities which are both likely to be $\sim 10^{-6}$ in the core, are often taken to be 0.1 or greater in the numerics.

The challenge in achieving geophysically relevant dimensionless values, particularly for the Ekman number, comes down to the dominance of rotation. In order to capture the effects of the rapid background rotation and therefore have a well-resolved code, it is necessary to take very small timesteps, less than a day each, when running a simulation. However, the magnetic field is known to persist over many millennia — and must be maintained against diffusion acting on a timescale $R_o^2/\eta \sim 10^5$yr. To cover these lengths of time taking such small steps, and over a sufficiently detailed spatial domain to resolve complex turbulent behaviour, requires considerable computational effort.

The disparity between reality and simulations may well reduce confidence in their output as a reliable source of intelligence on outer core dynamics. It is hoped, however, that the simulations are approaching regimes which are asymptotically equivalent to the Earth

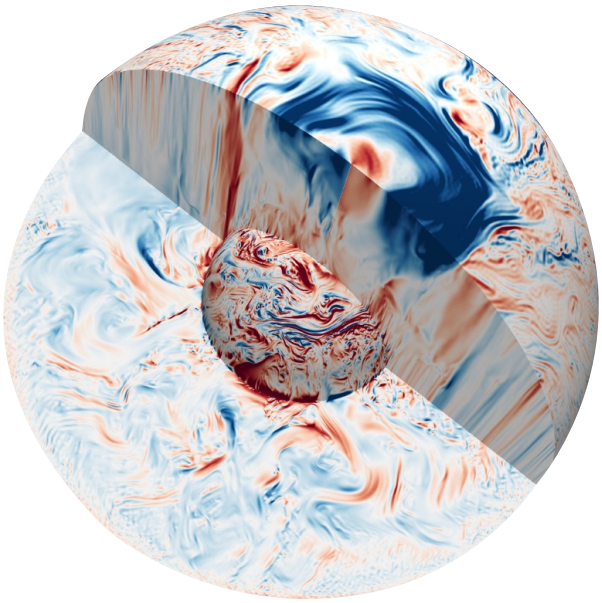

Fig. 1.1.4 Azimuthal velocity snapshot from a numerical dynamo simulation of Schaeffer et al. (2017).

(Christensen & Aubert, 2006; Christensen et al., 2010); that is to say, their viscosity could be "small enough", despite the nine orders of magnitude which separate them from the real planet. This contention, however, remains the subject of much debate (Oruba & Dormy, 2014; Davidson, 2016).

Nevertheless, what is reassuring about the simulations is their ability to yield magnetic fields which are somewhat 'Earth-like'. That is to say, they can have plausibly dipolar external fields and perform manoeuvres such as geomagnetic reversals (Glatzmaier & Roberts, 1995; Sheyko et al., 2016) and westward drift (Christensen & Wicht, 2007; Livermore et al., 2013). This is surprising, especially for early simulations in which aggressive methodologies and parameter values were required in order to ensure convergence, and suggests that, in some fundamental sense, the numerical dynamos should be able to provide some clue to the dynamics inside the Earth. Obviously, any such inferences must be made with considerable caution — though we outline a few findings useful for our purposes below.

Rotational dominance

Uncontroversially, the background rotation is a dominant influence in the numerical dynamos. This has a few consequences: first, the Coriolis force tends to organise flow structures along the rotation axis, as discussed above. Second, the outer core flow is divided into three rather distinct regions, delineated by the spherical inner core boundary and the *tangent cylinder* (TC), an imaginary surface circumscribing the inner core and aligned with the rotation axis. (Both of these consequences are evident in figure 1.1.4, taken from Schaeffer

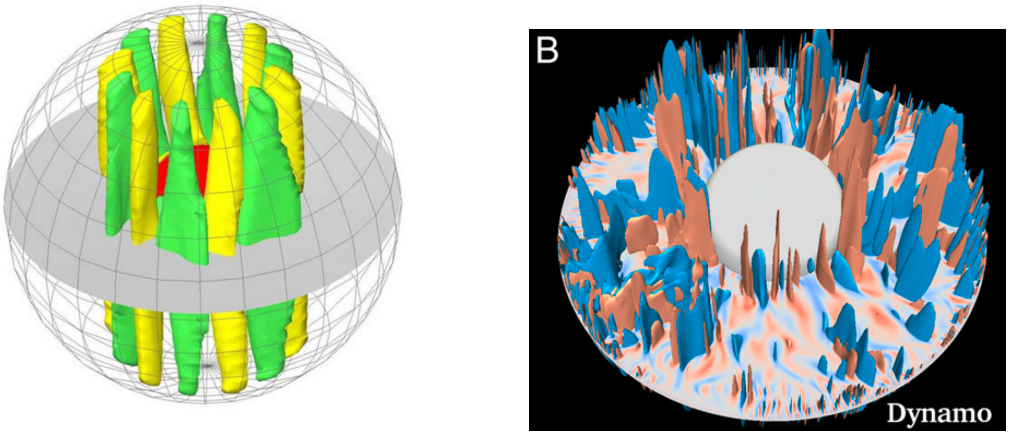

(a) Kageyama & Sato (1997) **(b)** Yadav et al. (2016)

Fig. 1.1.5 Increasing complexity of axially-elongated flows in numerical dynamos.

et al. (2017).) It happens that the majority of dynamo action occurs outside of the TC, and so this will be the region in which we concentrate our efforts, generally neglecting the inner core entirely.

The prevalence of axially-aligned structures serves as inspiration for a class of reduced models which presuppose it, rather than let it arise naturally through the complete governing equation set; such models are termed *quasi-geostrophic* (QG) and a more complete description of the rationale behind them may be found in Gillet et al. (2012). We make use of such a model in chapter 5.

As should be clear from figure 1.1.4, even if the flow is generally elongated along the axis, it is a long way from being orderly. The early numerical dynamos (Glatzmaier & Roberts, 1995; Kageyama & Sato, 1997; Olson et al., 1999) agreed with the early theories of linear convective onset (Busse, 1970), insofar as the velocity field consisted of a small number of well-ordered vortices, columnar along the rotation axis and neatly arranged around the TC (figure 1.1.5a). However, as the parameters of the simulations have become more extreme (larger Ra and smaller Ek), the columnar flows have become more irregular and chaotic (figure 1.1.5b). Understanding the dynamics of these types of flow is a powerful motivator for much of the work herein.

Magnetic field configuration

Numerical simulations may also provide useful hints as to the make-up of the invisible internal magnetic field. The early efforts often featured a strong toroidal component (figure 1.1.6a), with field lines wrapping around azimuthally inside the core a number of times. The toroidal field in these cases is maybe an order of magnitude larger than the poloidal, likely

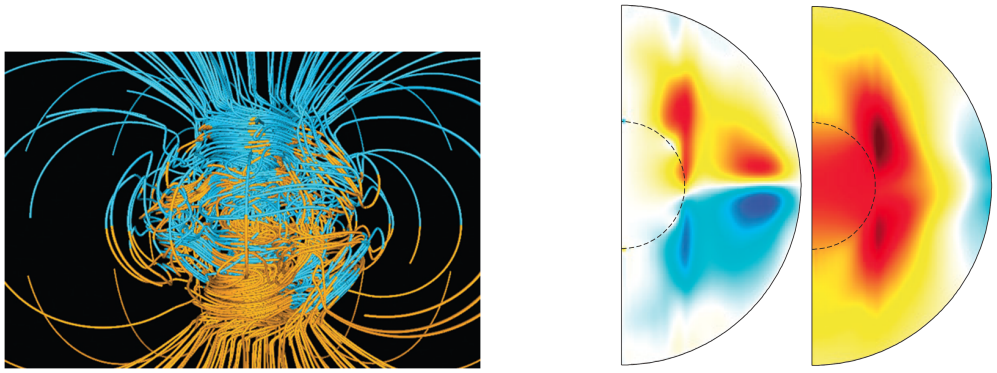

(a) Glatzmaier & Roberts (1995) **(b)** Sakuraba & Roberts (2009)

Fig. 1.1.6 Azimuthal magnetic fields in numerical dynamos.

being swept out by a potent "omega effect", in which strong differential rotation of the outer core fluid converts poloidal field lines into azimuthal ones. However, as simulation power has increased the azimuthal and poloidal magnetic fields have acquired more comparable magnitudes — for example, figure 1.1.6b shows azimuthal (B_ϕ, left pane) and axial (B_z, right pane) field on the same colour scale, from Sakuraba & Roberts (2009). Near the TC there is a stronger B_z, but closer to the CMB – particularly in the equatorial regions – the azimuthal field is larger. Overall, the two have similar absolute values, consistent with a dynamo which is on average operating in an *alpha-squared* sense, an idea which we discuss further in section 1.2. Crucially, the mechanism for generating poloidal field from azimuthal field is the same as azimuthal from poloidal in such a model, and therefore one might expect the two components to be of similar magnitudes. In any case, the dipolar poloidal field observed outside of the core is likely to be at least matched in value by the azimuthal field in its interior, and therefore both poloidal and azimuthal fields are of interest when studying outer core dynamics.

We also point out that the azimuthal field in figure 1.1.6b is, at least in this averaged picture, antisymmetric about the equator (and therefore zero in the equatorial plane), and goes to zero at the CMB. This will prove to be important both for the alpha-squared cartoon and the model problems we tackle in chapter 4.

Distribution of convection

The final piece of information for which we look to the numerical dynamos is the spatial distribution of the convective forcing — that is to say, where in the outer core are the processes which maintain the geodynamo being instigated? First, note that a significant portion of the heat flux heads north and south from the inner core, staying within the

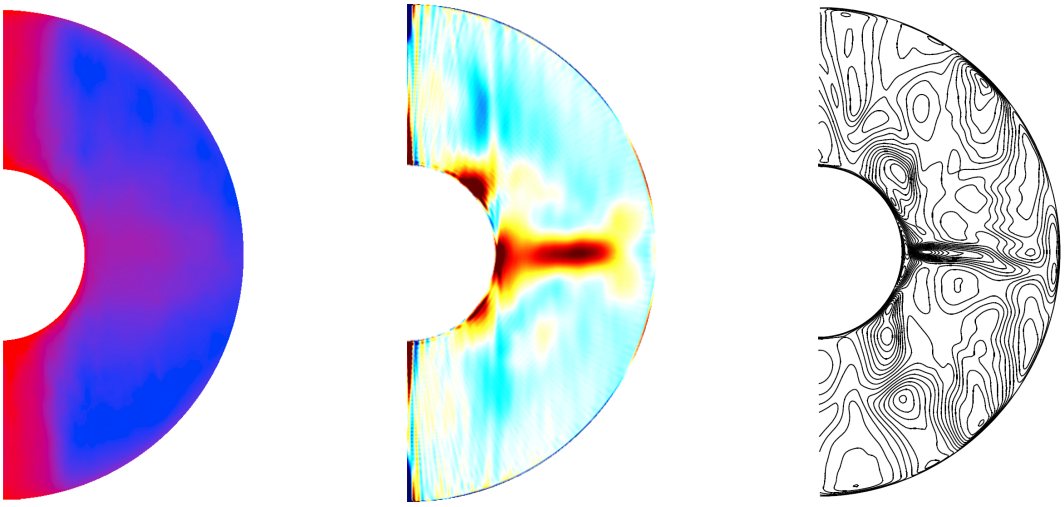

(a) Temperature in a meridional cross-section from Sheyko et al. (2018).

(b) Azimuthally-averaged radial velocity from Sakuraba & Roberts (2009).

(c) Azimuthal velocity in a meridional cross-section from Dormy (2016).

Fig. 1.1.7 Equatorial bias to convection in numerical dynamos.

TC. This can be seen in the example of figure 1.1.7a, taken from Sheyko et al. (2018), with the red colour indicating plenty of hot material above and below the inner core. Also perceptible in this plot is a tendency outside of the TC for hot material to congregate near to the equatorial plane. This is a reasonably common feature in the numerical dynamos — figure 1.1.7b shows a particularly extreme example from Sakuraba & Roberts (2009), in which the radial velocity field is dominated by a pronounced equatorial jet. The purpose of that study was to assess the impact of using fixed-flux (as opposed to fixed-temperature) thermal boundary conditions at the CMB, the more geophysically realistic option. The exact dependency of the equatorial jet on simulation parameters and boundary conditions is unclear, but it is suggested by Dormy (2016) (figure 1.1.7c) that it is related to the attainment of a magnetostrophic balance and concomitant loosening of the constraints imposed by rapid rotation. We discuss the equatorial jet further in section 2.1.3.

1.1.5 Comparison with other planets

So far we have focussed attention on Earth's magnetic field, but it is just one of many planets within our solar system which harbours its own dynamo, and this ubiquity motivates the search for a robust, ideally universal, mechanism for planetary magnetic field generation.

[(i)] Diagram credit to Ulrich Christensen:
http://cifs-isss.org/presentazioni/2016-september/14_09_2016_Christensen.pdf

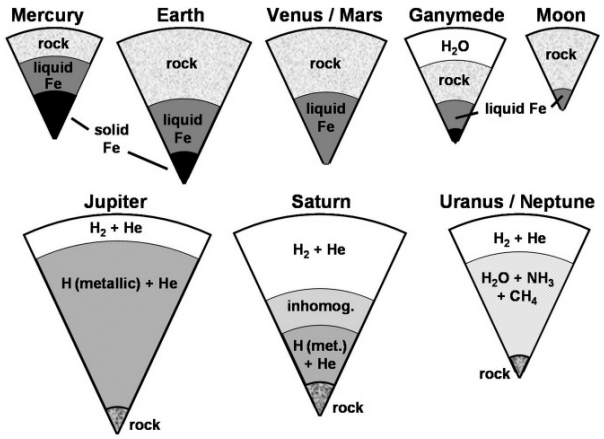

Fig. 1.1.8 Supposed interior structure (not to scale) of certain bodies within our solar system, after Stevenson (1983). Mercury, Earth, Ganymede, Jupiter and Saturn have dipolar magnetic fields[(i)].

Planet	**Rotation Period** $2\pi/\Omega$ (days)	**Core Radius** R_o (Mm)	**Mean Axial Field** $\bar{B}_z$ (G)	$\dfrac{\bar{B}_z/\sqrt{\rho\mu}}{\Omega R_o}$
Mercury	58.6	1.8	0.014	5.6×10^{-6}
Earth	1	3.5	3.7	13.0×10^{-6}
Jupiter	0.413	55.0	18.0	5.2×10^{-6}
Saturn	0.444	29.0	3.7	2.2×10^{-6}

Table 1.1.3 Comparison of the dipolar planetary magnetic fields in our solar system using estimated quantities, from Davidson (2014). The density is estimated to be $10^4\mathrm{kg\,m^{-3}}$ for the terrestrial planets and $10^3\mathrm{kg\,m^{-3}}$ for the gas giants.

Figure 1.1.8 shows the supposed structure of a few bodies in our solar system. The terrestrial planets have liquid iron outer cores, whereas the gas giants are mainly metallic hydrogen, also an electrically conducting fluid. The differences in size, rotation rate, and magnetic field strength – three crucial parameters – aren't shown in figure 1.1.8, but we can nevertheless show that their dynamos do appear to be similar in dimensionless terms. It is possible to estimate their volume-averaged axial field strength $\bar{B}_z$ from their *magnetic dipole moment* $\boldsymbol{m}$ (Jackson, 1998), defined by

$$\boldsymbol{m} = \frac{1}{2}\iiint_{V_o} \boldsymbol{r}\times\boldsymbol{J}\,\mathrm{d}V = \frac{3}{2\mu}\iiint_{V_o}\boldsymbol{B}\,\mathrm{d}V, \tag{1.1.1}$$

where V_o is the core volume. One can then estimate $\bar{B}_z$ as

$$\bar{B}_z \approx \frac{2\mu}{3V_o}|\boldsymbol{m}| \tag{1.1.2}$$

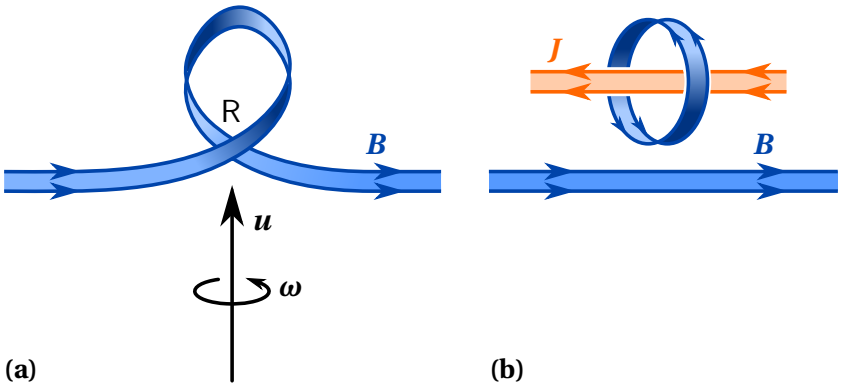

Fig. 1.2.1 The alpha effect: a positively helical flow lifts and twists a horizontal field line, producing an antiparallel current (adapted from similar figures in Moffatt (1978) and Roberts (2007)).

(Davidson, 2013), and form the dimensionless quantity $\left(\bar{B}_z/\sqrt{\rho\mu}\right)/\Omega R_o$ (an incarnation of the *Lehnert number*), which allows us to gauge the relative field strengths of the planets in our solar system with dipolar dynamos (table 1.1.3, adapted from Davidson (2014)). Despite widely varying field strengths, sizes and rotation rates, it seems there is some consistency in this parameter, suggesting that the mechanism of planetary magnetic field generation may be similar across them all, and therefore the same processes, robust to changes in both geometry and composition, could plausibly underlie them all. The results herein, although angled towards the Earth, may therefore have a wider range of applicability.

1.2 Helical wave dynamos

We now have in place all of the building blocks required to outline a cartoon for geodynamo action which we term the *helical wave model* (Davidson, 2014; Davidson & Ranjan, 2018*a*). Although this model provides the motivation for the present study, the results here may be considered to have a rather more general applicability.

1.2.1 The alpha effect

The basic element in the helical wave dynamo – and indeed other dynamo cartoons – is the *alpha effect*, a small-scale mechanism by which helical flows may pump energy into the magnetic field (Parker, 1955; Moffatt, 1978).

Consider figure 1.2.1. An initially horizontal magnetic field is approached by a parcel of positively helical flow — that is to say, a region of fluid in which the velocity and vorticity vectors are closely aligned, giving streamlines which spiral in a right-handed sense. Because of Alfvén's theorem – that magnetic field lines are frozen into an perfectly-conducting fluid –

this flow both lifts and twists the magnetic field lines, forming a significant kink as depicted in figure 1.2.1a. The fluid is not in fact perfectly conducting, however, and so at points where magnetic field lines get very close together, diffusive effects may come into play. Crucially, this is particularly intense at the bottom of the loop — the point marked 'R' in figure 1.2.1a. At this point, *magnetic reconnection* occurs and the field topology becomes a horizontal field line, much as the initial state, plus a detached loop (figure 1.2.1b). The sense of this loop is such that it induces a current antiparallel to the initial magnetic field by Ampère's law. Had the fluid parcel been negatively helical – i.e. velocity and vorticity antiparallel, or left-handed spiralling streamlines – the induced current would be in the same direction as the initial magnetic field.

In this way, helical flows may induce currents either parallel or anti-parallel to magnetic field lines on small scales. However, this is only a viable route towards explaining the geodynamo if two conditions are also met: first, that these small-scale events may work in concert to produce a large-scale field, and second, that there is a robust source of flows with the required helical structure.

1.2.2 The alpha-squared dynamo

The means by which small-scale alpha effect events may contribute constructively to the same global field is know as the *alpha-squared dynamo*, so called because it appeals to the alpha effect twice.

Consider figure 1.2.2, which shows schematically the zero-order mode of operation of an alpha-squared dynamo. Suppose that the helicity of the flow is spatially segregated, being negative (left-handed spiral) in the northern hemisphere and positive (right-handed spirals) in the south, much as found in the numerical dynamos (Olson et al., 1999). We begin with the dipolar poloidal magnetic field $\boldsymbol{B}_p$, which for argument's sake is assumed to run from south to north in the core, shown at the top of figure 1.2.2. The effect of the small-scale alpha effect upon this field will be to induce poloidal electric currents $\boldsymbol{J}_p$ parallel to $\boldsymbol{B}_p$ in the northern hemisphere and antiparallel to it in the south. Since currents must form closed circuits, this sets up the quadrupolar $\boldsymbol{J}_p$ distribution shown on the right of figure 1.2.2. Application of Ampère's law to these two doughnuts of current implies a toroidal field which is positive (west to east) in the north and negative (east to west) in the south; note that this is also seen in the numerical dynamos, e.g. figure 1.1.6b. We now make use of the small-scale alpha effect a second time, recognising that from this toroidal magnetic field distribution the derived currents – parallel in the north, antiparallel in the south – are in the same direction, i.e. west to east. One final application of Ampère's law to this current

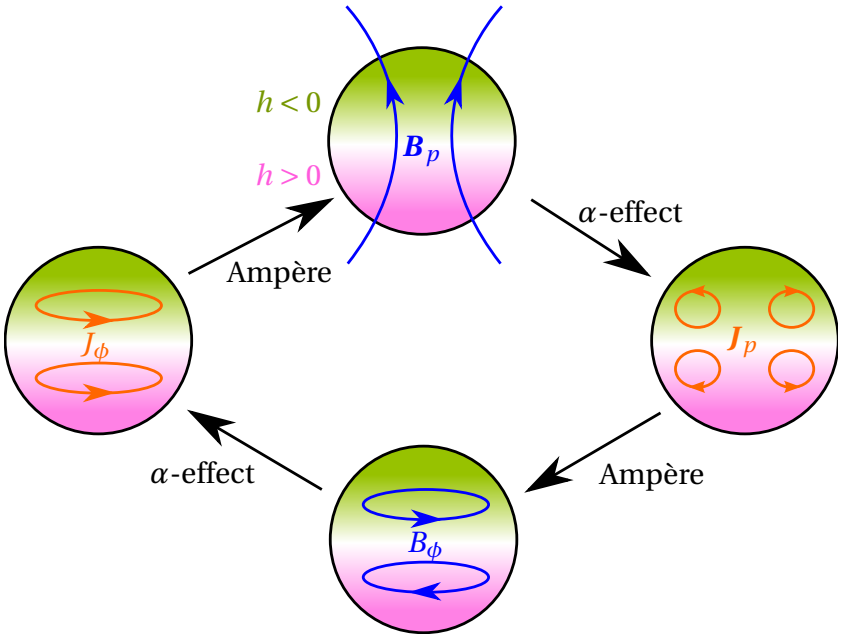

Fig. 1.2.2 The classical alpha-squared dynamo, adapted from Davidson (2014).

distribution yields exactly the poloidal field we started with, thereby completing this cartoon of dynamo action.

1.2.3 Helicity segregation

The alpha effect and alpha-squared dynamo discussed above hint at a viable route to a geodynamo. However, we have yet to approach the question of how they might come about in practice. That is to say, from where does the intensely helical flow required to drive an alpha effect derive, and how might it segregate itself (negative helicity to the north, positive to the south) in order to contrive an alpha-squared dynamo?

In the viscously-dominated early simulations (e.g. Olson et al., 1999), it appears that Ekman pumping – grinding of tall but reasonably fat columnar vortices against the core-mantle boundary – was the dominant source of flow helicity, and indeed gave exactly the distribution required for an alpha-squared dynamo. Unfortunately, this is probably still the case even in more modern simulations — figure 1.2.3a shows an $Ek = 10^{-5}$ case from Schaeffer et al. (2017), with a clear helicity concentration near to the CMB. However, as argued in Davidson (2014), Ekman pumping is unlikely to be responsible in a real planet. This is because, as the Ekman number is lowered to geophysical values, the aspect ratio of these columnar structures becomes incredibly large (widths in tens of metres) and the boundary layers incredibly narrow (around 10cm), so it seems implausible that these viscously-dominated structures maintain their coherence (Schaeffer & Cardin, 2006). Furthermore, gas giants

(a) Boundary-generated helicity segregation at $Ek = 10^{-5}$, from Schaeffer et al. (2017).

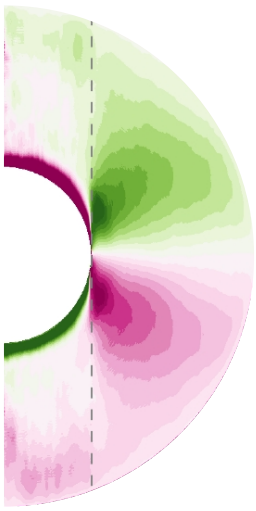

(b) Internal helicity generation and segregation at $Ek = 10^{-7}$, from Schaeffer et al. (2017).

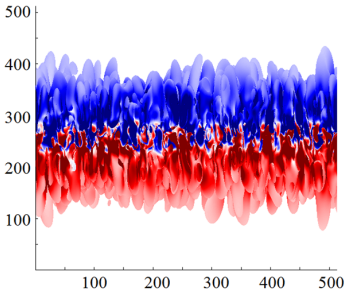

(c) Inertial wave packets from a buoyant cloud, from Davidson & Ranjan (2015). Axial velocity is coloured by relative helicity (red positive, blue negative).

Fig. 1.2.3 Segregation of helicity in numerical dynamos and by inertial waves.

which have no solid boundary such as the CMB, and indeed numerical dynamos with slip boundary conditions (Kuang & Bloxham, 1999; Yadav et al., 2013), nevertheless exhibit dipolar magnetic fields, suggesting the exact nature of the velocity boundary conditions cannot be relevant.

Instead, a more robust, internal means of generating and segregating helicity is sought, particularly in light of recent low Ekman number simulations producing helicity fields which no longer lean so heavily upon the boundaries (Schaeffer et al., 2017, figure 1.2.3b). Davidson (2014) proposes such a model: the helical wave dynamo. This theory hangs upon the observation that the convective forcing is biased towards the equatorial regions in the numerical dynamos (see figure 1.1.7). It is shown that this turbulent, buoyant region acts as a source of *inertial wave packets*, entities we study in detail in chapter 2, but it suffices for the moment to observe that they propagate energy preferentially along the rotation axis, that they are intensely helical – velocity and vorticity are always aligned for a monochromatic wave – and that their direction of propagation along the axis is determined by the sign of this helicity. In fact, from an equatorial source they will convey negative helicity into the northern hemisphere and positive helicity into the south, fully compatible with an alpha-squared dynamo as outlined above; this is confirmed in Davidson & Ranjan (2015), reproduced in figure 1.2.3c. Hence, these small-scale wave packets constitute a viable means for both generation and segregation of helicity.

1.3 Waves in the outer core

We will not discuss any further the viability of the helical wave cartoon for driving the real geodynamo, though a recent assessment can be found in Davidson & Ranjan (2018*a*). It provides motivation for this study of dispersive waves in Earth's outer core, but the results herein cover the subject more generally. Hence, we round off this introductory chapter by providing a basic introduction to the topic of waves in the outer core, in anticipation of the types of problems we will be solving for the remainder of the thesis, though a more comprehensive review can be found in Jault & Finlay (2015).

1.3.1 Wave packets vs modes

First, we iron out an important matter of semantics. In this thesis, most of the experiments (be they thought, analytical or numerical) take place in an infinite domain, with a specified localised disturbance acting as a source of *wave packets* which radiate away from it. That is to say, we are interested in a finite-sized batch of travelling waves as they propagate through an infinite space, as opposed to a set volume of fluid which is able to undergo oscillations in a set of discrete eigenmodes. This does not necessarily limit applicability — the radiation from a small (but finite) disturbance in a finite volume of fluid, which can in general be expressed as a sum of such eigenmodes, will display very similar behaviour to one planted in free space. The physical intuition garnered by understanding the life-cycles of wave packets is perhaps of more use than a detailed calculation of global eigenmodes (though we do pitch the two against each other in chapter 5).

1.3.2 Magnetic-Coriolis waves

A large portion of this thesis is occupied by the study of *magnetic-Coriolis* (MC) waves which, as the name suggests, are an amalgamation of effects due to the magnetic field and background rotation. These are fundamentally small-scale, low-amplitude, three-dimensional artefacts — meaning their wavelengths are generally shorter than (and fluctuations much less than) variations in the mean magnetic field, and they may arise naturally from any finite-size disturbance introduced into the fluid (such as a convecting buoyant anomaly). What's more, they are strongly dispersive and anisotropic. Whereas a conventional one-dimensional dispersive wave might have a propagation speed which depends on wavelength, an MC wave has a propagation *velocity* (both speed and direction) which depends on the wavevector orientation as well. That is to say, wave packets which have crests aligned in one

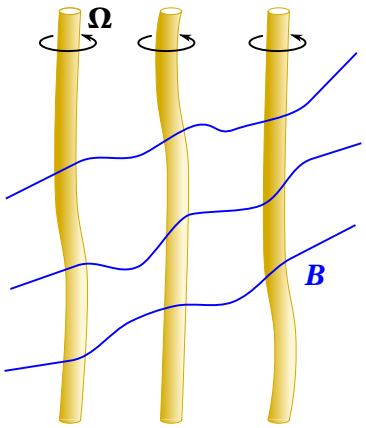

Fig. 1.3.1 Cartoon of MC wave motion — waves are propagated by both stiff vortex lines and comparatively floppy magnetic field lines.

direction will not in general have the same velocity as a similar-looking wave packet rotated by some angle. This point will prove very important going forward.

We postpone a full derivation of MC waves until chapter 3, but for now simply ask why it should be that both background rotation and magnetic fields have a propensity for oscillatory behaviour.

Consider background rotation first. In an ideal (non-conducting) fluid, vortex lines – which are everywhere parallel to the local rotation rate of fluid parcels – may be considered material curves, frozen into the fluid. Hence, the vorticity field for a volume of fluid rotating at a uniform angular velocity can be visualised (in the stationary reference frame) as a forest of aligned, equally-spaced, and equal-strength vortex lines orbiting around at the bulk rotation rate. Conservation of angular momentum implies a certain stiffness to these vortex lines — if one is locally perturbed radially inward, say, it must also gain angular velocity and therefore accelerate perpendicular to the perturbation (this is the Coriolis force in the rotating frame), thereby moving around in a circular path. The propagation of this motion along (and to some extent across) the strong vortex lines is essentially a manifestation of inertial waves.

The magnetic field may also harbour oscillations, in canonical form known as Alfvén waves (Alfvén, 1942); we discuss these in detail in chapter 3. Much like vortex lines, field lines are also frozen into the fluid. They, however, possess a more classical tension through their feedback on the fluid via the Lorentz force, which imparts field lines with a resistance to both bending and stretching. In an incompressible fluid, it is the bending which will interest us, and the associated propagation of transverse waves along field lines.

When both background rotation and a mean magnetic field are present, the resulting system is a mesh of two different wave-bearing mediums, which may (or may not) act in

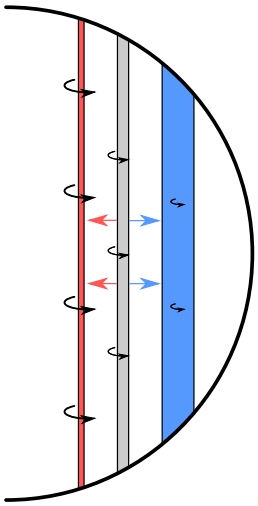

(a) Stretching of a columnar vortex due to radial displacement.

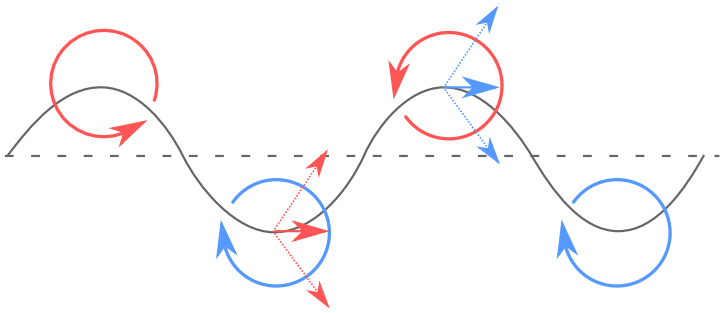

(b) Eastward-propagating wave crests due to the net induced velocity from alternately displaced columnar vortices. Bulk rotation is out of the page, and the top of the figure is inward.

Fig. 1.3.2 Mechanism behind the propagation of quasi-geostrophic Rossby waves.

different directions (figure 1.3.1). In the Earth's outer core, the dominance of rotation means the system is notably stiffer along the axis than it is in the direction of the magnetic field.

A good background to MC waves can be found in, for example, Finlay et al. (2010) or Davidson (2013) — and we will return to them at length in chapters 3 and 4.

1.3.3 Quasi-geostrophic Rossby waves

We now move onto a type of oscillation ubiquitous in atmospheric flows (Vallis, 2017), but also theorised to be possible in Earth's outer core (Hide, 1966). We discuss them from a physical point of view for the moment, as can be found in Busse (2002), before revisiting them mathematically in chapter 5.

The fundamental ingredient is one of the tall, columnar vortex lines mentioned in the previous section (figure 1.3.1), which constitute the background rotation of the Earth. As the outer core is a finite volume, the vortex lines span it completely, meeting the CMB at both ends — the grey structure in the meridional cross-section of figure 1.3.2a, say. Consider the effect of displacing this vortex line a small distance in the cylindrical radial direction (maintaining its axial coherence due to the action of inertial waves). If it is moved inward towards the inner core (shown in red on figure 1.3.2a), the distance between its ends increases and the vortex line is stretched out along the rotation axis, becoming longer and narrower. As the flux of vorticity must remain constant along its length, the vorticity magnitude must increase — the column acquires a rotation surplus compared to the bulk

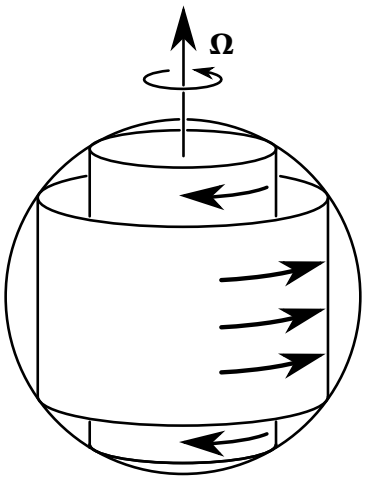

Fig. 1.3.3 Schematic of torsional oscillations (Braginsky, 1970; Finlay et al., 2010).

flow. Similarly, a column displaced outward (blue) becomes shorter, fatter, and less intense, acquiring a vorticity deficit.

Moving into the rotating frame – figure 1.3.2b – columns which move inward acquire a positive vorticity and columns which move outward, a negative vorticity. Consider therefore a sinusoidal disturbance to the fluid, which alternately displaces it inward then outward going around the azimuth. The inwardly-displaced portions become positive vortices, the net effect of which is to induce a velocity at the location of the outwardly-displaced columns, and vice versa. Referring to figure 1.3.2b, it can be seen that this velocity is purely azimuthal, and that it is eastward at all stations. Hence, the crests of QG Rossby waves always propagate eastward.

If a mean magnetic field is included as well, the dynamics of QG Rossby waves become especially rich (Finlay et al., 2010), and certain subclasses of the resulting waves have been cited as possible sources of geomagnetic secular variation (Hori et al., 2015; Hide, 1966; Finlay & Jackson, 2003).

1.3.4 Torsional Oscillations

Although we will not work directly on torsional oscillations (TOs), we do make reference to them later on, and therefore introduce them here for completeness; they were originally presented by Braginsky (1970) and Jault & Finlay (2015) contains a very useful review. The basic idea is to consider fluid motions in a sphere which are strictly invariant along the rotation axis (termed *geostrophic*). After a little thought, it can be seen that the only such motion possible is the purely azimuthal rotation of cylinders coaxial with $\mathbf{\Omega}$ (figure 1.3.3). Furthermore, it can be shown that the only (non-diffusive) force which can apply any torque

to such a cylinder is the Lorentz force due to the magnetic tension of the cylindrical radial magnetic field. This gives rise to oscillations not unlike Alfvén waves, acting in a pseudo-axisymmetric manner: the cylinder-averaged Lorentz force applies a net torque to the fluid within it, which accelerates the geostrophic cylinders accordingly. This competition between the inertia of the fluid and tension of the field lines may result in global-scale waves which propagate in the cylindrical radial direction.

1.4 Thesis outline

Within this thesis, we approach four subjects linked by the common theme that they all concern the propagation of dispersive waves in the context of Earth's outer core. We begin in chapter 2 by reviewing the theory of inertial waves in a rapidly-rotating fluid, confirming the link between their low-frequency incarnations and the proliferation of flow structures which are elongated along the rotation axis (Davidson et al., 2006). This is demonstrated through a pair of initial value problems particularly pertinent to Earth's outer core: first, we extend the theoretical work of Staplehurst et al. (2008) to the radiation of waves from a turbulent eddy of arbitrary orientation, and second, we look at the radiation of waves from a blob of buoyant material, studied numerically by Ranjan & Davidson (2014), with an eye on the interplay between inertial waves and convection.

The model problems in chapter 3 follow in a similar vein, but crucially include a mean magnetic field as well, in order to determine the importance of the various flavours of MC waves in the radiation of information from a localised disturbance. The conclusions, published in Bardsley & Davidson (2016), suggest that a hitherto overlooked class of waves – dubbed *inertial-Alfvén waves* – play a very important part in this process.

Chapter 4 builds upon this result, looking at what happens when an inertial-Alfvén wave packet travels through a mean magnetic field which varies through space, as must be the case in the core of the Earth. The key finding, which may also be found in Bardsley & Davidson (2017), is that the wave packets are forced to evolve into a more general form of MC wave, which may in some cases profoundly affect their dispersive behaviour.

Our final investigation connects the dispersive propagation of hydrodynamic Rossby waves with the observed westward drift of the non-dipolar part of Earth's magnetic field. This new theory, originally proposed in Bardsley (2018), stands somewhat apart from the rest of the thesis — as such, chapter 5 is a close reproduction of this recent publication.

Chapter 2

Waves at small scales I: Inertial waves

2.1 Introduction

The range of spatial scales involved in the operation of the geodynamo is vast; from the magnetosphere, extending tens of thousands of kilometres into space, down through the scales of Earth's interior – an outer core radius of 3485km and observable magnetic field features on the order of 1000km – to the radius of the smallest turbulent eddy within the fluid outer core, the interaction of physical processes over widely varying spatial scales is an intrinsic feature of any dynamo theory. Nested within this observation is perhaps the most profound question in the subject: how does the chaotic convective driving at the very smallest scales within Earth's outer core contrive to produce a mean magnetic field with such a reliable dipolar structure at global scales?

This chapter and the next concern themselves with the radiation of waves, and therefore information, from the smallest scales within Earth's core. This seems an obvious starting point if one is to begin to understand the up-scale energy transfer required to maintain the geodynamo. Much of this work follows a very traditional line of theoretical investigation into waves in an unconstrained, rapidly rotating and conducting fluid, yet rather surprisingly some of the conclusions drawn differ significantly from the classical analysis.

2.1.1 The importance of waves at the small scales

There is a lot to be said for having a good intuition for what is happening at the smallest scales of motion within Earth's core before beginning to discuss how global processes might be operating. As mentioned earlier, the story of the geodynamo really begins here, with the cooling and solidifying inner core driving strongly forced convection, providing a vigorous, chaotic, turbulent source upon which the magnetic field can feed. Exactly how this energy

transfer occurs is an open question, though it seems almost certain that waves are somehow involved, since both the rapid background rotation and mean magnetic field constitute wave-bearing systems. Whether one takes the view that the waves are directly responsible for the transport of energy between buoyancy and magnetic fields (Davidson, 2014) or not, there is no escaping the fact that MHD waves play an important role in the outer core ecosystem, since they underpin fundamental physical processes upon which the geodynamo relies.

There is also an important link between waves and numerical simulations, since waves represent information transport and simulations are required (by some sort of Courant condition) to time-march cautiously enough to retain this information. That is to say, an explicit time-stepping scheme, in order to remain stable, must take sufficiently small time-steps that the fastest waves cannot travel further than the width of a grid cell per step. An implicit scheme – which uses information from the latter time instant to update the solution – does not suffer the same stability requirements, but taking large time-steps will nevertheless compromise the accuracy of such a solution. The numerical dynamo problem suffers the misfortune of being incredibly stiff — one wishes to study the core's evolution over magnetic diffusion timescales on the order of tens of thousands of years, yet is obliged to capture inertial waves at the smallest scales whose propagation is measured in days or weeks. As such, numerics are forced to run on the very limit of accurately resolving these waves, and so it is not certain their dynamics are being correctly rendered. (Though note that Ranjan et al. (2018) have recently found inertial waves in numerical simulations run with smaller time-steps.)

Nevertheless, the idea can be taken a whole step further by making simplifying assumptions in the governing equations which remove the need to resolve these waves entirely. This is what is being done by assuming incompressibility, for example — the neglect of density perturbations filters out sound waves and the resulting system can be successfully computed using very much larger time-steps as the acoustic behaviour has been ignored. An appealing next step is to also filter out inertial waves, resulting in a so-called *quasi-geostropic* model (e.g. Cardin & Olson, 1994; Aubert et al., 2003; Schaeffer & Cardin, 2005; Gillet & Jones, 2006; Canet et al., 2014; Guervilly & Cardin, 2016; Maffei et al., 2017) which can be solved much faster, but neglects some physics in order to achieve this. Going even further, one could neglect inertia entirely (thereby filtering out both inertial and Alfvén waves) to produce a *Taylor-state* system which evolves only via magnetic induction (Taylor, 1963; Livermore et al., 2008; Roberts & Wu, 2014). The appeal of such approaches is that they remove the need for excessive time-stepping, but they are certainly not without their drawbacks (Walker et al., 1998); self-consistent Taylor-state dynamos in particular have proved difficult to find despite

over half a century of effort (though see Hardy et al. (2018); Li et al. (2018) for recent progress on this front).

Whether one is running a simulation which barely resolves the fastest waves, or utilising a reduced model which filters them out entirely, an understanding of their basic dynamics should be a prerequisite if any meaningful conclusions are to be drawn. This, and a more general desire to gain a deeper appreciation of the fundamental physical processes behind the geodynamo, motivates the present work.

2.1.2 How small is a small scale?

Since our objective is an understanding of the small-scale motion within Earth's outer core, a necessary first step is to conjecture how small these scales might be. A significant obstacle to geodynamo research is the dissonance between the scales we can observe – up to spherical harmonic degree 13 at the CMB, owing to the magnetic curtain (Roberts & King, 2013) – and the relevant lengthscales of the internal fluid flow. The former are distressingly large, whereas the latter are unknown and necessarily orders of magnitude smaller (Davidson, 2016; Holme et al., 2011). Determining exactly how small would be a major advance in the field, though present observational evidence allows only for best guesses. In essence, the question is by what mechanism the fluid selects the smallest scale. Is it the convective driving which fixes an eddy size, which the magnetic field then feeds off? Or is the dissipation method – of which the vast majority is Ohmic heating – prescribing a minimum lengthscale below which the flow is suppressed? Furthermore, the lengthscales are almost certainly a long way from isotropic, as the rapid rotation will tend to elongate structures along the polar axis, and are probably not even homogeneous, with forcing, energy transfer, and dissipation potentially inhabiting different, albeit overlapping, regions of the fluid. Any estimate will therefore involve a number of simplifications, caveats and assumptions, so should be taken with a strong pinch of salt.

Perhaps the simplest argument which produces a minimum lengthscale rests upon magnetic dissipation (Davidson, 2013). The postulate is that any flow structure with a magnetic Reynolds number $Rm = u\ell/\eta$ less than unity will be arrested by Ohmic losses so therefore cannot be physically significant. Using a characteristic flow speed of $0.4\text{mm}\,\text{s}^{-1}$ (Roberts & King, 2013) and diffusivity $0.5\text{m}^2\,\text{s}^{-1}$ (Pozzo et al., 2014) gives the condition $\ell \gtrsim 1.3\text{km}$ as an estimate for the smallest structures within the velocity field, so one should perhaps take $\ell \sim 10\text{km}$ as a characteristic lengthscale of the smallest scales of interest. Note that this dissipation argument does not necessarily imply heavy damping of waves with similar wavelengths; the waves we are to study will have propagation speeds generally

very much greater than the flow velocity, meaning they can still travel significant distances without appreciable attenuation.

It is worth noting that one could also attempt to extract a lengthscale from the results of numerical simulations. We choose not to do this — firstly, because it is not yet clear that the simulations have reached a small enough Ekman number for ℓ to be independent of viscosity, and secondly because ℓ still appears to be reducing as the simulation power (and therefore resolution) increases and the extreme parameters edge closer to geophysically realistic values (Schaeffer et al., 2017; Aubert, 2018).

2.1.3 The convective driving

To motivate the model problems which will occupy the majority of this section, we consider the principal means by which the outer core is stirred — namely, convection from the hot inner core out towards the comparatively cool mantle. This manifests itself in two ways; thermal convection, as the inner core gradually cools and the Earth as a whole radiates heat into space, and compositional convection. The latter occurs because the liquid iron outer core contains traces of light elements, such as sulphur and oxygen, which come out of solution as the metal gradually freezes at the ICB. This material is then buoyant compared to its surroundings, so acts as an additional energy source. The relative contribution of each mechanism is unknown (Braginsky & Roberts, 1995), but is of little consequence for our purposes; gravitating buoyant anomalies will act as sources of waves regardless of the means by which the buoyancy is derived.

Although the convection is strongly forced, in the sense that the Rayleigh number $Ra = \beta_T g \Delta T / \Omega^2 D$ is probably about 10^4 times its critical value (Christensen, 2011), the density perturbations and therefore convective velocities are very small compared to wave propagation speeds, with overturning times D/u on the order of hundreds of years comparing to inertial wave timescales of days or weeks, and Alfvén wave timescales of a couple of years. Hence, in what follows we consider any buoyant source to be effectively static — that is, we do not solve any kind of thermal or compositional evolution equation, but instead simply include a Boussinesq buoyancy term in the momentum balance. Whilst this is not utterly watertight physically, since the approach provides an effectively infinite energy source, on the shorter timescales of the waves the approximation is reasonable — we will show this is the case *a posteriori* through comparison with the direct numerical simulations (DNS) of Davidson & Ranjan (2015). In reality the density field will be gradually evolving, as a result of a combination of buoyancy, magnetic, rotational and diffusive effects, as well as mean flows instigated by the waves themselves. As it evolves, the flow is required to constantly re-adjust to the new density field, which on the fastest timescales means radiating yet more waves;

the convection therefore acts as a persistent, stochastic source of waves which endeavour on short length and time scales to establish global balance.

The spatial structure of outer core convection is, of course, largely unknown. It seems in numerical simulations that it depends somewhat upon the thermal boundary conditions used — in particular, whether one chooses a fixed temperature or a fixed heat flux at the CMB (Sakuraba & Roberts, 2009; Hori et al., 2010; Sakuraba & Roberts, 2011; Matsui et al., 2014; Amit et al., 2015). The latter is more challenging, but physically more realistic, and can lead to stronger convection and magnetic field. Inhomogeneity at the boundaries may also play a role, either at the CMB due to variations in mantle composition (Gubbins, 2013), or at the ICB due to intricacies of the solidification process. One possibility is a thin 'mushy zone' at the ICB, which acts as a porous layer in which buoyant material is accumulated, then erupts intermittently, releasing parcels of light fluid into the bulk of the outer core (Loper & Roberts, 1981; Moffatt & Loper, 1994). A paradigm such as this lends itself to the idea that the study of wave radiation from small, localised sources (hereafter *blobs*) will tell us a lot about the dynamics of the outer core. Note that each blob may lose some coherency as the flow evolves (St Pierre, 1996), so the blob model of Moffatt & Loper (1994) cannot be pushed too hard. However, any form of stochastic turbulent convection, whether isolated or a large region, may be thought of as a sum of localised features – buoyant blobs and/or turbulent eddies – across a range of scales, each of which acts as a source of waves. Since the waves are linear, the solution for any number of sources can be superimposed, so understanding the radiation from one localised source informs the picture for a larger convecting region.

As well as details of the structure of the convection itself, its global distribution is also of considerable importance for the dynamo's operation. The outer core can essentially be divided into three regions, separated by the tangent cylinder, an imaginary surface aligned with the rotation axis and circumscribing the inner core. The regions directly north and south of the inner core are probably of less relevance for the operation of an α^2-dynamo (Christensen, 2011), despite the fact they appear to carry a considerable heat flux away from the inner core in simulations (e.g. Sheyko et al., 2018). The region outside of the tangent cylinder is thought to harbour the majority of dynamo action, and therefore the distribution of convective flux there is of much more interest. A number of simulations have found this heat flux to be biased towards the equatorial regions — this is most pronounced in the results of Sakuraba & Roberts (2009, 2011), who employ a fixed heat flux boundary condition at the CMB (see figure 2.1.1a), though does appear to be more generally observed (Takahashi & Shimizu, 2012; Sheyko et al., 2018, for example). This equatorial bias to the forcing is a cornerstone of the helical wave model of planetary magnetic field generation of Davidson (2014), since it hinges upon the release of polewards-propagating waves from an equatorial

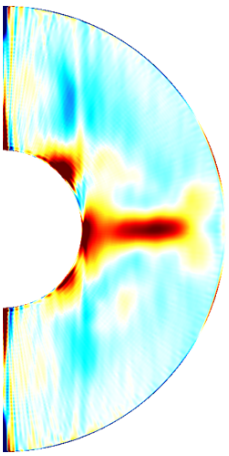

(a) Azimuthally-averaged radial velocity in a meridional slice, red outwards and blue inwards. From Sakuraba & Roberts (2009).

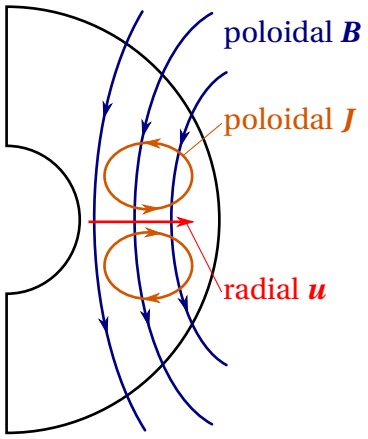

(b) The Lorentz force due to the poloidal electromagnetic field distribution is balanced by the Coriolis force at the equator, implying an outward flow.

Fig. 2.1.1 A possible explanation for the equatorial bias to convection in numerical dynamos, from Sakuraba & Roberts (2009, 2011).

source in order to establish the required helicity segregation (negative in the north, positive in the south) for an α^2-dynamo.

However, it is worth asking what the physical mechanism might be behind this preference for equatorial convection. Inspecting the numerical simulations (e.g. Sheyko, 2014), it seems that – all other parameters being equal – the equatorial bias appears most consistently in simulations featuring a magnetic field, making it a likely culprit. Since it is well-understood that a strong magnetic field inhibits convection (Chandrasekhar, 1981), simply arguing that $\boldsymbol{B}$ tends to be stronger away from the equatorial plane (at least in terms of its azimuthal component) provides a simplistic rationale behind the equatorial heat flux.

A plausible alternative, as presented by Sakuraba & Roberts (2011), rests upon a large-scale azimuthally-integrated force balance in which Coriolis, Lorentz and buoyancy forces are of similar magnitudes, the so-called MAC (*Magnetic-Archimedean-Coriolis*) balance. For an dynamo which is operating in some average sense as α^2, the poloidal field structure consists of a dipolar magnetic field which is chiefly axial at the equator and a quadrupolar current distribution which is chiefly radial at the equator (figure 2.1.1b). If the magnetic field runs north-south through the core, the current is outwards – and vice versa – so the associated Lorentz force $\boldsymbol{J} \times \boldsymbol{B}$ is azimuthal and eastward at the equator. Since the buoyancy term has no azimuthal component, and the pressure forces cancel as a result of the azimuthal

integration, the leading-order balance must be between Lorentz and Coriolis forces:

$$\oint \left(2\rho\boldsymbol{\Omega}\times\boldsymbol{u}\right)_\phi \mathrm{d}\phi \sim \oint \left(\boldsymbol{J}\times\boldsymbol{B}\right)_\phi \mathrm{d}\phi. \tag{2.1.1}$$

Using an axially-oriented cylindrical polar co-ordinate system with $\boldsymbol{\Omega} = \Omega\boldsymbol{e}_z$, $\boldsymbol{J} \approx J_s\boldsymbol{e}_s$ and $\boldsymbol{B} \approx -B_z\boldsymbol{e}_z$, we require

$$\oint u_s \mathrm{d}\phi \sim \frac{1}{2\rho\Omega}\oint J_s B_z \mathrm{d}\phi, \tag{2.1.2}$$

and therefore the radial velocity is positive near to the equatorial plane, as the need to balance Lorentz and Coriolis forces at the large scales draws out fluid from the hot inner core, carrying the buoyancy field with it.

Note that, in the case of helical wave dynamos, the reasoning here is somewhat circular; the equatorial heat flux releases waves which segregate helicity, which maintains an α^2-dynamo, which encourages an equatorial heat flux. This makes some sense, as the geodynamo is a self-excited system, so any plausible theory must include some element of feedback, but also – thanks in part to the dearth of observational evidence – makes the theory somewhat speculative. However, evidence from numerical simulations, particularly as their viscosities are further reduced (Schaeffer et al., 2017; Aubert, 2018), is beginning to point towards the importance of small-scale waves in their operation; whether they are actually driving magnetic field renewal or not, their relevance to Earth's interior cannot be ignored.

2.1.4 Choice of model problems

In our quest to better understand the dynamics of waves at the smallest scales within the Earth, we will make extensive use of simple initial value problems, in which either the velocity or buoyancy field is specified at $t = 0$ and the governing equations evolved in order to observe the various waves it gives off. In some sense, an initial value problem is somewhat artificial – a localised vortex or blob of buoyant material never spontaneously appears in Earth's outer core – but they are nevertheless very useful for gaining intuition as to how a continuously evolving system might behave.

We variously make use of a localised vortex or buoyant blob as the initial condition in the following problems. The former is useful because it provides a finite quantity of energy, which the system then radiates in the most favourable way, making it easier to identify the nature of the waves as they propagate away from their origin. The latter is perhaps more applicable to Earth's outer core, as a proxy for thermal or compositional convection, though the vortex could also represent a turbulent eddy in a similar context.

Section	Initial condition	Magnetic field
2.2.5	Vortex	None
2.2.6	Buoyant blob	None
3.1.4	Buoyant blob	Axial
3.2.2	Buoyant blob	Azimuthal
3.2.4	Vortex	Azimuthal

Table 2.1.1 Summary of initial value problems solved in this chapter and the next.

When considering a buoyant source, we assume both that it is not dynamically active, as discussed already, but also employ the Boussinesq approximation, including density perturbations only in the gravitational body force term of the momentum equation and neglecting the corresponding change in inertia.

In all cases we use a domain which is effectively infinite, though for obvious reasons only compute the solution over a finite region around the source. This is justified for sources which are both small and a long way from the CMB, for which reflections are of zero importance on the timescales considered.

We linearise the governing equations, thereby restricting the analysis to waves whose amplitude is small compared to the background quantities. Indeed, any large-scale velocity field (in excess of the planetary rotation) is neglected entirely. In addition, the background state is considered homogeneous, with the planetary rotation $\boldsymbol{\Omega}$, gravitational acceleration $\boldsymbol{g}$ and mean magnetic field $\bar{\boldsymbol{B}}$ all represented by constant vectors. In doing so, we are making the assumption that the source is much smaller than any spatial variations in the above quantities. This is reasonable for $\boldsymbol{\Omega}$ and $\boldsymbol{g}$, but perhaps not so good for $\boldsymbol{B}$; we address this issue in chapter 4.

We use a Cartesian co-ordinate system $[x, y, z]$ which may be thought of as a local system in which x is (cylindrically) radial, y azimuthal and z axial. The background rotation vector is always taken to be in the z-direction, $\boldsymbol{\Omega} = \Omega \boldsymbol{e}_z$, and for buoyant blob problems the gravitational acceleration is radially inwards, $\boldsymbol{g} = -g\boldsymbol{e}_x$; this places the blob somewhere in the equatorial region, mimicking the low-latitude concentration of heat flux observed in simulations. Finally, the magnetic field is allowed to have one of two orientations; either axial, $\bar{\boldsymbol{B}} = \bar{B}\boldsymbol{e}_z$, or azimuthal, $\bar{\boldsymbol{B}} = \bar{B}\boldsymbol{e}_y$. The former replicates the poloidal field near the equator, which will be in an average sense directed along the axis, whereas the latter captures the effect of the strong toroidal field expected within the core (Zhang & Fearn, 1993).

Table 2.1.1 summarises the initial value problems solved in this chapter. We first inspect the non-magnetic case, to understand the dynamics of inertial waves in a rapidly-rotating fluid stirred either by turbulence or convection. We then ask how these solutions will be

modified by a background magnetic field, detailing the various classes of waves which then become possible. A traditional line of reasoning then suggests that certain subsets of these waves – the inertial and magnetostrophic branches – should dominate the picture, and indeed we can show this is the case for an axial $\bar{\boldsymbol{B}}$. However, the final section focusses upon a very important situation in which the classical mode of thinking does not apply, and a third subset – dubbed inertial-Alfvén waves – in fact dominate. This observation raises fundamental questions over the correct paradigm for small-scale wave motion in planetary cores.

2.1.5 Mathematical approach

Since most of the mathematical working will be exiled to appendices, we briefly outline here how the solutions to the following initial value problems are calculated.

The basic idea is to use Fourier transforms in space to convert all spatial derivatives into algebraic expressions, then solving the resulting equations in time via standard differential equation techniques. The Fourier-space solution is then transformed back into real space by evaluating a series of integrals, some analytically and some numerically using multi-dimensional quadrature. For reference, the three-dimensional Fourier transform and its inverse are defined by

$$\hat{q} = \frac{1}{(2\pi)^{3/2}} \iiint_{-\infty}^{\infty} q e^{-i\boldsymbol{k}\cdot\boldsymbol{r}} \mathrm{d}^3\boldsymbol{r}, \qquad q = \frac{1}{(2\pi)^{3/2}} \iiint_{-\infty}^{\infty} \hat{q} e^{i\boldsymbol{k}\cdot\boldsymbol{r}} \mathrm{d}^3\boldsymbol{k}, \tag{2.1.3}$$

where $\hat{q}(\boldsymbol{k}, t)$ is the transform of some scalar field $q(\boldsymbol{r}, t)$.

In general, the Fourier-transformed solutions will take the form of harmonic functions of ϖt, where $\varpi(\boldsymbol{k})$ is a wave frequency, multiplied by certain coefficients (functions of $\boldsymbol{k}$); for initial value problems, these coefficients are found by matching the transform of the solution at $t = 0$ to the transform of the initial condition. The governing equations also give information about the time derivatives of the solution initially, which also must be used in determining other coefficients. For the buoyant blob problems, there also exists a particular integral – a steady solution which balances the buoyant forcing – which must be cancelled out by a complementary function at $t = 0$.

2.2 Inertial waves in a rapidly-rotating fluid

Our study of small-scale waves in Earth's outer core begins with a discussion of the behaviour of inertial waves, a cornerstone of rapidly-rotating fluid dynamics. In this section, we derive

their governing equations and rather unintuitive dispersive properties, then demonstrate their importance in establishing and maintaining axially-elongated flow structures in a rapidly-rotating fluid through a series of model problems.

2.2.1 The equations of motion for a rapidly-rotating fluid

To a very good approximation, the outer core of the Earth is believed to be in a state of solid-body rotation at a rate Ω of approximately 2π radians per day. There is unlikely to be much differential rotation since the inner core is thought to be gravitationally and magnetically locked to the mantle over long timescales (Dumberry & Mound, 2010). It is therefore advantageous to consider the problem in a rotating reference frame, for which the velocity field corresponding to the steady bulk rotation $\boldsymbol{u}_\Omega = \boldsymbol{\Omega} \times \boldsymbol{r}$ is cancelled out. That is, the velocity field in the inertial frame $\boldsymbol{u}_I$ may be separated in two,

$$\boldsymbol{u}_I = \boldsymbol{u}_R + \boldsymbol{u}_\Omega = \boldsymbol{u}_R + \boldsymbol{\Omega} \times \boldsymbol{r} \tag{2.2.1}$$

where $\boldsymbol{u}_R$ is the velocity field in the rotating frame. This can be rewritten

$$\left(\frac{\partial \boldsymbol{r}}{\partial t}\right)_I = \left(\frac{\partial \boldsymbol{r}}{\partial t}\right)_R + \boldsymbol{\Omega} \times \boldsymbol{r} \tag{2.2.2}$$

where the subscripts again indicate the reference frame. Hence, the equations of motion in the inertial frame may still be used in the rotating frame, so long as the operator $\frac{\partial}{\partial t}$ is replaced by $\frac{\partial}{\partial t} + \boldsymbol{\Omega}\times$. Thus, the fluid acceleration becomes

$$\frac{\partial \boldsymbol{u}}{\partial t} = \frac{\partial^2 \boldsymbol{r}}{\partial t^2} \implies \left(\frac{\partial}{\partial t} + \boldsymbol{\Omega}\times\right)\left[\frac{\partial \boldsymbol{r}}{\partial t} + \boldsymbol{\Omega} \times \boldsymbol{r}\right] = \frac{\partial \boldsymbol{u}}{\partial t} + 2\boldsymbol{\Omega} \times \boldsymbol{u} + \boldsymbol{\Omega} \times (\boldsymbol{\Omega} \times \boldsymbol{r}) \tag{2.2.3}$$

where time derivatives and velocities on the right-hand side are now understood to be taken in the rotating reference frame. The second term on the right-hand side is the Coriolis force, a fictitious contribution to the momentum equation which causes particle paths in the rotating frame to deflect in antithesis to the bulk rotation — so an inward-moving particle is pushed in a prograde direction, and an outward moving particle retrograde. In the inertial frame, this is a direct consequence of angular momentum conservation; a fluid lump displaced inwards gains angular velocity, and vice versa. The third term is the centrifugal force, which may be written as $\boldsymbol{\Omega} \times (\boldsymbol{\Omega} \times \boldsymbol{r}) = -\nabla\left(\frac{1}{2}\left[\boldsymbol{\Omega} \times \boldsymbol{r}\right]^2\right)$ and therefore absorbed into the pressure when considering the momentum conservation equation in the rotating frame:

$$\frac{\partial \boldsymbol{u}}{\partial t} + (\boldsymbol{u} \cdot \nabla)\, \boldsymbol{u} + 2\boldsymbol{\Omega} \times \boldsymbol{u} = -\nabla\left(\frac{p'}{\rho}\right) + \frac{\boldsymbol{F}}{\rho} + \nu\nabla^2 \boldsymbol{u} \tag{2.2.4}$$

	$Ro = U/\Omega L$	$Ek = \nu/\Omega L^2$
$L = D = 2254\text{km}$	$\sim 2 \times 10^{-6}$	$\sim 3 \times 10^{-15}$
$L = \ell = 10\text{km}$	$\sim 6 \times 10^{-4}$	$\sim 10^{-10}$

Table 2.2.1 Estimates of Rossby and Ekman numbers at Earth's core conditions, demonstrating the dominance of the Coriolis force. The estimates $U \sim 0.4\text{mm}\,\text{s}^{-1}$ (Roberts & King, 2013) and $\nu \sim 10^{-6}\text{m}^2\,\text{s}^{-1}$ (de Wijs et al., 1998) are used.

where $p' = p - \frac{1}{2}\rho\,[\boldsymbol{\Omega} \times \boldsymbol{r}]^2$ is the *reduced pressure* and $\boldsymbol{F}$ represents any body forces which may be acting. As the fluid is incompressible, this is supplemented by the solenoidal condition

$$\nabla \cdot \boldsymbol{u} = 0, \tag{2.2.5}$$

which completes the governing equations for the velocity field.

Now, in order to approach these equations from an analytical standpoint, it will be necessary to make some simplifying assumptions, and the most reasonable way to achieve this in the context of Earth's core is to make use of the fact that the background rotation is very rapid and therefore the Coriolis force is dominant. It is possible to gauge how dominant through two dimensionless numbers — the Rossby number $Ro = u/\Omega L \sim |(\boldsymbol{u}\cdot\nabla)\,\boldsymbol{u}|\,/\,|2\boldsymbol{\Omega}\times\boldsymbol{u}|$, which judges the relative importance of the non-linear advection and Coriolis terms, and the Ekman number $Ek = \nu/\Omega L^2 \sim \left|\nu\nabla^2\boldsymbol{u}\right|\,/\,|2\boldsymbol{\Omega}\times\boldsymbol{u}|$ which compares viscous and rotational effects. We make estimates of both Ro and Ek at the smallest and largest outer core lengthscales in table 2.2.1; both are clearly very much less than unity for any realistic choice of 'Earth-like' conditions. We therefore neglect both the non-linear advection and viscous terms in (2.2.4), and for the moment ignore body forces, giving the linear equation

$$\frac{\partial \boldsymbol{u}}{\partial t} + 2\boldsymbol{\Omega}\times\boldsymbol{u} = -\nabla\left(\frac{p'}{\rho}\right) \tag{2.2.6}$$

for the evolution of $\boldsymbol{u}$. Note we have made no approximations regarding the $\frac{\partial \boldsymbol{u}}{\partial t}$ term, and therefore have no preselected timescale of motion; it will instead arise naturally through the equation solution.

2.2.2 Dynamics of inertial waves

The momentum equation (2.2.6), coupled with (2.2.5), admits oscillatory solutions known as *inertial waves*, in recognition of the absence of any other forces acting upon the fluid. In order to unveil these solutions, we follow closely a standard derivation as can be found in Davidson (2013), for example. First, we eliminate pressure by taking the curl of (2.2.6),

giving the vorticity evolution equation

$$\frac{\partial \boldsymbol{\omega}}{\partial t} = (2\boldsymbol{\Omega} \cdot \nabla)\, \boldsymbol{u}, \tag{2.2.7}$$

which states that any variation in the velocity field along the rotation axis will act as a source of vorticity aligned with the flow — and that the only truly steady motions possible are those in which the velocity field is independent of distance along the axis (the Taylor-Proudman theorem: Proudman (1916); Taylor (1917)). To cast this as an equation for $\boldsymbol{u}$ alone, we take a further curl and time derivative, then substitute (2.2.7) itself into the result, giving the 'inertial wave equation'

$$\frac{\partial^2}{\partial t^2}\nabla^2 \boldsymbol{u} + (2\boldsymbol{\Omega} \cdot \nabla)^2\, \boldsymbol{u} = 0. \tag{2.2.8}$$

In an infinite domain, we may seek normal-mode solutions to this equation of the general form

$$\boldsymbol{u}(\boldsymbol{r}, t) = \mathbb{R}\left\{\tilde{\boldsymbol{u}} e^{i(\boldsymbol{k}\cdot\boldsymbol{r} - \varpi t)}\right\} \tag{2.2.9}$$

with some arbitrary complex amplitude $\tilde{\boldsymbol{u}}$, a wavenumber vector (or wavevector) $\boldsymbol{k}$ – which is perpendicular to the wave crests and troughs – and a frequency ϖ. The relationship between these last two quantities can be found by plugging (2.2.9) into the inertial wave equation (2.2.8):

$$\varpi = \pm \frac{2\boldsymbol{\Omega} \cdot \boldsymbol{k}}{k}. \tag{2.2.10}$$

This is the dispersion relationship for inertial waves. Note that the frequency is independent of the magnitude of the wavevector, and depends only on the angle between the wave crests and the rotation axis. Also, each choice of $\boldsymbol{k}$ admits two possible solutions for ϖ — we will see soon that these correspond to waves propagating parallel or antiparallel to the rotation axis. There is a certain redundancy in this dispersion relationship, since negating both $\boldsymbol{k}$ and ϖ in (2.2.9) would give no substantive change to the solution; to address this, we establish the convention that frequencies are always non-negative, $\varpi \geq 0$, and therefore the only valid solutions to (2.2.10) are those for which the sign of $\boldsymbol{\Omega} \cdot \boldsymbol{k}$ matches the choice of upper or lower sign in $\pm$. In other words, wavevectors with $\boldsymbol{\Omega} \cdot \boldsymbol{k} > 0$ take the upper sign, and those with $\boldsymbol{\Omega} \cdot \boldsymbol{k} < 0$ the lower sign. This means each choice of $\boldsymbol{k}$ corresponds to a single ϖ in (2.2.10). (Although it seems a little redundant here, this matter of bookkeeping will become important when tracking wave paths in chapter 4.)

The crests of inertial waves travel at the phase velocity

$$\boldsymbol{c}_p = \frac{\varpi}{k}\boldsymbol{e}_k = \pm \frac{2\boldsymbol{\Omega} \cdot \boldsymbol{k}}{k^2}\boldsymbol{e}_k, \tag{2.2.11}$$

and since this depends on $\boldsymbol{k}$ (both in its magnitude and orientation), the waves are dispersive; their propagation speed and direction are both functions of wavevector. It is a well-known result of dispersive wave theory (Lighthill, 1978; Acheson, 1990) that the wave energy propagates not at the phase velocity, but instead at the *group velocity* $\boldsymbol{c}_g$, defined as the gradient in $\boldsymbol{k}$-space of the frequency. For inertial waves, this is

$$\boldsymbol{c}_g = \pm\frac{\boldsymbol{k}\times(2\boldsymbol{\Omega}\times\boldsymbol{k})}{k^3} = \pm\frac{2\boldsymbol{\Omega}-(2\boldsymbol{\Omega}\cdot\boldsymbol{e}_k)\,\boldsymbol{e}_k}{k}, \tag{2.2.12}$$

and since

$$\boldsymbol{c}_g\cdot\boldsymbol{e}_\Omega = \pm\frac{2\Omega}{k}\left[1-(\boldsymbol{e}_\Omega\cdot\boldsymbol{e}_k)^2\right], \tag{2.2.13}$$

we can confirm that waves which take the upper sign travel along the rotation axis ('upwards' or 'northwards') and those which take the lower sign travel in the opposite direction ('downwards' or 'southwards') — as well as potentially having some component of $\boldsymbol{c}_g$ perpendicular to this.

An alternative viewpoint

The details of the dispersive characteristics of inertial waves are complicated, counter-intuitive, and often downright bizarre. A slightly neater way of studying them uses a spherical polar co-ordinate system aligned with the rotation axis, which we take to be $\boldsymbol{e}_z$ (i.e. choose $\boldsymbol{\Omega}=\Omega\boldsymbol{e}_z$). We then let θ_k be the angle between $\boldsymbol{\Omega}$ and $\boldsymbol{k}$, and $\boldsymbol{e}_{\theta_k}$ the corresponding unit vector coming down from the z-axis; this means the frequency, phase velocity and group velocity may be written

$$\varpi = \pm 2\Omega\cos\theta_k, \tag{2.2.14a}$$

$$\boldsymbol{c}_p = \pm\frac{2\Omega}{k}\cos\theta_k\boldsymbol{e}_k, \tag{2.2.14b}$$

$$\boldsymbol{c}_g = \mp\frac{2\Omega}{k}\sin\theta_k\boldsymbol{e}_{\theta_k}. \tag{2.2.14c}$$

This representation makes it easier to highlight a few interesting features of inertial waves:

1. Their frequencies are constrained to the range $|\varpi|\le 2\Omega$, so any forcing at a frequency greater than twice the rotation rate will not radiate energy — the solutions will be evanescent;

2. Both phase and group velocities scale as k^{-1}, and therefore are proportional to the wavelength, meaning longer waves propagate faster for a given θ_k;

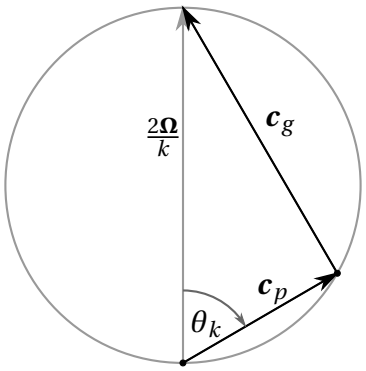

Fig. 2.2.1 Relationship between phase and group velocities for northward-propagating inertial waves. As θ_k varies the head of the $\boldsymbol{c}_p$ arrow (base of $\boldsymbol{c}_g$ arrow) traces out the grey circle with diameter $2\Omega/k$.

3. The phase velocity, group velocity and rotation vector are all coplanar, and moreover satisfy the condition $\boldsymbol{c}_p + \boldsymbol{c}_g = \pm 2\boldsymbol{\Omega}/k$. As one might expect, the azimuthal angle of $\boldsymbol{k}$ about the rotation axis has no effect;

4. The phase and group velocities are always perpendicular, $\boldsymbol{c}_p \cdot \boldsymbol{c}_g = 0$, and therefore energy always propagates along, rather than with, the wave crests;

5. If $\theta_k = 0$ (wave crests perpendicular to $\boldsymbol{\Omega}$), the group velocity also vanishes and no energy is propagated;

6. Conversely, as $\theta_k \to \pi/2$ (wave crests parallel to $\boldsymbol{\Omega}$), the phase velocity vanishes but the group velocity remains finite and directed along the rotation axis. This curious case will prove to be of utmost importance in the dynamics of rapidly-rotating fluids.

Furthermore, points 3 and 4 suggest a useful diagrammatic representation of the relationship between $\boldsymbol{c}_p$ and $\boldsymbol{c}_g$, shown for northward-propagating waves in figure 2.2.1. In this diagram, the vector $\boldsymbol{c}_p$ always starts at the bottom, with its end being constrained to move on the grey circle of diameter $2\Omega/k$ as θ_k varies. The group velocity vector $\boldsymbol{c}_g$ then starts where $\boldsymbol{c}_p$ finishes, and ends at the top of the same circle. Recall that northward-propagating waves necessarily have $\boldsymbol{\Omega} \cdot \boldsymbol{k} > 0$, and therefore $|\theta_k| < \pi/2$; the diagram for southward-propagating waves will simply be the vertical reflection of figure 2.2.1.

2.2.3 Axially-elongated flow structures

A ubiquitous feature of rapidly-rotating flows is the formation of flow features which are extended along the rotation axis, so as to be almost independent of the axial co-ordinate z. This is a hallmark of low Rossby number flows (typically $Ro \lesssim 0.4$, see Wang et al. (2004);

Staplehurst et al. (2008)) in which the magnitude of vorticity associated with the background rotation outweighs that of the flow in the rotating frame, and is commonly found in a wide range of numerical simulations and experiments into rapidly rotating turbulence and/or convection (Davidson, 2012; Julien et al., 2012; Baqui & Davidson, 2015). As we shall see – in the hydrodynamic case at least – this predilection for columnar flow structures is a direct consequence of the action of inertial waves.

The most simplistic and frequently-offered explanation for these axially-elongated flows is the *Taylor-Proudman theorem* (Proudman, 1916; Taylor, 1917). This considers the vorticity equation (2.2.7) in the case where the motion is either steady, or evolving very gradually compared to the rotation period. (This is attractive for the Earth, for which convective overturn times are centuries — but note that wave speeds may be much faster than fluid velocities.) In this *quasi-steady* situation, we have $\frac{\partial \boldsymbol{\omega}}{\partial t} \approx 0$, and therefore the velocity field obeys

$$(2\boldsymbol{\Omega}\cdot\nabla)\,\boldsymbol{u} \approx 0 \quad \Longrightarrow \quad \frac{\partial \boldsymbol{u}}{\partial z} \approx 0, \tag{2.2.15}$$

meaning variations of $\boldsymbol{u}$ along the rotation axis are small. It is worth questioning exactly what this means for a rapidly-rotating fluid. If we had $(2\boldsymbol{\Omega}\cdot\nabla)\,\boldsymbol{u} = 0$ (or $\frac{\partial \boldsymbol{u}}{\partial z} = 0$) exactly, any disturbance applied to the fluid at a point would have to be exactly copied at all heights above and below that point; the flow would be strictly two-dimensional. Hence, for example, an spherical obstacle within the fluid would command a two-dimensional column of fluid above and below it to act as a rigid body — fluid inside the column would remain inside and that outside would be forced to move around the column if the obstacle were to be moved in a quasi-steady manner. This rather restrictive agreement is called a *Taylor column*.

On reflection, the Taylor-Proudman theorem does not truly offer any explanation for why rapidly-rotating flows should be columnar, but rather a tantalising mathematical suggestion that it might be close to the right paradigm. It seems to ask more questions than it answers: just how small does the Rossby number need to be? How slow is 'quasi-steady'? What if the flow is confined? How does a fluid particle know it's in a Taylor column?

This last, most fundamental question provides a key to understanding rapidly-rotating flows, as explored in Davidson (2013). The problem is this: expressions like $\frac{\partial \boldsymbol{u}}{\partial z} = 0$ above suggest a state of instantaneous adjustment, where motion at one height is immediately matched at all other heights z. This is of course impossible, since the information of the initial motion requires time to reach the rest of the fluid, and moreover bizarre, since the information seems only to travel in one direction — axially. This is similar to a problem in incompressible flows, in which the properties at a given point seem to instantaneously affect every other point in the fluid; the solution there is that sound waves, which are filtered

out by the omission of density perturbations, are in reality relaying the information in finite (albeit minimal) time.

For rapidly-rotating flows, the answer is inertial waves, which are filtered out by neglecting the time derivative in (2.2.7). They are responsible for carrying the information away from a disturbance in a rapidly-rotating flow, thereby causing it to evolve in a manner which is approximately axially-invariant. The question is still begging, however, of how the Taylor column is enforced; it represents a very strong anisotropy in the dynamics of inertial waves, since in order to maintain a Taylor column they must be carrying very much more energy axially than they are off-axis. Indeed, one could argue that the Taylor column itself is nothing more than a sea of inertial waves running up and down its length, doing their very best to eliminate any discrepancies as they go. But why should it be that inertial waves display such a strong preference for axial propagation?

Since this question is of such significance to what follows, we offer two different – but complementary – answers to it.

Conservation of axial angular & linear momentum

Consider a localised disturbance in a rapidly-rotating fluid – a buoyant blob or turbulent eddy, say – which acts as a source of inertial waves. Although the waves may radiate energy in any direction (with the exception of perfectly horizontally), they can only transport axial angular momentum in one direction — along the rotation axis (Davidson et al., 2006). To see this, consider the axial component of $\boldsymbol{r}\times$(2.2.6):

$$\frac{\partial}{\partial t}(\boldsymbol{r}\times\boldsymbol{u})_z+\boldsymbol{e}_z\cdot[\boldsymbol{r}\times(2\boldsymbol{\Omega}\times\boldsymbol{u})]=\boldsymbol{e}_z\cdot\nabla\times\left(\frac{p'\boldsymbol{r}}{\rho}\right), \tag{2.2.16a}$$

$$\frac{\partial}{\partial t}(\boldsymbol{r}\times\boldsymbol{u})_z+\nabla\cdot\left(\Omega\boldsymbol{r}_\perp^2\boldsymbol{u}\right)=\nabla\cdot\left(\frac{p'}{\rho}\boldsymbol{r}\times\boldsymbol{e}_z\right), \tag{2.2.16b}$$

where $\boldsymbol{r}_\perp=\boldsymbol{r}-z\boldsymbol{e}_z$ is the component of the position vector perpendicular to $\boldsymbol{\Omega}$. Next, consider a co-ordinate system centred in the disturbance and a control volume $\mathcal{V}$ (with bounding surface $\mathcal{S}$) which is an axially-aligned cylinder of infinite length, which just contains the disturbance. Integrating (2.2.16b) over this volume gives

$$\frac{\mathrm{d}}{\mathrm{d}t}\iiint_{\mathcal{V}}(\boldsymbol{r}\times\boldsymbol{u})_z\,\mathrm{d}V+\Omega\boldsymbol{r}_\perp^2\oiint_{\mathcal{S}}\boldsymbol{u}\cdot\mathrm{d}\boldsymbol{S}=\oiint_{\mathcal{S}}\left(\frac{p'}{\rho}\boldsymbol{r}\times\boldsymbol{e}_z\right)\cdot\mathrm{d}\boldsymbol{S}. \tag{2.2.17}$$

Both of the surface integrals then vanish — the first because of continuity, the second because the integrand itself vanishes, a reflection of the fact pressure gradients cannot apply

any torque. Hence the axial angular momentum within $\mathcal{V}$ is conserved, meaning it may only be transferred north or south from the initial disturbance, and never transversely.

The same is true for axial linear momentum; considering the z-component of (2.2.6) and integrating over $\mathcal{V}$ gives

$$\frac{\partial u_z}{\partial t} + \boldsymbol{e}_z \cdot (2\boldsymbol{\Omega} \times \boldsymbol{u}) = -\boldsymbol{e}_z \cdot \nabla\left(\frac{p'}{\rho}\right) \tag{2.2.18a}$$

$$\frac{\mathrm{d}}{\mathrm{d}t} \iiint_{\mathcal{V}} u_z \,\mathrm{d}V = -\oiint_{\mathcal{S}} \frac{p'}{\rho} \boldsymbol{e}_z \cdot \mathrm{d}\boldsymbol{S}. \tag{2.2.18b}$$

The right-hand side term vanishes (since pressure cannot apply any axial force to the cylinder), and therefore axial momentum is also conserved within $\mathcal{V}$. These two results bias the radiation from a localised source onto the rotation axis, and in fact also provide a quantitative estimate for the rate of energy dispersal: $(\Omega t)^{-1}$ along the rotation axis but $(\Omega t)^{-\frac{3}{2}}$ away from it (Davidson et al., 2006).

'Self-focussing'

A second, more geometric interpretation is referred to as the *self-focussing* property of inertial waves, as outlined in Davidson (2013). Our starting point is again a localised disturbance, though now considered in Fourier transform, rather than physical, space. We pose the thought experiment as an initial value problem, in which the initial disturbance provides a certain distribution of wavevectors $\boldsymbol{k}$, then the governing equations prescribe how the wave associated with each $\boldsymbol{k}$ will evolve (independently of the others, as the problem is linear). Since the source is three-dimensional, it may be thought of as containing a reasonably complete spectrum of wavevectors — by which we mean, the Fourier transform of the initial condition will have non-negligible energy at most of the possible orientations of the wavevector $\boldsymbol{k}$.

Now, the direction and rate of energy propagation for a given $\boldsymbol{k}$ is provided by the group velocity $\boldsymbol{c}_g$ of (2.2.14c), though the diagram of figure 2.2.1 is perhaps a more useful reference. The key point is that $\boldsymbol{c}_g$ is always perpendicular to $\boldsymbol{k}$, and therefore wavevectors near to the horizontal plane ($\boldsymbol{\Omega} \cdot \boldsymbol{k} \approx 0$, or $\theta_k \approx \pi/2$) correspond to energy radiation along the rotation axis. Crucially, the problem is three-dimensional, so each choice of θ_k corresponds not to a single wavevector, but an ensemble of wavevectors at various azimuthal angles ϕ_k, tracing out a cone of internal angle θ_k (see figure 2.2.2a). This cone of wavevectors has a corresponding cone of group velocities orthogonal to the $\boldsymbol{k}$'s. Now, as the wavevectors get closer and closer to the plane $\boldsymbol{\Omega} \cdot \boldsymbol{k} = 0$, the cone of $\boldsymbol{k}$'s tends to a disc, and their group velocities collapse onto a vertical line along the axis. In this scenario, the energy from a

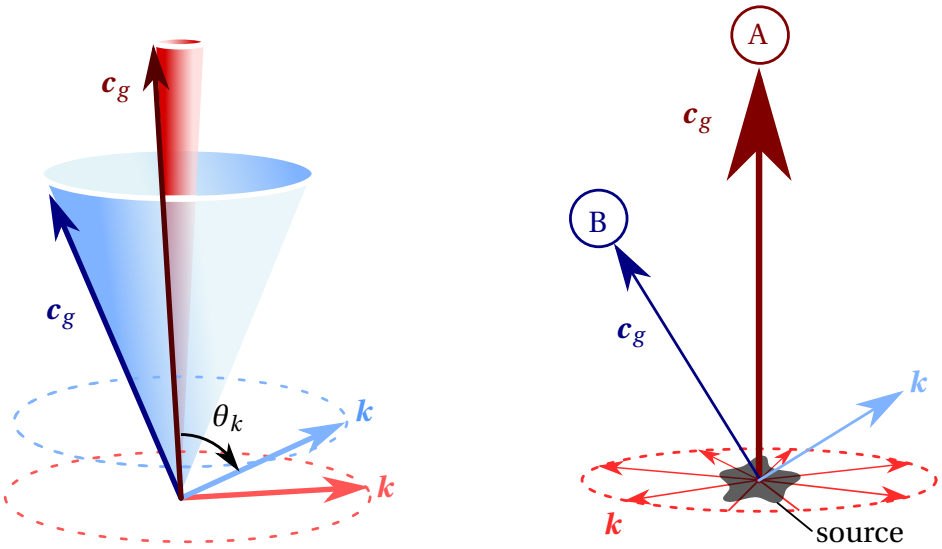

(a) At given θ_k, there exists a cone of possible $\boldsymbol{k}$'s, with a corresponding cone traced out by $\boldsymbol{c}_g$. As $\theta_k \to \pi/2$, the $\boldsymbol{k}$'s occupy a disc and the $\boldsymbol{c}_g$'s a vertical line, suggesting intense axial focussing.

(b) Alternatively, an observer at 'A', directly above the source, receives energy from an infinite number of $\boldsymbol{k}$'s, whereas the off-axis observer 'B' receives energy from only one orientation of $\boldsymbol{k}$.

Fig. 2.2.2 Explanation of the self-focussing property of inertial waves.

large, two-dimensional region of $\boldsymbol{k}$-space – the horizontal plane – is being channelled into a small, one-dimensional region of real space – the vertical axis. This is, in essence, the 'self-focussing' property of inertial waves, whereby the energy intensity is much greater along the rotation axis versus off-axis because the many $\boldsymbol{\Omega}\cdot\boldsymbol{k} \approx 0$ waves are all collaborating to radiate in that direction.

An alternative statement of the same idea is this. Consider observers at two different points in the fluid, both far from the initial disturbance, but one directly above it and one somewhere off-axis (see figure 2.2.2b). For the off-axis observer, there is only one choice of orientation for $\boldsymbol{k}$ which will relay energy from the source to their location. However, the on-axis observer receives energy from an infinite number of $\boldsymbol{k}$'s – all those in the horizontal plane – and therefore accrues a much larger dose overall.

Note that, despite the fact that all of the inertial wave solutions (2.2.14) are excited by a generic disturbance, particular significance is given to the waves which satisfy $\boldsymbol{\Omega}\cdot\boldsymbol{k} \approx 0$ (i.e. $\theta_k \approx \pi/2$), and therefore have zero frequency. That is not to say they do not propagate; although $\varpi \approx 0$ implies the phase velocity is also zero, their group velocity is finite, aligned with the rotation axis, and indeed attains its largest possible magnitude in this case. We expect the radiation from a localised source to be dominated by these solutions — not

because they contain the majority of the energy, but because they correspond to the highest energy density in the dispersion pattern.

2.2.4 The role of inertial waves in Earth's core

We conclude this introductory section on inertial waves with a remark of their significance in the core of the Earth. Since it is such a rotationally-dominated system, a thorough understanding of inertial waves is a very good starting point for understanding its more complicated dynamics.

As discussed above, inertial waves underpin the formation and maintenance of axially-elongated flow structures, believed to be a ubiquitous occurrence in Earth's core — as evidenced in simulations (Christensen, 2011; Schaeffer et al., 2017; Sheyko et al., 2018; Aubert, 2018) and experiments (Olson, 2011; Cardin & Olson, 1992). It seems unlikely that columnar structures in the Earth are very much like the rigid Taylor columns found in canonical experiments (Taylor, 1922, 1923), but rather dynamic features which are constantly interacting with both buoyancy and magnetic fields. Any evolution of columnar structures must be intrinsically linked to propagation of inertial waves – or possibly their magnetic cousins – since they are the party responsible for relaying energy, and therefore information, preferentially along the rotation axis.

In the model of Davidson (2014) and Davidson & Ranjan (2015), inertial waves – along with their magnetic cousins studied in chapters 3 and 4 – take on an even more important role in the operation of the geodynamo. In particular, it is suggested they are responsible for establishing the spatial segregation of helicity required to drive an α^2-dynamo — that is, a preference for negative helicity (left-handed spirals) in the northern hemisphere and positive (right-handed) in the south. Inertial waves achieve this because, for a monochromatic (single Fourier mode) wave at least, the direction of propagation (north or south) is directly related to the sign of helicity $\mathscr{H} = \boldsymbol{u}\cdot\boldsymbol{\omega}$.

To see this, consider the normal-mode solution (2.2.9), along with the ansatz $\boldsymbol{\omega}(\boldsymbol{r},t) = \mathbb{R}\left\{\tilde{\boldsymbol{\omega}}e^{i(\boldsymbol{k}\cdot\boldsymbol{r}-\varpi t)}\right\}$, substituted into the vorticity equation (2.2.7):

$$(-\varpi)\,\tilde{\boldsymbol{\omega}} = (2\boldsymbol{\Omega}\cdot\boldsymbol{k})\,\tilde{\boldsymbol{u}}. \tag{2.2.19}$$

Using the dispersion relation (2.2.10) (i.e. $\varpi = \pm(2\boldsymbol{\Omega}\cdot\boldsymbol{k})/k$) gives

$$\tilde{\boldsymbol{\omega}} = \mp k\tilde{\boldsymbol{u}}, \tag{2.2.20}$$

meaning the vorticity and velocity fields are always aligned, giving the maximum possible magnitude of helicity. Recall that the choice of sign is concomitant with the direction of axial propagation of the waves, with the upper sign belonging to northward-propagating waves and vice versa. Hence, monochromatic inertial waves are not only maximally helical, but have a propagation direction which depends on the sign of this helicity, taking negatively helical structures northwards and positively helical ones south. (Note this does not necessarily imply the same for a sum of such waves, though we will check it holds in what follows.) Combined with the observation that the convective excitation appears biased to the equatorial regions (section 2.1.3), this gives a plausible cartoon for how the helicity segregation necessary to support an α^2-dynamo might be established; helical waves (inertial, or related magnetic waves) launched from low latitudes carry energy away from the buoyancy field, along the rotation axis, with the waves heading northwards (southwards) carrying negative (positive) helicity into their respective hemispheres.

With this as motivation to learn more about the behaviour of inertial waves, the remainder of this section will be a study of their dispersive characteristics through a series of model initial value problems: first, a localised vortex of arbitrary orientation, as a proxy for a turbulent eddy, then a buoyant density anomaly, as a proxy for a convecting fluid 'blob'.

2.2.5 Radiation of inertial waves from a turbulent eddy

The simplest initial value problem we will tackle in this chapter takes as its starting point an isolated vortex of 'Gaussian' structure, as a cartoon representation for one of the many turbulent eddies within the Earth's core. This is related to previous analytical studies by Davidson & Siso-Nadal (2002); Siso-Nadal et al. (2003); Davidson et al. (2006), though the approach is slightly different and the initial condition more generic. The problem is purely hydrodynamic, so we solve the inertial wave equation (2.2.8) subject to the initial condition

$$\boldsymbol{u}(\boldsymbol{r}, t=0) = \boldsymbol{u}_0(\boldsymbol{r}) = \frac{U}{\ell}\,(\boldsymbol{e}_v \times \boldsymbol{r})\, e^{-\boldsymbol{r}^2/2\ell^2}. \tag{2.2.21}$$

This is a Gaussian vortex of characteristic size ℓ centred upon the origin; $\boldsymbol{e}_v$ is the unit vector along the vortex axis. If θ is the polar angle of $\boldsymbol{e}_v$ down from the rotation axis $\boldsymbol{e}_z$, we may write $\boldsymbol{e}_v = \boldsymbol{e}_z\cos\theta + \boldsymbol{e}_\perp \sin\theta$, where $\boldsymbol{e}_\perp$ is a unit vector in the horizontal plane. The governing equations are axisymmetric about $\boldsymbol{e}_z$, so the solution is unchanged by an arbitrary azimuthal rotation. Hence, the linear solution for a vortex of arbitrary orientation may be obtained from the weighted sum of two cases: the *aligned-axis* case $\boldsymbol{e}_v = \boldsymbol{e}_z$ and the *perpendicular-axis* case $\boldsymbol{e}_v = \boldsymbol{e}_x$ (say). The velocity field, once calculated, may then be rotated, translated,

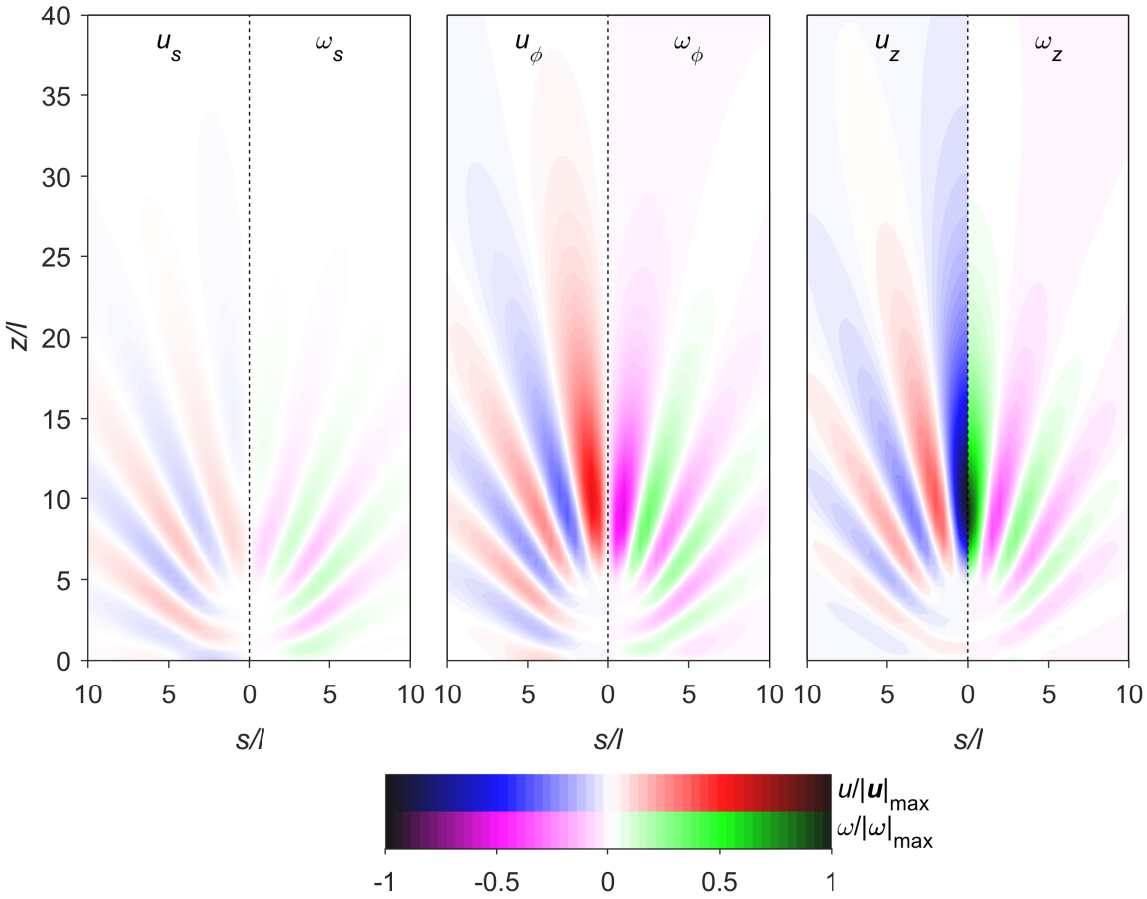

Fig. 2.2.3 Radiation pattern from an initial value problem with a Gaussian vortex with its axis aligned with the rotation axis z as the initial condition. The instant $\Omega t = 10$ is plotted, and lengths are in units of ℓ. The problem is axisymmetric, so the radial, azimuthal and axial components are plotted as functions of s and z. Each pane shows velocity on the left and vorticity on the right, normalised by their maximum absolute value across all three panes. We show $z > 0$ only: u_s, u_ϕ and ω_z are symmetric in z, whereas u_z, ω_x and ω_y are antisymmetric. (Mathematical description in Appendix A1.1.)

scaled and summed as desired, since the problem is both linear and homogeneous. (Note, however, that quadratic quantities such as energy and helicity do not obey superposition.)

The aligned axis case is solved using Fourier transforms in Appendix A1.1 and plotted in figures 2.2.3 (component-wise) and 2.2.4 (energy and helicity) at the instant $\Omega t = 10$. Since this problem is axisymmetric we solve for the cylindrical polar components of $\boldsymbol{u}$ and $\boldsymbol{\omega}$ as functions of s and z. Consider first the component-wise representation (figure 2.2.3), the most striking feature of which is the strong correlation between $\boldsymbol{u}$ and $\boldsymbol{\omega}$ across all three components — although remembering that the two are always parallel for a monochromatic wave (equation 2.2.20), this is hardly surprising. The radial component is weakest, and

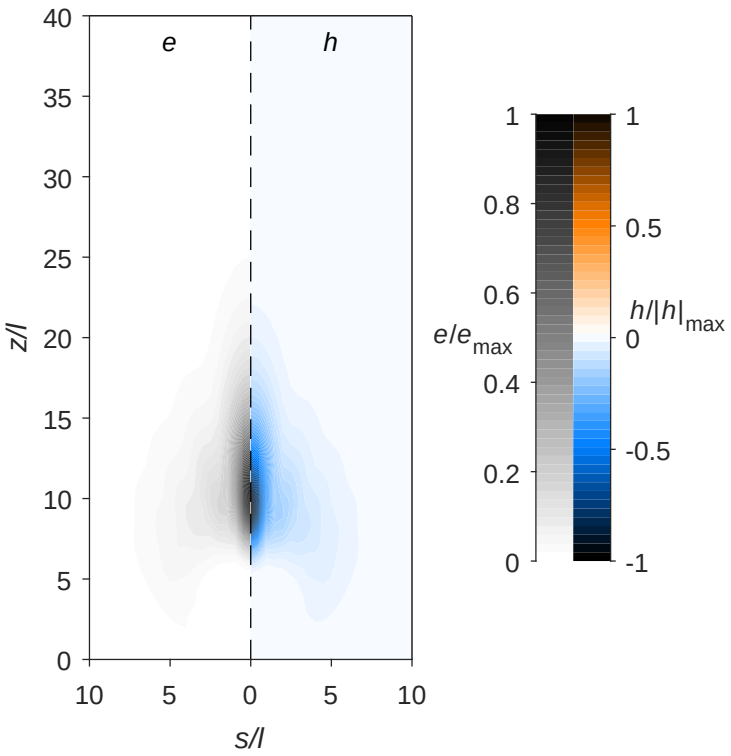

Fig. 2.2.4 Specific kinetic energy ($\mathscr{E} = \frac{1}{2}\boldsymbol{u}\cdot\boldsymbol{u}$) and helicity density ($\mathscr{H} = \boldsymbol{u}\cdot\boldsymbol{\omega}$) radiation from an initial value problem with a Gaussian vortex with its axis aligned with the rotation axis z as the initial condition. The instant $\Omega t = 10$ is plotted, and lengths are in units of ℓ. The problem is axisymmetric, so both quantities are plotted as functions of s and z. We show $z > 0$ only: $\mathscr{E}$ is symmetric and $\mathscr{H}$ antisymmetric in z. (Mathematical description in Appendix A1.1.)

shows no preference for on-axis propagation since u_s does not contribute to either linear or angular axial momentum (see section 2.2.3). The other components show a much stronger tendency for on-axis radiation, with the basic vortex structure – an azimuthal flow with axial vorticity – spreading almost exclusively in the z-direction, with the on-axis peak found at $z \sim \Omega t\ell$. We know this must correspond to the zero frequency ($\theta_k \sim \pi/2$) inertial waves, which have an axial group velocity $c_{g,z} = 2\Omega/k$; this suggests the dominant wavenumber in the initial condition is $k \sim 2\ell^{-1}$.

Also apparent in figure 2.2.3 are accompanying off-axis 'petals' of alternating sign which contain considerably less energy than the main vortex core. This is confirmed in the left half of figure 2.2.4, which shows the specific kinetic energy $\mathscr{E} = \frac{1}{2}\boldsymbol{u}\cdot\boldsymbol{u}$ is very strongly biased onto the rotation axis. The fact that the helicity density $\mathscr{H} = \boldsymbol{u}\cdot\boldsymbol{\omega}$ almost exactly mirrors the kinetic energy provides further evidence that the velocity and vorticity fields are strongly correlated — their dot product is in fact negative above the disturbance, signifying left-

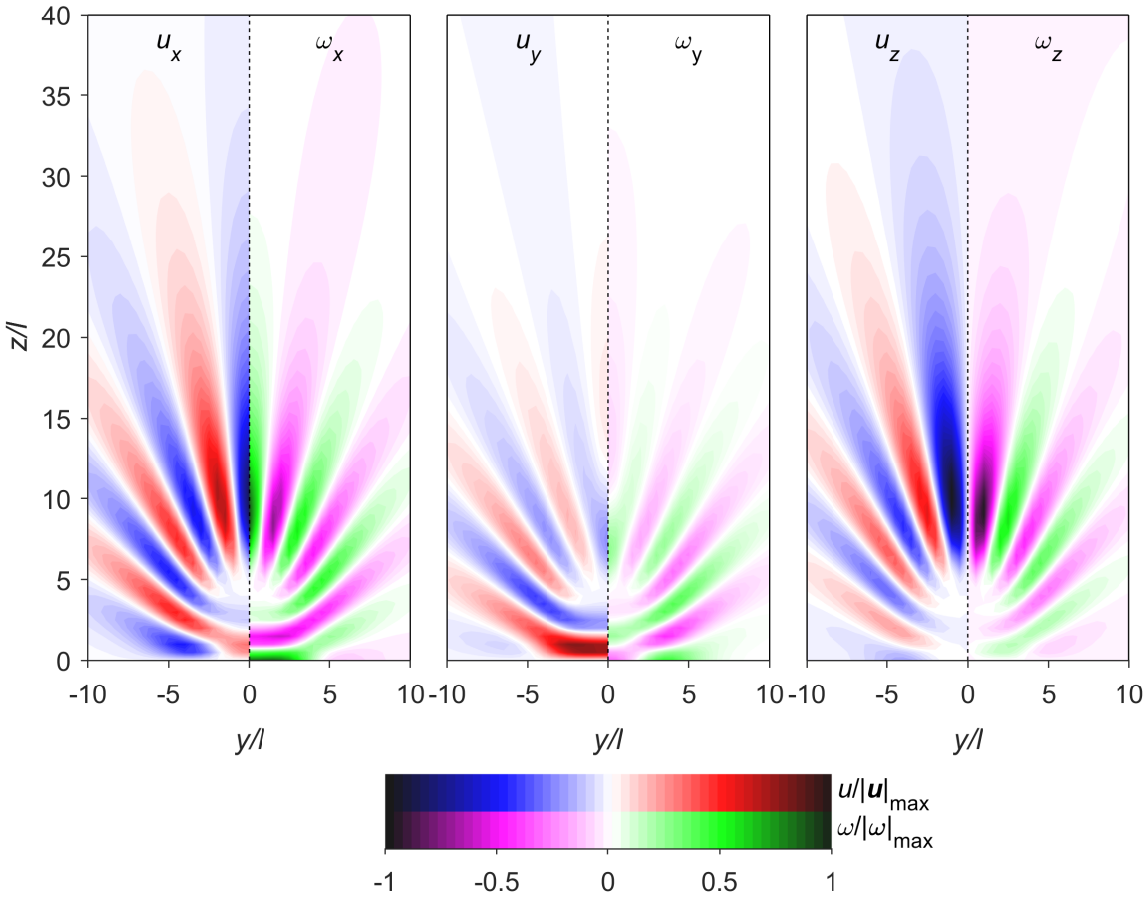

Fig. 2.2.5 Radiation pattern from an initial value problem with a Gaussian vortex with its axis aligned with the x-axis as the initial condition. The instant $\Omega t = 10$ is plotted, and lengths are in units of ℓ. The solution is plotted in the plane $x = 0$. Each pane shows velocity on the left and vorticity on the right, normalised by their maximum absolute value across all three panes. We show $z > 0$ only: u_z, ω_x and ω_y are symmetric in z, whereas u_x, u_y and ω_z are antisymmetric. x- and y-components are symmetric in y; z-components are antisymmetric. (Mathematical description in Appendix A1.2.)

hand spiralling streamlines in accordance with the result of Section 2.2.4 that negatively helical inertial waves propagate northwards. The plot for negative z would of course be unanimously positively helical.

The solution for the perpendicular-axis vortex initial condition (Appendix A1.2) is no longer axisymmetric, so we settle for plotting the components first in the plane $x = 0$ (initial vortex axis out of page, figure 2.2.5), then the plane $y = 0$ (initial vortex axis left to right, figure 2.2.6). The on-axis bias is noticeably reduced compared to the aligned-axis vortex case, with only the axial components in the plane $x = 0$ and the x-components in the plane $y = 0$ showing signs of it. This can be understood in two ways, corresponding to the two explanations offered in Section 2.2.3: firstly, the initial condition contains no net axial

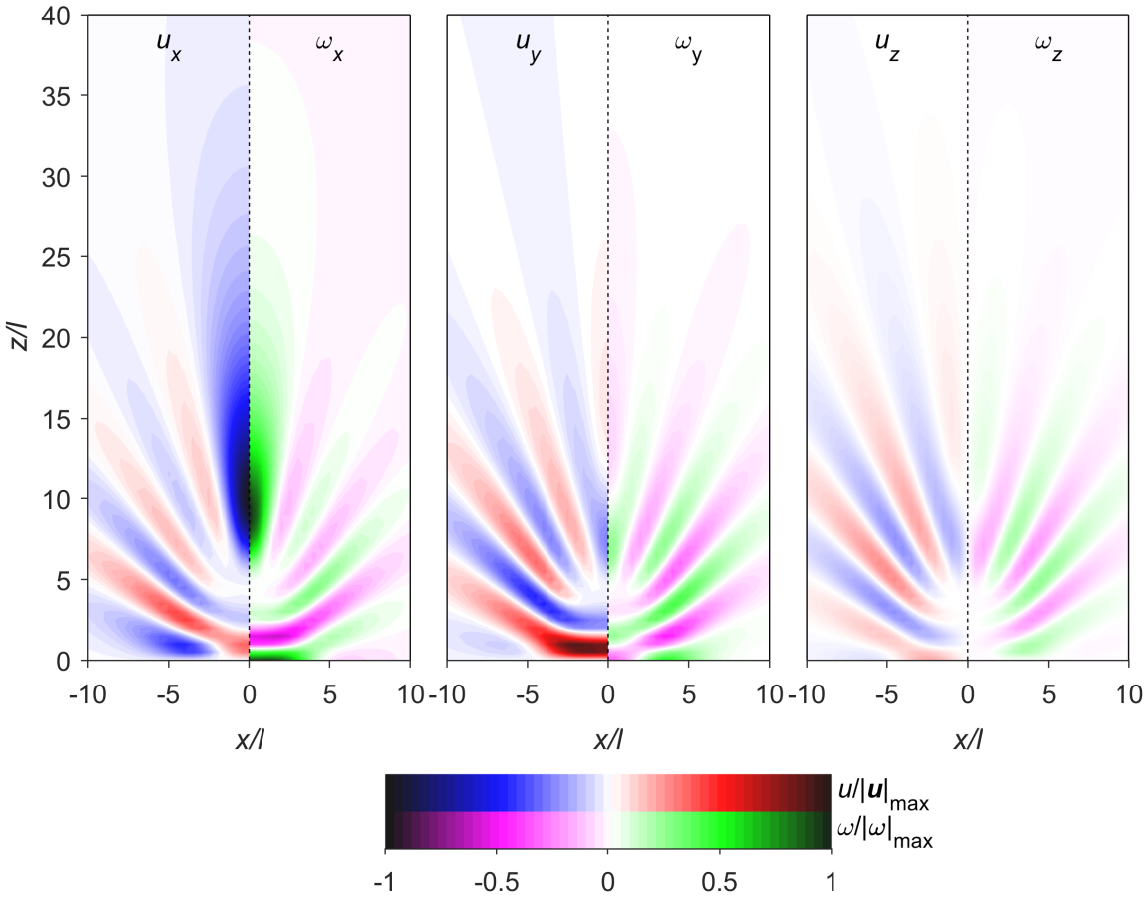

Fig. 2.2.6 Radiation pattern from an initial value problem with a Gaussian vortex with its axis aligned with the x-axis as the initial condition. The instant $\Omega t = 10$ is plotted, and lengths are in units of ℓ. The solution is plotted in the plane $y = 0$. Each pane shows velocity on the left and vorticity on the right, normalised by their maximum absolute value across all three panes. We show $z > 0$ only: u_z, ω_x and ω_y are symmetric in z, whereas u_x, u_y and ω_z are antisymmetric. x- and y-components are symmetric in x; z-components are antisymmetric. (Mathematical description in Appendix A1.2.)

momentum (linear or angular), which somewhat weakens the momentum conservation argument. Secondly, the perpendicular-axis initial condition contains less energy in waves which have $\theta_k \approx \pi/2$; this can be seen by integrating the power spectral density (i.e. the magnitude squared of the Fourier transform) of the initial condition azimuthally in $\boldsymbol{k}$-space, which we denote $\langle|\hat{\boldsymbol{u}}_0|^2\rangle = \oint |\hat{\boldsymbol{u}}_0|^2 \, k \sin\theta_k \mathrm{d}\phi_k$. For the aligned-axis case, we have $\hat{\boldsymbol{u}}_0$ given by (A1.1.12a) and

$$\left\langle |\hat{\boldsymbol{u}}_0|^2 \right\rangle \propto \sin^3\theta_k, \tag{2.2.22}$$

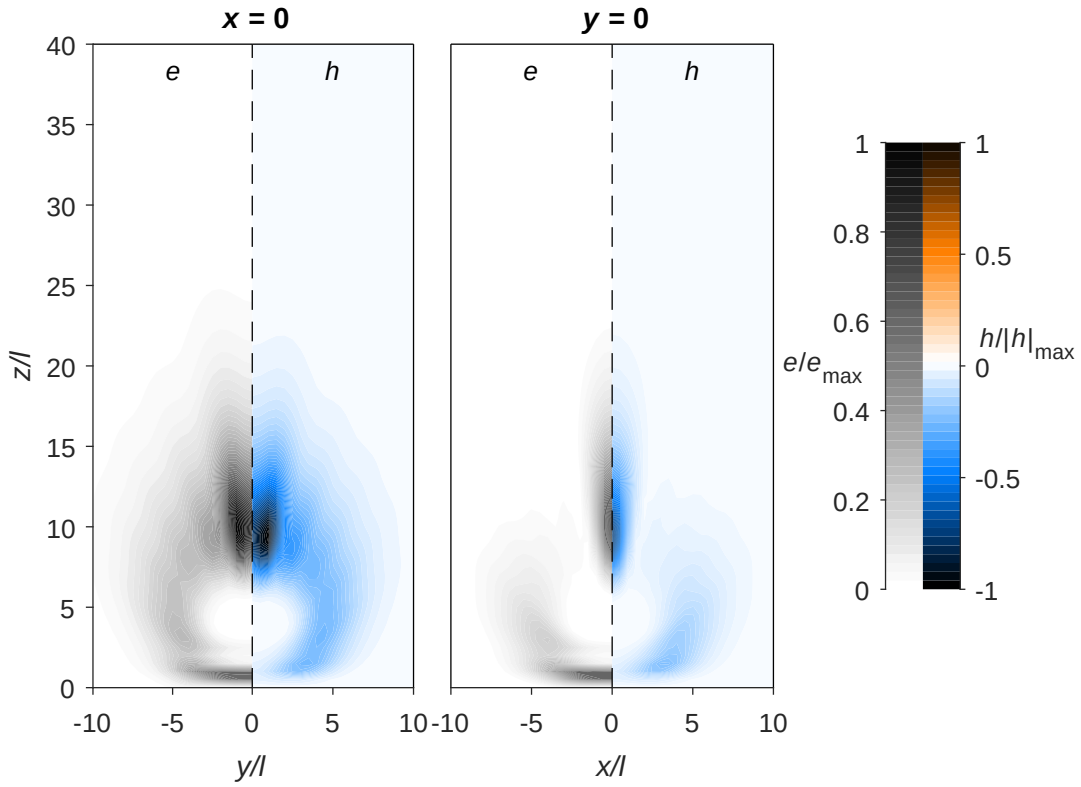

Fig. 2.2.7 Specific kinetic energy ($\mathscr{E} = \frac{1}{2}\boldsymbol{u}\cdot\boldsymbol{u}$) and helicity density ($\mathscr{H} = \boldsymbol{u}\cdot\boldsymbol{\omega}$) radiation from an initial value problem with a Gaussian vortex with its axis aligned with the x-axis as the initial condition. The instant $\Omega t = 10$ is plotted, and lengths are in units of ℓ. Both quantities are plotted in the planes $x = 0$ (left) and $y = 0$ (right). We show $z > 0$ only: $\mathscr{E}$ is symmetric and $\mathscr{H}$ antisymmetric in z. Both are symmetric in x and y. (Mathematical description in Appendix A1.2.)

whereas for the perpendicular-axis case we have (A1.2.3a) and

$$\left\langle |\hat{\boldsymbol{u}}_0|^2 \right\rangle \propto \frac{1}{2}\sin\theta_k \left(1+\cos^2\theta_k\right). \tag{2.2.23}$$

with the same 'constant' (function of k) of proportionality in both cases. The aligned-axis case therefore contains twice as much energy at $\theta_k = \pi/2$, whereas the perpendicular-axis case has more towards $\theta \sim 0$. Since the $\theta \sim \pi/2$ solutions may be thought of as responsible for the axial energy propagation, having fewer of them in the initial condition is a recipe for a less dramatic effect.

Indeed, there seems a reasonable amount of energy – particularly in the y-components – which has been unable to propagate away from the initial condition location at all. This is the energy in wavevectors which are closely aligned with the rotation axis ($\theta_k \sim 0$), which are absent in the aligned-axis case (see equation 2.2.22). Recall (e.g. figure 2.2.1) that the group

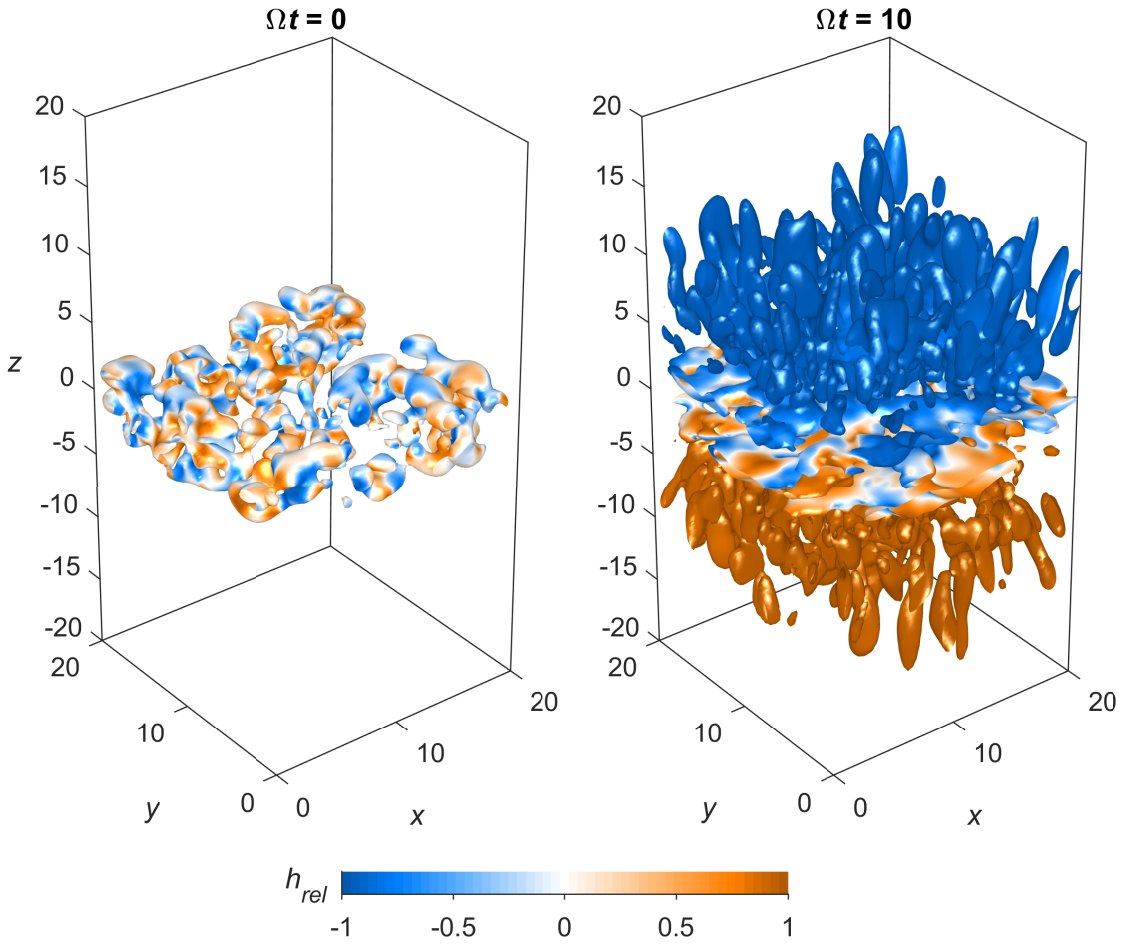

Fig. 2.2.8 Radiation of inertial waves from a 'cloud' of turbulence. The initial condition is a sum of 500 vortices, as per (2.2.21), with random orientations and centres located in the x-y plane and the region $|z| \leq 2$. Their sizes ℓ and strengths U are independently selected from a uniform distribution over $[0.5,\ 1]$. An isosurface of specific kinetic energy $\mathscr{E} = \frac{1}{2}\boldsymbol{u}\cdot\boldsymbol{u}$ is plotted at 10% of its maximum value in each pane, and colouring is by relative helicity $\mathscr{H}_{rel} = \boldsymbol{u}\cdot\boldsymbol{\omega}/u\omega$. The initial condition is on the left and instant $\Omega t = 10$ on the right.

velocity vanishes when $\theta_k \to 0$, and therefore these solutions cannot ever escape convey energy away from the disturbance. This is confirmed in figure 2.2.7, wherein the peaks of energy are found at $z \sim \Omega t\ell$ (as before, $\theta_k \sim \pi/2$ waves) and $z \sim 1$ ($\theta_k \sim 0$ waves). As found in figure 2.2.4, energy and helicity are again well-correlated, and there is no ambiguity over the result that negatively helical waves travel northwards (and vice versa).

As mentioned earlier, the linear and homogeneous nature of the problem means the above solutions may be resized, rescaled, rotated, translated and summed arbitrarily. This allows us to form a cartoon for the radiation of inertial waves from a region of turbulence

rather than a localised eddy, a more acceptable paradigm in the context of Earth's outer core. Figure 2.2.8 shows the evolution of a cloud of vortices of various complexions, initially seeded near to the plane $z = 0$. Although by all accounts this rather ad-hoc means of generating an initial condition is a poor representation of a turbulent region, it does generate an initial condition comparable with equivalent analytical, experimental and DNS studies (Siso-Nadal et al., 2003; Davidson et al., 2006; Ranjan & Davidson, 2014), and does serve to reinforce some important points. Firstly, by $\Omega t = 10$ energy has spread chiefly on-axis both north and south to the regions $|z| \sim 5-10$, exactly as expected for the low-frequency inertial waves from a set of vortices of sizes $\ell \sim 0.5-1$. Secondly, there is unequivocal helicity segregation as a result of wave propagation, negative north and positive south, revealed by the colouring of the energy isosurfaces by $\mathscr{H}_{rel}$, which is the cosine of the angle between $\boldsymbol{u}$ and $\boldsymbol{\omega}$, and is close to unity throughout the energetic wave region. This shows that the link between propagation direction and helicity established in Section 2.2.4 for a monochromatic inertial wave is robust when a vast number of such waves are superimposed. We might also remark that these plots show good qualitative agreement with the experiments of Davidson et al. (2006) and DNS of Ranjan & Davidson (2014), inspiring confidence in this means of exploring the dynamics of inertial waves.

2.2.6 Radiation of inertial waves from a buoyant blob

A second model problem, approached in a similar way to the turbulent eddy above, reinforces what we have learned about inertial waves, and makes a stronger case for their generation in Earth's core. We know already that regions of rapidly-rotating turbulence may radiate inertial waves — but clearly the turbulence in the planet's core does not appear from nowhere, as the above initial value problem seems to suggest. Rather, it is driven by thermal and compositional convection, so a more realistic choice of disturbance to generate inertial waves might be a distribution of buoyant material within the domain; we therefore tackle an initial value problem in which a density deficit is prescribed in an initially quiescent fluid. Granted, the spontaneous appearance of a buoyancy field is no less dubious than the appearance of a turbulent cloud — but the physical insight gained through this initial value approach will allow us to make inferences about the behaviour of a smoothly-evolving convecting fluid.

Description of model problem

The model problem we solve here is similar to that solved in a quasi-steady situation by Loper (2001), and by DNS in Davidson (2014) and Davidson & Ranjan (2015), though we are

interested in the rapid dynamics of inertial waves and employ an almost entirely analytical method. (This is related to the forced problem considered in Siso-Nadal & Davidson (2004).)

The chief difference between this problem and the turbulent eddy problem is that our fluid, as well as being rapidly-rotating, now sits in a gravitational field and exhibits density variations. The gravitational acceleration $\boldsymbol{g}$ is taken to be constant, on the basis that its variation through the Earth's outer core occurs on a scale much larger than ℓ, the typical size of small-scale features of the buoyancy field. We choose $\boldsymbol{g} = -g\boldsymbol{e}_x$, perpendicular to the rotation axis $\boldsymbol{\Omega} = \Omega\boldsymbol{e}_z$, in homage to the observation that convection shows a bias to the equatorial regions, where $\boldsymbol{\Omega}$ and $\boldsymbol{g}$ are approximately at right angles. (Note that, in any case, we are interested mainly in dynamo action outside of the tangent cylinder, so the case where the two are parallel is of less interest. However, arbitrary orientations of $\boldsymbol{g}$ could be solved for as a weighted sum of the two cases.)

The density field will consist of a localised buoyant anomaly, or 'blob', with density $\rho + \rho'(\boldsymbol{r})$, where ρ is the constant density of the bulk fluid. The characteristic magnitude of ρ' is estimated by Moffatt & Loper (1994) by considering conservation of mass for the expanding inner core alongside a leading-order force balance between Coriolis and gravitational forces. This produces the figure $\rho' \sim 8\times10^{-5}\mathrm{kg\,m^{-3}}$ and therefore $\rho'/\rho \sim 10^{-8}$. The fractional change in density is therefore very small, meaning we may employ the Boussinesq approximation, in which changes in density are included in the gravitational force term, but otherwise neglected. This analysis also gives the estimate $U \sim 0.3\mathrm{mm\,s^{-1}}$ for the characteristic velocity of the buoyant blob; this is comparable with estimates used previously, and therefore the assumption of very small Rossby number Ro (i.e. $|2\boldsymbol{\Omega}\times\boldsymbol{u}| \gg |(\boldsymbol{u}\cdot\nabla)\boldsymbol{u}|$) still holds. Furthermore, the convection timescale $D/U \sim 250\mathrm{yr}$ is very much greater than the inertial wave timescale (by a factor Ro), so that, as far as the waves are concerned, the buoyancy field is effectively stationary. To this end, we neglect the thermal and compositional evolution equations entirely, instead treating the gravitational force term in the momentum equation as an entirely static entity.

Hence, we solve only for the velocity field, which is governed by (2.2.4) with the nonlinear and viscous terms neglected, and the forcing $\boldsymbol{F} = \rho'\boldsymbol{g}$ being gravitational:

$$\frac{\partial \boldsymbol{u}}{\partial t} + 2\boldsymbol{\Omega}\times\boldsymbol{u} = -\nabla\left(\frac{p}{\rho}\right) + c\boldsymbol{g}. \tag{2.2.24}$$

Here, $c(\boldsymbol{r}) = \rho'/\rho$ is the fractional density variation, chosen to be of Gaussian structure:

$$c(\boldsymbol{r}) = Ce^{-\boldsymbol{r}^2/2\ell^2} \tag{2.2.25}$$

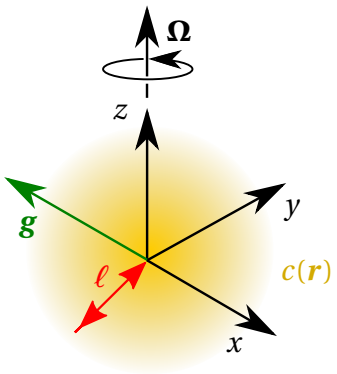

Fig. 2.2.9 Schematic of the initial condition for model problem studying radiation of inertial waves from a buoyant blob.

for some negative constant magnitude C and size ℓ. Since the fluid is Boussinesq, the solenoidal condition $\nabla\cdot\boldsymbol{u}=0$ still applies. The flow is solved subject to a quiescent initial condition $\boldsymbol{u}(\boldsymbol{r},t=0)=0$. We solve in a Cartesian co-ordinate system, with $\boldsymbol{\Omega}=\Omega\boldsymbol{e}_z$ and $\boldsymbol{g}=-g\boldsymbol{e}_x$; effectively, this imitates a local region of the outer core in the equatorial plane, with the x-axis pointing radially outwards, y eastwards and z axially. This set-up is sketched in Figure 2.2.9.

Solution

To solve this model problem, we first take the curl of (2.2.24) to eliminate pressure:

$$\frac{\partial\boldsymbol{\omega}}{\partial t}=(2\boldsymbol{\Omega}\cdot\nabla)\,\boldsymbol{u}+\nabla c\times\boldsymbol{g}. \tag{2.2.26}$$

A further curl and time derivative yields a partial differential equation for the velocity field:

$$\frac{\partial^2}{\partial t^2}\nabla^2\boldsymbol{u}+(2\boldsymbol{\Omega}\cdot\nabla)^2\,\boldsymbol{u}=(2\boldsymbol{\Omega}\cdot\nabla)\left(\boldsymbol{g}\times\nabla c\right). \tag{2.2.27}$$

This is much like the inertial wave equation (2.2.8), except with a source term on the right-hand side due to the buoyancy field. Clearly, the density anomaly acts as a source of inertial waves, whose objective is to facilitate a quasi-steady balance between gravitational and Coriolis forces by transmitting information on the fast timescale of the planet's rotation period.

We solve for $\boldsymbol{u}$ in Appendix A1.3 by splitting it into two halves; first, there is a particular integral $\boldsymbol{u}_{PI}$ which is steady and balances the buoyancy force. We can find it by setting $\frac{\partial\boldsymbol{\omega}}{\partial t}=0$ in (2.2.26) and integrating with respect to z, meaning it is determined to within an arbitrary z-independent (or *geostrophic*) function. The second half of $\boldsymbol{u}$ is a complementary

function $\boldsymbol{u}_{CF}$, which is time-dependent, obeys the standard inertial wave equation (2.2.8), and is subject to the initial conditions that it must entirely cancel out the particular integral at $t = 0$, and have an initial acceleration compatible with (2.2.26) when $\boldsymbol{u} = 0$. We solve for $\boldsymbol{u}_{CF}$ in Fourier space, reducing the inverse transforms analytically but finishing them off with numerical integrations for all components of $\boldsymbol{u}$ and $\boldsymbol{\omega}$.

Flow structure

Before any detailed calculations have taken place, it is possible to make a stab at what the flow will look like by considering the steady balance

$$(2\boldsymbol{\Omega}\cdot\nabla)\,\boldsymbol{u} \approx \boldsymbol{g}\times\nabla c, \tag{2.2.28}$$

which is the vorticity equation (2.2.26) with the unsteady term neglected. Following Davidson (2014), one can establish 'jump conditions' across the buoyant blob and therefore extract the broad structure of the flow it produces. Consider the z-component of (2.2.28) integrated along a vertical line from beneath the blob ($z = z_-$) to above it ($z = z_+$),

$$\Delta u_z = (u_z)_{z_+} - (u_z)_{z_-} \approx \frac{-g}{2\Omega}\int_{z_-}^{z_+}\frac{\partial c}{\partial y}\mathrm{d}z, \tag{2.2.29}$$

and if $z_\pm$ are far from the blob and c is as in (2.2.25),

$$\Delta u_z \approx \sqrt{\frac{\pi}{2}}\frac{gCy}{\Omega\ell}e^{-\boldsymbol{r}_\perp^2/2\ell^2}. \tag{2.2.30}$$

This represents the jump the axial component of velocity is forced by the buoyancy to take from below the horizontal plane $z = 0$ to above it; since u_z is antisymmetric in z (and therefore zero at $z = 0$), this tells us its sign either side. Recall that C is a negative constant, and therefore Δu_z is positive for $y < 0$ and negative for $y > 0$. This implies an axial flow which is diverging from the blob at negative y (to its west), and converging towards it at positive y (to its east). Hence, by continuity there must be a negative y-velocity (westward) through the blob itself.

Integrating the x and y components of (2.2.28) in the same way reveals $\boldsymbol{u}_\perp$ does not change across the blob, and therefore $\Delta\omega_z$ is also zero; the axial vorticity has the same sign both sides of the blob. Recalling that inertial waves are always maximally helical ($\boldsymbol{u}$ parallel with $\boldsymbol{\omega}$ below the source and antiparallel above it) suggests that positive u_z should be associated with negative ω_z above the blob and positive ω_z below it, and vice versa. This

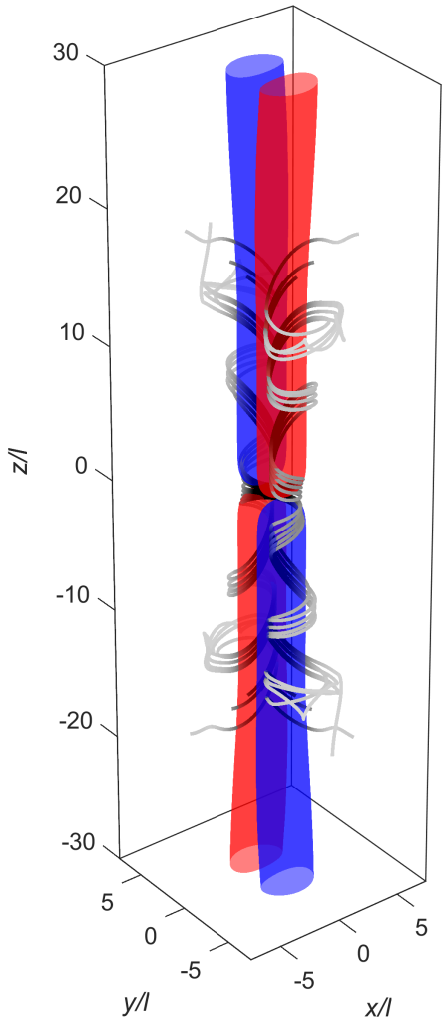

Fig. 2.2.10 Radiation of inertial waves by a buoyant blob. Isosurfaces of u_z at 20% of its maximum absolute value are plotted at $\Omega t = 20$, coloured red (blue) for positive (negative) values. Streamlines seeded at $x = y = 0$, $z = \pm(0.1 : 0.1 : 0.5)$ are plotted in grey, with darker shading indicating larger $|\boldsymbol{u}|$. Gravity acts in the negative x-direction.

implies a ω_z structure which is pair of columnar vortices, cyclonic ($\omega_z > 0$) at positive y and anticyclonic ($\omega_z < 0$) at negative y.

The expected radiation pattern, therefore, is fourfold, with a columnar vortex in each quadrant of the y-z plane. The flow converges towards the horizontal plane at positive y, passes through the buoyant blob, then diverges at negative y — all the time spiralling in such a way that the helices formed by the fluid paths are left-handed for $z > 0$ and right-handed for $z < 0$; this correspond to cyclonic motion at positive y and anticyclonic at negative y.

Thankfully, this expectation is borne out by reality; figure 2.2.10 shows the flow pattern at the instant $\Omega t = 20$, by which time the flow around the buoyant blob is well developed and the majority of inertial waves have propagated reasonably far from it. The velocity field is visualised by streamlines seeded within the blob itself, as well as contours of axial velocity to indicate the direction. There is a very clear four-vortex structure, with the signs of vorticity and axial velocity being as hypothesised above, and the streamlines make the helical structure of the flow eminently clear. Perhaps the most intuitive way to think of these columnar vortices is as transient Taylor columns, established and maintained by the emission of inertial waves from the buoyant blob.

To show that inertial waves are responsible for this process, we plot the time evolution of the flow in figure 2.2.11 — it turns out that axial velocity and vorticity are the most interesting quantities for this purpose. Over very short timescales by geophysical standards ($\Omega t = 10$ corresponds to about 38 hours), the four Taylor columns can be seen to grow from the buoyant anomaly, spreading chiefly along the rotation axis at a rate $z \sim \Omega t \ell$ as expected for the lowest frequency ($\theta_k \sim \pi/2$) inertial waves with dominant wavenumber $k \sim 2\ell^{-1}$.

We can further interrogate the radiation pattern by looking at all components of $\boldsymbol{u}$ and $\boldsymbol{\omega}$ in the y-z plane — figure 2.2.12 shows them all at $\Omega t = 10$, the same as the final pane of figure 2.2.11, but halfway to the 'well-established' state of figure 2.2.10. The transient Taylor columns are obvious in the x and z components, but the y components are much weaker, being significant only in the vicinity of the blob itself (though this is more an artefact of the plane $x = 0$ rather than generally true). The radiation pattern is best understood broken down into three separate zones:

1. **Blob zone:** Near to the blob, the steady balance of (2.2.28) dictates the form of the velocity field required to balance the static gravitational forcing;

2. **Taylor column zone:** Some distance above and below the blob, the buoyancy field is negligible, and therefore the fluid tries to satisfy the Taylor-Proudman constraint $\partial \boldsymbol{u}/\partial z \approx 0$, meaning the structures are columnar and (under the present formulation at least) stationary. This region stretches from the 'blob zone', which enforces the jump conditions which make the formation of Taylor columns necessary, up to a height $z \sim \Omega t \ell$ — this is the region of space through which the low-frequency inertial waves have propagated at time t;

3. **Wave front:** The Taylor column zone is always getting taller as time progresses, being extended at a rate equal to the group velocity of the fastest inertial waves, which crucially possess the self-focussing property discussed earlier. This extension is being driven by a wave front between a region of quiescent fluid above and below the

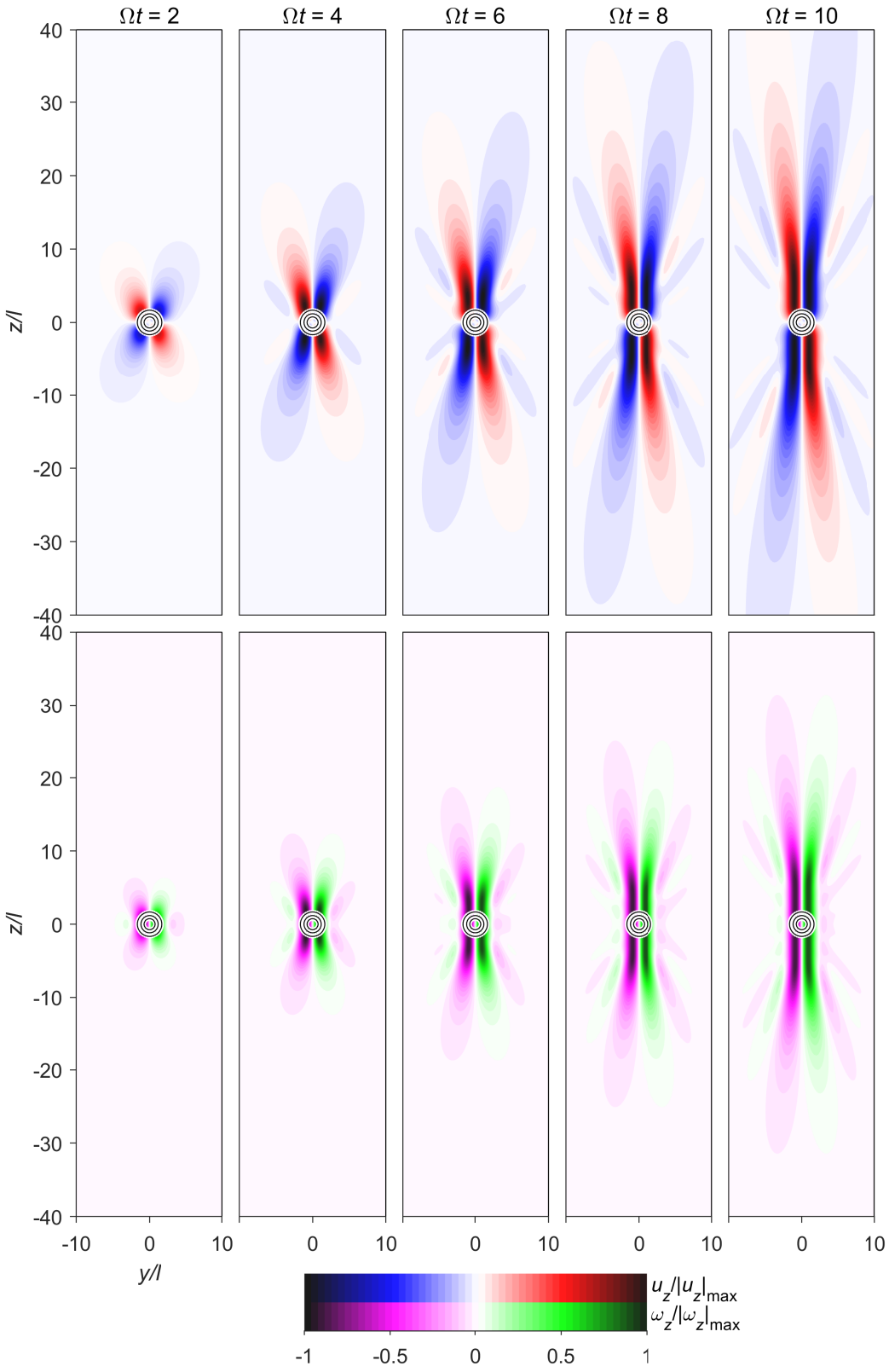

Fig. 2.2.11 Evolution of the inertial wave radiation pattern from a buoyant blob. The top panes show axial velocity and the bottom axial vorticity, both in the plane $x = 0$ for $\Omega t = 2 : 2 : 10$. Black contours are at quartiles of the buoyancy field. Gravity acts into the page.

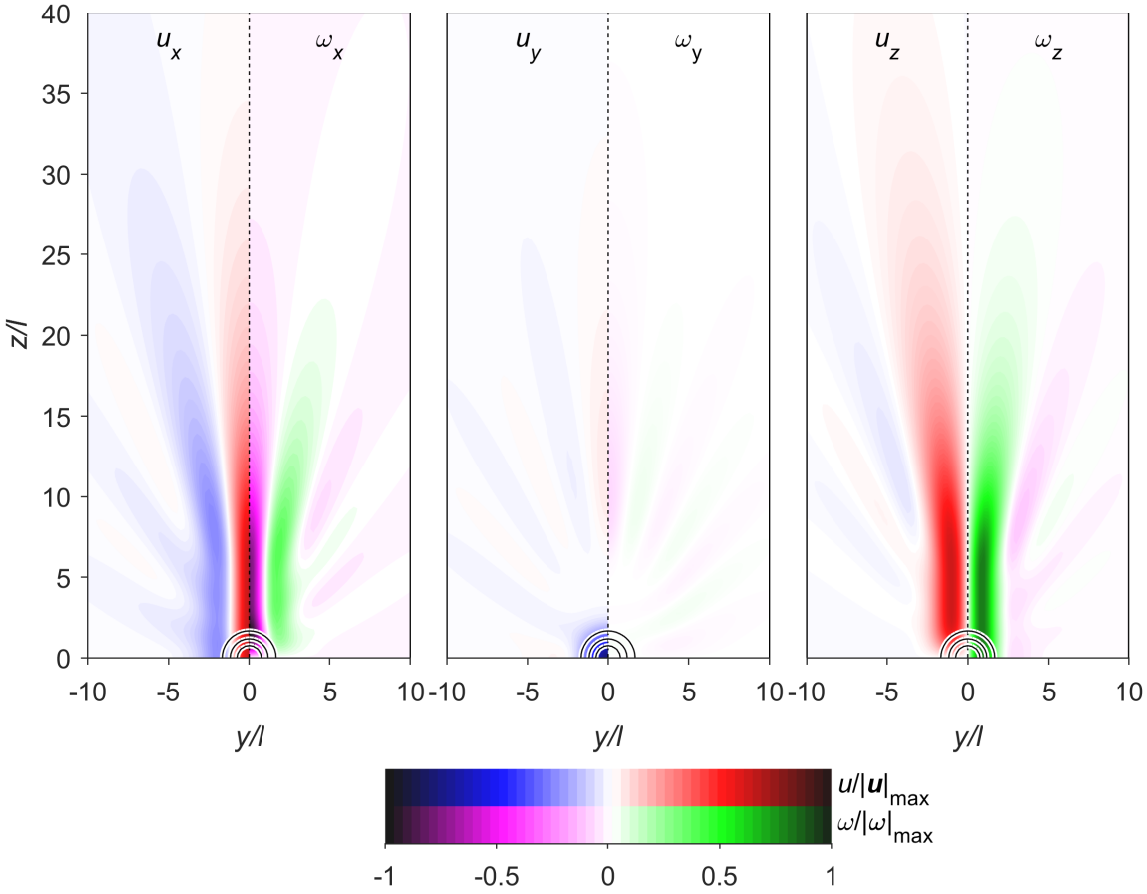

Fig. 2.2.12 Inertial wave radiation from a buoyant blob, showing all components of $\boldsymbol{u}$ and $\boldsymbol{\omega}$ in the plane $x = 0$ at $\Omega t = 10$. Only one quadrant of the y-z plane is shown for each: u_x, u_y and ω_z are symmetric in z whereas ω_x, ω_y and u_z are antisymmetric. Both have x and y components symmetric in y, and z components antisymmetric in y. Black contours are at quartiles of the buoyancy field. Gravity acts into the page.

columns, and the approximately z-invariant flow which stretches in either direction from the buoyant blob. Effectively, the inertial waves are constantly seeking to iron out the z-variation of the flow due to the difference between the two regions.

(This kind of decomposition is also explored in Ranjan & Davidson (2014).) As a description of the processes involved, this three-zone cartoon describes the radiation of inertial waves from a buoyant blob reasonably well; balancing the buoyancy force requires a disturbance to the velocity field, which invokes Taylor columns above and below the blob so that the Taylor-Proudman constraint is satisfied away from the source. This constraint is enforced by $\theta_k \approx \pi/2$ inertial waves, and so the Taylor column region extends axially at a rate $z \sim \Omega t \ell$.

However, in reality the buoyant blob will not be a static source, but will change shape and move around due to the very velocity field which it is responsible for creating. The solutions presented here should therefore be regarded as a 'quasi-steady' version of reality; in actual fact, the evolving buoyancy field will govern Taylor columns which are themselves unsteady, constantly needing to readjust in order to accommodate the ever-changing jump conditions demanded by the blob. The only way this readjustment can be facilitated is via the continual emission of low-frequency inertial waves by the blob as it evolves, forming a continuum of fronts propagating axially away from the source at the inertial wave group velocity.

A closer inspection of figure 2.2.12 reveals that the three-zone model of wave radiation does not quite capture the whole picture, as a small but observable quantity of wave energy can also be seen radiated off-axis, in a series of petals at various oblique angles to the principal Taylor columns. (This can also be seen, perhaps more distinctly, in the Gaussian eddy case, figures 2.2.3, 2.2.5 and 2.2.6.) This fourth zone betrays a subtle but important point relating to the self-focussing property of inertial waves. Obviously, the choice of initial condition will specify the make-up of the solution in wavevector space, and therefore the proportion of energy which is in wavevectors with $\theta_k \sim \pi/2$, the self-focussing solutions. For a generic initial condition, however, there will presumably be much more energy in wavevectors which do not satisfy this condition than those which do, and therefore the majority of the energy is in fact not radiated on-axis, but into the off-axis petals. This seems to go against all we have said so far — however, the important point is that the energy density will nevertheless be very much higher on-axis, due to the intensified dosage of inertial wave radiation in that direction, despite the fact it does not necessarily represent a majority of the energy of the initial condition.

We conclude this discussion of the structure of the radiation pattern from a buoyant blob with a short nod to energy and helicity. Figure 2.2.13 shows isosurfaces of specific kinetic energy $\mathscr{E} = \frac{1}{2}\boldsymbol{u}\cdot\boldsymbol{u}$ coloured by relative helicity density $\mathscr{H}_{rel} = \boldsymbol{u}\cdot\boldsymbol{\omega}/u\omega$ at $\Omega t = 10$; in agreement with previous findings, the helicity is entirely negative to the north of the blob and positive to the south, with the most energetic region of the flow appearing to have propagated to $z \sim \Omega t\ell$. The inertial waves' ability to spatially segregate helicity seems independent of the choice of disturbance.

Comparison with direct numerical simulations

To complete this study of inertial waves from buoyant blobs, we validate the current method against the direct numerical simulations (DNS) of Davidson & Ranjan (2015), who approach an near-identical problem using a spectral code in a periodic domain, and include every effect we have ignored in this analysis: non-linear advection and viscous dissipation are

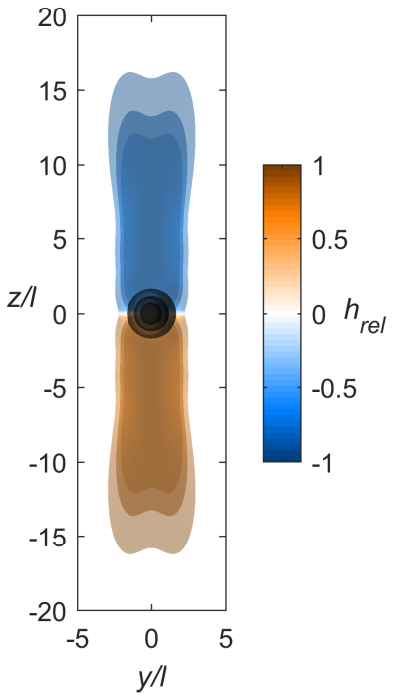

Fig. 2.2.13 Isosurfaces of specific kinetic energy $\mathscr{E} = \frac{1}{2}\boldsymbol{u}\cdot\boldsymbol{u}$, coloured by relative helicity density $\mathscr{H}_{rel} = \boldsymbol{u}\cdot\boldsymbol{\omega}/u\omega$ for inertial wave radiation from a buoyant blob. Translucent isosurfaces are drawn at $\mathscr{E}$ equal to $(5:5:20)\%$ of its maximum value at $\Omega t = 10$; the dark grey isosurfaces are at quartiles of the buoyancy field.

reinstated in the momentum equation (2.2.4), and a standard advection-diffusion equation with diffusivity κ is also solved for the buoyancy field $c(\boldsymbol{r},t)$. By comparing our results with the DNS, we achieve two things: first, to validate the linear analysis and the assumptions made in order to perform it; second, to confirm that the results of Davidson & Ranjan (2015) are indeed fully explainable by the linear dynamics of inertial waves.

Figure 2.2.14 shows a direct comparison with DNS of an isosurface of u_z at one instant; the fact that the two are indistinguishable is very reassuring, and suggests that, for a single blob at least, the linear analysis is doing a very good job. It is also of geophysical interest, however, to study a buoyant region rather than a localised individual source, as a cartoon for the thermal flux in the equatorial plane of the Earth's outer core. Davidson & Ranjan achieve this by considering an initial condition which is a random sum of Gaussian blobs (as per (2.2.25)) then running the DNS again in a periodic domain. For the linear formulation, however, we can of course translate, rescale and sum the solution for a single blob in order to calculate that for many blobs, so imitating the solutions of Davidson & Ranjan is reasonably trivial. Figure 2.2.15 shows a comparison for a very large number of buoyant blobs placed in

(a) DNS at $Ro = 0.01$ (Davidson & Ranjan, 2015).

(b) analytical at $Ro \to 0$.

Fig. 2.2.14 Comparison with DNS for a single buoyant blob. Isosurfaces of u_z at 10% of its maximum absolute value, at $\Omega t = 8$, coloured by sign - red positive, blue negative. Gravity acts into the page, rotation is vertical, and the black sphere shows the location of the blob.

the mid-plane of rapidly-rotating cube, which again shows a very good qualitative similarity between the two — though note that the blob placement is randomised so we do no expect them to be identical. In both, the convecting region sprouts a forest of columnar vortices, tending to pair next to each other in opposing sign of u_z, which convey strong negative helicity to the north and positive to the south.

2.3 Conclusions

In this chapter, we have confirmed the importance of low-frequency inertial waves in establishing axially-elongated structures in a rapidly-rotating hydrodynamic system. This has been done through the study of two simple model problems: the first aligns itself with the theoretical and experimental work of Davidson et al. (2006), generalising their analysis of an aligned-axis vortex to one of arbitrary orientation. This is a problem which has also been studied under a low magnetic Reynolds number regime by Siso-Nadal & Davidson (2004). The ability of inertial waves to self-focus energy onto the rotation axis, and segregate helicity by their propagation direction, has been demonstrated both in the context of a single eddy, and a random collection of such eddies.

The second problem looks at the radiation of these same inertial waves from a slowly-gravitating blob of buoyant material, with an eye towards the excitation of helical waves in the core of the Earth. This is a task previously approached by Davidson & Ranjan (2015) via DNS, and we show a convincing agreement between the two approaches in both single- and multiple-blob cases. In the situation considered, analogous to the equatorial plane in Earth's outer core, the basic flow structure, as predicted in Davidson (2014), consists of four columnar vortices – two above the blob, and two below – which extend away from the blob

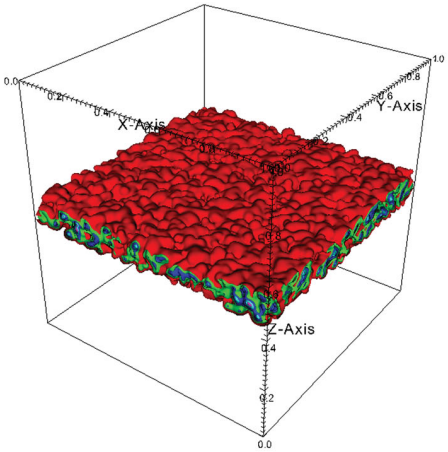

(a) DNS, buoyancy field

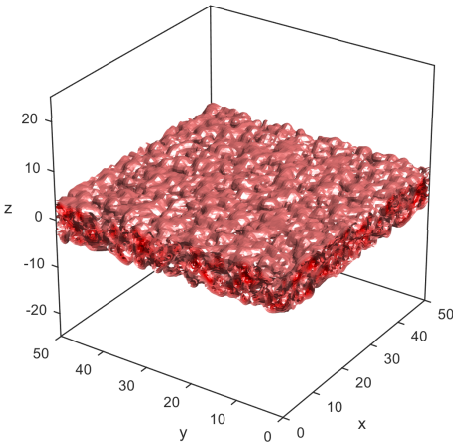

(b) Analytic, buoyancy field

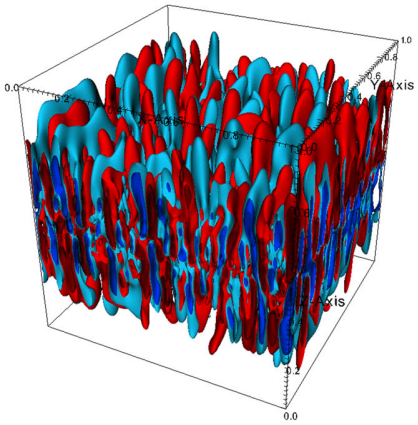

(c) DNS, u_z

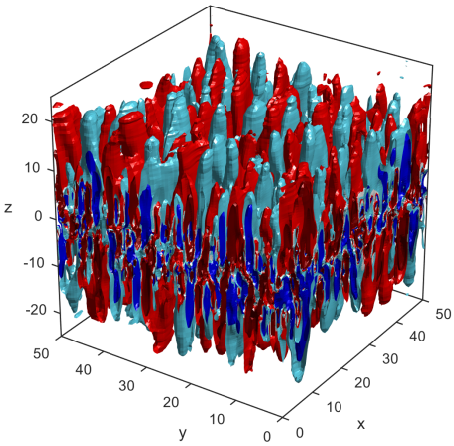

(d) Analytic, u_z

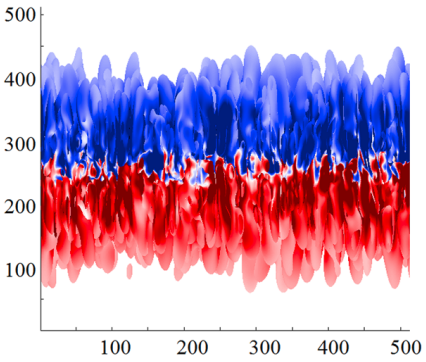

(e) DNS, helicity

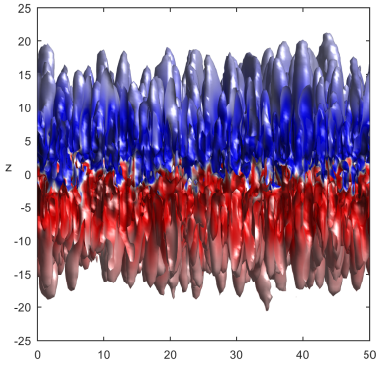

(f) Analytic, helicity

Fig. 2.2.15 Comparison with DNS (Davidson & Ranjan, 2015) for a cloud of buoyant blobs. The instant $\Omega t = 10$ is plotted. 10^4 blobs with sizes ℓ uniformly distributed over $[0.5,\ 1]/\sqrt{2}$ are randomly placed in the x-y plane and the region $|z| \le 3.75$. The cube has side length 50. The top panes show the buoyancy field; middle panes show isosurfaces of $|u_z|$ at 10% of its maximum value, coloured by the sign of u_z (red positive, blue negative); bottom panes show surfaces of u_z^2 at 2.5% of its maximum, coloured by helicity $\mathscr{H} = \boldsymbol{u}\cdot\boldsymbol{\omega}$ (red positive, blue negative), viewed down the x-axis. Rotation $\boldsymbol{\Omega}$ is vertical and gravity $\boldsymbol{g}$ in the negative x-direction. (Note that the DNS has axes $X = -y$ and $Y = x$.)

at the group velocity of low-frequency inertial waves, $z \sim \Omega t\ell$. The wave propagation is driven by this front, which leaves behind it a region of virtually z-invariant (geostrophic) flow, terminated at the buoyant blob itself by the need to balance the buoyancy force due to the three-dimensional disturbance.

Admittedly, the results of this chapter are not particularly ground-breaking or controversial, but they do serve as a very useful introduction to the questions we are to ask in the next. In particular, we will concern ourselves with the alterations brought about by the imposition of a large-scale magnetic field – such as Earth's – on the propagation of inertial waves from a localised source. The techniques used, and rationales employed to interpret the results, are very similar to those above, though the observed behaviour is much more diverse.

Chapter 3

Waves at small scales II: Magnetic waves

We now move from discussion of the dynamics of a rapidly-rotating fluid to those of one which is also conducting, and therefore able to host an even richer assortment of fluid-mechanical phenomena.

This chapter is organised as follows. We motivate the discussion of magnetohydrodynamic (MHD) waves in the context of Earth's outer core in section 3.1.1, before introducing the relevant physical and mathematical theory in section 3.1.2. Section 3.1.3 extends the lessons learned in chapter 2 to the case of a fluid which is both conducting and rapidly-rotating, outlining current perceived wisdom on small-scale rotating-MHD waves in Earth's outer core. We then show that this mode of thinking applies well in the case of a mean magnetic field which is aligned with the rotation axis in section 3.1.4. However, section 3.2 is devoted to a very important situation in which the classical analysis does not apply, and instead a new class of wave – termed the *inertial-Alfvén wave* – plays a particularly important role, as reported in Bardsley & Davidson (2016). Their theory is outlined in section 3.2.1 before showing their importance through a 'buoyant blob' initial value problem (just like section 2.2.6) in section 3.2.2. Various properties of, and evidence for, these new waves are presented in section 3.2.3, before a discussion of the possible consequences of this discovery in the final section, 3.2.4.

3.1 Magnetohydrodynamic waves in a rotating fluid

3.1.1 The relevance of MHD waves in Earth's outer core

The motivation behind the inclusion of a magnetic field in our study of waves within Earth's interior is clear; the observed geomagnetic field is a direct consequence of dynamo action – the conversion of potential energy into magnetic through fluid motion – and therefore

must be an active player in the outer core's dynamics. The relationship between velocity and magnetic fields is two-way: the motion of the fluid must be responsible for twisting and manipulating field lines in order to regenerate the magnetic field (which if treated in isolation comprises the *kinematic dynamo problem*, see Backus (1958); Gubbins (1973, 2008); Chen et al. (2018) for examples), yet the magnetic field also acts back upon the fluid through the Lorentz force, resisting or redirecting the velocity field's attempts to reconfigure it. Furthermore, the electromagnetic field may also dissipate energy through Ohmic heating, providing a means by which the fluid's movements may be quenched. The complicated interplay between these processes in the context of a planetary interior is at the very centre of the dynamo problem, and on some fundamental level understanding the conveyance of energy between thermal, velocity and magnetic fields is the object of our study.

Of course, waves are a very important means by which energy – or equivalently, information – is transferred from place to place through a continuum. We have already seen how the background rotation enables inertial wave motion to take place, but the presence of a magnetic field is also well-known to facilitate oscillations in a conducting fluid (Alfvén, 1942; Davidson, 2013). The inclusion of both, therefore, may be expected to open the door to a diverse collection of possible wave motions. Unpicking these possibilities, which is the objective of this section and the next, should aid fundamental understanding of the dynamics of wave motion at small scales within the Earth.

The internal magnetic field strength

Before we can begin any meaningful investigations into hybrid rotational/magnetic wave motion, we are required to speculate on what the key features of Earth's internal magnetic field might be, both in terms of its magnitude and configuration. Unfortunately speculation is pretty much the best we can achieve, owing to the magnetic curtain (Roberts & King, 2013), but we can make use of certain observational and computational evidence to ensure our estimates have some grain of truth.

Observations of the spherical radial magnetic field at the CMB are available (see Jackson & Finlay, 2015, and references therein) and reliable, at least up to degree 13. They show a predominantly dipolar field with a magnitude of up to 10G (Gauss, where $1\text{G} = 10^{-4}$ Tesla) with an average about 3G, though it does vary considerably as a function of both space and time. It is also possible to infer the volume-averaged axial field strength $\langle B_z \rangle_V$ from measurement of the dipole moment (Jackson, 1998), giving a value of approximately 3.7G. The other components of $\boldsymbol{B}$, being confined to the interior, are much harder to uncover: Gillet et al. (2010) use data from length-of-day variations to suggest a cylindrical radial field of the order 20G; assuming isotropy, they infer a typical field magnitude of around 40G. This

figure agrees with the physical reasoning of Starchenko & Jones (2002), though the scaling arguments of Christensen & Aubert (2006), extrapolated from a suite of numerical dynamos, suggest a slightly weaker field of ~12G. The magnitude of the azimuthal magnetic field has also been estimated at up to 50G (Zhang & Fearn, 1993), or even as high as 120G (Hori et al., 2015), but the majority of guesses for the magnitude of the non-axial field seem to fall in the region of 20-40G.

In any case, it seems likely that the internal field is somewhat stronger than the directly observable values at the outer core periphery, and the azimuthal field in particular could be very intense; this was certainly the case in early numerical simulations (Glatzmaier & Roberts, 1995; Olson et al., 1999; Kono & Roberts, 2002), which displayed many 'Earth-like' properties in their surface magnetic fields (including westward drift and geomagnetic reversals), whilst also featuring a strong internal toroidal field. However, note that modern efforts seem to be approaching a state in which azimuthal and poloidal fields are of more similar magnitudes (e.g. Sakuraba & Roberts, 2009), as one might expect for a dynamo of α^2 type (Jones, 2011). Alternatively, for an α-Ω dynamo, in which the sweeping out of poloidal field lines is the dominant mechanism of toroidal field generation (Davidson, 2013), the toroidal field tends to be stronger; unfortunately, it is not known how powerful this effect is in actuality, and therefore B_ϕ remains a mystery.

Magnetic dissipation

Any non-ideal fluid must dissipate energy to heat in some way, and for the liquid iron of Earth's interior it is believed that the majority of these losses occur through Ohmic heating rather than the fluid's viscosity (Christensen & Tilgner, 2004; Sheyko et al., 2018). This is mainly because the ratio of the respective diffusivities, called the *magnetic Prandtl number* $Pm = \nu/\eta$, is believed to be of the order 10^{-6} for iron at the conditions of the outer core, and therefore diffusion of the magnetic field is many orders of magnitude faster than diffusion of momentum (turbulent effects notwithstanding). This seems reasonable grounds to neglect ν entirely, and instead concern ourselves only with the contribution from η.

The key dimensionless parameter in this context is the *magnetic Reynolds number* $Rm = UL/\eta$, which measures the comparative rates of advection and diffusion of the magnetic field at the lengthscale L. We previously selected our smallest lengthscale ℓ on the grounds that the minimum scales within the core are unlikely to have a value of Rm below unity – as they would simply be blurred out by diffusion – so it should come as no surprise that the selected wave scales have a reasonably small Rm (of order 10 for $u \sim 0.4\text{mm}\,\text{s}^{-1}$, $\ell \sim 10\text{km}$ and $\eta \sim 0.5\text{m}^2\,\text{s}^{-1}$), though it is still larger than unity, suggesting that advection is a somewhat more important process than diffusion.

In fact, we choose to completely neglect η in our discussion of wave motion, despite the fact Rm is only a little greater than unity. This is because the pertinent velocity for our causes is not that of the fluid itself, but rather the speed at which the waves propagate energy, i.e. the group velocity magnitude c_g. For inertial waves we have $c_g \sim \Omega\ell$, and therefore a "wave magnetic Reynolds number" $c_g\ell/\eta \sim \Omega\ell^2/\eta \sim 10^4$ — meaning the waves may propagate energy a very long way before being significantly arrested by dissipation. The diffusion time $\tau_\eta = \ell^2/\eta \sim 6$yr, giving diffusion lengths of $L_\eta = c_g\tau_\eta \sim 10^5$km, hundreds of times the outer core thickness. We shall see that oscillations in the magnetic field occur at the Alfvén wave speed $c_g \sim \bar{B}/\sqrt{\rho\mu}$, where $\bar{B}$ is some mean field strength, and so $c_g\ell/\eta \sim \bar{B}\ell/\eta\sqrt{\rho\mu} \sim 10^3$ (using $\bar{B} \sim 20$G); these magnetic waves still far outstrip dissipation in this context, despite not being quite as fast as inertial waves.

However, as we shall see in section 3.2, there exists a special class of waves when both rotation and magnetic field are present which are very much slower than either inertial or Alfvén waves would be alone, and for this class we might expect heavy Ohmic losses to occur in a planetary core. These are even further magnified when the possibility of a changing wavelength is incorporated — although this story will have to wait until chapter 4. For the remainder of this chapter, our fluid will be considered ideal.

3.1.2 MHD wave theory

We now consider the phenomenology of magnetohydrodynamic waves in an ideal conducting fluid threaded by a large-scale magnetic field, though for the moment ignore any background rotation. This is a well-trodden route, and MHD fundamentals with consideration for planetary interiors may be found in a number of textbooks on the subject (Moffatt, 1978; Davidson, 2013; Galtier, 2016), so we lay down only the bare essentials here.

The equations of electrodynamics

In classical electrodynamics, the electric field $\boldsymbol{E}$, magnetic field $\boldsymbol{B}$ and current density $\boldsymbol{J}$ are governed by Maxwell's equations. The MHD approximation for a conducting (but non-magnetic) fluid neglects all terms involving change density in these equations, on the grounds that charge flows freely through the continuum so may never build up. This gives the so-called *pre-Maxwell equations*, which comprise Faraday's law of magnetic induction,

$$\frac{\partial \boldsymbol{B}}{\partial t} = -\nabla \times \boldsymbol{E}, \tag{3.1.1}$$

Ampère's law,

$$\nabla \times \boldsymbol{B} = \mu \boldsymbol{J} \tag{3.1.2}$$

(where μ is the magnetic permeability), Ohm's law for moving charge carriers,

$$\boldsymbol{J} = \sigma \left(\boldsymbol{E} + \boldsymbol{u} \times \boldsymbol{B} \right), \tag{3.1.3}$$

where σ is the electrical conductivity, and the macroscopic Lorentz force per unit volume

$$\boldsymbol{F} = \boldsymbol{J} \times \boldsymbol{B}. \tag{3.1.4}$$

Note that (3.1.1) and (3.1.2) imply that the current density and magnetic flux are both solenoidal fields,

$$\nabla \cdot \boldsymbol{J} = \nabla \cdot \boldsymbol{B} = 0. \tag{3.1.5}$$

We may combine the above equations (3.1.1)–(3.1.3) to give an evolution equation for the magnetic field $\boldsymbol{B}$, which may then be solved simultaneously with the momentum equation (2.2.4) for $\boldsymbol{u}$, the two being coupled by the inclusion of (3.1.4) as a body force. Substituting $\boldsymbol{J}$ from (3.1.2) into (3.1.3), then $\boldsymbol{E}$ from the result into (3.1.1) gives the *induction equation*,

$$\frac{\partial \boldsymbol{B}}{\partial t} = \nabla \times (\boldsymbol{u} \times \boldsymbol{B}) - \nabla \times \left(\eta \nabla \times \boldsymbol{B} \right), \tag{3.1.6}$$

where $\eta = \left(\mu \sigma \right)^{-1}$ is the magnetic diffusivity. Assuming this is constant and using the solenoidal nature of both $\boldsymbol{u}$ and $\boldsymbol{B}$, the induction equation becomes

$$\frac{\partial \boldsymbol{B}}{\partial t} + (\boldsymbol{u} \cdot \nabla) \boldsymbol{B} = (\boldsymbol{B} \cdot \nabla) \boldsymbol{u} + \eta \nabla^2 \boldsymbol{B}. \tag{3.1.7}$$

We will use this as the evolution equation for $\boldsymbol{B}$ throughout the remainder of this thesis.

Frozen flux, magnetic tension and Alfvén waves

A remarkable feature of the induction equation (3.1.6) is that it is utterly identical to the vorticity equation of conventional hydrodynamics, and therefore familiar results in vortex theory also apply to magnetic field lines. Most significantly, there exist analogues of the Helmholtz laws for an ideal fluid: magnetic field lines are necessarily material curves (constrained to move with the fluid) and furthermore conserve their flux as the flow evolves. Note that this only strictly applies for $\eta = 0$, and that $\boldsymbol{u}$ is not derived from $\boldsymbol{B}$ in the same way as it would be from $\boldsymbol{\omega}$, but rather through the action of the Lorentz force in the momentum

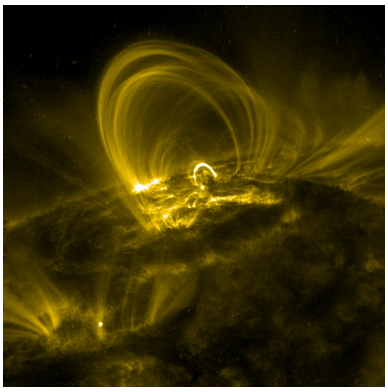

(a) Magnetic flux loops in a solar flare within the sun's corona.[(i)]

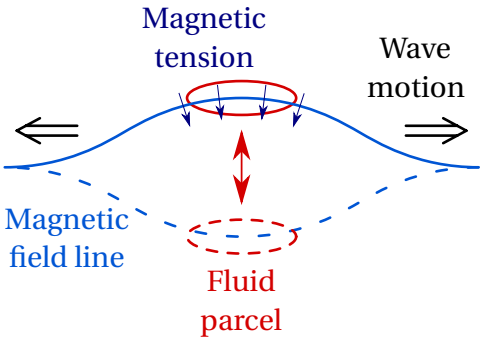

(b) Schematic explanation of Alfvén waves, a consequence of magnetic tension and fluid inertia.

Fig. 3.1.1 Alfvén waves in an ideal conducting fluid

equation. This does not, however, affect the hypothesis that, at large Rm, magnetic field lines may be considered 'frozen in' to the conducting fluid they pervade.

Clearly the nature of the feedback of the magnetic field on the fluid through the Lorentz force of (3.1.4) requires consideration. Note that, using Ampère's law (3.1.2), we may write it as

$$\boldsymbol{F} = \frac{1}{\mu}(\nabla \times \boldsymbol{B}) \times \boldsymbol{B} = \frac{1}{\mu}(\boldsymbol{B}\cdot\nabla)\,\boldsymbol{B} - \nabla\left(\frac{B^2}{2\mu}\right). \tag{3.1.8}$$

The second term is a magnetic pressure which may be absorbed into p in much the same way as the centrifugal term was for a rotating fluid. The first may be written in magnetic field line co-ordinates as

$$\frac{1}{\mu}(\boldsymbol{B}\cdot\nabla)\,\boldsymbol{B} = \frac{\partial}{\partial S}\left(\frac{B^2}{2\mu}\right)\boldsymbol{e}_T - \frac{B^2}{\mu R}\boldsymbol{e}_N, \tag{3.1.9}$$

where S is a co-ordinate measured along the field line, R is the local radius of curvature of the field line, and $\boldsymbol{e}_T$ and $\boldsymbol{e}_N$ are the local unit vectors tangent and (principal) normal to the field line respectively. The interpretation here is that there are forces acting both along and perpendicular to the field line, with the normal force being proportional to the local field line curvature. This is much in line with what one might expect from a taught elastic rope under a tension B^2/μ; it resists both stretching along its length and bending across it.

Importantly, this opposition to motion transverse to the field lines, combined with the 'frozen-in' property, allows a large-scale magnetic field in a conducting fluid to support oscillations known as *Alfvén waves* (Alfvén, 1942), a ubiquitous feature of ideal MHD flow (for

[(i)] Courtesy of the Transition Region and Coronal Explorer (TRACE), a mission of the Stanford-Lockheed Institute for Space Research and part of the NASA Small Explorer program.

example, in the solar corona, figure 3.1.1a). To conceptualise their dynamics, we consider a localised disturbance which perturbs a small parcel of fluid in magnetic field which is locally uniform (figure 3.1.1b). Because the magnetic field lines are effectively glued into an ideal fluid, they must move with it, bowing out in the direction of motion. The field line tension, however, resists this deformation, acting like a taught elastic band to return the field lines to their equilibrium position. However, the fluid which is pinned to the field lines attributes them with some mass, and therefore inertia, meaning they overshoot their original location, causing the field lines to bow out in the opposite direction — and in this manner continue to oscillate. This is the basic premise behind Alfvén waves, which propagate energy along magnetic field lines in a non-dispersive manner; in fact, they have the frequency, phase velocity and group velocity

$$\varpi = \pm \frac{\boldsymbol{B}\cdot\boldsymbol{k}}{\sqrt{\rho\mu}}, \qquad \boldsymbol{c}_p = \boldsymbol{c}_g = \pm \frac{\boldsymbol{B}}{\sqrt{\rho\mu}} \tag{3.1.10}$$

(Alfvén, 1950). These waves are a cornerstone of MHD processes and find application across its many various facets (Parker, 1958; Roberts et al., 1984; Keiling, 2009), often transporting energy from place to place within a conducting continuum pervaded by a mean magnetic field.

3.1.3 Rotating-MHD waves

We now reach the most important piece of theory necessary for the studies of the rest of this chapter and the next; the properties of the small-scale waves possible when both a bulk rotation and background magnetic field are present, which we refer to in general as *hybrid* or *magnetic-Coriolis* waves. The following derivation is a reasonably common one (e.g. Finlay et al., 2010; Davidson, 2013), though the work which follows on from it casts the results in a new light which should be of considerable interest to the geodynamo researcher.

Our starting point is the inviscid momentum equation in a rapidly-rotating frame, now featuring both Coriolis and Lorentz forces:

$$\frac{\partial \boldsymbol{u}}{\partial t} + (\boldsymbol{u}\cdot\nabla)\,\boldsymbol{u} + 2\boldsymbol{\Omega}\times\boldsymbol{u} = -\nabla\left(\frac{p''}{\rho}\right) + \frac{1}{\rho\mu}(\boldsymbol{B}\cdot\nabla)\,\boldsymbol{B}. \tag{3.1.11}$$

The 'modified modified pressure' $p'' = p - \frac{1}{2}\rho\,(\boldsymbol{\Omega}\times\boldsymbol{r})^2 + \frac{1}{2\mu}B^2$ now includes both centrifugal and magnetic contributions. We also have the induction equation (3.1.7), within which we set $\eta = 0$, and the solenoidal conditions $\nabla\cdot\boldsymbol{u} = \nabla\cdot\boldsymbol{B} = 0$.

The first step is to split the magnetic field into a steady portion $\bar{\boldsymbol{B}}$ – which is assumed to be locally constant, or rather variations in $\bar{\boldsymbol{B}}$ occur on lengthscales much greater than the pertinent wavelengths – and a fluctuating portion $\boldsymbol{b}$ with a magnitude much less than the total field. This means the equations can be sensibly linearised: writing $\boldsymbol{B}(\boldsymbol{r},t)=\bar{\boldsymbol{B}}+\boldsymbol{b}(\boldsymbol{r},t)$ and ignoring all quadratic quantities in $\boldsymbol{u}$ and/or $\boldsymbol{b}$ converts the governing equations into the more manageable

$$\frac{\partial \boldsymbol{u}}{\partial t}+2\boldsymbol{\Omega}\times\boldsymbol{u}=-\nabla\left(\frac{p''}{\rho}\right)+\frac{1}{\rho\mu}\left(\bar{\boldsymbol{B}}\cdot\nabla\right)\boldsymbol{b}, \tag{3.1.12a}$$

$$\frac{\partial \boldsymbol{b}}{\partial t}=\left(\bar{\boldsymbol{B}}\cdot\nabla\right)\boldsymbol{u}, \tag{3.1.12b}$$

$$\nabla\cdot\boldsymbol{u}=\nabla\cdot\boldsymbol{b}=0. \tag{3.1.12c}$$

We now manipulate these into a single equation for $\boldsymbol{u}$ (though one could choose $\boldsymbol{b}$ instead if desired). To eliminate $\boldsymbol{b}$, substitute the curl of the induction equation (3.1.12b) into $\nabla\times\frac{\partial}{\partial t}$ of the momentum equation (3.1.12a) to give

$$\left[\frac{\partial^2}{\partial t^2}-\frac{1}{\rho\mu}\left(\bar{\boldsymbol{B}}\cdot\nabla\right)^2\right]\boldsymbol{\omega}=\left(2\boldsymbol{\Omega}\cdot\nabla\right)\frac{\partial \boldsymbol{u}}{\partial t}. \tag{3.1.13}$$

Applying the operator "$\left[\frac{\partial^2}{\partial t^2}-\frac{1}{\rho\mu}\left(\bar{\boldsymbol{B}}\cdot\nabla\right)^2\right]\nabla\times$" to this equation, then substituting it back into itself, we get our promised equation for $\boldsymbol{u}$,

$$\left[\frac{\partial^2}{\partial t^2}-\frac{1}{\rho\mu}\left(\bar{\boldsymbol{B}}\cdot\nabla\right)^2\right]^2\nabla^2\boldsymbol{u}+\left(2\boldsymbol{\Omega}\cdot\nabla\right)^2\frac{\partial^2 \boldsymbol{u}}{\partial t^2}=0. \tag{3.1.14}$$

We refer to this as the "hybrid wave equation" as the solutions it supports are a subtle blend of both rotational and magnetic effects. Carrying straight on and seeking normal-mode solutions of the form $\boldsymbol{u}(\boldsymbol{r},t)=\mathbb{R}\left\{\tilde{\boldsymbol{u}}e^{i(\boldsymbol{k}\cdot\boldsymbol{r}-\omega t)}\right\}$ gives a quartic dispersion relation which may be expressed in a number of ways:

$$\left(\omega^2-\omega_B^2\right)^2=\left(\omega_\Omega\omega\right)^2 \tag{3.1.15a}$$

$$\omega^2\mp\omega_\Omega\omega-\omega_B^2=0 \tag{3.1.15b}$$

$$\omega=\frac{\omega_\Omega}{2}\left[\pm1\,(\pm)\sqrt{1+\left(\frac{2\omega_B}{\omega_\Omega}\right)^2}\right]. \tag{3.1.15c}$$

The term $\omega_\Omega=2\boldsymbol{\Omega}\cdot\boldsymbol{k}/k$ represents the inertial wave frequency (in analogy with 2.2.10) and $\omega_B=\boldsymbol{B}\cdot\boldsymbol{k}/\sqrt{\rho\mu}$ is the Alfvén wave frequency (in analogy with 3.1.10) — though note

that neither contains the ± from whence they were originally defined. Instead, this choice is included explicitly in the forms (3.1.15b) and (3.1.15c). Since the dispersion relation is quadratic, there are four possible choices for ϖ which satisfy it once a wavevector $\boldsymbol{k}$ has been prescribed. This makes sense because each wave-bearing system (rotation or magnetic field) can propagate equivalent waves in two opposite directions (along/against the axis, or in both senses along field lines), and two binary choices gives a total of four options. To represent this, we use a conventional ± for the 'inertial wave choice' – where the upper (*lower*) sign still corresponds to northwards (*southwards*) propagation, see section 2.2.2 – alongside a bracketed (±) for the 'Alfvén wave choice', with the upper sign being propagation in the direction of $\bar{\boldsymbol{B}}$, and the lower sign antiparallel to it.

It is worth noting that, in the case of no magnetic field, the above dispersion relation simplifies to that of pure inertial waves (as per 2.2.10), $\varpi = \pm\varpi_\Omega$, and similarly when there is no background rotation we obtain post-hoc the dispersion relation for Alfvén waves (3.1.10), or $\varpi = (\pm)\,\varpi_B$, as expected. The full dynamics, however, are much richer — to unearth them, we will of course also need to consider the group velocity, given by the gradient in $\boldsymbol{k}$-space of (3.1.15b) or (3.1.15c):

$$\boldsymbol{c}_g = \frac{(2\varpi_B/\varpi)\,\boldsymbol{c}_{gB} \pm \boldsymbol{c}_{g\Omega}}{1+(\varpi_B/\varpi)^2} \tag{3.1.16a}$$

$$= (\pm)\frac{2\varpi_B/\varpi_\Omega}{\sqrt{1+(2\varpi_B/\varpi_\Omega)^2}}\boldsymbol{c}_{gB} + \frac{1}{2}\left[\pm 1(\pm)\frac{1}{\sqrt{1+(2\varpi_B/\varpi_\Omega)^2}}\right]\boldsymbol{c}_{g\Omega}. \tag{3.1.16b}$$

We use $\boldsymbol{c}_{gB} = \bar{\boldsymbol{B}}/\sqrt{\rho\mu}$ for the group velocity of Alfvén waves and $\boldsymbol{c}_{g\Omega} = \boldsymbol{k}\times(2\boldsymbol{\Omega}\times\boldsymbol{k})/k^3$ for that of inertial waves; again, the signs (which correspond to propagation directions) are provided explicitly in (3.1.16).

Dominance of rotation and well-separated roots

At this stage, it is common – almost universal – practice in the literature to seek to leverage the fact that, in planetary cores, the rotation is in some sense dominant over all other effects, including the magnetic field. This is as measured by the Lehnert number $Le = \left(\bar{B}/\sqrt{\rho\mu}\right)/\Omega\ell$, which is the ratio of Alfvén wave speed to inertial wave speed (Lehnert, 1954); since the latter can reasonably be expected to be at least an order of magnitude faster, the Lehnert number is thought to be rather small in the core of the Earth ($\sim 10^{-4}$ at the global scales (Jault, 2008) and $\sim 0.01-0.1$ at the very smallest). Note that the dispersion relation in the form (3.1.15c) and group velocity in the form (3.1.16b) are functions of the term $2\varpi_B/\varpi_\Omega$, which we might

suppose has an order of magnitude

$$\frac{2\varpi_B}{\varpi_\Omega} = \frac{\bar{\boldsymbol{B}}\cdot\boldsymbol{k}/\sqrt{\rho\mu}}{\boldsymbol{\Omega}\cdot\boldsymbol{k}/k} \sim \frac{\bar{B}/\sqrt{\rho\mu}}{\Omega\ell} = Le \ll 1 \tag{3.1.17}$$

and is hence a small parameter (though note that for certain special cases, such as $k\to\infty$ and $\boldsymbol{\Omega}\cdot\boldsymbol{k}\to 0$, this is violated — an important point to which we shall return). Writing (3.1.15c) and (3.1.16b) as power series expansions for small $2\varpi_B/\varpi_\Omega$, we get

$$\varpi \approx \frac{\varpi_\Omega}{2}\left(\pm 1(\pm)\left[1+\frac{1}{2}\left(\frac{2\varpi_B}{\varpi_\Omega}\right)^2 - \frac{1}{8}\left(\frac{2\varpi_B}{\varpi_\Omega}\right)^4 + \cdots\right]\right), \tag{3.1.18a}$$

$$\begin{aligned}\boldsymbol{c}_g \approx (\pm)&\left[\frac{2\varpi_B}{\varpi_\Omega} - \frac{1}{2}\left(\frac{2\varpi_B}{\varpi_\Omega}\right)^3 + \cdots\right]\boldsymbol{c}_{gB}\\ &+\frac{1}{2}\left(\pm 1(\pm)\left[1-\frac{1}{2}\left(\frac{2\varpi_B}{\varpi_\Omega}\right)^2 + \frac{3}{8}\left(\frac{2\varpi_B}{\varpi_\Omega}\right)^4 + \cdots\right]\right)\boldsymbol{c}_{g\Omega}.\end{aligned} \tag{3.1.18b}$$

The nature of these waves is now strongly dependent on the choice of signs. For clarity, consider only northward-propagating waves, which take the upper sign from the (unbracketed) $\pm$; now, if the upper bracketed sign is also chosen, we get

$$\varpi \approx \varpi_\Omega + \left(\frac{\varpi_B^2}{\varpi_\Omega}\right) + \cdots, \tag{3.1.19a}$$

$$\boldsymbol{c}_g \approx \left(\frac{2\varpi_B}{\varpi_\Omega} + \cdots\right)\boldsymbol{c}_{gB} + \left(1 - \left[\frac{\varpi_B}{\varpi_\Omega}\right]^2 + \cdots\right)\boldsymbol{c}_{g\Omega}. \tag{3.1.19b}$$

These are, to leading order, simple inertial waves (2.2.10, 2.2.12), only slightly modified by the presence of the magnetic field; this is a reasonably predictable outcome, as assuming dominance of rotational effects should give us a solution from the case in which they were the only player. The second set of roots, however, are something quite different; choosing the lower sign in $(\pm)$, the dispersion equations (3.1.18a) and (3.1.18b) become

$$\varpi \approx \left(-\frac{\varpi_B^2}{\varpi_\Omega}\right) + \left(\frac{\varpi_B^4}{\varpi_\Omega^3}\right) + \cdots, \tag{3.1.20a}$$

$$\boldsymbol{c}_g \approx \left(-\frac{2\varpi_B}{\varpi_\Omega} + 4\left(\frac{\varpi_B}{\varpi_\Omega}\right)^3 + \cdots\right)\boldsymbol{c}_{gB} + \left(\left(\frac{\varpi_B}{\varpi_\Omega}\right)^2 - 3\left(\frac{\varpi_B}{\varpi_\Omega}\right)^4 + \cdots\right)\boldsymbol{c}_{g\Omega}. \tag{3.1.20b}$$

These are very low-frequency, very slow solutions known as *magnetostrophic waves*. The term *magnetostrophic* was coined in analogy with *geostrophic*, which is taken to mean an inertialess balance between Coriolis and pressure forces; a magnetostrophic balance

includes the Lorentz force as well, i.e. the momentum equation (3.1.11) is devoid of both $\partial \boldsymbol{u}/\partial t$ and $(\boldsymbol{u}\cdot\nabla)\,\boldsymbol{u}$, becoming a diagnostic equation for $\boldsymbol{u}$ as a function of $\boldsymbol{B}$.

The well-known paradigm, then, is that the hybrid wave equation, in the limit of rapid rotation, has roots with well-separated frequencies and wildly varying group velocities; the fast weakly-modified inertial waves from the non-magnetic case, plus the slow magnetostrophic waves which evolve through the magnetic induction equation alone. It is expected that the radiation from a localised source, therefore, should be dominated by a combination of these two wave types — and we present in section 3.1.4 a situation where this is indeed the case. However, section 3.2 is devoted to showing that the 'well-separated root hypothesis' is highly misleading, and does not in fact accurately represent the radiation from a localised source at all, for a reasonable choice of mean magnetic field.

Kinetic and magnetic helicity

We finish off this theoretical survey of rotating-MHD waves with a quick note on the flow and field structure, in particular the helicity. Recall that pure inertial waves are maximally helical, and furthermore the north-south propagation direction is uniquely determined by the sense of that helicity (left-handed spirals north, right-handed ones south) — see section 2.2.4. It turns out the same is true for all hybrid wave solutions, and also for other helicities, such as magnetic, current and cross helicity. Let $\boldsymbol{j}$ and $\boldsymbol{a}$ be the current density associated with and solenoidal vector potential for $\boldsymbol{b}$, respectively, and let all vector fields take on a normal mode form $\left(\boldsymbol{u},\,\boldsymbol{\omega},\,\boldsymbol{b},\,\boldsymbol{j},\,\boldsymbol{a}\right) = \mathbb{R}\left\{\left(\tilde{\boldsymbol{u}},\,\tilde{\boldsymbol{\omega}},\,\tilde{\boldsymbol{b}},\,\tilde{\boldsymbol{j}},\,\tilde{\boldsymbol{a}}\right) e^{i(\boldsymbol{k}\cdot\boldsymbol{r}-\omega t)}\right\}$. We can see by substituting this into (3.1.13) and using the dispersion relation (3.1.15b) that we still have

$$\tilde{\boldsymbol{\omega}} = \mp k\tilde{\boldsymbol{u}} \tag{3.1.21}$$

and therefore the spatial structure of the velocity field is the same for all hybrid waves: maximally helical, at least for monochromatic (single Fourier-mode) solutions. Using the linearised induction equation (3.1.12b) and its curl, plus $\nabla\times\boldsymbol{a}=\boldsymbol{b}$, we can derive similar expressions involving the magnetic field variables:

$$\frac{\tilde{\boldsymbol{b}}}{\sqrt{\rho\mu}} = -\frac{\omega_B}{\omega}\tilde{\boldsymbol{u}}, \tag{3.1.22a}$$

$$\mu\tilde{\boldsymbol{j}} = \mp k\tilde{\boldsymbol{b}}, \tag{3.1.22b}$$

$$\tilde{\boldsymbol{b}} = \mp k\tilde{\boldsymbol{a}}. \tag{3.1.22c}$$

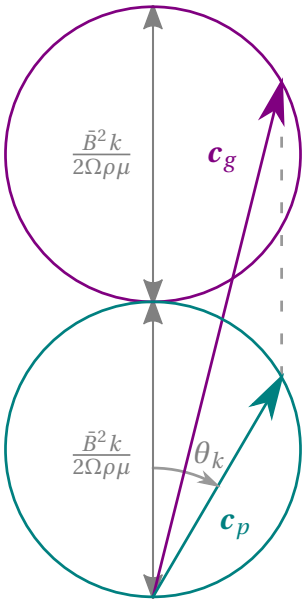

Fig. 3.1.2 Relationship between phase and group velocities for northward-propagating magnetostrophic waves. As θ_k varies the heads of the $\boldsymbol{c}_p$ and $\boldsymbol{c}_g$ arrows trace out the teal- and purple-coloured circles respectively — both have diameter $\bar{B}^2 k/2\Omega\rho\mu$.

We can see that current helicity $\boldsymbol{j}\cdot\boldsymbol{b}$ and magnetic helicity $\boldsymbol{a}\cdot\boldsymbol{b}$ behave exactly like kinetic helicity $\boldsymbol{u}\cdot\boldsymbol{\omega}$, being both maximal and determining the axial travel direction; we might expect the hybrid waves to segregate these helicities in exactly the same way as the inertial waves did for kinetic helicity. The cross helicity $\boldsymbol{u}\cdot\boldsymbol{b}$ is also maximal ($\boldsymbol{u}$ and $\boldsymbol{b}$ are aligned), but its sign is not segregated in the same way.

3.1.4 Magnetostrophic waves

In this section, we study a model problem in which the 'well-separated roots' hypothesis of section 3.1.3 does appear to withstand scrutiny, and the radiation from a localised source is indeed dominated by a combination of inertial and magnetostrophic waves; specifically, we consider the case when the mean magnetic field is aligned with the rotation axis, and the inertial wave speed is much greater than the Alfvén wave speed, as one might expect in a geophysical context.

Magnetostrophic wave theory

Consider the well-separated roots of equations (3.1.19a)-(3.1.20b) in the situation $\bar{\boldsymbol{B}} \parallel \boldsymbol{\Omega}$. The fast roots are weakly modified inertial waves, essentially identical to the hydrodynamic waves studied extensively in section 2.2, so we will not dwell upon them any longer. The slow

roots (magnetostrophic waves) are however worth further investigation. The northward-propagating versions have a frequency

$$\varpi_M = \frac{\varpi_B^2}{\varpi_\Omega} = \frac{\left(\bar{\boldsymbol{B}}\cdot\boldsymbol{k}\right)^2/\rho\mu}{2\boldsymbol{\Omega}\cdot\boldsymbol{k}/k} = \frac{\bar{B}^2k^2}{2\Omega\rho\mu}\cos\theta_k, \tag{3.1.23}$$

where θ_k is the angle of $\boldsymbol{k}$ down from the z-axis (cf. (2.2.14a)). For small Lehnert numbers, this frequency is always much less than that of inertial waves, $\varpi_\Omega = 2\Omega\cos\theta_k$. The phase and group velocities corresponding to (3.1.23) are

$$\boldsymbol{c}_p = \frac{\bar{B}^2k}{2\Omega\rho\mu}\cos\theta_k\boldsymbol{e}_k, \tag{3.1.24a}$$

$$\boldsymbol{c}_g = \frac{\bar{B}^2k}{2\Omega\rho\mu}\left(2\cos\theta_k\boldsymbol{e}_k - \sin\theta_k\boldsymbol{e}_{\theta_k}\right), \tag{3.1.24b}$$

where $\boldsymbol{e}_k$ and $\boldsymbol{e}_{\theta_k}$ are the unit vectors in the directions of increasing k and θ_k respectively (cf. (2.2.14)). Noticing that, for a given choice of azimuthal wavevector angle, the locus of $\boldsymbol{c}_p$ describes a circle of diameter $\bar{B}^2k/2\Omega\rho\mu$ situated directly above the origin (much like inertial waves, figure 2.2.1), and that

$$\boldsymbol{c}_g = \boldsymbol{c}_p + \frac{\bar{B}^2k}{2\Omega\rho\mu}\boldsymbol{e}_z, \tag{3.1.25}$$

we come across a useful diagrammatic representation of the relationship between phase and group velocities for magnetostrophic waves. This is sketched in figure 3.1.2, which tells us that:

- Both phase and group velocities are proportional to k, meaning smaller wavelengths travel faster than longer ones, which is the opposite of inertial waves;
- For a given wavevector magnitude k, the phase velocity behaves in much the same way as inertial waves, being constrained to move upon a circle (or in three-dimensional $\boldsymbol{k}$-space, a sphere) directly above the origin;
- The group velocity is constrained to move upon a circle (sphere) of the same size as, and stacked on top of, that for the phase velocity. The $\boldsymbol{c}_g$ vector starts at the origin and ends at the point on that circle exactly $\bar{B}^2k/2\Omega\rho\mu$ above the end of $\boldsymbol{c}_p$;
- Even though the frequency (and therefore phase velocity) can vanish at $\theta_k = \pi/2$, the group velocity is never zero — all waves propagate energy with finite speed in

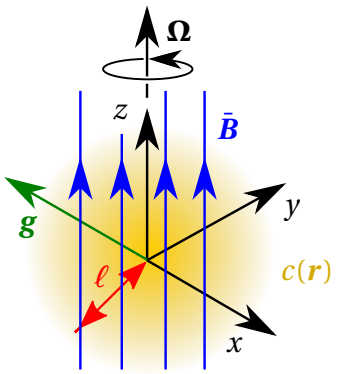

Fig. 3.1.3 Schematic of the initial condition for model problem studying radiation of magnetostrophic waves from a buoyant blob.

the range $\frac{\bar{B}^2 k}{2\Omega\rho\mu} \leq \left|\boldsymbol{c}_g\right| \leq \frac{\bar{B}^2 k}{\Omega\rho\mu}$. Interestingly, the group velocity is constrained to being within an axially-aligned cone of internal half angle $\sin^{-1}(1/3) \approx 19.5°$;

- The 'self-focussing' property of inertial waves also applies to magnetostrophic waves in this context, despite the fact their dispersive characteristics are not identical. That is to say, all wavevectors with $\theta_k \approx \pi/2$ and thus $\varpi_M = \boldsymbol{c}_p = 0$ (of which there are many in three-dimensional $\boldsymbol{k}$-space) have a group velocity which is aligned with the rotation axis/mean magnetic field direction $\boldsymbol{e}_z$. Thus, axially-elongated structures will spread along $\boldsymbol{e}_z$ in much the same way as we observed for pure inertial waves — though note that these hydrodynamic solutions are still present, so we expect to see both doing similar jobs, albeit on very different timescales.

Clearly, the dynamics of these waves are as rich as, if not richer than, those found for inertial waves. As we did in section 2.2 for the hydrodynamic case, we now seek to gain a deeper understanding of magnetostrophic waves by studying them in the context of a simple initial value problem.

Model problem

The set-up for the model problem to study magnetostrophic waves is very similar to the non-magnetic problem of section 2.2.6, in that our source of waves is a Gaussian buoyant density anomaly with profile $c(\boldsymbol{r}) = Ce^{-\boldsymbol{r}^2/2\ell^2}$, and the rotation vector and gravitational acceleration are at right angles. The difference here (see figure 3.1.3) is that we now include a mean magnetic field $\bar{\boldsymbol{B}} = \bar{B}\boldsymbol{e}_z$ aligned with the rotation axis. This could plausibly represent the axial field within the core, with a large-scale structure such that it may be considered locally uniform as far as the blob is concerned. Using $\bar{B} \sim 3.7$G (the mean value of axial field across the core), we get a Lehnert number $Le = \left(\bar{B}/\sqrt{\rho\mu}\right)/\Omega\ell \sim 0.005$, suggesting that the

speeds of magnetic and inertial waves are reasonably disparate. Indeed, it can be seen from the limiting dispersion relations (3.1.19a) and (3.1.20a) that the magnetostrophic waves are a factor $Le^{-2} \sim 5 \times 10^4$ slower than inertial waves for this choice. For computational tractability, however, we calculate the following results with $Le = 0.1$, so the magnetostrophic waves are merely a factor of 100 slower. The general ideas will remain the same so long as we have $Le < O(1)$, however — we will simply need to adjust the timescales accordingly in our discussion.

Our fluid is governed by the ideal linearised momentum and induction equations (3.1.12a) and (3.1.12b), with the addition of a buoyancy term in the former, and the solenoidal conditions on $\boldsymbol{u}$ and $\boldsymbol{b}$:

$$\frac{\partial \boldsymbol{u}}{\partial t} + 2\boldsymbol{\Omega} \times \boldsymbol{u} = -\nabla\left(\frac{p''}{\rho}\right) + \frac{1}{\rho\mu}\left(\bar{\boldsymbol{B}} \cdot \nabla\right)\boldsymbol{b} + c\boldsymbol{g}, \tag{3.1.26a}$$

$$\frac{\partial \boldsymbol{b}}{\partial t} = \left(\bar{\boldsymbol{B}} \cdot \nabla\right)\boldsymbol{u}, \tag{3.1.26b}$$

$$\nabla \cdot \boldsymbol{u} = \nabla \cdot \boldsymbol{b} = 0. \tag{3.1.26c}$$

Taking the curl of (3.1.26a) gives the vorticity equation

$$\frac{\partial \boldsymbol{\omega}}{\partial t} = \left(2\boldsymbol{\Omega} \cdot \nabla\right)\boldsymbol{u} + \frac{1}{\rho\mu}\left(\bar{\boldsymbol{B}} \cdot \nabla\right)\nabla \times \boldsymbol{b} + \nabla c \times \boldsymbol{g}, \tag{3.1.27}$$

from which we may see that any steady particular integral must now be picked up by the magnetic field perturbation rather than the velocity field (since (3.1.26b) requires $\partial \boldsymbol{u}_{PI}/\partial z = 0$). This means that $\boldsymbol{u}$ still satisfies the hybrid wave equation (3.1.14). We solve this system by means of Fourier transforms in appendix A2.1, subject to the initial condition $\boldsymbol{u} = \boldsymbol{b} = 0$, which is enforced into repeated time derivatives of (3.1.27) at $t = 0$ to calculate the Fourier coefficients of the solution. The velocity field is a sum of harmonic functions of time with frequencies of the form

$$\varpi_\pm = \frac{\varpi_\Omega}{2}\left(1 \pm \sqrt{1 + Le^2\kappa^2}\right), \tag{3.1.28}$$

where $\varpi_\Omega = 2\boldsymbol{\Omega} \cdot \boldsymbol{k}/k$ and $\kappa = k\ell$ is the dimensionless wavevector magnitude. We note that:

- In the case $Le = 0$ (non-magnetic), the two frequencies become $\varpi_+ = \varpi_\Omega$ (simple inertial waves) and $\varpi_- = 0$. The latter, zero frequency solution is simply the steady particular integral from the non-magnetic problem; when the magnetic field is added, it morphs into the magnetostrophic branch;

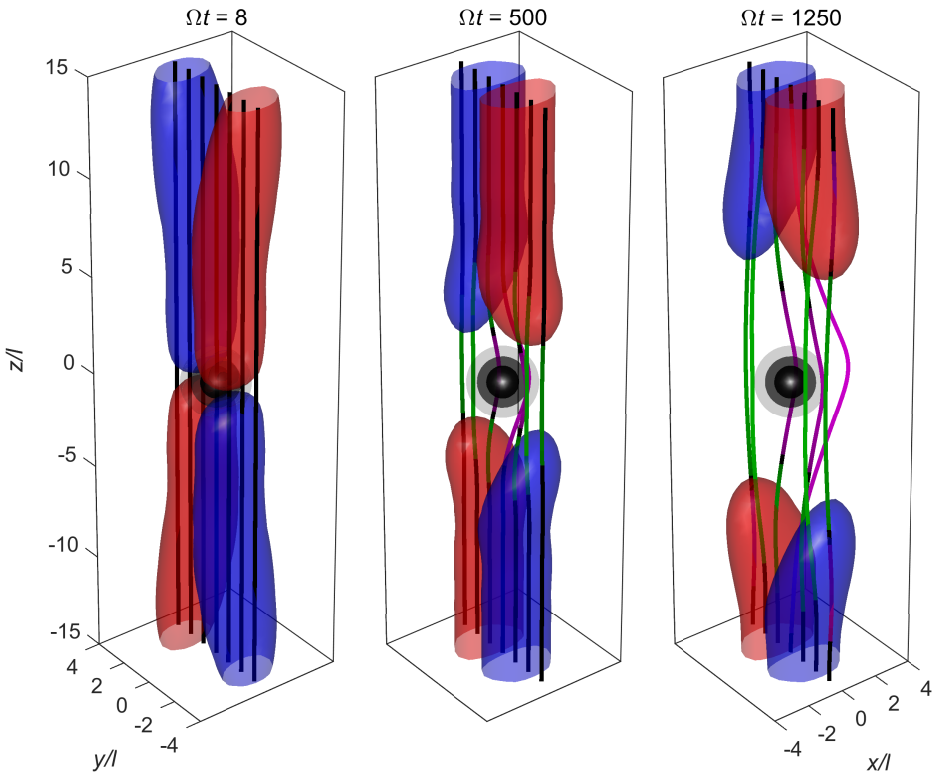

Fig. 3.1.4 Radiation of magnetostrophic waves from a buoyant blob. We take $\boldsymbol{\Omega} = \Omega \boldsymbol{e}_z$, $\bar{\boldsymbol{B}} = \bar{B}\boldsymbol{e}_z$, and $\boldsymbol{g} = -g\boldsymbol{e}_x$, with $Le = \left(\bar{B}/\sqrt{\rho\mu}\right)/\Omega\ell = 0.1$. Isosurfaces show $|u_z|$ at 20% of its maximum value, coloured red for $u_z > 0$ and blue for $u_z < 0$. Field lines seeded at $x = 0$, $y = (-3:1:3)\ell$, $z = -15\ell$ are coloured purple (green) for positive (negative) x-displacement. Grey isosurfaces are at quartiles of the buoyancy field. (Mathematical description in appendix A2.1.1.)

- The modification from the non-magnetic case is only a function of κ, the wavevector magnitude. Hence the results of appendix A1.3 (non-magnetic buoyant blob) carry over to this problem, subject to minor alterations (see appendix A2.1.1).

We calculate the inverse Fourier transforms numerically, as in section 2.2.6, and plot in figure 3.1.4 the solution at three choice times: $\Omega t = [8,\ 500,\ 1250]$ — note that the latter two are much later than we ever considered in the hydrodynamic problem. Axial velocity again turns out to be a useful quantity to plot isosurfaces of in order to follow the waves' progress, and we also calculate a few magnetic field lines in order to assess the contribution of $\bar{\boldsymbol{B}}$ to the dynamics.

Not long after the clock has started ($\Omega t = 8$; left pane) the radiation pattern is very much the same as the non-magnetic case, with inertial waves spreading rapidly on-axis at a rate $z \sim \Omega t \ell$ and no perceptible change to the magnetic field. The flow structure is exactly as

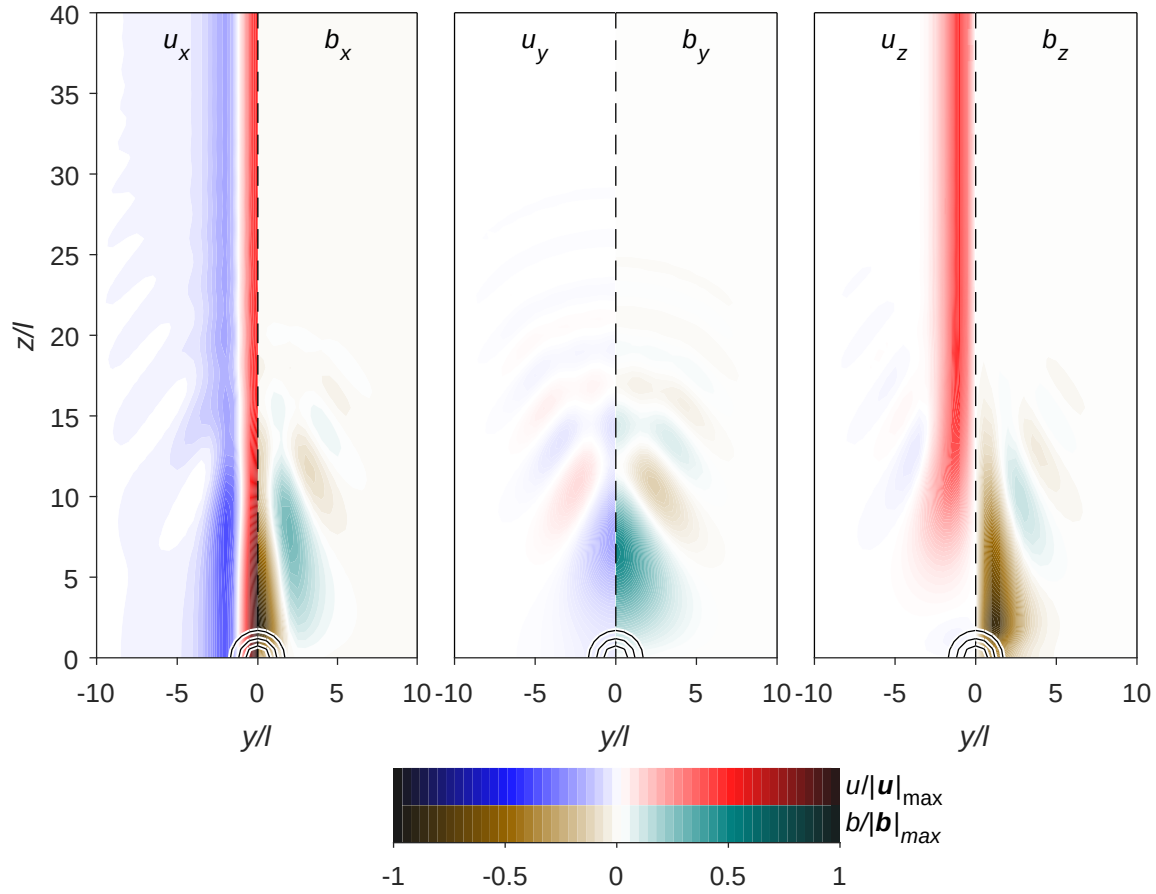

Fig. 3.1.5 Magnetostrophic wave radiation from a buoyant blob, showing all components of $\boldsymbol{u}$ and $\boldsymbol{b}$ in the plane $x = 0$ at $\Omega t = 1250$. Gravity acts into the page and the background rotation and magnetic field are both vertical, with $Le = \left(\bar{B}/\sqrt{\rho\mu}\right)/\Omega\ell = 0.1$. Only one quadrant of the y-z plane is shown for each component: u_x, u_y and b_z are symmetric in z whereas b_x, b_y and u_z are antisymmetric. Both have x and y components symmetric in y, and z components antisymmetric in y. Black contours are at quartiles of the buoyancy field. (Working in appendix A2.1.)

before, with four transient Taylor columns – two above the blob, two below – bringing helical flow towards the blob at positive y and away from it at negative y. The magnetic field only becomes dynamically active some time later ($\Omega t = 500,\ 1250$; centre and right panes). The timescale for this motion is of the order $Le^{-2} \sim 100$ longer than the inertial waves, and the magnetic field is clearly now involved in their propagation, so therefore these must be our promised magnetostrophic solutions.

We plot in figure 3.1.5 a more informative picture of the state of the magnetostrophic waves at $\Omega t = 1250$, corresponding to the right-hand pane of figure 3.1.4. Both the velocity and perturbation magnetic fields are shown, and it is possible to see – particularly

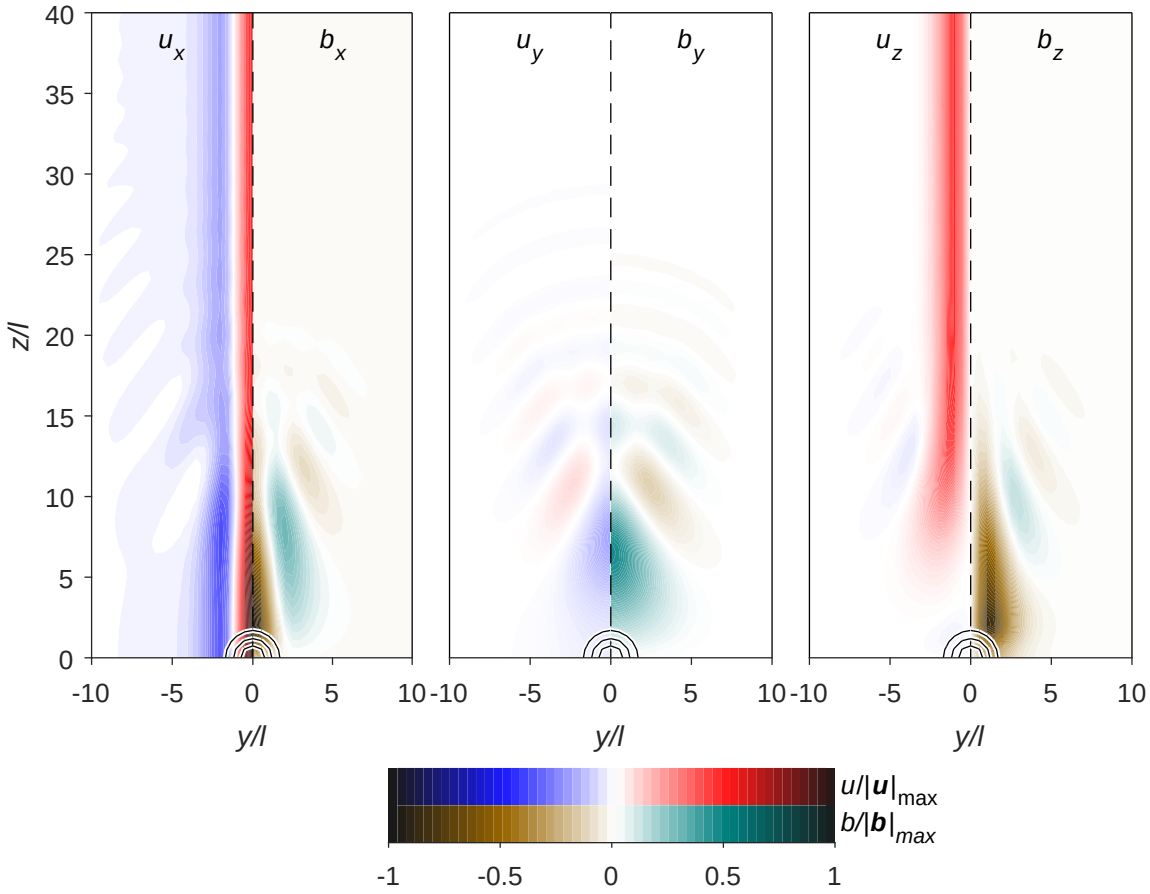

Fig. 3.1.6 As figure 3.1.5, but with the integrands in the dispersion integrals (appendix A2.1.1) truncated after $O(Le^2)$.

in the z-components – the handover from kinetic to magnetic energy taking place as the magnetostrophic waves gradually propagate along the axis at a rate $z/\ell \sim Le^{-2}\Omega t = 12.5$. Not shown, for practical reasons, is the low-frequency weakly-modified inertial wave front (as seen in section 2.2.6), which will have reached the geophysically implausible height $z \sim \Omega t\ell \sim 12\,500$km by this point — emphasising the massive gulf between the two wave speeds. Much like the non-magnetic case, in which the solution was dissected into 3 regions, it is helpful to divide the domain up into 4 (or 5) different zones in order to understand what is going on:

1. **Inertial wave front:** As before, the self-focussing property of low-frequency ($\theta_k \approx \pi/2$) inertial waves means there is intense energy radiation onto the axis, with an ever-extending quartet of Taylor columns emanating from the blob being driven by fast-moving inertial wave fronts at $z \sim \pm\Omega t\ell$;

2. **Taylor column zone:** Behind the inertial wave fronts are regions of very nearly geostrophic (z-invariant) flow, i.e. a set of transient Taylor columns;

3. **Magnetostrophic wave front:** The regions of columnar $\boldsymbol{u}$ are terminated by another wave front, moving much more slowly at the magnetostrophic speed $z \sim \pm Le^2 \Omega t \ell$, which demarcates the transition from a dynamically irrelevant to dynamically active magnetic field. Since magnetostrophic waves self-focus onto the axis when $\bar{\boldsymbol{B}}$ is vertical, this front follows the same path previously taken by the fast inertial waves;

4. **Blob zone:** The buoyancy force from the blob is initially balanced by the Coriolis force due to the $\boldsymbol{u}$-field around the origin, as in the non-magnetic case, because it is by far the fastest to act. However, over the longer timescale this balance is exchanged for magnetic field line tension, as the particular integral in the $\boldsymbol{b}$-field takes over responsibility for balancing the buoyant forcing;

(5. **Off-axis zone:** As just about visible in figure 3.1.5, there is also a non-negligible portion of energy radiated to locations away from the z-axis, though with a much lower energy density, just as in the non-magnetic case. Recall, however, that the magnetostrophic waves can only radiate energy within $\approx 19.5°$ of the z-axis, so there really is very little outside of the cone this describes.)

We can show very convincingly that these results are compatible with the hypothesis that the roots separate well into 'fast' (inertial) and 'slow' (magnetostrophic) wave solutions. The plots of figures 3.1.4 and 3.1.5 are generated by calculating dispersion integrals, given in appendix A2.1.1, wherein the integrands are functions of Le through the expression $\sqrt{1+Le^2\kappa^2}$ in various guises. If we take any such expression and truncate its power series at $O(Le^2)$, we get a new, simpler set of integrands which approximate the full solution, but crucially contain frequencies which are explicitly the fast and slow roots (as in (3.1.19a) and (3.1.20a)). Evaluating these integrals gives the solution plotted in figure 3.1.6, for comparison with the full version (figure 3.1.5); the two are utterly indistinguishable, implying the paradigm of section 3.1.3 is working very well in this case.

3.1.5 Discussion

It is worth asking why the 'well-separated roots' hypothesis, which allows the simplification of the four roots of (3.1.15a) into two pairs of the forms (3.1.19a) and (3.1.20a), works so well in this case. Recall that the necessary assumption was that the magnitude of the Alfvén wave

	τ_M/τ_η	τ_M/τ_U
$Le = 0.1$	~ 0.007	~ 0.05
$Le = 0.005$	~ 3	~ 20

Table 3.1.1 Estimates for the magnetostrophic timescale $\tau_M = \Omega\ell^2/\left(\bar{B}^2/\rho\mu\right)$ relative to the diffusion timescale $\tau_\eta = \ell^2/\eta$ and advection timescale $\tau_U = \ell/U$ for different choices of Lehnert number $Le = \left(\bar{B}/\sqrt{\rho\mu}\right)/\Omega\ell$. The estimates $\ell \sim 10\text{km}$, $\eta \sim 0.5\text{m}^2\,\text{s}^{-1}$ (Pozzo et al., 2014) and $U \sim 0.4\text{mm}\,\text{s}^{-1}$ (Roberts & King, 2013) are used.

frequency $\varpi_B = \bar{\boldsymbol{B}}\cdot\boldsymbol{k}/\sqrt{\rho\mu}$ is much less than the inertial wave frequency $\varpi_\Omega = 2\boldsymbol{\Omega}\cdot\boldsymbol{k}/k$:

$$|\varpi_B| \ll |\varpi_\Omega| \qquad \Longrightarrow \qquad \frac{\bar{B}/\sqrt{\rho\mu}}{2\Omega\ell}\left|\frac{\boldsymbol{e}_B\cdot\boldsymbol{e}_k}{\boldsymbol{e}_\Omega\cdot\boldsymbol{e}_k}\right| k\ell \ll 1. \tag{3.1.29}$$

Now, the choice of a small Lehnert number $\left(\bar{B}/\sqrt{\rho\mu}\right)/\Omega\ell$ means that this condition can only be violated in two eventualities. Firstly, if the wavenumber is particularly large, $k\ell \gg 1$ — but by construction the initial condition, being a localised source of characteristic size ℓ, has most of its energy around that scale ($k \sim \ell^{-1}$) and very little in large wavenumbers (small spatial scales), so they are inconsequential in the radiation pattern. The second manner in which (3.1.29) may be violated is if the term $|(\boldsymbol{e}_B\cdot\boldsymbol{e}_k)/(\boldsymbol{e}_\Omega\cdot\boldsymbol{e}_k)|$, a function only of the wavevector orientation, is allowed to get larger than $\sim Le^{-1}$ for some choices of $\boldsymbol{k}$. As the magnetic field and rotation vectors are aligned in this model problem, there are no choices of wavevector orientation for which this is possible (since $\boldsymbol{e}_B\cdot\boldsymbol{e}_k = \boldsymbol{e}_\Omega\cdot\boldsymbol{e}_k$), and therefore smallness of Lehnert number is sufficient to ensure smallness of $|\varpi_B/\varpi_\Omega|$ universally. Hence, the 'well-separated roots' hypothesis is watertight, and represents what we observe very well indeed.

Remember that we chose $Le = 0.1$ for our model problem in order to obtain a solution which was computationally manageable whilst still observing the requirement $Le \ll 1$, despite the best estimate for the small scales within Earth's core being $Le \sim 0.005$ (using $\bar{B} \sim 3.7\text{G}$, $\ell \sim 10\text{km}$). We consider now the effect of this disparity in Lehnert number, and whether the assumptions required to for this analysis can withstand such an extrapolation. The key question is how the time it takes the magnetostrophic waves to escape the buoyant blob region compares to other timescales of interest — namely, the rate of magnetic dissipation, and speed at which the buoyancy field is convected. We define the magnetostrophic timescale τ_M as the blob size ℓ divided by the axial group velocity of the self-focussing ($\theta_k \sim \pi/2$) waves, which is $\left(\bar{B}^2/\rho\mu\right)/\Omega\ell$ (as per figure 3.1.2 with $k \sim 2/\ell$, cf. section 2.2.6),

and the dissipative and convective timescales τ_η and τ_U are defined in a predictable manner:

$$\tau_M = \frac{\Omega\ell^2}{\bar{B}^2/\rho\mu}, \qquad \tau_\eta = \frac{\ell^2}{\eta}, \qquad \tau_U = \frac{\ell}{U}. \tag{3.1.30}$$

The ratios of these quantities are estimated in table 3.1.1 for both $Le = 0.1$ (the model problem) and $Le = 0.005$ (Earth's core). Clearly, in order for magnetostrophic waves to be relevant, they must act faster than both diffusion of the magnetic field and advection of the buoyant source, i.e. $\tau_M \ll \tau_\eta, \tau_U$. Evidently, this is the case when the Lehnert number is large enough, so the background magnetic field is sufficiently strong to carry the magnetostrophic waves away from the source before it has a chance to evolve significantly by other processes. However, using the mean value of axial field in the Earth ($\bar{B} = 3.7$G, so $Le = 0.005$), the ratio of timescales becomes larger than unity for both of the competing processes — meaning the magnetostrophic waves are not carrying energy away quickly enough for their dynamics to be considered independent of either dissipation or convection of the buoyancy field. Note that the crossovers between these regimes occur at $\tau_M \approx \tau_\eta \implies \bar{B} \approx 7$G and $\tau_M \approx \tau_U \implies \bar{B} \approx 15$G for the parameters used in table 3.1.1, so it is plausible that the axial magnetic field could be locally strong enough for magnetostrophic waves of this form to exist within Earth's outer core (and note that a smaller choice of ℓ would help their case as well). However, in general it seems unlikely that magnetostrophic waves riding upon the background rotation and axial magnetic field in this way are particularly important; on fast timescales weakly-modified inertial waves will dominate, and on slow timescales the magnetostrophic waves' dynamics will become inseparable from those of convection and/or dissipation processes.

We shall see shortly that a non-axial magnetic field has a much more profound effect on the fast dynamics of hybrid waves, and therefore to a good approximation we may neglect the axial field entirely when studying them. Essentially, the fact that rotation is dominant over the magnetic field means that, when the two are aligned, the former always prevails. As discussed in the next section, however, the magnetic field can overcome this deficit — but only if the hybrid waves are able find some way to overcome the dominance of $\boldsymbol{\Omega}$ over $\bar{\boldsymbol{B}}$.

3.2 Inertial-Alfvén waves

We now consider a very important case in which the hypothesis of well-separated roots demonstrably fails, and an entirely separate class of waves, dubbed *inertial-Alfvén waves*, are in fact dominant, a result first published by the author in Bardsley & Davidson (2016). This section, therefore, is a somewhat fleshed-out version of that study, aiming to explain

what inertial-Alfvén waves are, show why they take precedence over the inertial and magnetostrophic solutions, and outline their relevance to Earth's outer core.

3.2.1 Theory

Consider again the dispersion relation (3.1.15b) for MHD waves in a rapidly-rotating ideal conducting fluid, now in the case where the mean magnetic field is allowed to take an arbitrary orientation relative to $\boldsymbol{\Omega}$. In separating the roots of this equation into the fast and slow solutions (3.1.19a) and (3.1.20a), we leveraged the dominance of rotation over magnetic field (small Lehnert number) to assert that $|\varpi_\Omega| \gg |\varpi_B|$ (i.e. $|2\boldsymbol{\Omega}\cdot\boldsymbol{k}/k| \gg \left|\bar{\boldsymbol{B}}\cdot\boldsymbol{k}/\sqrt{\rho\mu}\right|$), but briefly acknowledged that this may not hold in the particular case $\boldsymbol{\Omega}\cdot\boldsymbol{k}\approx 0$. By choosing a mean magnetic field aligned with rotation in section 3.1.4, we sidestepped this issue entirely, but for a more general $\bar{\boldsymbol{B}}$ this will not be possible.

What's more, we learned in section 2.2 that, in the hydrodynamic case where only inertial waves exist, solutions with wavevectors almost perpendicular to the rotation axis ($\boldsymbol{\Omega}\cdot\boldsymbol{k}\approx 0$) had a particularly important role in establishing axially-elongated flow structures by focussing wave energy radiation onto the z-axis. Therefore, we entertain the notion that these $\boldsymbol{\Omega}\cdot\boldsymbol{k}\approx 0$ waves might continue to be important when a mean magnetic field is added — and they certainly cannot be studied by assuming $|\varpi_\Omega| \gg |\varpi_B|$, even when the Lehnert number is much less than unity. Instead, we ask what the polar opposite case $|\varpi_\Omega| \ll |\varpi_B|$ might look like. Taking the rotating-MHD dispersion relation in the explicit form (3.1.15c) and expanding about $\varpi_\Omega/\varpi_B = 0$, we get

$$\varpi \approx (\pm)\left[1+\frac{1}{8}\left(\frac{\varpi_\Omega}{\varpi_B}\right)^2-\frac{1}{128}\left(\frac{\varpi_\Omega}{\varpi_B}\right)^4+\cdots\right]\varpi_B \pm \frac{\varpi_\Omega}{2}, \tag{3.2.1}$$

or to first order in ϖ_Ω/ϖ_B,

$$\varpi \approx (\pm)\varpi_B \pm \frac{\varpi_\Omega}{2}. \tag{3.2.2}$$

Recall that we have $\boldsymbol{\Omega}\cdot\boldsymbol{k}\approx 0$ so the inertial wave frequency ϖ_Ω also vanishes; these are solutions which oscillate at the Alfvén frequency. They are not, however, classical Alfvén waves, which would simply propagate energy non-dispersively along magnetic field lines, and it would be a mistake to try to calculate their group velocity by differentiating $\varpi \approx (\pm)\varpi_B$. The subtlety lies in the $\varpi_\Omega/2$ term above, which makes a vanishingly small contribution to the frequency — but, since its gradient in $\boldsymbol{k}$-space is non-zero, actually appears as the dominant term in the group velocity expression. This arises when the full $\boldsymbol{c}_g$ equation

(3.1.16b) is expanded in the same way:

$$\boldsymbol{c}_g \approx (\pm)\left[1-\frac{1}{8}\left(\frac{\varpi_\Omega}{\varpi_B}\right)^2+\frac{3}{128}\left(\frac{\varpi_\Omega}{\varpi_B}\right)^4+\cdots\right]\boldsymbol{c}_{gB} + \left[\pm 1(\pm)\frac{1}{2}\left(\frac{\varpi_\Omega}{\varpi_B}\right)(\mp)\frac{1}{16}\left(\frac{\varpi_\Omega}{\varpi_B}\right)^3+\cdots\right]\frac{\boldsymbol{c}_{g\Omega}}{2} \tag{3.2.3a}$$

$$\approx (\pm)\boldsymbol{c}_{gB}\pm\frac{\boldsymbol{c}_{g\Omega}}{2} \tag{3.2.3b}$$

$$\approx (\pm)\frac{\bar{\boldsymbol{B}}}{\sqrt{\rho\mu}}\pm\frac{\boldsymbol{\Omega}}{k}. \tag{3.2.3c}$$

Note that this uses the fact $\boldsymbol{c}_{g\Omega}\approx 2\boldsymbol{\Omega}/k$ when $\boldsymbol{\Omega}\cdot\boldsymbol{k}\approx 0$, as per low-frequency inertial waves in the hydrodynamic case. From (3.2.3c) we can clearly see that these waves radiate energy both along magnetic field lines – similarly to Alfvén waves – and along the rotation axis, much like inertial waves. Hence, we dub them *inertial-Alfvén waves*. In fact, the smallness of *Le* in the geophysical context suggests that the axial group velocity of these solutions is much greater than that in the $\bar{\boldsymbol{B}}$-direction, despite the frequency (3.2.2) being dominated by the Alfvén term.

Recall that our motive for studying this limiting case was that the $\boldsymbol{\Omega}\cdot\boldsymbol{k}\approx 0$ solutions dominated the radiation pattern in the hydrodynamic case, since all solutions with wavevectors in this horizontal plane propagate in the same direction – axially – thus focussing the radiated energy density there. It can be seen that exactly the same reasoning may still be applied here; the infinity of wavevectors which satisfy $\boldsymbol{\Omega}\cdot\boldsymbol{k}\approx 0$ still all have the same group velocity (3.2.3c), only now it is not purely on-axis, but also contains a smaller component in the direction of $\bar{\boldsymbol{B}}$. Hence these inertial-Alfvén waves also possess the self-focussing property, even though it is now onto paths which are slightly oblique to the rotation axis. Furthermore, it should be noted that the self-focussing inertial wave solutions no longer exist in this set-up, since the $\boldsymbol{\Omega}\cdot\boldsymbol{k}\approx 0$ solutions are now inertial-Alfvén waves instead; for this reason, we might now expect axially-elongated flow structures to be established by these hybrid waves rather than by any inertial waves, weakly modified or otherwise.

Note that, unlike the two disparate pairs of roots obtained when $|\varpi_\Omega|\gg|\varpi_B|$ (section 3.1.3), the four inertial-Alfvén roots are all essentially equivalent, differing merely in propagation direction; the bracketed $(\pm)$ informs the sense of radiation along magnetic field lines, whereas the unbracketed $\pm$ gives the sense along the rotation axis. Hence there are four paths along which radiation may be focussed from a localised source.

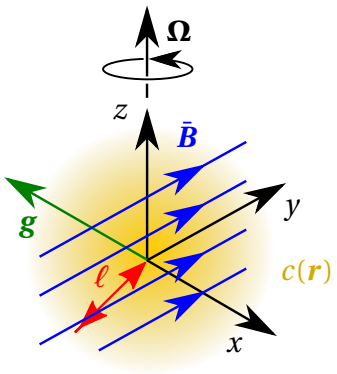

Fig. 3.2.1 Schematic of the initial condition for model problem studying radiation of hybrid waves from a buoyant blob, with the gravitational acceleration, background rotation, and mean magnetic field all mutually perpendicular.

3.2.2 Radiation of hybrid waves from a buoyant blob

To support the claim above that inertial-Alfvén waves – as opposed to pure inertial or magnetostrophic waves – dominate the radiation from a localised source, we return to the 'buoyant blob' initial value problem used to great effect for studying inertial waves in section 2.2.6 and magnetostrophic waves in section 3.1.4. The problem here is much like the latter of these two, only now the ambient magnetic field $\bar{\boldsymbol{B}} = \bar{B}\boldsymbol{e}_y$ is taken to be perpendicular to both the background rotation $\boldsymbol{\Omega} = \Omega\boldsymbol{e}_z$ and the local gravitational acceleration $\boldsymbol{g} = -g\boldsymbol{e}_x$ (figure 3.2.1). Crucially, the misalignment of $\boldsymbol{\Omega}$ and $\bar{\boldsymbol{B}}$ allows for some wavevectors which violate the condition $|\varpi_\Omega| \gg |\varpi_B|$ despite having $Le \ll 1$. It is also arguably rather geophysically relevant, as a magnetic field in the y-direction in our local Cartesian co-ordinates may be thought of as representing a large-scale azimuthal field in the context of Earth's outer core, somewhere in the neighbourhood of the equatorial plane (since $\boldsymbol{g} \perp \boldsymbol{\Omega}$). We have already seen (section 3.1.4) that the axial field makes a negligible difference to the fast dynamics; on the assumption (verifiable post-hoc) that the perpendicular component of any $\bar{\boldsymbol{B}}$ does have such an effect, it may therefore be considered quite separately from the axial component. We use an 'azimuthal' mean field (as opposed to a 'radial' field $\bar{\boldsymbol{B}} = \bar{B}\boldsymbol{e}_x$) because B_ϕ is thought to be important in the dynamo process (Davidson, 2013), though there is no reason why these waves could not ride upon the cylindrical radial mean field instead. As for the magnetostrophic wave case, we pick a Lehnert number $Le = \left(\bar{B}/\sqrt{\rho\mu}\right)/\Omega\ell = 0.1$, less than unity but not excessively small. The approximation to Earth's interior is perhaps a little better than it was for an axial field, since the magnitude of the azimuthal field could be somewhat larger on average (Hide & Roberts, 1979). However, its utter invisibility – combined with the fact that estimates of ℓ are also unreliable – means there is scope for Le to take on a

considerable range values at the small scales within Earth's core. (For example, the value $Le = 0.1$ is obtained for $\bar{B} = 40$G and $\ell = 5$km, though $\bar{B} = 4$G and $\ell = 20$km gives $Le = 0.002$.)

We solve this initial value problem in a similar way to the magnetostrophic wave problem, only now the integrals required are more complicated since the modification from the non-magnetic case involves functions of the wavevector orientation and not just its magnitude (appendix A2.1.2). Hence, calculating the full vector fields requires triple integrals in Fourier space at every point on a 3D grid in real space, a very computationally costly exercise. However, if the domain of interest is limited to just the y-z plane (i.e. the 2D region $x = 0$, which is the plane of $\boldsymbol{\Omega}$ and $\bar{\boldsymbol{B}}$), we can reduce this calculation to mere double integrals on a 2D grid, which are an order of magnitude quicker to evaluate.

We plot in figure 3.2.2 the axial velocity u_z at the instant $\Omega t = 50$, intermediate between the times chosen for the non-magnetic plots ($\Omega t = 10$) and the magnetostrophic plots ($\Omega t = 1250$). Comparing the left (non-magnetic) and centre (magnetic) panes, it is clear that the magnetic field is having a considerable effect on the fast-timescale dynamics. Whilst the flow is schematically the same, with a pair of columnar structures emanating northwards from the blob, it is clear that these columns have been bent significantly off-axis by the action of the mean magnetic field. Indeed, the magnetic field lines can be seen to be bending as the motion of the fluid across them drags them away from their equilibrium position, and therefore a magnetic tension force can be expected to act back upon the fluid. This occurs on a timescale which is much faster than that of magnetostrophic waves (compare with figure 3.1.4), yet also considerably slower than inertial waves. It seems likely, therefore, that hybrid waves with velocities intermediate between the two – including the inertial-Alfvén waves described above – are playing a key role in the dispersal of energy from the buoyant source.

We include the right-hand pane of figure 3.2.2 in order to validate our choice to simply plot in the plane $x = 0$ as opposed to solving for the full 3D fields. Quite clearly, the 2D slice is representative of the full 3D picture – and arguably contains more information – which one might expect since the dynamically relevant background features ($\boldsymbol{\Omega}$ and $\bar{\boldsymbol{B}}$) both lie in this plane.

Energy radiation by hybrid waves

In order to better classify the different species of waves radiated in this initial value problem, it will be helpful to consider both the types of energy they convey, and the rate at which they do so. We consider the former here, leaving a discussion of propagation velocities to section 3.2.3. Specifically, we ask in what proportions the hybrid waves are able to transport both kinetic and magnetic energy. The relationship between $\boldsymbol{u}$ and $\boldsymbol{b}$ (3.1.22a) tells us that the

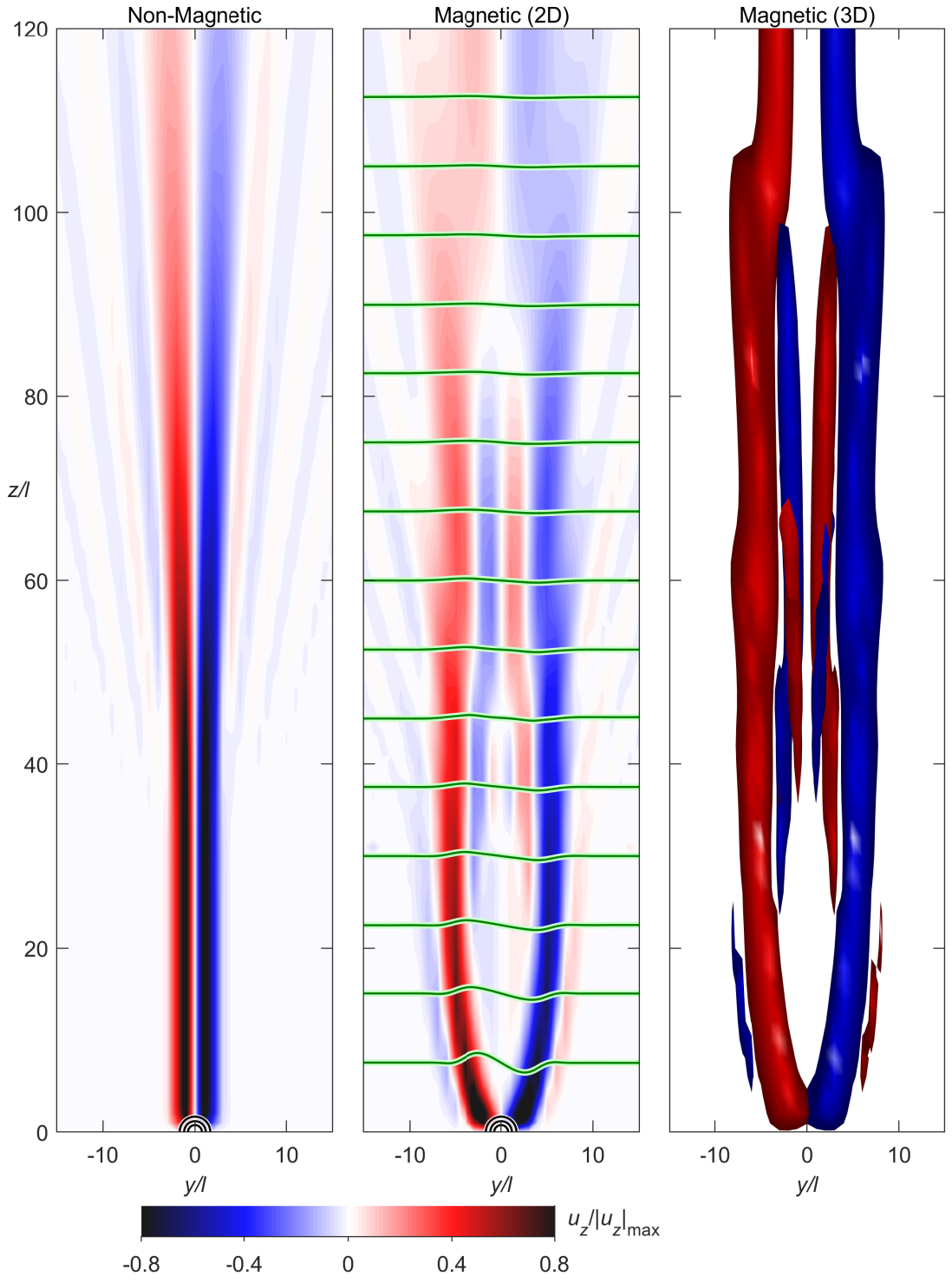

Fig. 3.2.2 Axial velocity u_z at $\Omega t = 50$. Rotation is vertical and gravity acts into the page ($\boldsymbol{\Omega} = \Omega \boldsymbol{e}_z$, $\boldsymbol{g} = -g\boldsymbol{e}_x$). **Left pane:** non-magnetic case ($Le = 0$, as per section 2.2.6) in the plane $x = 0$. Black contours are at quartiles of the buoyancy field. **Middle pane:** as left, except with a mean field $\bar{\boldsymbol{B}} = \bar{B}\boldsymbol{e}_y$ such that $Le = \left(\bar{B}/\sqrt{\rho\mu}\right)/\Omega\ell = 0.1$; magnetic field lines overlaid in green. **Right pane:** same as middle, only calculated in 3D space; isosurfaces of $|u_z|$ are plotted at 8% of its maximum value, coloured red (blue) for $u_z > 0$ ($u_z < 0$). (Working in appendix A2.1.2.)

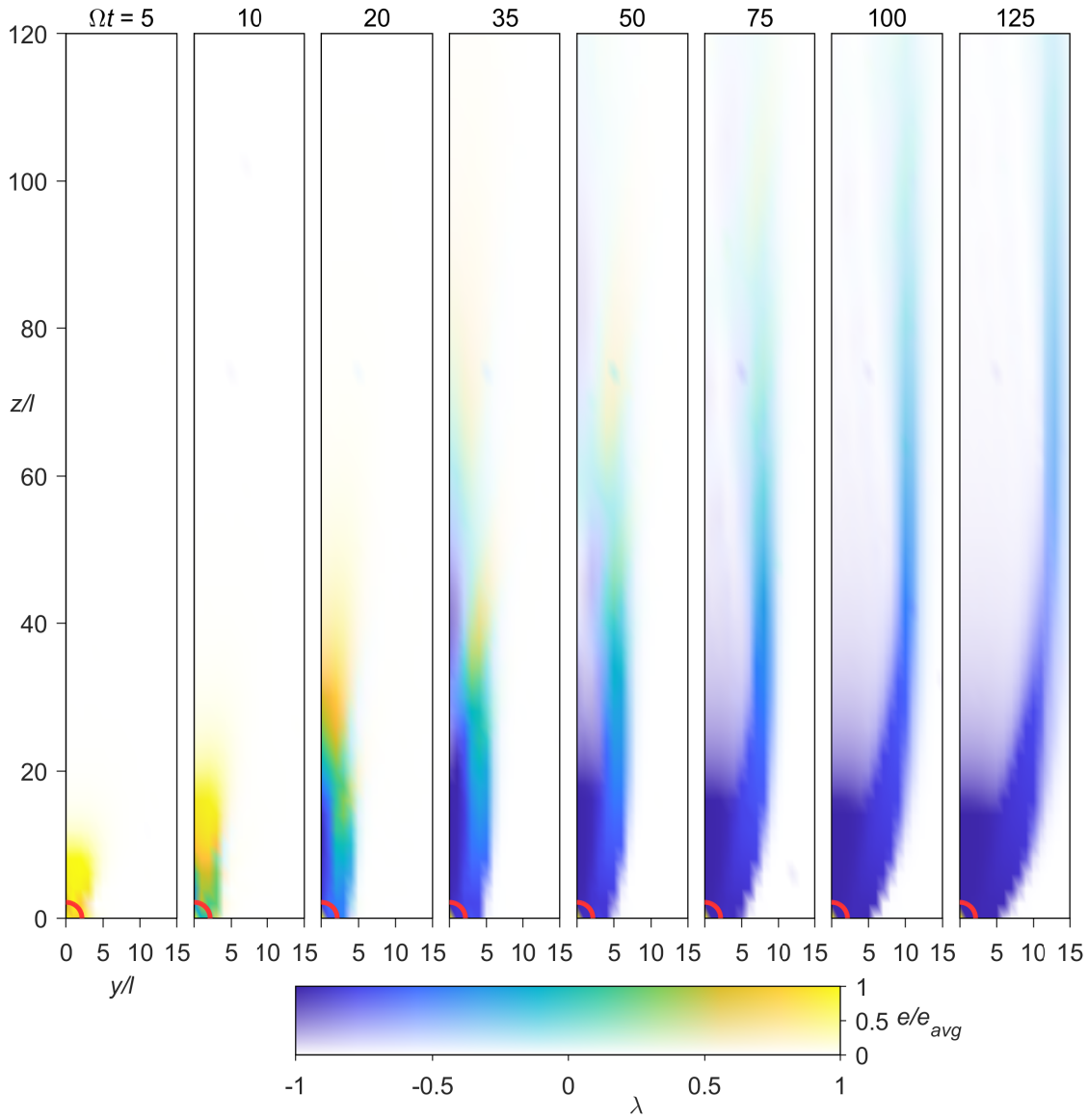

Fig. 3.2.3 Energy radiation from a buoyant blob by hybrid waves. Intensity of shading is proportional to specific wave energy $\mathscr{E} = \frac{1}{2}\left(\boldsymbol{u}^2 + \frac{\boldsymbol{b}^2}{\rho\mu}\right)$ normalised by its average over each pane, whereas hue is a function of the diagnostic $\lambda = \frac{1}{2}\left(\boldsymbol{u}^2 - \frac{\boldsymbol{b}^2}{\rho\mu}\right)/\mathscr{E}$ in order to distinguish the three classes of wave. The red contour is at 10% of the buoyancy field. (Working in appendix A2.1.2.)

waves' specific kinetic energy $\mathscr{E}_k$ and magnetic energy $\mathscr{E}_m$ are linked by

$$\mathscr{E}_m = \frac{\boldsymbol{b}^2}{2\rho\mu} = \left(\frac{\varpi_B}{\varpi}\right)^2 \frac{\boldsymbol{u}^2}{2} = \left(\frac{\varpi_B}{\varpi}\right)^2 \mathscr{E}_k. \tag{3.2.4}$$

Now, for weakly-modified inertial waves we have $\varpi \approx \varpi_\Omega$ and $|\varpi_\Omega| \gg |\varpi_B|$, so $(\varpi_B/\varpi)^2$ is small and the kinetic energy of the wave greatly outweighs its magnetic energy. At the other end of the spectrum, magnetostrophic waves have $\varpi \approx \varpi_B^2/\varpi_\Omega$ and $|\varpi_\Omega| \gg |\varpi_B|$, so $(\varpi_B/\varpi)^2 \approx (\varpi_\Omega/\varpi_B)^2$ is much greater than unity — the energy they convey is almost entirely magnetic. Our third limiting case – inertial-Alfvén waves – have the intermediate frequency $\varpi \approx \varpi_B$ so $\mathscr{E}_m \approx \mathscr{E}_k$. Much like classical Alfvén waves, these solutions exhibit an equipartition between kinetic and magnetic energies. This suggests an informative means by which to distinguish the different wave classes when looking at the output from this initial value problem; the difference between $\mathscr{E}_k$ and $\mathscr{E}_m$ should be positive for inertial waves and negative for magnetostrophic waves, but approximately zero for inertial-Alfvén waves.

In figure 3.2.3 we use the diagnostic $\lambda = (\mathscr{E}_k - \mathscr{E}_m)\,/\,(\mathscr{E}_k + \mathscr{E}_m)$ to highlight the prevalence of different wave classes as the solution evolves. The intensity of shading gives the total energy, whereas the hue is dictated by λ. A yellow colour ($\lambda \approx 1$) indicates the dominance of kinetic energy, and therefore inertial waves. These are observed at the very earliest times ($\Omega t = [5,\ 10]$), before the magnetic field has had a chance to react to the disturbance, though their energy density drops due to dispersion very quickly; unlike the non-magnetic case, in which self-focussing ($\boldsymbol{\Omega} \cdot \boldsymbol{k} \approx 0$) inertial waves existed, there are no such solutions in this problem. Early on and close to the blob, we still observe some inertial waves, since the blob's finite size means off-axis waves can fill the space above it anyway, but as time progresses they spread throughout space, with their energy density decreasing accordingly; in figure 3.2.3 we see almost no evidence of inertial waves for $\Omega t \gtrsim 35$.

Ignoring for a moment the mess of the intermediate panes at $\Omega t = [20,\ 35,\ 50]$ in figure 3.2.3, we can see that the most striking feature of the radiation at later times is a tall columnar structure which propagates horizontally at a rate somewhat slower than the rapid on-axis spreading. Its turquoise colour is indicative of $\lambda \approx 0$, i.e. an equipartition between kinetic and magnetic energy, and therefore strongly suggestive of an inertial-Alfvén wave. Unlike the off-axis inertial waves seen initially, the energy density within the column shows no sign of decreasing, in accordance with the self-focussing property of these solutions.

Also at later times, there is a strong blue-coloured region near to the source, signifying that the wave energy there is mostly magnetic, and therefore the waves are closer to the magnetostrophic limit. Whilst the inertial and inertial-Alfvén waves, along with a broad spectrum of not-so-easily-categorised intermediate hybrid waves, have vacated the source quickly, the magnetostrophic solutions with their slow group velocities are left to bring up the rear. This is much like the aligned-field case, in which two very distinct timescales were found, in the sense that the job of balancing the buoyancy force is handed from the velocity field to the magnetic field on the magnetostrophic timescale. Now, however, the

misalignment between $\boldsymbol{\Omega}$ and $\bar{\boldsymbol{B}}$ means that a rich variety of intermediate hybrid waves are present as well. The snapshots plotted in figure 3.2.3 are at times of the order a few weeks, far shorter than the magnetostrophic timescale (see section 3.1.4), and therefore the significant wave radiation observed must be chiefly down to these intermediate solutions, and particularly the inertial-Alfvén waves — which hold the trump card thanks to their ability to self-focus.

We return for a moment to the intermediate panes $\Omega t = [20,\ 35,\ 50]$ of figure 3.2.3. The dynamics at these times are particularly rich, as visualised by the range of colours in these plots, because all hybrid solutions of (3.1.15) are still present. What's more, the group velocity expression (3.1.16b) is sufficiently complicated that off-axis weakly-modified inertial waves (which are in fact the only inertial waves possible) can occupy the same region of space as the inertial-Alfvén solutions at this time. It is only after about $\Omega t = 50$ that the inertial solutions have dispersed sufficiently for the dominance of the hybrid solution to become apparent; though note that this is still very fast, about 8 days.

3.2.3 Group velocity considerations

We now inspect in a little more detail the group velocity of these inertial Alfvén waves, explaining why it should have the form it does, and proving that the solution to our initial value problem is indeed dominated by waves which move at this velocity. Recall that, in the limit $\boldsymbol{\Omega}\cdot\boldsymbol{k} \approx 0$, the group velocity for hybrid waves becomes

$$\boldsymbol{c}_g \approx (\pm)\frac{\bar{\boldsymbol{B}}}{\sqrt{\rho\mu}} \pm \frac{\boldsymbol{\Omega}}{k} \tag{3.2.5}$$

(see (3.2.3c)), and so has components in both the transverse ($\bar{\boldsymbol{B}} = \bar{B}\boldsymbol{e}_y$) and axial ($\boldsymbol{\Omega} = \Omega\boldsymbol{e}_z$) directions. The transverse portion is at the Alfvén velocity, perfectly reasonably as their frequency is $\varpi \approx (\pm)\varpi_B$, but the axial portion is at precisely half that for the corresponding low-frequency ($\boldsymbol{\Omega}\cdot\boldsymbol{k} \approx 0$) inertial waves in the non-magnetic case. The reasoning for this factor of a half may be understood in two ways:

1. The quantity which carries over from the non-magnetic to the magnetic case is the axial energy *flux*, rather than propagation velocity. Since inertial-Alfvén waves are equipartitioned, for a given $\tilde{\boldsymbol{u}}$ their energy density is twice that for inertial waves because $\tilde{\boldsymbol{b}}/\sqrt{\rho\mu} = (\mp)\tilde{\boldsymbol{u}}$ contributes an equal amount. Hence, a group velocity which is halved compared to inertial waves means the net energy flux is the same.

2. Alfvén waves are conveniently studied in Elsasser variables $\boldsymbol{v}^{(\mp)} = \boldsymbol{u}(\mp)\boldsymbol{b}/\sqrt{\rho\mu}$, and these variants are no exception. We may use them, alongside their vector potentials

$\boldsymbol{\kappa}^{(\mp)}$, to write the governing equations (3.1.12) as

$$\frac{\partial \boldsymbol{v}^{(\mp)}}{\partial t} = (\mp)\frac{\left(\bar{\boldsymbol{B}}\cdot\nabla\right)\boldsymbol{v}^{(\mp)}}{\sqrt{\rho\mu}} + (\boldsymbol{\Omega}\cdot\nabla)\left(\boldsymbol{\kappa}^{+}+\boldsymbol{\kappa}^{-}\right), \qquad \boldsymbol{v}^{(\mp)} = \nabla\times\boldsymbol{\kappa}^{(\mp)}. \tag{3.2.6}$$

We may single out the dynamics of inertial-Alfvén waves by prescribing a certain relationship between the velocity field and perturbation magnetic field. This formulation is particularly convenient here, since an Alfvén wave travelling in the positive $\bar{\boldsymbol{B}}$-direction has $\boldsymbol{v}^{+}=\boldsymbol{\kappa}^{+}=0$ (i.e. $\boldsymbol{u}=-\boldsymbol{b}/\sqrt{\rho\mu}$), whereas one travelling in the negative $\bar{\boldsymbol{B}}$-direction has $\boldsymbol{v}^{-}=\boldsymbol{\kappa}^{-}=0$ (i.e. $\boldsymbol{u}=\boldsymbol{b}/\sqrt{\rho\mu}$); in either case, making this ansatz decouples the equations (3.2.6) to

$$\frac{\partial \boldsymbol{v}^{(\mp)}}{\partial t} = (\mp)\frac{\left(\bar{\boldsymbol{B}}\cdot\nabla\right)\boldsymbol{v}^{(\mp)}}{\sqrt{\rho\mu}} + (\boldsymbol{\Omega}\cdot\nabla)\,\boldsymbol{\kappa}^{(\mp)}, \qquad \boldsymbol{v}^{(\mp)} = \nabla\times\boldsymbol{\kappa}^{(\mp)}. \tag{3.2.7}$$

Note the absent factor of 2 in the $(\boldsymbol{\Omega}\cdot\nabla)$ compared to, say, the non-magnetic vorticity equation (2.2.7). Indeed, the dispersion relation corresponding to (3.2.7) can be shown to be $\varpi=(\pm)\varpi_B\pm\frac{1}{2}\varpi_\Omega$, which is the same as the inertial-Alfvén limit (3.2.2) of the complete dispersion relation (3.1.15).

Having ascertained that inertial-Alfvén waves should have the group velocity (3.2.5), it is necessary to confirm that the axially-elongated structures in our buoyant blob initial value problem do indeed move at this pace. To do this, we need some way of distinguishing the inertial-Alfvén solutions from the multitude of other possible hybrid waves; the parameter $\lambda=(\mathscr{E}_k-\mathscr{E}_m)/(\mathscr{E}_k+\mathscr{E}_m)$ was useful for highlighting inertial, inertial-Alfvén, and magnetostrophic waves simultaneously, but we would prefer a parameter which is small for all but the inertial-Alfvén solutions in order to track them. The answer is cross-helicity $\mathscr{H}_\times=\boldsymbol{u}\cdot\boldsymbol{b}/\sqrt{\rho\mu}$, which we again normalise with total energy $\mathscr{E}$; the resulting quantity is maximised when $\boldsymbol{u}$ and $\boldsymbol{b}/\sqrt{\rho\mu}$ are parallel and of equal magnitude, as they are for an Alfvén wave, but is small in the cases of negligible $\boldsymbol{b}$ (weakly-modified inertial waves) or $\boldsymbol{u}$ (magnetostrophic waves). The magnitude of this diagnostic is plotted in figure 3.2.4, where it dictates the colour choice (intensity again being given by $\mathscr{E}$), for the instants $\Omega t=50:12.5:100$ — late enough that the inertial-Alfvén solutions have emerged from the initial mess, but early enough that they are still within the domain.

We now seek to segregate the inertial-Alfvén wave packet from the rest of the flow field. Defining the region of intense inertial-Alfvén wave radiation as that bounded above by the red contour $\mathscr{E}=0.3\mathscr{E}_{avg}$ (where $\mathscr{E}_{avg}$ is the average over each pane) and below by the black contour $|\mathscr{H}_\times|=0.9\mathscr{E}$ gives a reasonable means by which to do this. (Note that the following results are insensitive to the exact numerical values chosen.) We therefore have

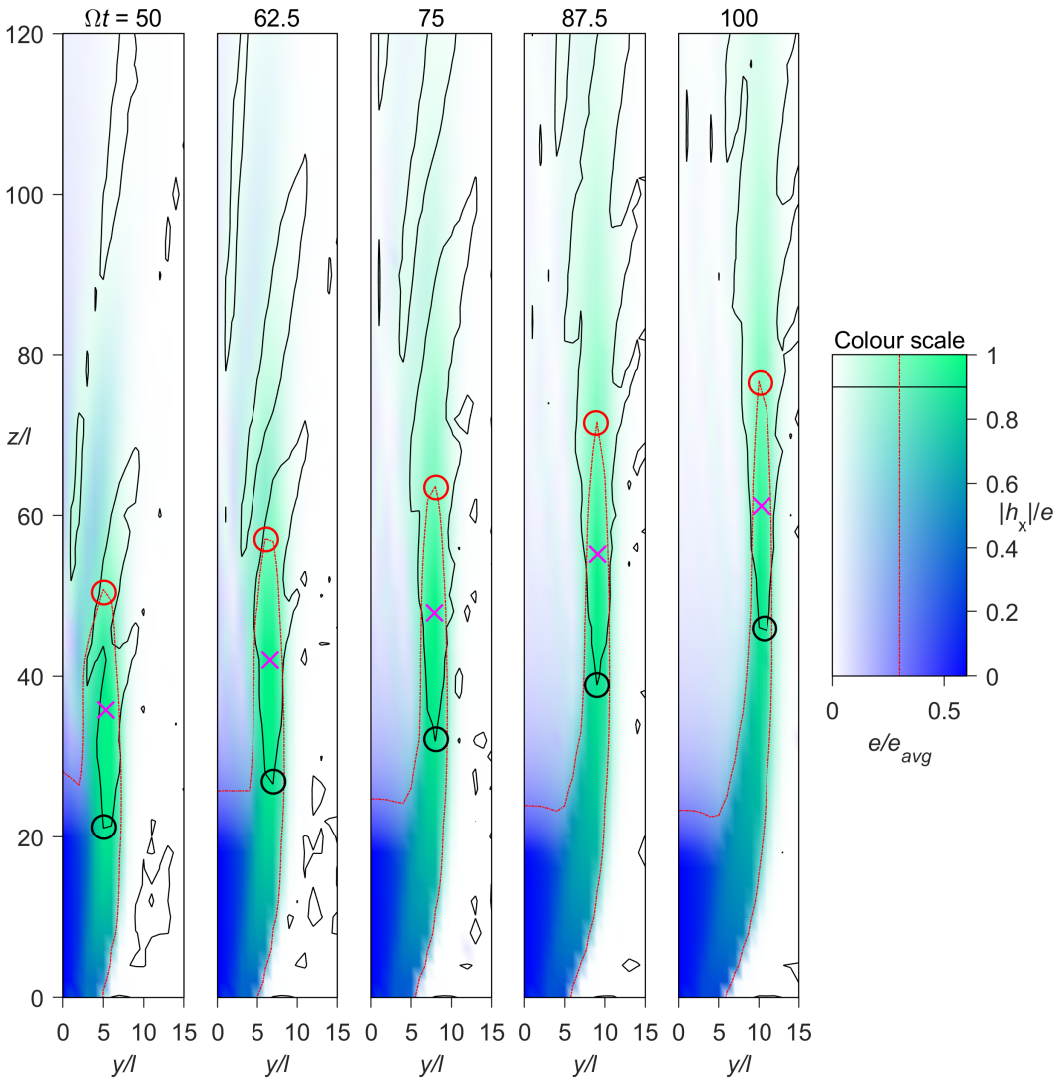

Fig. 3.2.4 Energy radiation from a buoyant blob by hybrid waves. Intensity of shading is proportional to specific wave energy $\mathscr{E} = \frac{1}{2}\left(\boldsymbol{u}^2 + \frac{\boldsymbol{b}^2}{\rho\mu}\right)$ normalised by its average over each pane, whereas hue is a function of the normalised cross-helicity $|\mathscr{H}_\times|/\mathscr{E}$ where $\mathscr{H}_\times = \boldsymbol{u}\cdot\boldsymbol{b}/\sqrt{\rho\mu}$. The solid black contours are at $|\mathscr{H}_\times| = 0.9\mathscr{E}$, with their lowermost tips marked by black circles, and the dashed red contours are at $\mathscr{E} = 0.3\mathscr{E}_{avg}$, with their uppermost tips marked by red circles. The pink crosses mark the inferred 'centre' of the wave packet at each time.

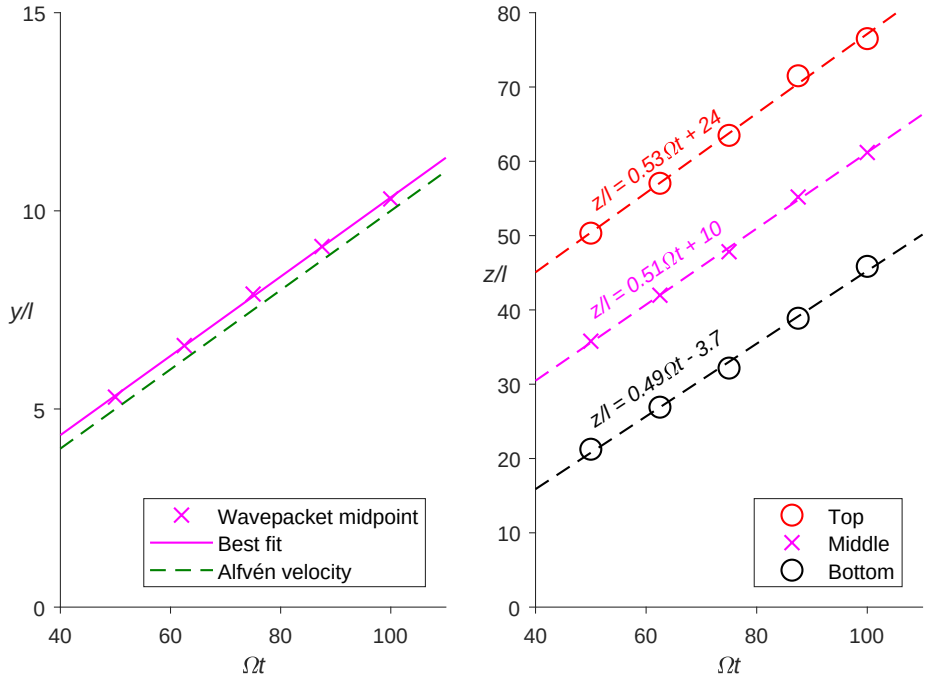

Fig. 3.2.5 Tracking the spatio-temporal evolution of the inertial-Alfvén wave packet identified in figure 3.2.4 using normalised cross helicity. The left pane shows it propagating along field lines at the Alfvén velocity $y = \bar{B}t/\sqrt{\rho\mu}$, whereas the right pane shows it propagating axially at half the low-frequency inertial wave velocity, i.e. $z = 0.5\Omega t\ell$ (linear best-fit lines are shown, dashed, with their equations). Markers correspond to those in figure 3.2.4.

our 'inertial-Alfvén wave region' defined as that between the black circle at the bottom and red circle at the top in figure 3.2.4; the pink cross, being the midpoint of the two, constitutes the wave packet centre.

We can therefore plot both the y- and z-locations of the wave packet as time progresses from $\Omega t = 50$ to 100 (figure 3.2.5). The left pane shows the centre propagating along magnetic field lines at the Alfvén velocity $y/t = \bar{B}/\sqrt{\rho\mu} \implies (y/\ell) = Le \times \Omega t$; since this element of the group velocity expression is non-dispersive, this is reasonably trivial to show. Using this method, however, we may also track the axial group velocity $c_{g,z} = \Omega/k \implies (z/\ell) = (k\ell)^{-1}\Omega t$. We have from the non-magnetic case (section 2.2.6) that the relevant dominant wavenumber is $k \sim 2/\ell$, and hence we are looking for propagation of waves such that $z = 0.5\Omega t\ell$. The gradients of the regression lines in the right-hand pane of figure 3.2.5 are all very close to this value – whether one looks at the top, middle, or bottom of the wave packet – and therefore we may say with confidence that the objects found here are indeed inertial-Alfvén waves.

3.2.4 Discussion

Having established the surprising precedence of inertial-Alfvén waves over inertial or magnetostrophic solutions in our model problem, we now ask what bearing this result might have upon small-scale dynamics within Earth's fluid outer core, and how this new discovery fits into our present understanding of the geodynamo's operation.

Axially-elongated flow structures

As discussed before, numerical simulations of planetary dynamos suggest a strong prevalence for axially-elongated flow structures, often in the form of columnar cyclonic–anticyclonic vortex pairs (Kageyama & Sato, 1997; Olson et al., 1999; Sreenivasan & Jones, 2006). These are larger, more regular structures in the early simulations, but as computing power has increased the pictures have got ever more chaotic and complex, though columnar structures are still favoured. The columns do not act in isolation, but rather respond to the evolving density and magnetic fields, so quite clearly this evolution requires some mechanism by which approximate axial invariance is maintained on a timescale much shorter than that of convection. In the literature to date, it is implicitly assumed that this enforcement is done by fast inertial waves, propagating directly on-axis. However, we have shown here that in the presence of a locally-uniform mean magnetic field, even one which is weak compared to the rotation rate, this task could in fact be undertaken by hybrid inertial-Alfvén waves, with an axial group velocity half that of the corresponding inertial waves and an additional component of motion along magnetic field lines.

The common hypothesis of well-separated roots to the hybrid wave equation (3.1.14) is therefore shown to be potentially misleading, even erroneous, in the important situation in which a mean magnetic field with a component perpendicular to the rotation axis is applied. These limiting-case roots – inertial and magnetostrophic waves – do exist, but are shown to be of subordinate importance in our model problem. The inertial waves, in the absence of any self-focussing solutions, transport energy very rapidly, but only in somewhat off-axis directions — and because of this, their energy is dispersed over a large area very quickly. The magnetostrophic solutions, in contrast, will have barely escaped from the blob before the convective motions could be expected to play a part, much as for the aligned magnetic field case, section 3.1.4. The full dynamics of this MAC (*Magnetic-Archimedean-Coriolis*) balance are not explored, so it is difficult from our position to say what role the magnetostrophic waves will play in reality.

However, an alternative model problem may provide a clue. Consider the same background set-up (i.e. rotation and magnetic field perpendicular), only now without buoyancy,

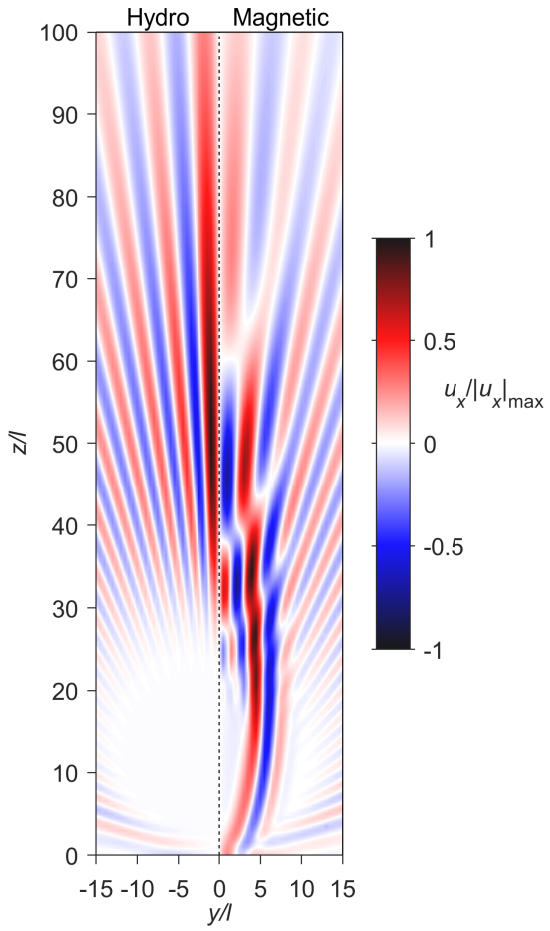

Fig. 3.2.6 Comparison of the radiation of inertial and hybrid waves in an initial value problem with an axis-aligned Gaussian vortex of size ℓ as the initial condition. Velocity out of the page u_x is plotted, normalised by its respective absolute maxima, in the plane $x = 0$ at $\Omega t = 50$. The background rotation is vertical ($\boldsymbol{\Omega} = \Omega \boldsymbol{e}_z$). Left half: no magnetic field, $Le = 0$. Right half: horizontal magnetic field, $\bar{\boldsymbol{B}} = \bar{B}\boldsymbol{e}_y$ with $Le = 0.1$. Solution is antisymmetric in y and symmetric in z. (Working in appendix A2.2.)

and instead a localised velocity field (an aligned-axis vortex as per section 2.2.5, say) is prescribed initially. The advantage of this 'initial value' set-up is that it contains a finite quantity of energy, which the system is then free to disperse as it sees fit, rather than the static buoyant blob, which provides an effectively infinite source of waves. This problem is solved in much the same way as the others of this chapter in appendix A2.2, and the x-component of the velocity field plotted in the plane $x = 0$ in figure 3.2.6, which also compares it with the equivalent hydrodynamic solution (appendix A1.1). This provides a good demonstration of a few points from the above discussion:

1. The peak in u_x has propagated roughly half the distance in the magnetic case (to $z \sim 25\ell$ rather than $z \sim 50\ell$), as inertial-Alfvén waves have half the axial group velocity of low-frequency inertial waves;

2. This peak has also migrated in the direction of the mean magnetic field by an amount consistent with Alfvén wave propagation ($y \sim Le\Omega t\ell = 5\ell$);

3. There is notable fast, but low energy-density, inertial wave radiation off-axis in both cases, its form being broadly unaffected by the addition of a magnetic field.

Furthermore, the solution can be seen to be relatively weak close to the origin, suggesting the magnetostrophic waves contain a comparatively small portion of the energy, though a spectrum of fairly slow intermediate hybrid wave solutions are nevertheless visible in the region $z \lesssim 20$.

In final homage to the idea that inertial-Alfvén waves might underpin columnar structures in numerical and physical dynamos, we present an initial value problem comparable to that for inertial waves at the end of section 2.2.6, in which a cloud of buoyant blobs in the vicinity of the plane $z = 0$ are spontaneously introduced into the fluid, rather than just one blob (figure 3.2.7). Whereas section 2.2.6 included a range of blob sizes, the fact that the parameter Le depends upon ℓ means that we may only efficiently use one size of blob now — but the problem is still linear so we may superimpose any number of such blobs at will. Axial velocity (which is known to be a good proxy for axial vorticity, to within a possible change of sign) is plotted in figure 3.2.7, showing a pattern of alternating cyclones and anticyclones which looks tantalisingly similar to numerical geodynamo simulations, with an apparent complexity beyond what one might expect for the simple superposition of linear phenomena.

Energy and helicity

Of paramount importance for the operation of the geodynamo is the ability of hybrid waves to transport both energy and helicity. With a magnetic field present, it is no longer just kinetic energy and helicity which are relevant, but their magnetic counterparts as well. All four of these, as well as the cross helicity $\mathscr{H}_\times = \boldsymbol{u}\cdot\boldsymbol{b}$, are plotted for the buoyant blob problem in figure 3.2.8. We examine them from left to right. Firstly, the kinetic energy $\mathscr{E}_k$ seems to be reasonably evenly distributed throughout the column region, as one might expect for an approximately z-invariant solution. There is a little kinetic energy carried by inertial waves to the top of the domain and a region of strong flow near to the buoyant blob, where the Coriolis force is – on the timescales plotted at least – balancing the buoyancy force. The

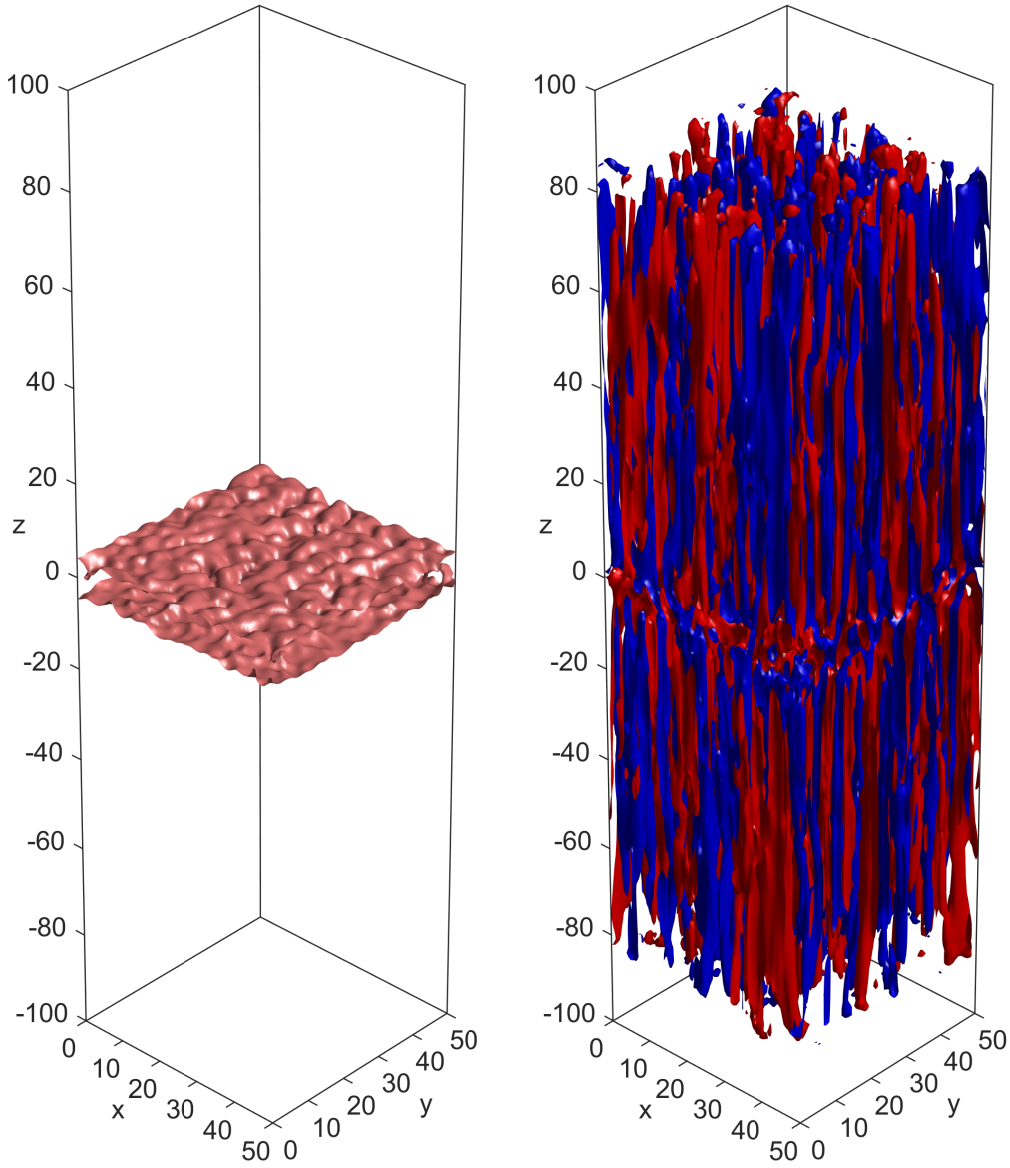

Fig. 3.2.7 Radiation of hybrid waves from a cloud of 10^4 buoyant Gaussian anomalies of size $\ell = 1/\sqrt{2}$ randomly located in the x-y plane and the region $|z| \leq 3.75$. Rotation is vertical, magnetic field in the y-direction, and buoyancy acts in the negative x-direction. Instant shown is $\Omega t = 50$, with $Le = \left(\bar{B}/\sqrt{\rho\mu}\right)/\Omega\ell = 0.1$. Left pane: buoyancy field at 20% of its maximum. Right pane: $|u_z|$ at 10% of its maximum, coloured red (blue) for positive (negative) values.

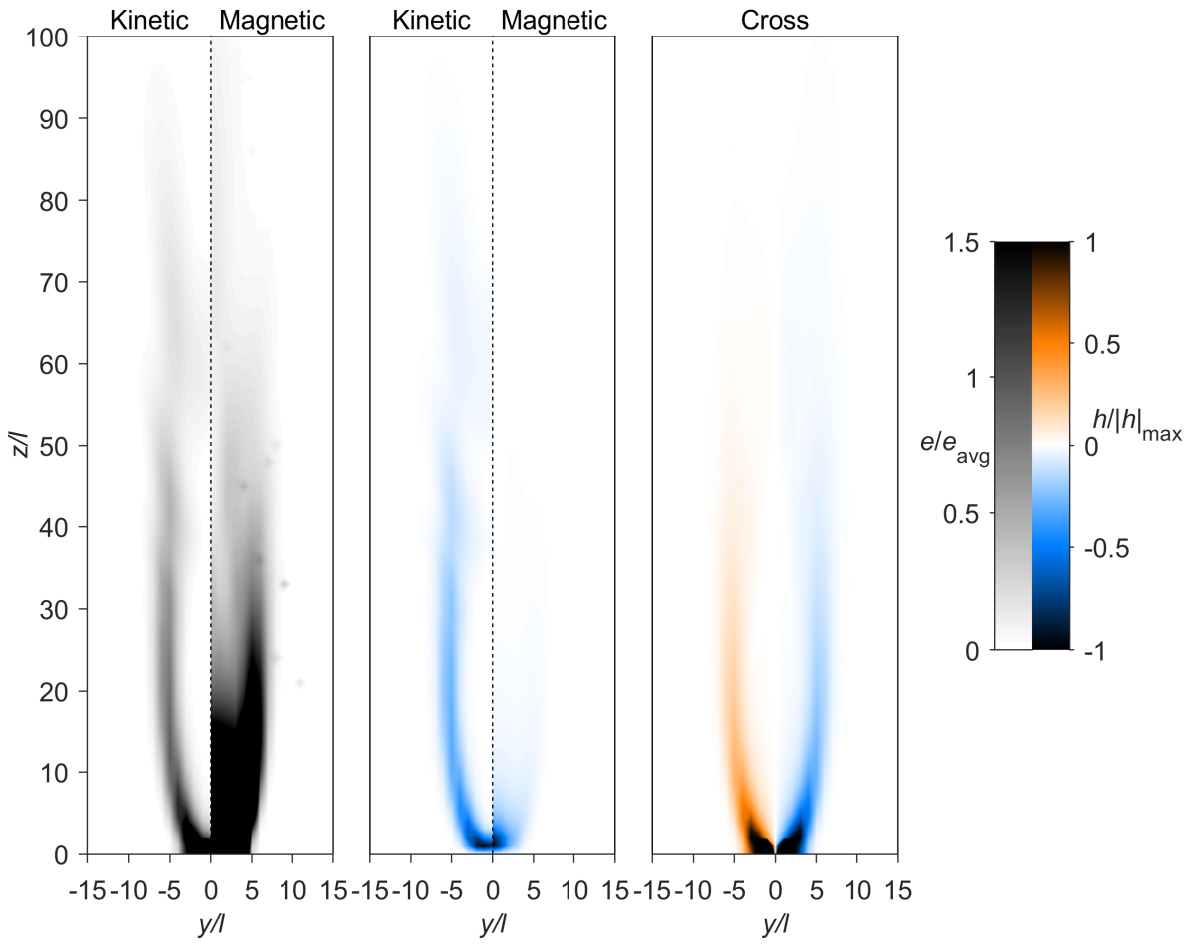

Fig. 3.2.8 Energies and helicities of hybrid waves from a buoyant blob (appendix A2.1) in the plane $x = 0$ at $\Omega t = 50$. Left pane: specific kinetic energy $\mathscr{E}_k = \frac{1}{2}\boldsymbol{u}^2$ and magnetic energy $\mathscr{E}_m = \frac{\boldsymbol{b}^2}{2\rho\mu}$, normalised by the average total energy across the domain (symmetric in y and z). Centre pane: kinetic helicity $\mathscr{H}_k = \boldsymbol{u}\cdot\boldsymbol{\omega}$ and magnetic helicity $\mathscr{H}_m = \boldsymbol{a}\cdot\boldsymbol{b}$, normalised by their respective maxima (symmetric in y, antisymmetric in z). Right pane: cross helicity $\mathscr{H}_\times = \boldsymbol{u}\cdot\boldsymbol{b}$ normalised by its maxima over $z \geq 3$, i.e. outside of the blob region (symmetric in z).

magnetic energy $\mathscr{E}_m$ is comparable to $\mathscr{E}_k$ at and above the location of the inertial-Alfvén wave front ($z \sim 25\ell$), but dominant near to the blob where the waves are expected to be closer to the magnetostrophic limit. Clearly, there is a large proportion of the total energy in these waves on the magnetostrophic branch of the dispersion relation — although it is not clear how realistic this is because the static buoyant blob provides a rather unphysical infinite energy source, as discussed above.

Both kinetic ($\mathscr{H}_k$) and magnetic ($\mathscr{H}_m$) helicity are negative north of the blob (and positive south of it), as expected from the theory of section 3.1.3, and are clearly being carried by the inertial-Alfvén waves, whose flow structure consists of tall helical columns

much like the hydrodynamic solution of section 2.2.6. Hence, the helical-wave dynamo model (Davidson, 2014; Davidson & Ranjan, 2015) is in principle unaffected by the fact that hybrid inertial-Alfvén waves are preferred over inertial solutions. Indeed, any form of hybrid wave (inertial, magnetostrophic, inertial-Alfvén, or something in between) could in theory maintain such a dynamo, though the rate at which energy is propagated differs widely across the wave types.

Finally, consider the cross helicity $\mathscr{H}_\times = \boldsymbol{u}\cdot\boldsymbol{b}$ plotted in the right-hand pane of figure 3.2.8. Whereas the sign of $\mathscr{H}_k$ or $\mathscr{H}_m$ is concomitant with axial propagation direction, that of $\mathscr{H}_\times$ gives the direction of wave motion along magnetic field lines (i.e. with or against $\bar{\boldsymbol{B}}$), being negative – $\boldsymbol{u}$ and $\boldsymbol{b}$ antiparallel – for waves travelling in the direction of $\bar{\boldsymbol{B}}$, and vice versa. (This can be seen from 3.1.22a, or the discussion of Elsasser variables in section 3.2.3.)

Relation to torsional oscillations

Of course, this is not the first time that Alfvén waves have been proposed to exist in Earth's outer core. A well-established class of waves known as *torsional oscillations* (TOs) are thought to play an important role in the geomagnetic secular variation — that is to say, fluctuations to the observable magnetic field on timescales of the order decades to centuries, along with associated changes in the length of a day due to angular momentum exchanges. For a full introduction to torsional oscillations see, for example, Braginsky (1970), Jault (2003), or Finlay et al. (2010). In simplest terms, they arise from the observation that the only truly axially-independent flow in a rotating spherical geometry is that in which cylinders of fluid coaxial with the rotation axis move as coherent objects, with an axisymmetric azimuthal velocity which is a function only of cylindrical distance from the axis, and time. We might ask which forces are available to exert a net torque on such a 'geostrophic cylinder' in order to accelerate the flow. Clearly buoyancy cannot, being directed exclusively towards the rotation axis, and tangential pressure forces will always cancel out. The Coriolis force is also impotent, besides creating the axially-invariant flow in the first place; only flow in the cylindrical radial direction results in an azimuthal Coriolis force $(2\boldsymbol{u}\times\boldsymbol{\Omega})_\phi$, but conservation of mass implies the flows into and out of a given geostrophic cylinder must cancel — and therefore so too does the net torque. Reynolds and viscous stresses are thought to be tiny in the Earth's outer core, leaving only the Lorentz force $(\boldsymbol{J}\times\boldsymbol{B})_\phi$ to act upon the cylinder. Coupled with the induction equation, the resulting system is then able to support oscillations in which azimuthal fluid inertia and tension due to the cylindrical radial magnetic field play off against each other — or in other words, Alfvén waves.

Torsional oscillations are by their very nature an axisymmetric (or rather, azimuthally-averaged) phenomenon. However, it seems somewhat puzzling that the physical mecha-

nisms behind their operation should be restricted to the axisymmetric case. In fact, we can see now that the existence of inertial-Alfvén waves suggests that they are not, and in fact Alfvén-like oscillations within Earth's outer core could be far more versatile than previously believed, not necessarily restricted to fully axially-independent or axisymmetric flows, and being able to propagate along both azimuthal and radial components of the mean magnetic field. Because inertial-Alfvén waves and torsional oscillations share many of their general properties – flows stretched along the rotation axis, an invariance to the mean axial magnetic field, and an underlying fast timescale (filtered out for TOs) propagating information along the rotation axis – it seems natural to think of torsional oscillations as a macroscopic "mode of oscillation" version of the small-scale "travelling wave" inertial-Alfvén solutions.

This relationship is hinted at by the results of Jault (2008), who examines motions in a spherical shell which are assumed axisymmetric but not axially-invariant, forced by an impulsive change in inner core angular momentum. The resulting disturbance propagates rapidly along the rotation axis, roughly following the tangent cylinder, and radially outward at a velocity consistent with Alfvén waves; this behaviour appears to bridge the gap between inertial-Alfvén waves and torsional oscillations, and has recently been explored experimentally by Tigrine et al. (2018).

We note finally that torsional oscillations are a well-documented feature of the available evidence, both within observations (Gillet et al., 2010) and numerical simulations (Dumberry & Bloxham, 2003; Teed et al., 2014, 2015), so it is has already been demonstrated that Alfvén waves can exist in the Earth's outer core. For obvious reasons, no study has yet attempted to observe inertial-Alfvén waves in similar contexts — but it is worth speculating upon how this might be achieved.

Scope for the observation of inertial-Alfvén waves

The observation of inertial-Alfvén waves in the simple model problems covered in this chapter suggests that it should be possible to observe them amidst more complicated systems, either physical or numerical. The prospects for a 'real-world' observation of inertial-Alfvén waves are unfortunately pretty poor, as they are fundamentally small-scale structures with very low-amplitude perturbations to the background state, and hence are unlikely to be detectable via any modern observational means. Nevertheless, very recent work has attempted to link these waves to elements of the secular variation, including geomagnetic jerks (Kloss & Finlay, 2019; Aubert & Finlay, 2019). Additionally, experimental approaches are often able to identify some wave motions (Nataf & Gagnière, 2008; Nornberg et al., 2010), although classifying them precisely is difficult, and only a limited number of field topologies are possible.

There is perhaps more promise in the interrogation of numerical simulation results, as has proved successful for torsional oscillations (Teed et al., 2014, 2015) and magnetic Rossby waves (Hori et al., 2015, 2018). The main challenge in using simulations is to somehow separate the wave dynamics from all the other processes, such as convection and dynamo action. That being said, since the publication of Bardsley & Davidson (2016), a promising first attempt at such an investigation has been made by Aubert (2018), who observes "quasi-geostrophic Alfvén waves" propagating along the cylindrical radial magnetic field from the tip of a convective plume — a situation (nomenclature notwithstanding!) with very strong parallels to the buoyant blob problem looked at here.

Seeking to expand upon this early hint at success, a future study into inertial-Alfvén waves would need to take into account the following important points:

- The spatial and temporal resolution will need to be sufficiently high to resolve the inherently fast, small-scale waves. As found in Ranjan et al. (2018), this will probably mean pausing a fully-developed numerical dynamo mid-run and restarting it with a smaller choice of time-step.

- There will be significant challenges in separating both $\boldsymbol{u}$ and $\boldsymbol{B}$ into mean and fluctuating components; Aubert (2018) uses temporal averages over epochs somewhat greater than the relevant wave periods (i.e. the Alfvén period in this case) in order to generate a mean field, which seems the most straightforward means despite being somewhat subjective.

- Once the mean magnetic field $\bar{\boldsymbol{B}}$ has been separated from the total field, it is reasonable to neglect its axial component $\bar{B}_z$ in the search for waves, and instead define the relevant Alfvén speed as that perpendicular to the rotation axis, $\bar{\boldsymbol{B}}_\perp/\sqrt{\rho\mu}$. (This is clearly the case from the aligned-field model problem of section 3.1.4.)

- It is then advantageous to search for waves in regions of space where the background variables – meaning the density distribution and perpendicular magnetic field – are reasonably homogeneous. Variations of density will obviously be useful as sources of waves, but will confuse attempts to identify a travelling wave which has already been launched. Variations to $\bar{\boldsymbol{B}}_\perp$ in the perpendicular plane can probably be dealt with, as Alfvén waves will to leading order just follow field lines which are non-straight, but variations of $\bar{\boldsymbol{B}}_\perp$ with the axial co-ordinate should be avoided when searching for inertial-Alfvén waves (for reasons which will become clear in the next chapter).

- Thresholding on normalised cross helicity $\mathscr{H}_\times/\mathscr{E}$ and total wave energy simultaneously, as per figure 3.2.4, works very well for identifying inertial-Alfvén waves in our

model problem, and should also work well in a full simulation once the fluctuating field has been extracted. Using the parameter $\lambda = (\mathscr{E}_k - \mathscr{E}_m)/\mathscr{E}$ (figure 3.2.3) may also prove useful if seeking to extract other wave types as well.

- Owing to the dispersive nature of the axial wave propagation, pinning down motion at the Alfvén speed along field lines (which is non-dispersive) is much more likely to be tractable.

The challenges of identifying small-scale wave motions in geodynamo simulations, particularly in any quantitative way, are great — see Ranjan et al. (2018) or Aubert (2018) for a flavour of the techniques required. However, as evidenced by this new literature attempting such a feat, this is a fertile avenue for investigation, and there can be no doubt that deeper and deeper interrogation of the numerical dynamos in this manner will play an important part in geodynamo research over the years to come.

Concluding remarks

The results of this chapter raise an important question over our fundamental understanding of wave dynamics at the smallest scales of motion in the Earth's outer core, calling upon us to reassess how axially-elongated structures might be established and maintained, possibly by the radiation of self-focussing waves from gravitating buoyant anomalies. It appears that inertial-Alfvén waves might be an influential, but previously overlooked, player in these important processes — though it is fair to say that their exact role in the planet's interior is not well-appreciated nor fully understood. A number of significant questions remain unanswered; for example:

- What is the effect of inertial-Alfvén wave radiation on the buoyancy field? Its assumptions mean the model problem of section 3.2.2 is completely ill-equipped to answer this, as discussed above. In DNS of the hydrodynamic case (Davidson & Ranjan, 2018*b*) the density anomaly itself paid little heed to the wave-induced velocity field over inertial wave timescales, though looking further into the future (and adding in a magnetic field as well) this may not be the case.

- How will spatial variations in the background magnetic field affect inertial-Alfvén wave propagation? The magnetic field within the core must be non-uniform, though in all likelihood varies over distances much greater than the small-scale disturbances considered here (Takahashi et al., 2008). This question forms the basis of the next chapter.

- Will variations in magnetic field strength (i.e. changes to the Lehnert number) affect the above conclusions? Of course, a weaker magnetic field will mean a greater disparity between inertial and Alfvén wave timescales, i.e. a trajectory closer to the rotation axis for inertial-Alfvén waves. In any case, it will surely still be the self-focussing ($\boldsymbol{\Omega} \cdot \boldsymbol{k} \approx 0$) solutions which dominate the dispersion pattern, by virtue of their disproportionately high energy density.

- What effect will diffusive and non-linear phenomena have on inertial-Alfvén waves? Owing to their small amplitudes and rapid propagation velocities, it seems likely that these terms will make only a negligible difference to inertial-Alfvén wave dynamics, though this is yet to be rigorously tested.

- How does an inertial-Alfvén wave (or indeed any hybrid magnetic-Coriolis wave) behave when it reaches a boundary? This has been studied for plain inertial waves (Greenspan, 1968) and for torsional oscillations (Maffei & Jackson, 2016; Schaeffer et al., 2012), though not for inertial-Alfvén waves. Since the toroidal magnetic field vanishes at the CMB, only the poloidal portion might be of relevance as far as reflections are concerned; since the source of waves will likely be a long way from the boundary, this question cannot meaningfully be approached before having a good handle on the effect of spatial variations in $\bar{\boldsymbol{B}}$.

Nevertheless, the insights presented here, as first reported in Bardsley & Davidson (2016), represent a novel, intriguing, and potentially very important contribution to our understanding of fundamental wave dynamics in Earth's fluid interior.

Chapter 4

Magnetic-Coriolis waves in a non-uniform magnetic field

In this chapter, which covers work published in Bardsley & Davidson (2017) – plus a few additional topics – we address the propagation of hybrid magnetic-Coriolis waves through a mean magnetic field which varies gradually in space.

This chapter is organised as follows. We set the scene and introduce a canonical problem with a one-dimensional, monotonic horizontal mean field in section 4.1, then devote section 4.2 to its solution: the necessary tools are introduced in section 4.2.1 and immediately turned towards the analysis of this case in section 4.2.2; section 4.2.3 leverages the results of chapter 3 to enable the practical ray tracing which is then performed in sections 4.2.4 and 4.2.5. Section 4.3 then examines a number of extensions to the basic problem with the aim of making it more geophysically applicable: Ohmic dissipation is considered in 4.3.1, a sinusoidal mean magnetic field which drops back to zero at the CMB in 4.3.2, a more general horizontal field in 4.3.3, and an axial field in 4.3.4. Section 4.4 addresses a technical point concerned with the propagation of wave packets through the inertial-Alfvén limit using the WKB approximation (section 4.4.1) in concert with a local analysis, raising the intriguing possibility of a partial reflection of wave energy and therefore the existence of trapped wave solutions (section 4.4.2). The results of this chapter are then brought back to the context of the outer core in section 4.5.

4.1 Introduction

We have so far shown that, in the case of a uniform background magnetic field, the until-recently overlooked *inertial-Alfvén wave* solutions to the general magnetic-Coriolis (MC)

wave equation (3.1.14) play a particularly important role in the dispersion of energy from a localised source. These waves are characterised by a wavevector which is approximately perpendicular to the rotation axis, $\boldsymbol{\Omega}\cdot\boldsymbol{k}\approx 0$, and a group velocity which is rapid on-axis (at half the maximum inertial wave speed) but a degree slower along magnetic field lines (at the local Alfvén velocity).

A serious limitation when attempting to place the preceding work in the context of Earth's interior dynamics is the fact that it uses a uniform background magnetic field, constant in magnitude and direction across all space and time. Clearly this is an unrealistic situation for Earth's outer core, wherein the magnetic field is likely to show significant, complicated variations with both position and time (Jackson & Finlay, 2015). However, the approximation is nevertheless helpful for localised disturbances which are much smaller than the spatial scales over which the mean magnetic field varies; if $\left|\partial\bar{\boldsymbol{B}}/\partial x\right| \sim |\bar{\boldsymbol{B}}|/L$ for some spatial co-ordinate x and large lengthscale L, the wavenumber k of the relevant waves must satisfy $kL \gg 1$ for this to be true. Similarly, if the speed of the waves of interest is much faster than variations of $\bar{\boldsymbol{B}}$ with time, treating the mean magnetic field as steady is reasonable. In this chapter, we address the problem of spatial variations in $\bar{\boldsymbol{B}}$ rather than temporal (since the waves are in general quite fast), and restrict analysis to cases where variations in the mean field are gradual in comparison to the wavelengths in question.

It will be necessary to choose a useful form of $\bar{\boldsymbol{B}}(\boldsymbol{r})$ for use in our model problems going forward. In the interests of simplicity, we retain a Cartesian domain and choose a mean magnetic field which is a function of one Cartesian co-ordinate only; specifically, we set $\bar{\boldsymbol{B}} = \bar{\boldsymbol{B}}(z)$, where z is the axial co-ordinate. This is of the most interest since we are principally interested in the axial propagation characteristics of MC waves, as we already know that both inertial and inertial-Alfvén waves have the ability to self-focus on-axis, forming columnar structures. As discussed in section 3.1.4, the axial component of the magnetic field is seemingly of less significance to wave packets than the perpendicular components, since the smallness of $Le = \left(\bar{B}/\sqrt{\rho\mu}\right)/\Omega\ell$ implies rotation will always dominate the magnetic field in the z-direction; we therefore for the most part neglect $\bar{B}_z$ in what follows, leaving $\bar{\boldsymbol{B}} = \bar{\boldsymbol{B}}_\perp(z)$ (though we will reintroduce a $\bar{B}_z$ in section 4.3.4). The problem is further simplified if only one Cartesian component is permitted, $\bar{\boldsymbol{B}} = \bar{B}(z)\boldsymbol{e}_y$ say. We might have in mind the east-west component of Earth's interior magnetic field, as we did for the initial value problem of section 3.2.2, which is shown in numerical simulations to be reasonably strong and (on average) antisymmetric about the equatorial plane (e.g. Sakuraba & Roberts, 2009; Sheyko et al., 2018). Our most primitive non-uniform background magnetic field would therefore be a linear function of axial distance from the equatorial plane, $\bar{B}(z) = B^* z/L$, for some characteristic magnetic field strength B^* and large lengthscale L. However, in Earth's outer

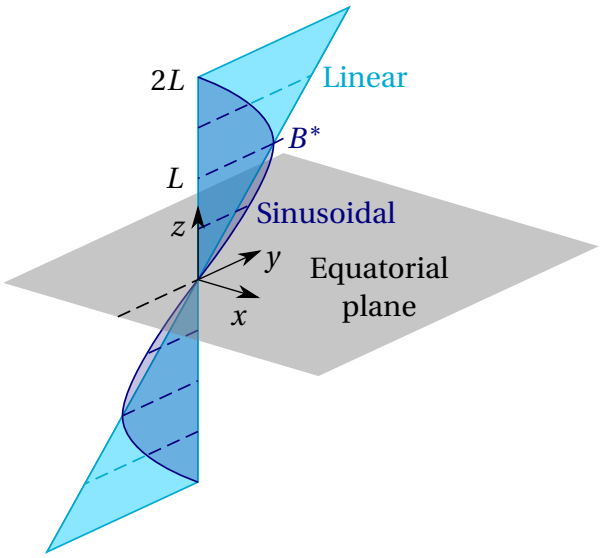

Fig. 4.1.1 Schematic of antisymmetric mean magnetic fields $\bar{\boldsymbol{B}} = \bar{B}(z)\boldsymbol{e}_y$ used in model problems in this chapter. Light blue: $\bar{B} = B^* z/L$; dark blue: $\bar{B} = B^* \sin(\pi z/2L)$.

core (assuming a perfectly insulating mantle) the azimuthal magnetic field must drop back down to zero at the CMB — and hence a slightly more physically realistic choice might be a shape like $\bar{B}(z) = B^* \sin(\pi z/2L)$, with $z = 2L$ representing the CMB (note that both choices have $\bar{B}(L) = B^*$). These two distributions of azimuthal magnetic field are shown schematically in figure 4.1.1; for the most part, we focus discussion on the linearly increasing field as it will prove easier to fix thoughts with a monotonic $\bar{B}(z)$. However, this work will also address situations in which $\bar{B}$ is non-monotonic, as well as those in which an axial component $\bar{B}_z$ is added, and also a more general distribution of $\bar{\boldsymbol{B}}_\perp(z)$ which changes direction as well as magnitude with z.

In essence, the objective of this chapter is to assess the importance of inertial-Alfvén waves within the outer core more generally. We ask whether this limiting case of the hybrid wave dispersion relation is of any special significance once the wave packets have dispersed from the localised source and embarked upon their journeys through an inhomogeneous medium. Clearly, the MC wave equation (3.1.14) has a whole spectrum of solutions; as well as the limiting cases of inertial, inertial-Alfvén and magnetostrophic waves, there are more general hybrid waves possible between these named roots. Given that the previous section questioned the 'well separated roots' hypothesis and brought inertial-Alfvén waves into the game, what may be said for this continuum of intermediate solutions?

4.2 Ray tracing in a simple 1D magnetic field

In this section, we address the problem in which the background magnetic field is in one direction only, and also a function of only one spatial co-ordinate; specifically, we take

$$\bar{\boldsymbol{B}}(z) = \bar{B}(z)\boldsymbol{e}_y, \tag{4.2.1}$$

in which $\bar{B}(z)$ is an antisymmetric function of the axial co-ordinate which varies only gradually on the scale of the waves considered. For discussion purposes, we will also take it as monotonic and non-decreasing – canonically, the linear field in figure 4.1.1 – in order to build up an understanding of the methodology and basic results, though this will be relaxed later in the chapter. (It turns out to be relatively trivial mathematically to consider an arbitrary $\bar{B}(z)$, but the linear field case is best for developing intuition.)

We wish to understand the propagation of small-scale wave packets through this large-scale background field, and therefore abstract the idea of a wave source to be more general than the initial value problems of chapters 2 and 3, taking it to be an arbitrary point source within the domain which could represent a turbulent vortex, buoyant blob, or other such feature. The source is presumed to radiate waves of all types — by which we mean, all orientations of wavevector $\boldsymbol{k}$, though dominated by some magnitude $k \sim \ell^{-1}$ representative of the source size. The frequency of the waves at launch may not be chosen independently of the wavevector, however, but rather must satisfy the MC wave dispersion relation (3.1.15) for a given $\boldsymbol{k}$ and local field strength. Moreover, we consider sources placed at various z-locations; whilst the helical wave dynamo model requires a statistical bias of wave generation towards the equatorial regions (Davidson, 2014), launching at $z \approx 0$ represents a very atypical launch location with negligible magnetic field (since $\bar{B}$ is antisymmetric in z). We therefore look at results across a range of possible source locations. Note that, as the problem is homogeneous in the perpendicular plane, there is no merit to altering the x or y launch position.

We use a subscript "0" to denote the launch characteristics of each wave packet — namely, the wavevector $\boldsymbol{k}_0$, frequency $\varpi_0(\boldsymbol{k}_0)$, and axial location z_0 (with $x_0 = y_0 = 0$). A given source of specified size will radiate wave packets with many different orientations of $\boldsymbol{k}_0$ (though one dominant magnitude) and therefore in general a selection of ray paths for these multiple orientations will need to be computed for each source.

4.2.1 Theoretical basis of ray tracing

To begin our exploration of this model problem, we outline the fundamentals of *ray tracing* – as may be found in Lighthill (1978), for example – the foremost mathematical tool which will allow us to make progress in this chapter. The basic assumption underlying this technique is that variations of the background state – in our case, the mean magnetic field – are gradual compared to the wavelengths of the wave packets in question, i.e. $kL \gg 1$. This leads to a few important simplifications:

1. Since the source is much smaller than any spatial variations in $\bar{B}(z)$, it will launch waves in much the same way as it would in a uniform magnetic field. The initial value problem of section 3.2.2, for example, therefore provides a launch condition and the wave packets may be considered well-dispersed from the source before they are affected by any changes in the mean field. Furthermore, we already know that the radiation from a localised source will in general be dominated by inertial-Alfvén waves, and so the most pertinent cases to look at will be those in which the wavevector at launch is that of an inertial-Alfvén wave, $\boldsymbol{\Omega} \cdot \boldsymbol{k}_0 = 0$.

2. The governing equation is still the hybrid wave equation (3.1.14), only now the mean magnetic field depends on z:

$$\left[\frac{\partial^2}{\partial t^2} - \frac{1}{\rho\mu}\left(\bar{\boldsymbol{B}}(z)\cdot\nabla\right)^2\right]^2 \nabla^2\boldsymbol{u} + (2\boldsymbol{\Omega}\cdot\nabla)^2\frac{\partial^2\boldsymbol{u}}{\partial t^2} = 0. \tag{4.2.2}$$

   Note that, in order to derive this, we now additionally need to neglect all spatial gradients in $\bar{\boldsymbol{B}}(z)$ compared to those in $\boldsymbol{u}$ or $\boldsymbol{b}$, the former being of order $(kL)^{-1}$ smaller (see appendix A3.1); this implies the mean current density $\bar{\boldsymbol{J}} = \mu^{-1}\nabla\times\bar{\boldsymbol{B}}$ is negligible too.

3. The normal-mode solutions we used when $\bar{\boldsymbol{B}}$ was constant (section 3.1.2) still approximately satisfy the wave-like equation (4.2.2) locally at each height z, and therefore the dispersion relation and group velocity may be thought of as still applying in a local sense. The challenge of ray tracing is to work out how the wave properties (its frequency and wavenumber) vary as it propagates smoothly through a domain in which the dispersion relation and group velocity change as functions of space.

We now schematically derive the machinery of ray tracing in a three-dimensional, inhomogeneous and anisotropic domain, as can be found in Lighthill (1978). Suppose some

quantity u pertinent to the wave motion has a local harmonic dependence

$$u \sim \exp\left[i\alpha(\boldsymbol{x}, t)\right] \tag{4.2.3}$$

where the phase α has partial derivatives

$$\frac{\partial \alpha}{\partial x_i} = k_i, \tag{4.2.4a}$$

$$\frac{\partial \alpha}{\partial t} = -\varpi. \tag{4.2.4b}$$

The governing equation then links $\boldsymbol{k}$ and ϖ by providing a dispersion relation $\varpi(\boldsymbol{k})$. In ray tracing, this relationship is dependent on position as well, so we may write

$$\varpi = \varpi(\boldsymbol{k}, \boldsymbol{x}). \tag{4.2.5}$$

The velocity of energy propagation is still given locally by the group velocity, and so the ray position $\boldsymbol{x}$ satisfies

$$\frac{\mathrm{d}x_i}{\mathrm{d}t} = c_{g,i} = \left.\frac{\partial \varpi}{\partial k_i}\right|_{\boldsymbol{x}} \tag{4.2.6}$$

with the derivatives in $\boldsymbol{k}$-space now evaluated holding not only the other components of $\boldsymbol{k}$ fixed, but also the position $\boldsymbol{x}$ as well. We also require an evolution equation for the wavevector $\boldsymbol{k}$ along a ray. Taking $\partial/\partial x_i$ of (4.2.4b) gives

$$\frac{\partial^2 \alpha}{\partial t \partial x_i} = -\left.\frac{\partial \varpi}{\partial x_i}\right|_{\boldsymbol{k}} - \sum_{j=1}^{3} \left.\frac{\partial \varpi}{\partial k_j}\right|_{\boldsymbol{x}} \left(\frac{\partial k_j}{\partial x_i}\right). \tag{4.2.7}$$

Using (4.2.4a), this becomes

$$\frac{\partial k_i}{\partial t} + \left.\frac{\partial \varpi}{\partial k_j}\right|_{\boldsymbol{x}} \left(\frac{\partial k_i}{\partial x_j}\right) = -\left.\frac{\partial \varpi}{\partial x_i}\right|_{\boldsymbol{k}}, \tag{4.2.8}$$

or equivalently, for an observer moving with the ray (i.e. at the local group velocity as in 4.2.6),

$$\frac{\mathrm{d}k_i}{\mathrm{d}t} = -\left.\frac{\partial \varpi}{\partial x_i}\right|_{\boldsymbol{k}}. \tag{4.2.9}$$

The six equations (4.2.6) and (4.2.9) must be solved in order to track a wave packet in the general case. Note that these also imply that frequency is conserved along a ray,

$$\frac{\mathrm{d}\varpi}{\mathrm{d}t} = \sum_{i=1}^{3} \left(\frac{\mathrm{d}k_i}{\mathrm{d}t} \left.\frac{\partial \varpi}{\partial k_i}\right|_{\boldsymbol{x}} + \frac{\mathrm{d}x_i}{\mathrm{d}t} \left.\frac{\partial \varpi}{\partial x_i}\right|_{\boldsymbol{k}} \right) = 0. \tag{4.2.10}$$

This is to be expected since, in a system governed by linear equations with steady coefficients, there can be no transfer of energy between different frequencies.

The analysis is simplified somewhat if the varying background is a function of one spatial co-ordinate only, as demanded in this analysis. Then $\partial\varpi/\partial x_i|_{\boldsymbol{k}}$ is zero for all but the chosen spatial co-ordinate (z, in our case, so $\partial\varpi/\partial x = \partial\varpi/\partial y = 0$), and therefore (4.2.9) says that the corresponding components of $\boldsymbol{k}$ are constant along the ray ($\mathrm{d}k_x/\mathrm{d}t = \mathrm{d}k_y/\mathrm{d}t = 0$). The 'free' component (k_z) can be found by integrating (4.2.9) alongside (4.2.6), yielding the ray's location and wavevector as functions of time.

Alternatively, we can avoid solving the evolution equation (4.2.9) for k_z directly, instead replacing it by the law that frequency must be conserved, (4.2.10). The governing equations for a given ray at position $\boldsymbol{x} = [x, y, z]^T$ are then

$$\boldsymbol{k}_\perp = \boldsymbol{k}_{\perp 0} = const. \tag{4.2.11a}$$

$$\varpi(\boldsymbol{k}, z) = \varpi(\boldsymbol{k}_0, z_0) = \varpi_0 = const. \tag{4.2.11b}$$

$$\frac{\mathrm{d}\boldsymbol{x}}{\mathrm{d}t} = \boldsymbol{c}_g(\boldsymbol{k}, z). \tag{4.2.11c}$$

The requirement that frequency is conserved means that the wavevector $\boldsymbol{k}$ will need to be constantly adjusting in order to make sure that the dispersion relation (4.2.11b) remains satisfied at all z. However, since the perpendicular component of $\boldsymbol{k}$ cannot change because of (4.2.11a), all of the adjustment must occur in the z-component of $\boldsymbol{k}$ alone. Assuming (4.2.11b) can be easily inverted for $k_z(\boldsymbol{k}_{\perp 0}, \varpi_0, z)$, this then gives the group velocity in (4.2.11c) as a function of some constants (including $\boldsymbol{k}_{\perp 0}$ and ϖ_0) and z (through the dependence on $k_z(z)$ implicitly *and* $\bar{B}(z)$ explicitly), which can then be integrated in z for the ray paths and wave packet evolution. Specifically, the ray is found by integrating (4.2.11c) rearranged as

$$\mathrm{d}t = \frac{\mathrm{d}z}{c_{g,z}(z)}, \qquad \frac{\mathrm{d}x}{\mathrm{d}z} = \frac{c_{g,x}(z)}{c_{g,z}(z)}, \qquad \frac{\mathrm{d}y}{\mathrm{d}z} = \frac{c_{g,y}(z)}{c_{g,z}(z)}, \tag{4.2.12}$$

for time and horizontal position as functions of z.

Note that a convention must be defined in order to avoid the fact that negation of both $\boldsymbol{k}$ and ϖ will leave the solution unchanged, thereby counting all waves twice. It will be more convenient in what follows to require that frequencies are always non-negative ($\varpi \geq 0$), but that the wavevector $\boldsymbol{k}$ may take any orientation in 3D space. (The alternative would be to confine $\boldsymbol{k}$ to a half-space and let the frequency take either sign.)

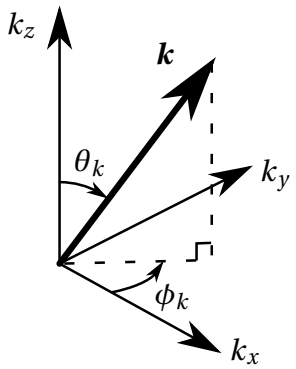

Fig. 4.2.1 Definition of wavevector $\boldsymbol{k}$ in Cartesian $[k_x,\ k_y,\ k_z]$ and spherical polar $[k,\ \theta_k,\ \phi_k]$ co-ordinate systems; note $0 \le \theta_k \le \pi$ and $0 \le \phi_k < 2\pi$.

4.2.2 Application of ray tracing to a 1D magnetic field

We now wish to apply (4.2.12) to the problem at hand, the propagation of hybrid MC waves in an inhomogeneous magnetic field. Recall that the relevant dispersion relation is (3.1.15), which we repeat here:

$$\varpi^2 \mp \varpi_\Omega \varpi - \varpi_B^2(z) = 0, \tag{4.2.13}$$

where $\varpi_\Omega = 2\boldsymbol{\Omega}\cdot\boldsymbol{k}/k = 2\Omega\cos\theta_k$ (if $\boldsymbol{k}$ is expressed in spherical polars $[k,\ \theta_k,\ \phi_k]$ about the z-axis — figure 4.2.1) and $\varpi_B(z) = \bar{\boldsymbol{B}}(z)\cdot\boldsymbol{k}/\sqrt{\rho\mu}$ is now a function of the axial co-ordinate; the upper (lower) sign in (4.2.13) corresponds to positive (negative) axial group velocity. Noting that, when ray tracing, the frequency is a constant (and equal to ϖ_0, see 4.2.11b), a more useful form may be derived by dividing through by ϖ_0^2:

$$\frac{\varpi_\Omega}{\varpi_0} = \pm\left(1 - \frac{\varpi_B^2(z)}{\varpi_0^2}\right), \tag{4.2.14a}$$

$$\cos\theta_k = \pm\frac{\varpi_0}{2\Omega}\left(1 - \frac{\left(\bar{\boldsymbol{B}}\cdot\boldsymbol{k}\right)^2/\rho\mu}{\varpi_0^2}\right). \tag{4.2.14b}$$

Examining this form of the dispersion relation, we see that Ω, ρ and μ are constants, whilst ϖ_0 is also constant along a ray by virtue of (4.2.11b), its value being fixed by the choice of launch condition ($\boldsymbol{k}_0$ and z_0). Furthermore, we may take advantage of the fact we are considering a mean magnetic field with no z-component, and therefore $\bar{\boldsymbol{B}}\cdot\boldsymbol{k} = \bar{\boldsymbol{B}}(z)\cdot\boldsymbol{k}_{\perp 0}$. Since $\boldsymbol{k}_{\perp 0}$ is constant along a given ray by (4.2.11a), ϖ_B is an explicit function of z with no implicit dependence on $k_z(z)$. Hence, for a given ray at a given height, (4.2.14b) prescribes the angle of the wavevector to the vertical; since $\boldsymbol{k}_{\perp 0}$ is fixed, this is equivalent to setting $k_z(z)$.

Once the wavevector is known as a function of z, so too is the group velocity. It comes from plugging (4.2.14b) and the magnetic field (4.2.1) into the group velocity expression found during the discussion of wave dispersion in free space, (3.1.16). This result is given component-wise in appendix A3.2, which enables one to calculate the ray path, given the background field distribution, the source height z_0, and the wavevector at launch $\boldsymbol{k}_0$.

4.2.3 The launch condition

So far, we have considered a generic wavevector $\boldsymbol{k}_0$ as the launch condition, thereby ignoring any specific details of both the nature of the disturbance which first generates the rays, and the means by which they are launched. The mechanics of ray tracing really only apply once the wave packets are far from the source and well dispersed, and therefore the process of wave dispersal from a localised source in a gradually-varying medium may be thought of as two separate processes (see Lighthill, 1978). First, particulars relating to the exact nature of the disturbance and the governing equations will specify the initial distribution of energy in wavevector space. Second, once the waves have escaped the source, such that the local wavevector varies only gradually in space, ray tracing techniques may be applied in order to track the subsequent energy propagation. Typically, the first step could be completed using asymptotic methods, particularly the *method of stationary phase* (Bleistein & Handelsman, 1986). However, in this case there is little need for such an elaborate analysis; instead, the fundamental conclusion of chapter 3 may be leveraged. We know (from figure 3.2.2, for example) that wavevectors with $\boldsymbol{\Omega} \cdot \boldsymbol{k} \approx 0$ will dominate the radiation pattern from the localised source, even in the presence of a background magnetic field. Hence, the most important rays emanating from the source will be those which start off with $k_z \approx 0$ (i.e. $\theta_k \approx \pi/2$), and therefore tracking these features will give a reasonable picture of the energy radiation pathways from the initial disturbance through the inhomogeneous medium. There is still, however, no account made for the exact form of the wave source – though we have in mind the buoyant blobs and turbulent eddies of chapters 2 and 3 – but the dominance of inertial-Alfvén waves found previously inspires confidence that the general picture should be broadly independent of such details.

As well as a launch wavevector, ray tracing also requires a source location. We are most interested in the release of waves from the equatorial regions $z \approx 0$, as motivated by the structure of convection in numerical dynamos and the idea of spatial segregation of helicity by hybrid waves (section 1.2.3). However, $z_0 = 0$ is a rather special location characterised by zero magnetic field, and therefore allowing the rays to be launched at different heights is of much interest; in what follows, we use three different launch heights, $z_0 = [0.025,\ 0.1,\ 0.5]L$, which may be though of as in the 'equatorial regions' rather than the equatorial plane exactly.

Our launch condition, therefore, is that waves are released from the source at some height $z_0 < L$ with wavevectors $\boldsymbol{k}_0$ which satisfy $\boldsymbol{\Omega} \cdot \boldsymbol{k}_0 = 0$. Of course, there are many wavevectors which fit this description, as it places no constraint on the magnitude $k_0 = k_{\perp 0}$ or the azimuthal orientation ϕ_{k0}. For simplicity, we limit discussion to one choice of k_0, representative of the dominant lengthscale of the disturbance — using $k_0 \sim 2/\ell$ with $\ell \sim 10$km and $L \sim 1000$km gives $k_0 L \sim 200$, a value we use throughout. Furthermore, we trace 32 different rays with equispaced azimuthal wavevector orientations ϕ_{k0}, giving a set of rays which constitute the walls of a ray tube corresponding to what were originally the self-focussing $\boldsymbol{\Omega} \cdot \boldsymbol{k} \approx 0$ solutions.

4.2.4 Ray tracing in a linear horizontal field

For our first foray into a ray tracing problem, we consider the simplest possible inhomogeneous magnetic field — one which varies linearly with z:

$$\bar{\boldsymbol{B}}(z) = \bar{B}(z)\boldsymbol{e}_y, \qquad \bar{B}(z) = \frac{B^* z}{L}. \tag{4.2.15}$$

In this problem and all others, the constant B^* is defined as the magnitude of the y-component of the background magnetic field at $z = L$, and may be thought of as representing a characteristic maximum azimuthal field in the Earth's core. We have in mind a typical B^* of around ~ 40G and lengthscale $L \sim 1000$km, which means the controlling dimensionless parameter, the Lehnert number, is

$$Le^* = \frac{B^*/\sqrt{\rho\mu}}{\Omega L} \sim 5 \times 10^{-4}, \tag{4.2.16}$$

a value which we use throughout. Note that the linear-field case, although easier to understand, does suffer the deficiency that the magnetic field keeps on increasing to what might be considered implausibly large mean field values of ~ 80G at $z \sim 2L$, an issue which we address in section 4.3.2. The advantage of the form (4.2.15) is the monotonic relationship between field strength and z — a stronger field implies a greater distance from the equatorial plane, and vice versa.

Consider now how the wavevector of a given ray, launched as an inertial-Alfvén wave with $\theta_k = 0$, will change as it propagates into the varying field. We specify the launch frequency $\varpi_0 = |\varpi_B(z_0)|$, in which case the dispersion relation equation for θ_k (4.2.14b) becomes

$$\cos\theta_k = \pm \frac{|\varpi_B(z_0)|}{2\Omega}\left(1 - \frac{\bar{B}^2(z)}{\bar{B}^2(z_0)}\right) \tag{4.2.17a}$$

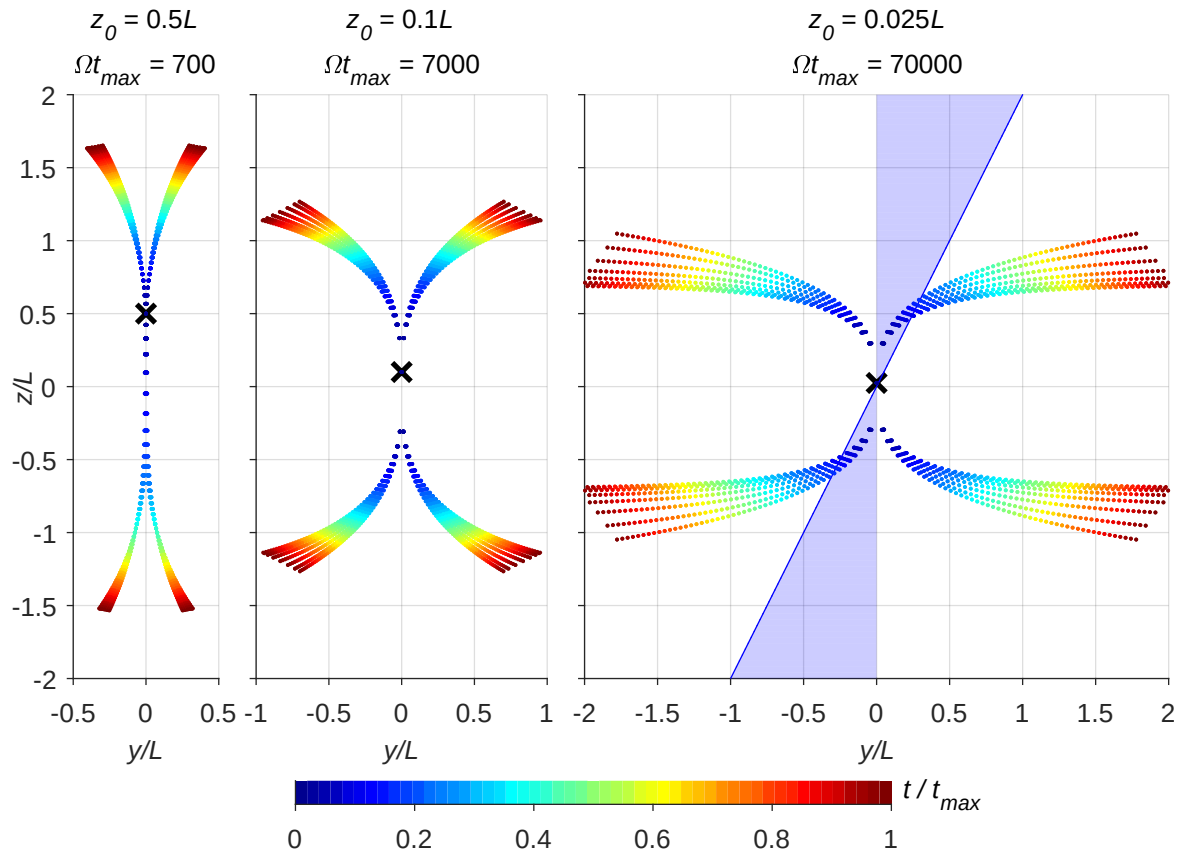

Fig. 4.2.2 Primary rays dispersing from a localised anomaly of scale $k_0 L = 200$ at various launch locations z_0, marked by ×. The ambient field, indicated in the right pane, is linear in z, with $Le^* = 5 \times 10^{-4}$. Ray locations are plotted at 50 equispaced time intervals, coloured by $t/t_{\max}$; note that $t_{\max}$ differs considerably between the three panes.

$$= \pm \frac{1}{2} Le^* k_0 \left| z_0 \sin\phi_{k0} \right| \left(1 - \frac{z^2}{z_0^2} \right). \tag{4.2.17b}$$

The first applies to a mean field of the more generic form (4.2.1), whereas the second is only for the linear field (4.2.15). What is immediately clear is that, while $\cos\theta_k = 0$ at $z = z_0$, the wavevector must be at an angle to the horizontal at most other heights, and therefore what started out as inertial-Alfvén wave packets will not necessarily stay so for long, but rather evolve into other hybrid waves with a finite k_z as they propagate. Since the inertial wave component of $\boldsymbol{c}_g$ (i.e. $\boldsymbol{c}_{g\Omega}$ in (3.1.16a)) is perpendicular to $\boldsymbol{k}$, this implies ray paths which deviate from axial propagation, heading obliquely to the rotation vector instead.

However, note that the factor $Le^* k_0 |z_0 \sin\phi_{k0}|$ pre-multiplying (4.2.17b) can be expected to be reasonably small in the core of the Earth, and therefore the change in θ_k will be small if the ratio $\bar{B}(z)/\bar{B}(z_0)$ remains modest. That is to say, so long as the magnetic field is never

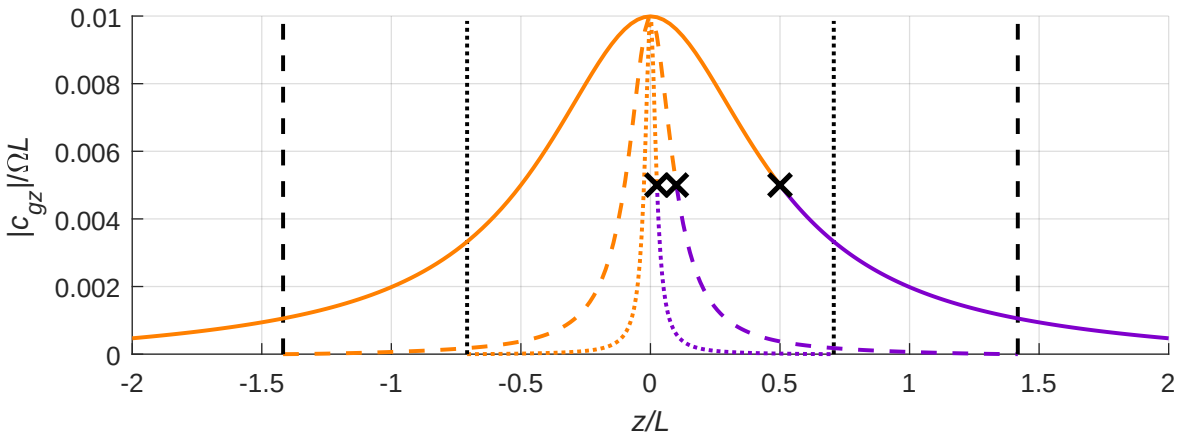

Fig. 4.2.3 Axial group velocity of hybrid waves, as ray-traced through a linear background field $\bar{B}(z) = B^* z/L$, with $k_0 L = 200$ and $Le^* = 5 \times 10^{-4}$. The three launch locations are marked by ×, dotted/dashed/solid lines correspond to $z_0 = 0.025/0.1/0.5$, and northward (southward) propagating trajectories are coloured purple (orange). The vertical black lines denote the respective *wave ceilings* at which $c_{gz} \to 0$. The ray with $\boldsymbol{k}_{\perp 0}$ aligned with $\bar{\boldsymbol{B}}$ (i.e. $\phi_{k0} = \pi/2$) is shown in each case.

dramatically different from its value at launch, k_z will stay small and therefore the wave packets will propagate for the most part on-axis. This can be seen in the left pane of figure 4.2.2, in which the launch location is chosen to be $z_0 = 0.5L$ (i.e. $\bar{B}(z_0) = 0.5B^*$). The rays propagate mainly along the rotation axis and remain reasonably fast, reaching $z \sim 1.5L$ (1500km) by $\Omega t = 700$ (111 days). This does, however, represent a reduction in axial group velocity compared to the waves at launch, since in the constant-field case pure inertial-Alfvén waves would cover an axial distance L in about 30 days. This is accounted for by the fact that, despite $\cos\theta_k$ remaining small, the special limiting case $|\varpi_\Omega| \ll |\varpi_B|$ which is characteristic of inertial-Alfvén waves is not necessarily maintained as the waves push north and south. Instead, the waves are likely to satisfy the more vague condition $|\varpi_\Omega| \sim |\varpi_B|$, being rather more general intermediate solutions to the hybrid dispersion relation (4.2.13), which nevertheless propagate mostly on-axis — at least, for the chosen launch location.

However, if the ratio $\bar{B}(z)/\bar{B}(z_0)$ is allowed to become much larger than unity, k_z may become comparable with $k_{\perp 0}$ and therefore $\boldsymbol{c}_{g\Omega}$ significantly misaligned with $\boldsymbol{\Omega}$. This situation is realisable only if the magnetic field strength at launch is particularly small (i.e. close to the equator, $z_0 \ll L$). Such waves, as well as being deflected off-axis by the rotation of the $\boldsymbol{c}_{g\Omega}$ vector as $\boldsymbol{k}$ varies, are also severely arrested by the ever-increasing magnetic field. To see this, consider the axial component of group velocity as given by (A3.2.4),

$$c_{gz} = \pm \frac{2\Omega}{k_{\perp 0}} \left(1 + \frac{\varpi_B^2}{\varpi_0^2}\right)^{-1} \left[1 - \left(\frac{\varpi_0}{2\Omega}\right)^2 \left(1 - \frac{\varpi_B^2}{\varpi_0^2}\right)^2\right]^{3/2}, \tag{4.2.18}$$

which is plotted for the parameters of figure 4.2.2 in figure 4.2.3. The rays launched at $z_0 = 0.5L$, shown as a solid line, maintain a reasonably large axial group velocity as they propagate. If, however, we launch the rays much closer to the equator – say at $z_0 = 0.025L$, the dotted line – c_{gz} drops away rapidly, even at very modest distances from the launch location. The corresponding ray tracing result, the right-hand pane of figure 4.2.2, is therefore evaluated at a much later time ($t_{\max} \approx 30$yr), and the waves clearly exhibit both a comparative sluggishness and tendency to bend along the field lines.

In fact, these properties can be taken to the extreme, with rays bending over so much that they stop propagating axially at all. This was first noticed by Acheson (1972), who describes it as a critical level through which wave packets may pass in one direction only; as our wave packets come from a single localised source, it makes more sense to think of this level as a solid barrier rather than a non-return valve. Inspecting (4.2.18), we see that the axial group velocity drops to zero at

$$\left(\frac{\varpi_0}{2\Omega}\right)^2 \left(1 - \frac{\varpi_B^2}{\varpi_0^2}\right)^2 = 1. \tag{4.2.19}$$

This corresponds to the point at which the dispersion relation (4.2.14b) stops having valid solutions, since the condition $|\cos\theta_k| \leq 1$ implies

$$\left|1 - \frac{\varpi_B^2}{\varpi_0^2}\right| \leq \frac{2\Omega}{\varpi_0} \tag{4.2.20}$$

as a requirement for waves to exist. This constitutes what we term a *wave ceiling*, a critical level $z = z_c$ through which the waves cannot pass, at which

$$\frac{\bar{B}(z_c)}{\bar{B}(z_0)} = \sqrt{1 + \frac{2\Omega}{\varpi_0}} \approx \sqrt{\frac{2\Omega}{\varpi_0}}. \tag{4.2.21}$$

There is an equivalent level for downwards-propagating waves at $z = -z_c$ since $\bar{B}(z)$ is antisymmetric. This ceiling is shown on figure 4.2.3 by the vertical black lines; clearly, for $z_0 \ll L$ the rays launched close to the equator do not travel very far at all before being brought to a stop, meaning wave energy may be trapped in the equatorial regions rather than continuing on to promote axially-elongated structures spanning the core.

Notice that these rays, despite their axial group velocity vanishing to nothing, still carry on propagating along magnetic field lines, as seen in the right-hand pane of figure 4.2.2. The perpendicular component of the group velocity (A3.2.5) does not in fact vanish at the

ceiling; rather, it becomes

$$\boldsymbol{c}_{g\perp} \approx \frac{2\varpi_B}{\varpi_0}\left(1+\frac{\varpi_B^2}{\varpi_0^2}\right)^{-1}\frac{\bar{\boldsymbol{B}}}{\sqrt{\rho\mu}} \approx \frac{2\varpi_0}{\varpi_B}\frac{\bar{\boldsymbol{B}}}{\sqrt{\rho\mu}} = \frac{2\bar{B}(z_0)}{\sqrt{\rho\mu}}\boldsymbol{e}_y \tag{4.2.22}$$

since $\bar{B}(z_c) \gg \bar{B}(z_0)$ implies $\varpi_B \gg \varpi_0$. This also suggests that this surviving component of group velocity is very slow, and very much less than the local inertial or Alfvén wave speeds. It seems, therefore, that the solutions at this point are in the magnetostrophic regime, with the ranking $\varpi_0 \ll \varpi_B \ll \varpi_\Omega$ having been achieved.

For completeness we also show an intermediate launch location in the middle pane of figure 4.2.2; releasing the waves at $z_0 = 0.1L$, they are noticeably diverted from the axis and slowed down (the plot is at ~ 3yr from launch), but have not reached the wave ceiling at the instant plotted. In fact, the ceiling for these rays is at $z_c \sim 1.5L$ (1500km) — higher than for the right hand pane, when the rays were launched right next to the equator, but still probably below the core-mantle boundary. However, the choice of a linear $\bar{B}(z)$ is deceptive; because it keeps on increasing with z, a ray launched from any location will invariably encounter a ceiling at some point, but at what may be at an unrealistically large value of magnetic field strength. In this model problem, rays launched at $z_0 = 0.1L$ have $\bar{B}(z_c) \sim 60$G, for example. Investigating what happens in a slightly more realistic field – one which dies away again towards the CMB – is the subject of section 4.3.2.

Diagrammatic interpretation

The findings of this section are well-summarised diagrammatically. Consider figure 4.2.4, which is a representation of the dispersion relation in the form (4.2.14a). Since $\bar{B}(z)$ is monotonic increasing, the horizontal axis may be though of as a surrogate for axial co-ordinate; rays propagating northwards will move to the right, and rays propagating south to the left. The vertical axis tells us something about the angle $\boldsymbol{k}$ makes with the horizontal plane as it propagates; if ϖ_Ω is positive, $\boldsymbol{k}$ is above the horizontal, whereas if ϖ_Ω is negative, $\boldsymbol{k}$ points somewhat southwards — and the further one is from $\varpi_\Omega = 0$, the greater the angle made with the horizontal plane (i.e. the greater the alignment between $\boldsymbol{k}$ and $\boldsymbol{\Omega}$).

The two branches are shown, corresponding to northward and southward propagation. To fix thoughts, consider rays launched at positive z. Our launch condition is inertial Alfvén waves, which have wavevectors in the horizontal plane, $\varpi_\Omega = 0$, and therefore sit on the crossover point $\varpi_B = \varpi_0$ on the right-hand side of the horizontal axis. First, consider northward-propagating rays, following the purple curve in figure 4.2.4 to the right. As they travel, the value of ϖ_Ω demanded by the dispersion relation becomes negative, and therefore

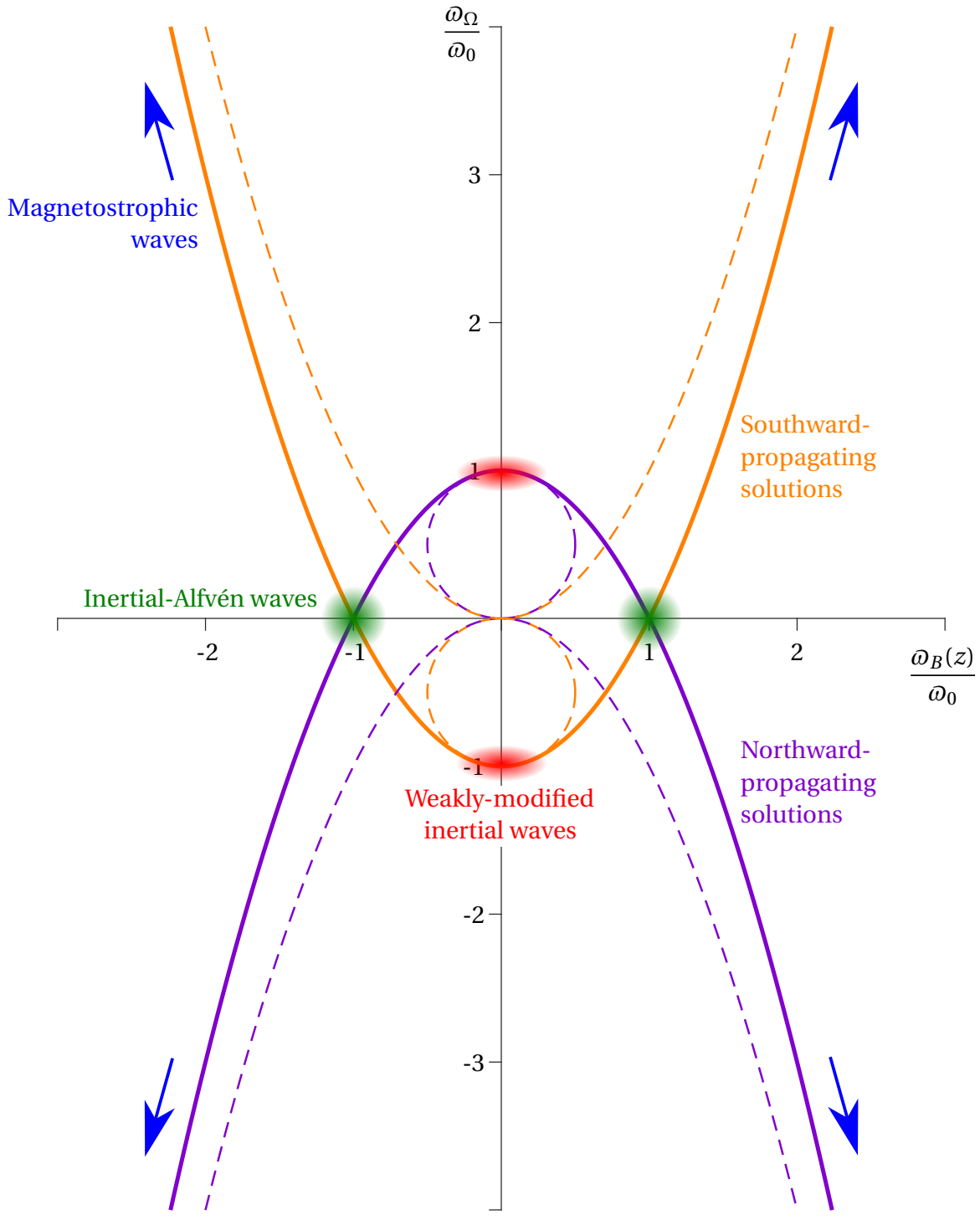

Fig. 4.2.4 The dispersion relation (4.2.14a) diagrammatically. Solid lines show the exact equation, and dashed lines the 'well-separated roots' limit from (3.1.18a), $\varpi_0 \approx \frac{\varpi_\Omega}{2}\left(\pm 1(\pm)\left[1+\frac{2\varpi_B^2}{\varpi_\Omega^2}\right]\right)$, with northward (southward)-propagating rays coloured purple (orange). The named limits – inertial, inertial-Alfvén and magnetostrophic waves – are also indicated (the latter occupies the far corners of the diagram).

so too must k_z — the wavevector points more and more southward as the ray heads north, though does so keeping $\boldsymbol{k}_\perp$ constant, implying that the wavevector magnitude is increasing.

This change in $\boldsymbol{k}$ has two effects on the group velocity, which cannot be appreciated in figure 4.2.4 alone. Firstly, the rate of propagation drops off (figure 4.2.3) as a large ϖ_B/ϖ_0 substantially reduces $|\boldsymbol{c}_g|$ (see e.g. (3.1.16a)). Secondly, the angle $\boldsymbol{k}$ now makes to the horizontal plane means the $\boldsymbol{c}_{g\Omega}$ term (which is always perpendicular to $\boldsymbol{k}$) acts in tandem with the Alfvén velocity $\boldsymbol{c}_{gB}$ to take the wave packet somewhat off-axis.

As $\boldsymbol{k}$ gets further below the horizontal plane, and the magnetic field gets stronger (i.e. as we move to the bottom-right corner of figure 4.2.4) the waves approach the magnetostrophic limit $\varpi_\Omega/\varpi_0 \approx -\varpi_B^2/\varpi_0^2$ depicted by a dashed line. They do not, however, carry on indefinitely, being brought to a complete halt (at least in terms of axial propagation) by the wave ceiling at $\varpi_\Omega = -2\Omega$ (see (4.2.19)), which arises when the dispersion relation effectively demands an infinite $|k_z|$.

For southward propagating rays, the story is similar. They follow the orange path in figure 4.2.4 to the left from the point $\varpi_B = \varpi_0$ and so their wavevector also initially dips slightly below the horizontal plane as the magnetic field strength reduces. At $z = 0$ there is no mean magnetic field, so the rays are propagating rapidly as pure inertial waves (almost exactly on-axis because k_z is still very small). Beyond this point, the field strength increases again, causing the wavevector to angle back up toward the horizontal. At $z = -z_0$ they return to being inertial-Alfvén waves, exactly as they were at launch, with a wavevector in the horizontal plane. Heading further south, k_z must become positive and the situation is much as for the northward-propagating waves, though of course with all directions reversed.

4.2.5 Alternative launch conditions

Although we have focussed attention on the primary rays emitted by the localised source – those solutions which have $\boldsymbol{\Omega}\cdot\boldsymbol{k} = 0$ at z_0, and so $\varpi_0 = \varpi_B(z_0)$ – they are clearly not the only waves which will be present (figure 3.2.3). It is therefore of interest to consider the fate of wave packets which instead make an angle to the horizontal plane, and are therefore launched as more general hybrid waves. For moderate values of this angle, the 'well-separated roots' hypothesis is acceptable, since $|\varpi_\Omega| \gg |\varpi_B|$ is implied by $Le \ll 1$ in all cases except $\boldsymbol{\Omega}\cdot\boldsymbol{k} \approx 0$. Hence, such waves may be classified as 'inertial' (or *fast*) and 'magnetostrophic' (or *slow*) roots. We choose an angle of $\boldsymbol{k}_0$ which is $\frac{\pi}{8} = 22.5°$ from the horizontal ($\theta_{k0} = \frac{\pi}{2}(\pm)\frac{\pi}{8}$) and, keeping the magnitude k_0 constant, take a range of azimuthal wavevector angles as before. The wave frequency is given not by $\varpi_0 = \varpi_B(z_0)$, but rather (3.1.15c) with the requirement

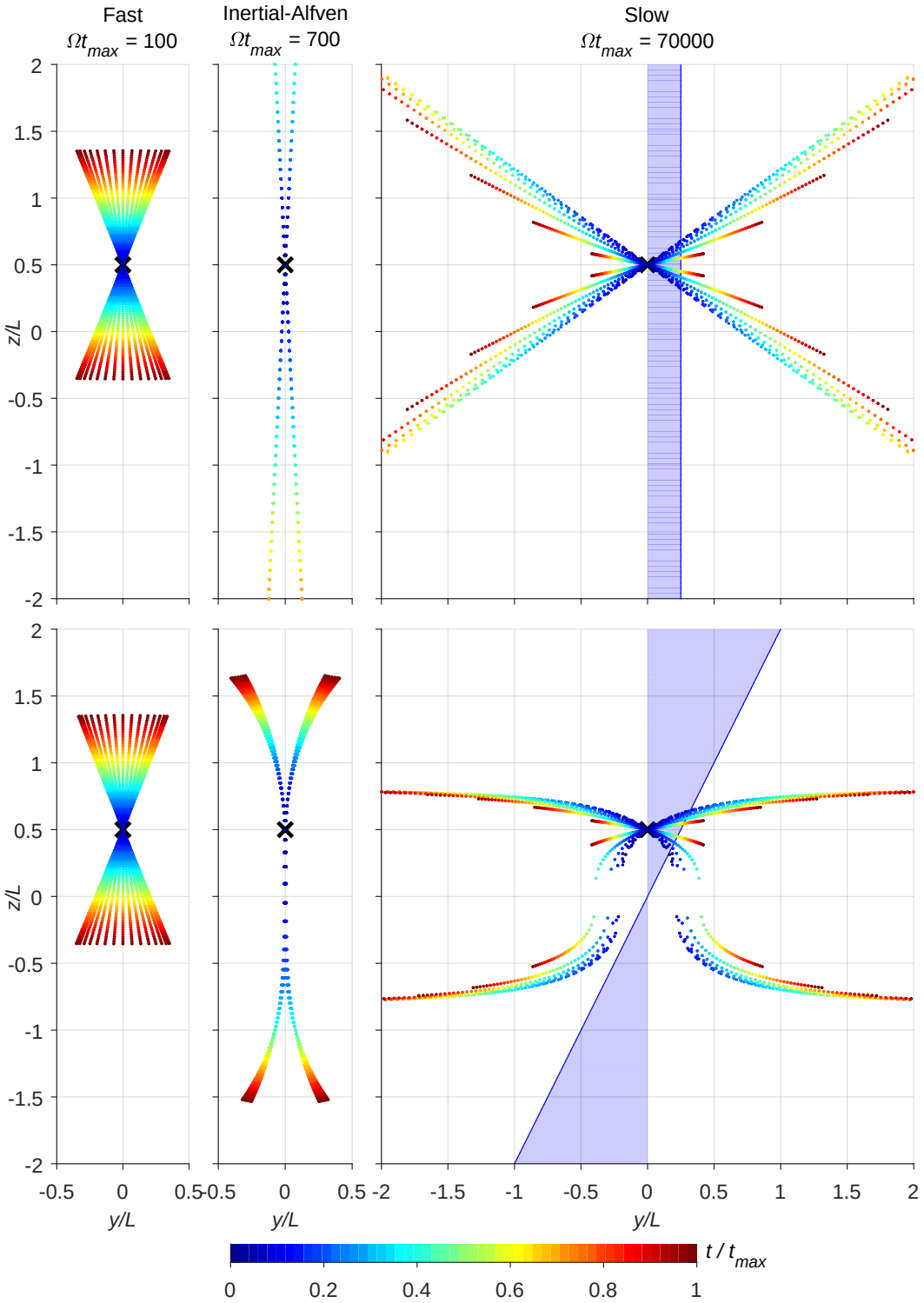

Fig. 4.2.5 Rays dispersing from a localised anomaly of scale $k_0 L = 200$ with various launch conditions. Left panes: $\theta_{k0} = \frac{\pi}{2}(\pm)\frac{\pi}{8}$, fast roots. Middle panes $\theta_{k0} = \frac{\pi}{2}$, inertial-Alfvén roots. Right panes: $\theta_{k0} = \frac{\pi}{2}(\pm)\frac{\pi}{8}$, slow roots. The mean magnetic field, indicated in the right-hand panes, is constant ($\bar{B} = 0.5B^*$) in the top row and linear ($\bar{B}(z) = B^* z/L$) in the bottom row, with $Le^* = 5 \times 10^{-4}$. The launch location, marked by ×, is $z_0 = 0.5L$. Ray locations are plotted at 50 equispaced time intervals, coloured by $t/t_{\max}$.

$\varpi_0 \geq 0$,

$$\varpi_0 = \sqrt{\left(\frac{\varpi_{\Omega 0}}{2}\right)^2 + \varpi_{B0}^2} \pm \frac{\varpi_{\Omega 0}}{2}, \tag{4.2.23}$$

where $\varpi_{\Omega 0} = 2\Omega\cos\theta_{k0}$ and $\varpi_{B0} = \left(\bar{B}(z_0)k_0/\sqrt{\rho\mu}\right)\sin\theta_{k0}\sin\phi_{k0}$ are the inertial and Alfvén wave frequencies at launch. The upper/lower sign in (4.2.23) still corresponds to north/southward propagation, but care must be take to distinguish the fast and slow roots; if the sign of $\cos\theta_{k0}$ matches that of $\pm$, the roots are fast, and vice versa.

Figure 4.2.5 shows the results of tracing rays which are not the primary rays from the source. For comparison, the top three panes show a 'ray tracing' analysis for the trivial case of a uniform background field, with a value chosen so it matches the linearly-varying field at the launch location $z_0 = 0.5L$. The bottom three panes have the same background field as section 4.2.4, and in fact the central-bottom pane of figure 4.2.5 is identical to the left-hand pane of figure 4.2.2 as it shows rays launched as inertial-Alfvén waves. The left-hand panes in figure 4.2.5 show weakly-modified inertial waves and the right-hand panes magnetostrophic waves.

Inspecting the ray paths in figure 4.2.5, it can be seen that

1. The weakly-modified inertial waves are imperceptibly affected by the variation in the background magnetic field; this makes sense, since it plays very little part in their dynamics, so variations in $\bar{\boldsymbol{B}}$ along inertial wave rays are of little consequence.

2. The magnetostrophic waves are also reasonably indifferent to whether the field is constant or linearly-varying; although changes in the direction of $\boldsymbol{c}_g$ alter the wave paths somewhat, making them bend along the field lines at large z, the wave generally occupy a region where $|\bar{B}(z)| \sim |\bar{B}(z_0)|$ and so the rate of energy propagation is broadly the same. The obvious exception is the equatorial plane, where the rays must momentarily become fast inertial waves in order to navigate the region $\bar{B} \approx 0$.

3. Inertial-Alfvén waves are the most affected by the variations in the magnetic field, notably slowing and bending off-axis as discussed previously.

4. In general, the waves tend to 'defocus' as they propagate – that is to say, geometrically, adjacent ray paths spread out in space – whether the field is uniform or varying. In the uniform-field case, however, the inertial-Alfvén waves do not defocus and only one ray path is seen, which is what made them so dominant in the model problem of section 3.2.2. The inertial wave solutions defocus perpendicular to the direction of travel (adjacent rays diverge whilst travelling at the same speed), whereas for the magnetostrophic waves defocussing occurs along the direction of travel (adjacent rays

travel in approximately the same direction, but at different speeds). When the field varies, the picture is broadly the same; inertial and magnetostrophic waves defocus in the same way, whereas those launched as inertial-Alfvén waves stay reasonably well-focussed. Hence, the justification for the dispersion of energy from a localised source – that the inertial-Alfvén solutions may 'self-focus' a large portion of the $\boldsymbol{k}$-space energy into a small region of physical space – appears to hold true even when the field varies, despite the fact that the waves themselves morph into more general magnetic-Coriolis solutions with $|\varpi_\Omega| \sim |\varpi_B|$ as they propagate.

4.3 Extensions to a more geophysical context

Having treated the dispersion of MC waves in a non-uniform magnetic field from a reasonably canonical point of view so far – that is to say, with the largest possible number of assumptions and a very simple background field – we now attempt to push the analysis towards a more geophysically relevant situation. We do this by altering the canonical problem above in a number of different ways, only ever considering one alteration at a time in order to isolate the particular effect of relaxing each assumption.

First (section 4.3.1), we look at the Ohmic dissipation of hybrid wave packets, with particular focus on the magnetostrophic regime. We then perform ray tracing through a non-monotonic background field, which is nevertheless still one-dimensional (section 4.3.2), and then with a direction as well as magnitude which changes with height, choosing a distribution inspired by the numerical dynamo simulations (section 4.3.3). Finally, in section 4.3.4 we look at an interesting phenomenon which occurs when a constant axial field $\bar{B}_z$ is applied as well.

4.3.1 Ohmic dissipation of MC waves

Our first extension looks at the effects of dissipation on hybrid MC waves as they propagate. We previously ignored any dissipative effects on the grounds that the timescales associated with wave motions are much shorter than the rate of attenuation (section 3.1.1). However, as we have seen in section 4.2, the propagation of waves through a varying magnetic field can dramatically alter the rate of propagation, even if the waves started out with a frequency comparable to the Earth's rapid rotation rate.

As discussed before, Ohmic dissipation is very likely to overwhelm viscous effects in the outer core, by a factor $Pm^{-1} \sim 10^6$, and we therefore neglect viscous effects entirely. Our treatment of Ohmic losses here is rather heuristic — the ray tracing methodology does not

strictly apply to dissipative systems, but we will nevertheless assume it does and use the output to estimate a decay rate. If the calculated figure is negligible compared to the wave speed, the ray tracing analysis has survived the test and may be considered valid. However, if the dissipation timescale drops to a value comparable to the time it would take a wave packet to traverse core-relevant distances, we might expect the waves to be appreciably damped, and therefore the ideal analysis to no longer apply. Instead, the wave packets will lose the majority of their energy to Ohmic heating, thereby ceasing to be of any particular relevance.

From the induction equation (3.1.6), it can be seen that the Ohmic dissipation timescale for MHD waves of wavenumber k is $\tau_\eta \sim \left(\eta k^2\right)^{-1} \sim \ell^2/4\eta$. Note that for $\ell \sim 10$km and $\eta \sim 0.5\mathrm{m}^2\,\mathrm{s}^{-1}$, we have $\tau_\eta \sim 600$ days, much longer than the inertial (or inertial-Alfvén) wave timescales. However, during the ray tracing analysis, it has been seen that the angle of the wavevector to the horizontal plane may change considerably in order to accommodate the dispersion relation (4.2.14b). At constant $\boldsymbol{k}_\perp$, this implies an increase in the wavevector magnitude k, in accordance with $k = k_{\perp 0}\csc\theta_k$, and therefore an increased rate of dissipation since $\tau_\eta \sim k^{-2}$ — as the wavelength gets shorter, the rate of dissipation increases. In fact, using the expression (4.2.14b) for θ_k as a function of z, we have

$$\tau_\eta \sim \frac{1}{\eta k_{\perp 0}^2}\sin^2\theta_k \tag{4.3.1a}$$

$$\sim \frac{1}{\eta k_{\perp 0}^2}\left[1-\left(\frac{\varpi_0}{2\Omega}\right)^2\left(1-\frac{\varpi_B^2(z)}{\varpi_0^2}\right)^2\right]. \tag{4.3.1b}$$

Clearly, any variation in the mean field (i.e. changes to ϖ_B from its launch value ϖ_0) will tend to reduce the timescale for Ohmic dissipation. The question is, at what point does this effect become significant compared to the timescales required for wave packets to travel appreciable distances within the core? In order to assess this, we introduce a 'dissipation lengthscale' $\ell_\eta = c_g\tau_\eta$, which is the above timescale multiplied by the magnitude of the MC wave group velocity, which is also a function of z through θ_k, given by (A3.2.4) and (A3.2.5). This may be thought of as the distance over which a wave packets is attenuated — in order for ray tracing to be relevant, this length should be at least as large as our macro-lengthscale L.

In terms of the input parameters of our problem, we may measure the strength of Ohmic dissipation dimensionlessly via the group $\Omega/\eta k_0^2$, which is related to the magnetic Ekman number $Em = \eta/\Omega L^2$ — for small-scale waves as discussed above, we have $\Omega/\eta k_0^2 \sim 4000$. For this choice, and all other parameters as in section 4.2.2, we plot ℓ_η/L for the various launch locations in figure 4.3.1. If this ratio is large, the wave packets make traverse distances

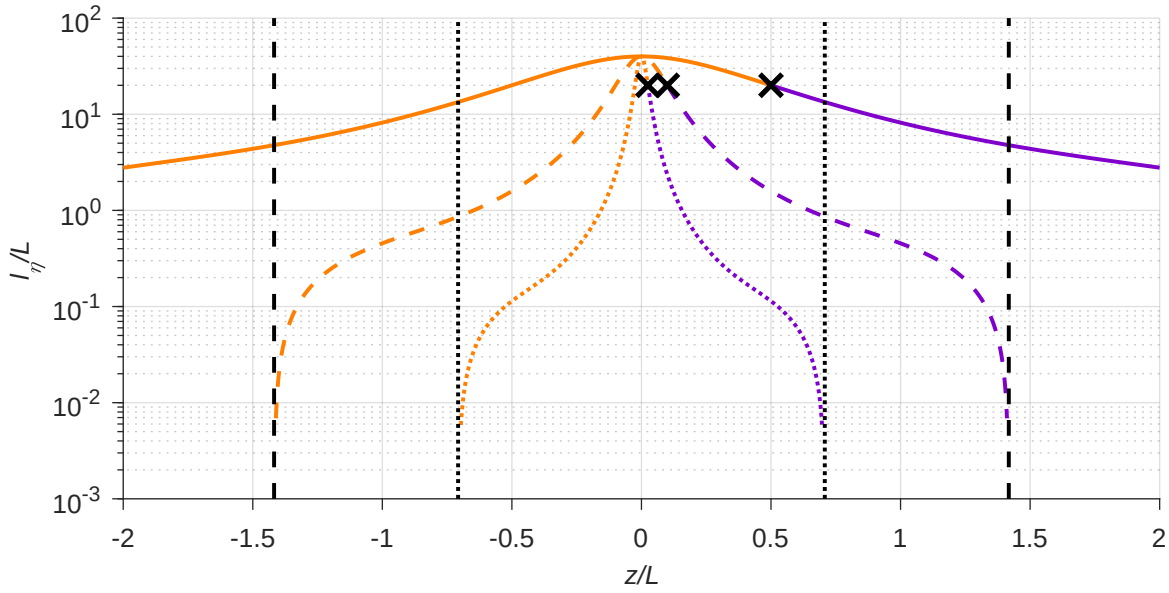

Fig. 4.3.1 Dissipation lengthscale ℓ_η of hybrid waves, as ray-traced through a linear background field $\bar{B}_y(z) = B^* z/L$, with $k_0 L = 200$, $Le^* = 5 \times 10^{-4}$ and $\Omega/\eta k_0^2 = 4000$. The three launch locations are marked by ×, dotted/dashed/solid lines correspond to $z_0 = 0.025/0.1/0.5$, and northward (southward) propagating trajectories are coloured purple (orange). The vertical black lines denote the respective *wave ceilings* at which $c_{gz} \to 0$. The ray with $\boldsymbol{k}_{\perp 0}$ aligned with $\bar{\boldsymbol{B}}$ (i.e. $\phi_{k0} = \pi/2$) is shown in each case.

comparable to the core radius with relative impunity, and this is indeed seen to be the case for most of rays in figure 4.3.1, particularly those which remain reasonably fast, on-axis waves because they were launched at $z = 0.5L$. If ℓ_η becomes significantly less than L, however, the wave packets will dissipate energy faster than they propagate it over the large scales; we can see from figure 4.3.1 that this is only the case in the immediate vicinity of the wave ceiling. This occurs for two reasons: first, the increasing wavevector magnitude k towards the ceiling (owing to the constancy of $\boldsymbol{k}_{\perp 0}$ and ever-increasing angle of $\boldsymbol{k}$ from the horizontal) reduces the timescale τ_η; second, the dramatic reduction in group velocity (see figure 4.2.3) as the waves tend to the magnetostrophic limit means wave packets are not going as quickly, so dissipation per unit length along the ray increases.

Hence, wave packets which encounter the wave ceiling are likely not only to be seriously arrested by their transition to the magnetostrophic branch of the dispersion relation, but also heavily dissipated as they reach it, owing to their very small wavelengths and ponderous propagation speeds.

4.3.2 Ray tracing in a sinusoidal horizontal field

As mentioned therein, the use in section 4.2.4 of an ambient magnetic field which is linear in z is rather unphysical, as it carries on increasing all the way to our fictitious core-mantle boundary at $z = 2L$. Instead, we would prefer a $\bar{B}_y(z)$ which drops back to zero at this point, as the mean azimuthal magnetic field must do in Earth's outer core (assuming an insulating mantle). Perhaps the simplest such field would be sinusoidal,

$$\bar{\boldsymbol{B}}(z) = B^* \sin\left(\frac{\pi z}{2L}\right) \boldsymbol{e}_y, \tag{4.3.2}$$

which is much the same as the linear field for $|z| \leq L$, but falls away for $|z| > L$, with both having the value B^* at $z = L$ (see figure 4.1.1). The mechanics of ray tracing through this background state are much the same as the linear field – i.e. we integrate (A3.2.4) and (A3.2.6) with respect to z – though the interpretation is slightly different, since the horizontal axis of the dispersion relation diagram of figure 4.2.4 is no longer commensurate with axial distance — ϖ_B/ϖ_0 may fall as z increases due to the reducing mean field strength.

The effect is that rays may speed up as well as slow down as they propagate; in general, a strengthening of $\bar{B}_y$ implies a reduction in $\boldsymbol{c}_g$, and vice versa. This can be seen in figure 4.3.2, which may be compared with the linear-field equivalent in figure 4.2.2. Consider the central pane, which shows rays launched at $z_0 = 0.1L$. Initially, their trajectories are familiar from section 4.2.4, bending out along field lines and slowing considerably. This continues as long as the ambient field is increasing, i.e. up to $z \sim L$. Above the peak mean field value, the process is the opposite — rays speed up and bend back toward the rotation axis, though they are no longer as focussed as the were at launch because rays with different values of ϕ_{k0} have taken subtly different paths.

If the rays are launched further from the equator (left-hand pane of figure 4.3.2) they stay well-focussed and do not deviate very far from the axis at all, because the magnitude of the mean field is never very different from its value at launch. The waves remain potent reinforcers of axially-elongated structures despite the best efforts of the mean magnetic field.

If the rays are launched closer to the equator (right-hand pane of figure 4.3.2), they may be trapped beneath the wave ceiling, as for the linear-field case, or they may not, depending on the precise values of z_0 and ϕ_{k0}. Any ray which makes it beyond $|z| = L$ is no longer at risk of hitting the ceiling, since the ambient field decreases thereafter. However, if the ceiling is reached below $|z| = L$, the ray asymptotes along it as before. In figure 4.3.2, rays of both fates can be observed; the turning point in $\bar{B}_y$ at $z = |L|$ segregates the ensemble of rays, allowing some to pass through, but trapping others. One can predict which wave will be

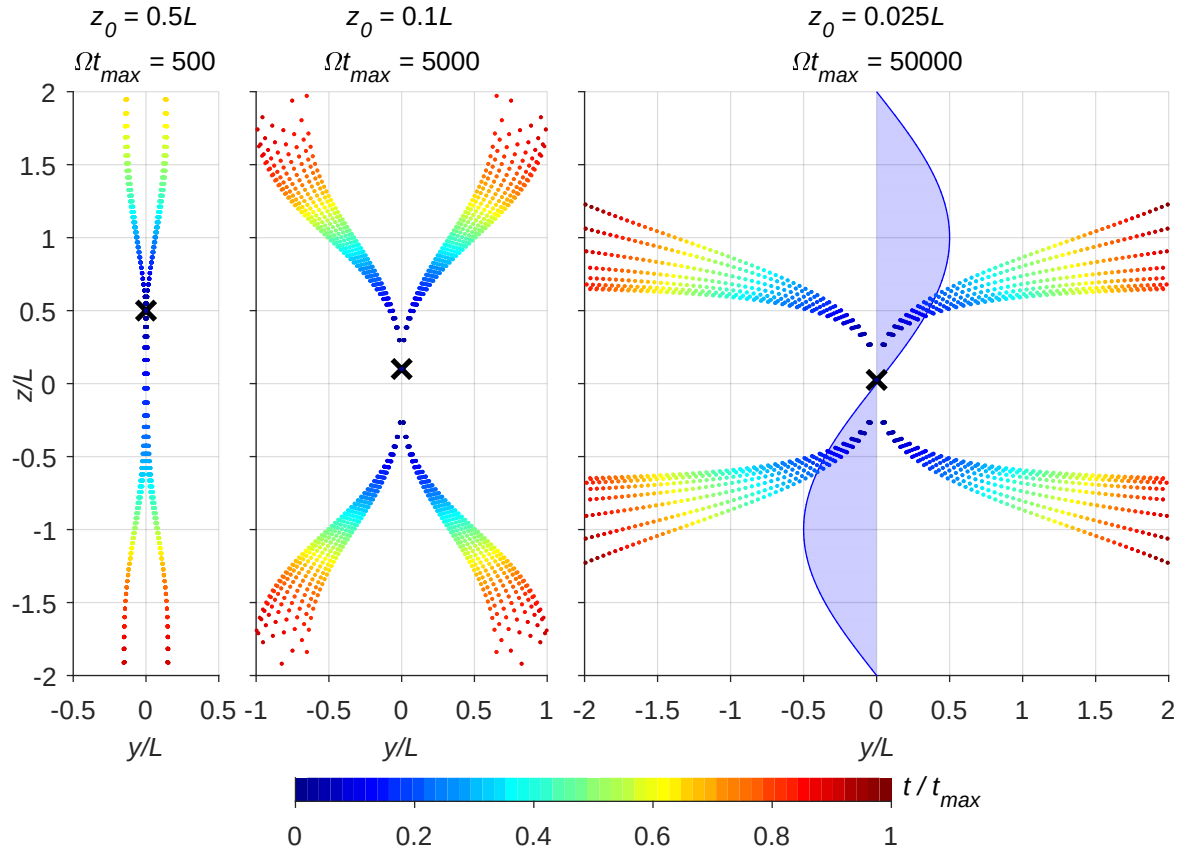

Fig. 4.3.2 As figure 4.2.2, except the ambient magnetic field is now sinusoidal as indicated in the right-hand pane. Note $t_{\max}$ is also marginally lower.

trapped using (4.2.21); the ray which reaches the ceiling at the maximum value of $\bar{B}(y)$ (i.e. B^*) will mark the transition. Letting $\bar{B}_y(z_c) = B^*$ in (4.2.21), with $\varpi_0 = \varpi_B(z_0)$, we get

$$\bar{B}_y(z_0) \approx \frac{(B^*)^2 k_{\perp 0} \sin\phi_{k0}}{2\Omega\sqrt{\rho\mu}}, \tag{4.3.3a}$$

$$\frac{z_0}{L} \approx \frac{B^* k_{\perp 0} \sin\phi_{k0}}{\pi\Omega\sqrt{\rho\mu}}, \tag{4.3.3b}$$

wherein we have used $\bar{B}_y(z_0) = B^* \sin\left(\frac{\pi z_0}{2L}\right) \approx \pi B^* z_0/2L$ for $z_0 \ll L$ (i.e. sources close to the equatorial plane). For the present parameters, the condition for trapping becomes $z_0 \lesssim 0.03L \sim 30$km, suggesting the wave ceiling only manifests itself for waves launched very close to the equator.

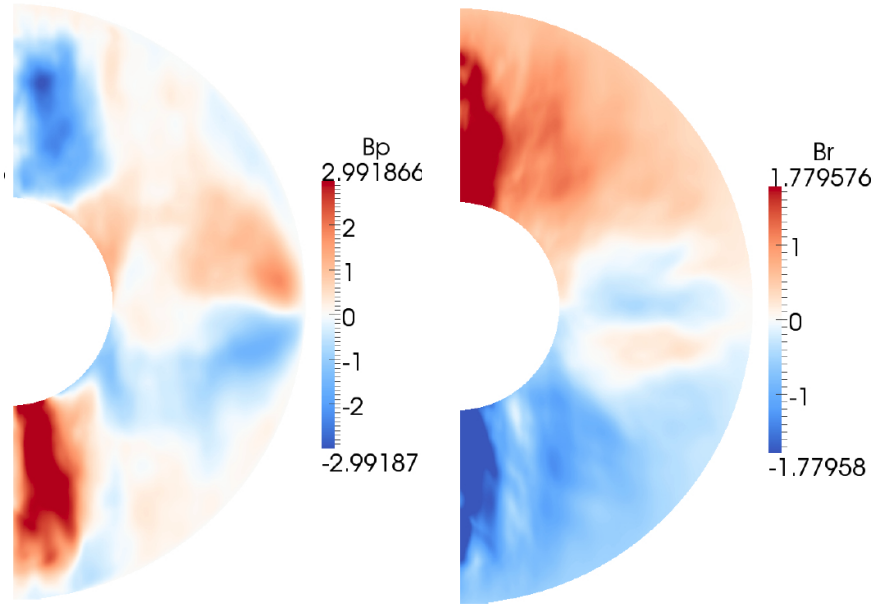

(a) B_ϕ **(b)** B_r

Fig. 4.3.3 Azimuthally-averaged azimuthal and radial magnetic fields from Sheyko (2014).

4.3.3 Ray tracing in a general perpendicular field

Quite clearly, the mean magnetic field within Earth's core will possess more than just one component – in this section and the next, we discuss the effect of including components other than $\bar{B}_y$ in the ray tracing analysis. First, we approach the problem of a general perpendicular field; that is to say, we constrain $\bar{\boldsymbol{B}}(z)$ to the horizontal plane, but let both its magnitude and direction vary with the axial co-ordinate, rather than just magnitude as in section 4.2. The mechanics of ray tracing are fundamentally unchanged by this extension — since we still have $\bar{\boldsymbol{B}} \cdot \boldsymbol{k} = \bar{\boldsymbol{B}}_\perp(z) \cdot \boldsymbol{k}_\perp$, the dispersion relation (4.2.14b) is still an explicit equation for θ_k as a function of z, which can be substituted into the group velocity (now with an extra term) and integrated along the ray.

It remains to choose a geophysically meaningful form for $\bar{\boldsymbol{B}}_\perp(z)$. Consider figure 4.3.3, which shows the azimuthally-averaged azimuthal and radial magnetic fields in a numerical dynamo simulation from Sheyko (2014), which may be considered typical. Recall that our Cartesian x, y and z axes are locally representing the radially outward, azimuthally eastward and axially northward directions in the vicinity of the equatorial plane respectively, so $\bar{B}_y = B^* \sin(\pi z/2L)$ (say) represents an azimuthal field which is positive in the northern hemisphere and negative in the south, dropping to zero at the equator and $z = \pm 2L$; this is broadly the behaviour seen in figure 4.3.3a. The radial field in figure 4.3.3b is analogous to $\bar{B}_x$ in our model problem. It too is antisymmetric about the equator, though is somewhat

weaker than the azimuthal field and exhibits an extra sign change around the equatorial regions. To imitate this behaviour, we take in our model problem the background field

$$\bar{B}_y = B^* \sin\left(\frac{\pi z}{2L}\right), \qquad \bar{B}_x = -0.2B^* \sin\left(\frac{\pi z}{L}\right), \tag{4.3.4}$$

as plotted in the upper-right pane of figure 4.3.4; note that the period of $\bar{B}_x$ is half that of $\bar{B}_y$. The launch locations, $z_0 = 0.025/0.1/0.5$, are the same as ever, so we may compare with the sinusoidal-$\bar{B}_y$ results of section 4.3.2. This is done in figure 4.3.4; the three left-hand panes are the same cases as figure 4.3.2, though now rendered in 3D, whereas the three on the right include an x-component in the ambient magnetic field as well.

At a cursory inspection, the results are similar between the two cases — the dominant quartet of ray tubes follow broadly the same paths at comparable speeds, regardless of the mean field configuration or launch location. However, owing to the fact that the mean field orientation as well as magnitude may now change, it becomes possible for certain wave packets to become weakly-modified inertial waves because $\varpi_B = \bar{\boldsymbol{B}}(z) \cdot \boldsymbol{k}_{\perp 0}/\sqrt{\rho\mu}$ has dropped to zero despite $\bar{\boldsymbol{B}}(z)$ being finite, and therefore these packets rapidly accelerate through regions where this happens. Conversely, wave packets may find themselves in a much stronger 'effective field' if they are launched with $\boldsymbol{k}_\perp$ almost perpendicular to $\bar{\boldsymbol{B}}$ but propagate into a region where the two become more closely aligned; in this case, the packet is forced to slow down and may even encounter the wave ceiling.

The addition of an x-directed mean field therefore adds complexity to the problem, introducing a degree of defocussing through the effects mentioned above, but also introducing a greater scope for rays to be both trapped by the wave ceiling, or to propagate rapidly on-axis — even though the majority of ray paths remain approximately the same.

4.3.4 Ray tracing with an axial field

Our final modification to the basic ray tracing problem of section 4.2 is to include an axial field $\bar{B}_z$ as well as the now-traditional horizontal field $\bar{\boldsymbol{B}}_\perp$. As well as producing some interesting results, this has obvious application to the Earth's core, which has a measurable volume-averaged mean axial field of 3.7G (Jackson, 1998; Davidson, 2013).

For simplicity, we return to a mean perpendicular field which is a linear function of z, and in one direction only, i.e. $\bar{\boldsymbol{B}}_\perp = (B^* z/L)\,\boldsymbol{e}_y$ exactly as in section 4.2.2. The axial field must consequently be independent of z, and we take it to be a positive constant one-tenth of the value of the characteristic perpendicular field, $\bar{B}_z = 0.1B^*$. (This is in line with the estimate $B^* \sim 40$G.)

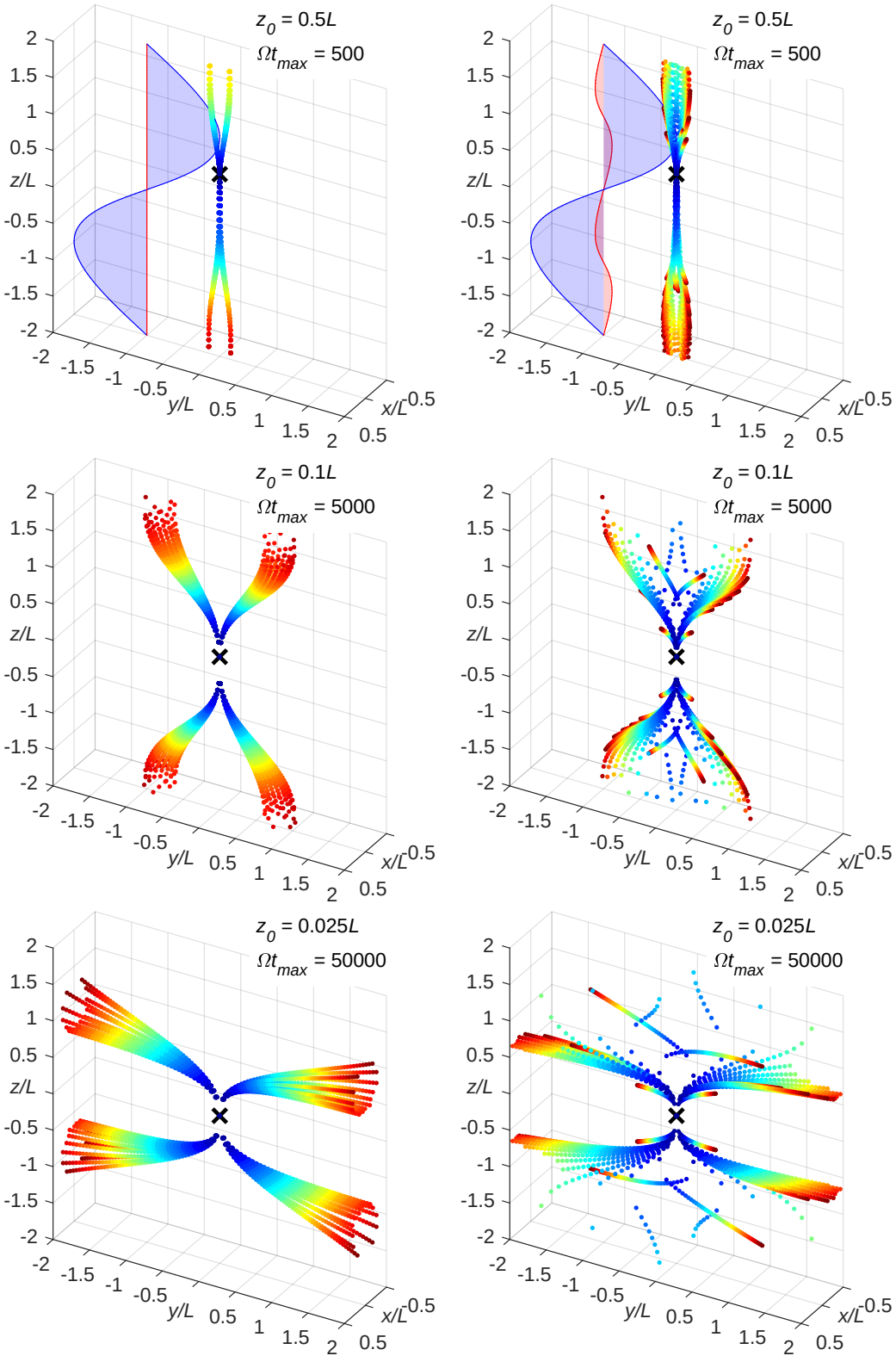

Fig. 4.3.4 Ray tracing in a perpendicular mean magnetic field which changes direction as well as magnitude with z. The mean y-field, indicated in the top row in blue, is $\bar{B}_y = B^* \sin\left(\frac{\pi z}{2L}\right)$. The right-hand column also features a mean x-field $\bar{B}_x = -0.2B^* \sin\left(\frac{\pi z}{L}\right)$, indicated in red. Each row has a different launch location and $t_{\max}$.

The mechanics of ray tracing are somewhat different in this case; the dispersion relation (4.2.14a) now reads

$$\frac{2\Omega}{\omega_0}\cos\theta_k = \pm\left(1 - \frac{1}{\rho\mu}\left[\frac{\bar{B}_y(z)k_{y0} + \bar{B}_z k_z}{\omega_0}\right]^2\right), \tag{4.3.5}$$

which is no longer an explicit equation for θ_k as a function of z because it also appears on the right-hand side through $k_z(= k_{\perp 0}\cot\theta_k)$ — note that $\boldsymbol{k}_{\perp 0}$ is still conserved as (4.2.11a) holds. Instead of substituting $\theta_k(z)$ into the axial group velocity expression (see (A3.2.4)), we are therefore forced to return to the equations (4.2.6) and (4.2.9) which define the ray. Their axial components read

$$\frac{\mathrm{d}z}{\mathrm{d}t} = \frac{\partial\omega}{\partial k_z}, \tag{4.3.6a}$$

$$\frac{\mathrm{d}k_z}{\mathrm{d}t} = -\frac{\partial\omega}{\partial z}. \tag{4.3.6b}$$

We already have $\partial\omega/\partial k_z = c_{g,z}$, the axial group velocity, as a function of θ_k from equation (A3.2.3):

$$\frac{\mathrm{d}z}{\mathrm{d}t} = \left(1 + \frac{\omega_B^2}{\omega_0^2}\right)^{-1}\left[2\frac{\omega_B}{\omega_0}\frac{\bar{B}_z}{\sqrt{\rho\mu}} \pm \frac{2\Omega}{k_{\perp 0}}\sin^3\theta_k\right]. \tag{4.3.7}$$

Furthermore, we can use (4.3.6b) to account for the evolution of θ_k:

$$\frac{\mathrm{d}\theta_k}{\mathrm{d}t} = \frac{\partial\theta_k}{\partial k_z}\frac{\mathrm{d}k_z}{\mathrm{d}t} = \left(-\frac{\sin^2\theta_k}{k_{\perp 0}}\right)\cdot\left(-\frac{\partial\omega}{\partial z}\right) \tag{4.3.8a}$$

$$= \frac{2\omega_B}{\omega_0}\sin^2\theta_k\left(1 + \frac{\omega_B^2}{\omega_0^2}\right)^{-1}\boldsymbol{e}_{k_{\perp 0}}\cdot\frac{\partial\bar{\boldsymbol{B}}_\perp/\sqrt{\rho\mu}}{\partial z}. \tag{4.3.8b}$$

Equations (4.3.7) and (4.3.8b) therefore supply an ODE for the ray of the form $\frac{\mathrm{d}}{\mathrm{d}t}[z,\theta_k] = f^{\underline{n}}(z,\theta_k)$ which may be easily integrated numerically. What then remains is to calculate the perpendicular displacement of the ray path, given by integrating the relevant components of the group velocity (A3.2.3) with respect to time, employing the already-calculated $\theta_k(t)$.

The addition of an axial magnetic field introduces new possibilities for the ray paths; in particular, they are no long restricted to propagating solely upwards or downwards — rather, the rays may bend back upon themselves in cases where the Alfvén-wave component of the axial group velocity (4.3.7) comes to outweigh the inertial-wave component. Figure 4.3.5 shows the result of ray tracing in the presence of an axial field, as described above, with the launch location being the closest to the equatorial plane, $z_0 = 0.025L$. This may be compared with the right-hand pane of figure 4.2.2 for which $\bar{B}_z = 0$, though the end time does vary by a

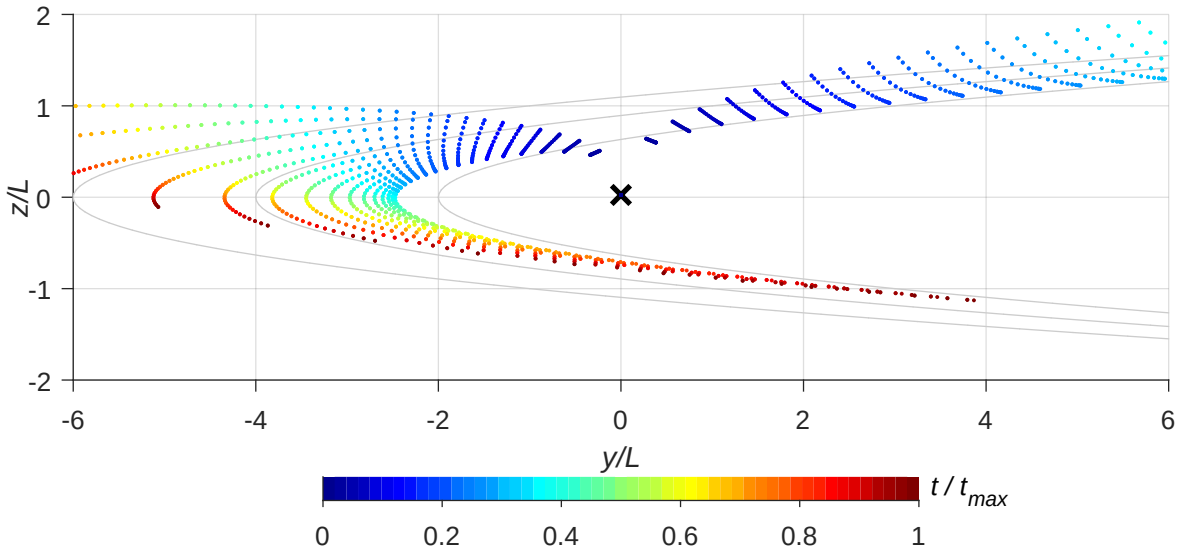

Fig. 4.3.5 Ray tracing with the addition of a constant axial mean field $\bar{B}_z = 0.1B^*$. The horizontal field is $\bar{\boldsymbol{B}}_\perp = (B^* z/L)\,\boldsymbol{e}_y$ with $Le^* = 5\times10^{-4}$. The rays are launched as inertial-Alfvén waves at $z_0 = 0.025L$, indicated by ×. Ray locations are plotted at 50 equispaced time intervals, coloured by $t/t_{\max}$, with $\Omega t_{\max} = 5\times10^5$. Light grey curves show ambient magnetic field lines. Only initially northward-propagating waves are shown.

factor of about seven. For clarity, only those rays which are initially northward-propagating are shown.

Clearly, the behaviour of the wave ceiling has been modified by this alteration. Those rays which head to the right now asymptote along a slightly oblique – rather than perfectly horizontal – ceiling, being tilted upward slightly by the Alfvén contribution to the group velocity from $\bar{B}_z$. Those which head to the left are tilted downward by the same effect, to such an extent that they eventually reverse direction entirely, plunging southward back through the equatorial plane. This phenomenon is best understood by noting that a ray approaches a wave ceiling not necessarily at a particular height, but rather along a particular magnetic field line. For the chosen background field, the field lines are contours satisfying

$$\bar{A}(\boldsymbol{r}) = \frac{B^* z^2}{2L} - \bar{B}_z y = const. \tag{4.3.9}$$

where $\bar{\boldsymbol{B}} = \nabla\times\left(\bar{A}\boldsymbol{e}_x\right)$. A few of these parabolae are plotted in light grey on figure 4.3.5 and clearly correspond to the wave ceiling both above and below the equatorial plane. This suggests that magnetostrophic waves are most likely to be found in the regime in which their group velocity is closely aligned with the ambient magnetic field, which may itself be at any angle to the rotation axis.

Note, however, that the discussion of wave dissipation in section 4.3.1 still applies to these solutions — as they approach the wave ceiling, they are likely to be vulnerable to intense Ohmic dissipation as k_z becomes very large, and therefore the wavelength $\lambda = 2\pi/k$ very small. Furthermore, they are incredibly slow – figure 4.3.5 is plotted at $\Omega t_{\max} = 5 \times 10^5$, or $t_{\max} \approx 218$yr – which both reduces the dissipation lengthscale and infringes upon the assumptions underlying this investigation; in particular, the ambient magnetic field is unlikely to be steady over such centennial timescales (Yukutake, 1979; Jackson et al., 2000). This phenomenon should therefore be considered more an interesting consequence of the present analytical formulation rather than a profound result in geodynamo theory. It does, however, hint at a mechanism by which wave energy, and therefore the energy of the turbulent convective driving, may be contained within the equatorial regions. Wave packets launched on-axis in areas of very low magnetic field strength close to the equator may propagate with a relatively tight radius of curvature as the magnitude of $\bar{\boldsymbol{B}}$ increases, turning back on themselves and returning their energy to the region $z \approx 0$, though they will of course be dissipating energy through Ohmic heating the entire time. One might speculate that this trapping of radiated energy at low latitudes could play some part in creating the equatorial jet observed in figure 2.1.1a.

4.4 WKB analysis

A closer inspection of the above work reveals a subtle deficiency of the ray tracing analysis which it is necessary to address, one which has intriguing consequences for the propagation of MC waves through a non-uniform magnetic field. The issue is this: most wave packets, whether they started life as inertial-Alfvén waves or not, are at some point required to propagate through a location at which their frequency is equal to the local Alfvén frequency (i.e. they are themselves inertial-Alfvén waves). This is a problem because it requires the vertical component of the wavevector to go to zero ($k_z \to 0$), and therefore the vertical wavelength is momentarily demanded to be infinite, so the condition for validity of ray-tracing ($\mathrm{d}\lambda_z/\mathrm{d}z \ll 1$) is violated. This difficulty is remedied by a local analysis around the dangerous point, which is shown to fuse to an approximate Wentzel-Kramers-Brillouin(-Jeffreys) (WKB(J)) solution, which may be considered analogous to the ray-tracing result, in the bulk of the domain (Lighthill, 1978).

4.4.1 Application of WKB analysis to hybrid magnetic-Coriolis waves

The analysis begins with the hybrid wave equation in an inhomogeneous magnetic field, (4.2.2), with a mean magnetic field which is horizontal ($\bar{B}_z = 0$):

$$\left[\frac{\partial^2}{\partial t^2} - \frac{1}{\rho\mu}\left(\bar{\boldsymbol{B}}_\perp(z)\cdot\nabla\right)^2\right]^2 \nabla^2\boldsymbol{u} + (2\boldsymbol{\Omega}\cdot\nabla)^2\frac{\partial^2\boldsymbol{u}}{\partial t^2} = 0. \tag{4.4.1}$$

Instead of seeking solutions which are locally plane waves as per (2.2.9), which would lead us down the ray-tracing route followed extensively above, we keep the z-dependence of the solution free. That is to say, if $u(\boldsymbol{r},t)$ represents any one component of $\boldsymbol{u}(\boldsymbol{r},t)$, we let

$$u(\boldsymbol{r},t) = \mathbb{R}\left\{\tilde{u}(z)\exp\left(i\left[\boldsymbol{k}_\perp\cdot\boldsymbol{r}_\perp - \varpi t\right]\right)\right\} \tag{4.4.2}$$

for some undetermined function $\tilde{u}(z)$. As previously, ϖ is the wave frequency and $\boldsymbol{k}_\perp = [k_x, k_y, 0]$ the horizontal wavenumber vector (its magnitude being $k_\perp$). Substituting (4.4.2) into (4.4.1) produces an inhomogeneous modal equation,

$$\tilde{u}'' + k_\perp^2\, a(z)\,\tilde{u} = 0 \tag{4.4.3}$$

where

$$a(z) = \left[\left(\frac{2\Omega\varpi}{\varpi_B^2(z) - \varpi^2}\right)^2 - 1\right]^{-1}. \tag{4.4.4}$$

As before, $\varpi_B(z) = \bar{\boldsymbol{B}}_\perp(z)\cdot\boldsymbol{k}_\perp/\sqrt{\rho\mu}$. The solutions to (4.4.3) are characterised by the sign of $a(z)$; if it is positive, they will be oscillatory, whereas if it is negative they will exponentially growing and decaying. We will therefore be most interested in the 'wave-bearing' regions in which $a(z) \geq 0$. Furthermore, if the variations in $a(z)$ are gradual compared to those in $\tilde{u}$, it is reasonable to consider the solution to be locally sinusoidal, with gradual changes in amplitude and phase with z due to the spatial dependence of $a(z)$. In this regime, the solution is well-approximated by the WKB solution

$$\tilde{u} \approx C\,|a(z)|^{-\frac{1}{4}}\, e^{i\Phi(z)} + D\,|a(z)|^{-\frac{1}{4}}\, e^{-i\Phi(z)} \tag{4.4.5}$$

as can be found in, for example, Bender & Orszag (1999). Here C and D are arbitrary complex constants, corresponding to waves travelling in the positive and negative z-directions respectively. The phase $\Phi(z)$ is given by an integration in z

$$\Phi(z) = k_\perp \int_{z_d}^{z} |a(\check{z})|^{\frac{1}{2}}\,\mathrm{d}\check{z} \tag{4.4.6}$$

from some arbitrary datum height z_d. As mentioned above, we expect this approximate solution to work very well (with errors of the order $\left(a'/a\right)^2$ or a''/a (Lighthill, 1978)) when $a(z)$ is both positive and varies gradually with height z. Inspecting (4.4.4) carefully, it can be seen there are in fact two possible situations in which these conditions may be violated, which correspond to two particular features of hybrid MC waves which are now well-known to us.

1. The first situation is what we term a *turning point zero* of $a(z)$. As the name suggests, it is a point z_c at which both $a(z_c)$ and $a'(z_c)$ are zero; this occurs whenever $\varpi_B^2(z_c) = \varpi^2$, i.e. the frequency of the solution is matched by the local Alfvén frequency. We have $a(z) > 0$ (and therefore oscillatory solutions) both sides of z_c, but at the critical point itself a''/a becomes infinite — and therefore so too does the error in the WKB approximation. From a ray-tracing perspective, this point corresponds to that at which the wave packets are inertial-Alfvén waves.

2. The second situation occurs wherever $a(z)$ has a simple pole, i.e. $a(z) \sim (z - z_c)^{-1}$; this occurs at a location z_c such that $\left(\varpi_B^2(z_c) - \varpi^2\right)^2 = (2\Omega\varpi)^2$. We have $a(z) > 0$ (and therefore oscillatory solutions) one side of the pole and $a(z) < 0$ (exponential solutions) the other, with $z = z_c$ being an asymptote. We have $\left|a'/a\right| \to \infty$ at the critical level, and therefore the WKB approximation breaks down. This corresponds to the wave ceiling discovered in the ray tracing above.

In order to heal the WKB solution near to these critical points, one must employ the method of *matched asymptotic expansions* (Hinch, 1991). That is to say, we are required to find a special 'inner' solution to (4.4.3) which applies exclusively in the neighbourhood of a given critical point z_c, then stitch it to the 'outer' WKB solution (4.4.5) by demanding that the limiting form of the outer solution as it gets very close to z_c is identical to what one would find when taking the inner solution out to infinity towards it. Below, we perform this procedure for the turning point zero, showing that the presence of this critical point opens up the interesting possibility of partial reflection of wave energy there.

4.4.2 Matching at a turning point zero

We now perform asymptotic matching across a critical point z_c at which $a(z_c) = a'(z_c) = 0$, our so-called *turning point zero*; this occurs wherever the local Alfvén frequency of the solution matches that of the travelling wave's, i.e. $\varpi_B^2(z_c) = \varpi^2$. Our plan of attack is as follows: we first seek an inner solution to (4.4.3) which is valid only in the locality of the turning point. We then find the limiting form of this solution as z gets far away from z_c in

both directions — since $a(z)$ is positive in both regions, both limiting forms will be oscillatory. Each of these is then asymptotically matched to its own WKB solution of the form (4.4.5), which constitute approximate solutions to the full ODE (4.4.3) when a'/a is small.

Inner solution

When $z \approx z_c$, we may find a local solution to (4.4.3) by expanding the function $a(z)$ as a Taylor series about the critical point:

$$a(z) \approx a(z_c) + (z - z_c)a'(z_c) + \frac{1}{2}(z - z_c)^2 a''(z_c) + \cdots \tag{4.4.7}$$

Now, at the critical point both $a(z_c)$ and $a'(z_c)$ are zero, so the approximation of $a(z)$ must make use of the quadratic term (assuming $\tilde{\boldsymbol{B}}'_\perp(z_c) \neq 0$). We have

$$\frac{1}{2}a''(z_c) = \left(\frac{1}{2\Omega\varpi}\left.\frac{\mathrm{d}\varpi_B^2}{\mathrm{d}z}\right|_{z_c}\right)^2 = \left(\frac{\varpi'_B(z_c)}{\Omega}\right)^2 > 0, \tag{4.4.8}$$

so near to z_c, the governing ODE (4.4.3) for the inner solution $\tilde{u}_{\mathrm{in}}(z)$ becomes

$$\tilde{u}''_{\mathrm{in}} + \frac{1}{2}k_\perp^2 a''(z_c)(z - z_c)^2 \tilde{u}_{\mathrm{in}} \approx 0. \tag{4.4.9}$$

If we introduce the shorthand $\kappa^2 = \frac{1}{2}k_\perp^2 a''(z_c)$, this has the general solution

$$\tilde{u}_{\mathrm{in}}(z) \approx \sqrt{\tfrac{\pi k_\perp}{2}}\,|z - z_c|^{\frac{1}{2}}\left[\gamma J_{\frac{1}{4}}\left(\frac{1}{2}\kappa(z - z_c)^2\right)\mathrm{sgn}(z - z_c) + \delta J_{-\frac{1}{4}}\left(\frac{1}{2}\kappa(z - z_c)^2\right)\right], \tag{4.4.10}$$

where $J_{\pm\frac{1}{4}}$ are Bessel functions of the first kind and $\mathrm{sgn}(\cdot)$ is the signum function, with γ and δ two arbitrary constants. We are interested in the form of this inner solution as the axial co-ordinate gets very far from z_c in one direction or another; this can be shown to be

$$\begin{aligned}\tilde{u}_{\mathrm{in}}(z - z_c \to \pm\infty) \approx \sqrt{\frac{k_\perp}{\kappa|z - z_c|}}\Big[&\tfrac{1}{\sqrt{2}}\left(\gamma e^{-i\frac{\pi}{8} \pm i\frac{\pi}{2}} + \delta e^{i\frac{\pi}{8}}\right)e^{-\frac{1}{2}i\kappa(z - z_c)^2} \\ &+ \tfrac{1}{\sqrt{2}}\left(\gamma e^{i\frac{\pi}{8} \mp i\frac{\pi}{2}} + \delta e^{-i\frac{\pi}{8}}\right)e^{\frac{1}{2}i\kappa(z - z_c)^2}\Big].\end{aligned} \tag{4.4.11}$$

Outer solution near the critical level

We now turn out attention to the outer WKB solution, aiming to find its asymptotic form as it approaches the critical level z_c. Take two distinct WKB solutions: $\tilde{u}_-$ which applies below the critical level ($z < z_c$) and $\tilde{u}_+$ which applies above it ($z > z_c$). These each have the form of

(4.4.5):

$$\tilde{u}_\pm(z) = C_\pm |a(z)|^{-\frac{1}{4}} e^{i\Phi(z)} + D_\pm |a(z)|^{-\frac{1}{4}} e^{-i\Phi(z)}. \tag{4.4.12}$$

Note that the integration for $\Phi(z)$ (equation 4.4.6) is from the same datum z_d for both solutions. The objective of the asymptotic matching procedure is to find connection formulae for C_+ and D_+ as functions of C_- and D_-. The next step towards this ambition is to find the asymptotic form of (4.4.12) as $z \to z_c$; for this, we require

$$\Phi(z \approx z_c) = k_\perp \int_{z_d}^{z_c} |a(\check{z})|^{\frac{1}{2}} \,\mathrm{d}\check{z} + k_\perp \int_{z_c}^{z} |a(\check{z})|^{\frac{1}{2}} \,\mathrm{d}\check{z}, \tag{4.4.13a}$$

$$\approx \Phi(z_c) + k_\perp \int_{z_c}^{z} \left| \frac{1}{2} a''(z_c)(\check{z} - z_c)^2 \right|^{\frac{1}{2}} \mathrm{d}\check{z}, \tag{4.4.13b}$$

$$\approx \Phi(z_c) + \frac{1}{2}\kappa(z - z_c)^2 \mathrm{sgn}(z - z_c). \tag{4.4.13c}$$

This again makes use of (4.4.7) in approximating the integrand. The WKB solutions (4.4.12) therefore take the form

$$\tilde{u}_\pm(z \approx z_c) \approx \sqrt{\frac{k_\perp}{\kappa |z - z_c|}} \left[C_\pm e^{i\Phi(z_c) \pm \frac{1}{2} i\kappa (z - z_c)^2} + D_\pm e^{-i\Phi(z_c) \mp \frac{1}{2} i\kappa (z - z_c)^2} \right] \tag{4.4.14}$$

as they approach the critical level.

Asymptotic matching

We are now in a position to blend the inner and outer solutions in order to circumvent the critical level; that is, we set the limiting form of the WKB solution as it approaches z_c, (4.4.14), equal to the inner solution as it vacates it, (4.4.11). Thus,

$$C_\pm e^{i\Phi(z_c)} = \frac{1}{\sqrt{2}} \left(\gamma e^{-i\frac{\pi}{2} \pm i\frac{\pi}{8}} + \delta e^{\mp i\frac{\pi}{8}} \right), \tag{4.4.15a}$$

$$D_\pm e^{-i\Phi(z_c)} = \frac{1}{\sqrt{2}} \left(\gamma e^{i\frac{\pi}{2} \mp i\frac{\pi}{8}} + \delta e^{\pm i\frac{\pi}{8}} \right). \tag{4.4.15b}$$

Or, inverting for the coefficients of the inner solution,

$$\gamma = C_\pm e^{i\left(\Phi(z_c) + \frac{\pi}{2} \pm \frac{\pi}{8}\right)} + D_\pm e^{-i\left(\Phi(z_c) + \frac{\pi}{2} \pm \frac{\pi}{8}\right)}, \tag{4.4.16a}$$

$$\delta = C_\pm e^{i\left(\Phi(z_c) \mp \frac{\pi}{8}\right)} + D_\pm e^{-i\left(\Phi(z_c) \mp \frac{\pi}{8}\right)}. \tag{4.4.16b}$$

The corresponding matching equation is, in matrix form,

$$\begin{pmatrix} C_{\pm}e^{i\Phi(z_c)} \\ D_{\pm}e^{-i\Phi(z_c)} \end{pmatrix} = \begin{pmatrix} \sqrt{2} & \mp i \\ \pm i & \sqrt{2} \end{pmatrix} \begin{pmatrix} C_{\mp}e^{i\Phi(z_c)} \\ D_{\mp}e^{-i\Phi(z_c)} \end{pmatrix}. \tag{4.4.17}$$

This equation allows one to calculate the coefficients of the travelling-wave solutions (4.4.5) one side of the critical level given their values at the other, and thereby circumvent the difficulty experienced by the WKB solution at $z = z_c$.

Partial reflection of wave energy

To see that the matching equation (4.4.17) implies a partial reflection of MC waves at the turning point zero, recall that the 'C' coefficients correspond to upwards-propagating waves, and the 'D' coefficients to downwards-propagating waves. Consider the situation in which an incoming wave approaches z_c from below — which is to say, a specified value of C_-. We must apply a *radiation condition* above the critical level, which demands that no waves are generated at $z = +\infty$ and therefore $D_+ = 0$; the wave field above z_c simply comprises the upward-travelling solution corresponding to C_+. Setting $D_+ = 0$ in (4.4.17) gives explicit equations for the transmitted and reflected waves:

$$C_+ = \frac{C_-}{\sqrt{2}}, \qquad D_- = \frac{-iC_-}{\sqrt{2}}e^{2i\Phi(z_c)}. \tag{4.4.18}$$

The corresponding transmission and reflection coefficients (T and R respectively) are

$$T = \frac{|C_+|^2}{|C_-|^2} = \frac{1}{2}, \qquad R = \frac{|D_-|^2}{|C_-|^2} = \frac{1}{2}. \tag{4.4.19}$$

Clearly, half of the wave's energy propagates through the critical level, and half is reflected back.

An example of this matching procedure is plotted in figure 4.4.1; notice how the WKB solution is oscillatory both sides of the turning point, but tends to infinity close to it, indicative of violation of the assumptions of ray tracing theory. The waveform is, however, very quickly picked up by the inner solution which takes it across z_c. Note that the magnitude of this inner solution is larger below z_c, indicating a greater wave energy density (due to partial reflection) there; the solution is therefore a sum of upward- and downward-travelling waves below z_c, but a purely upward-travelling wave above it.

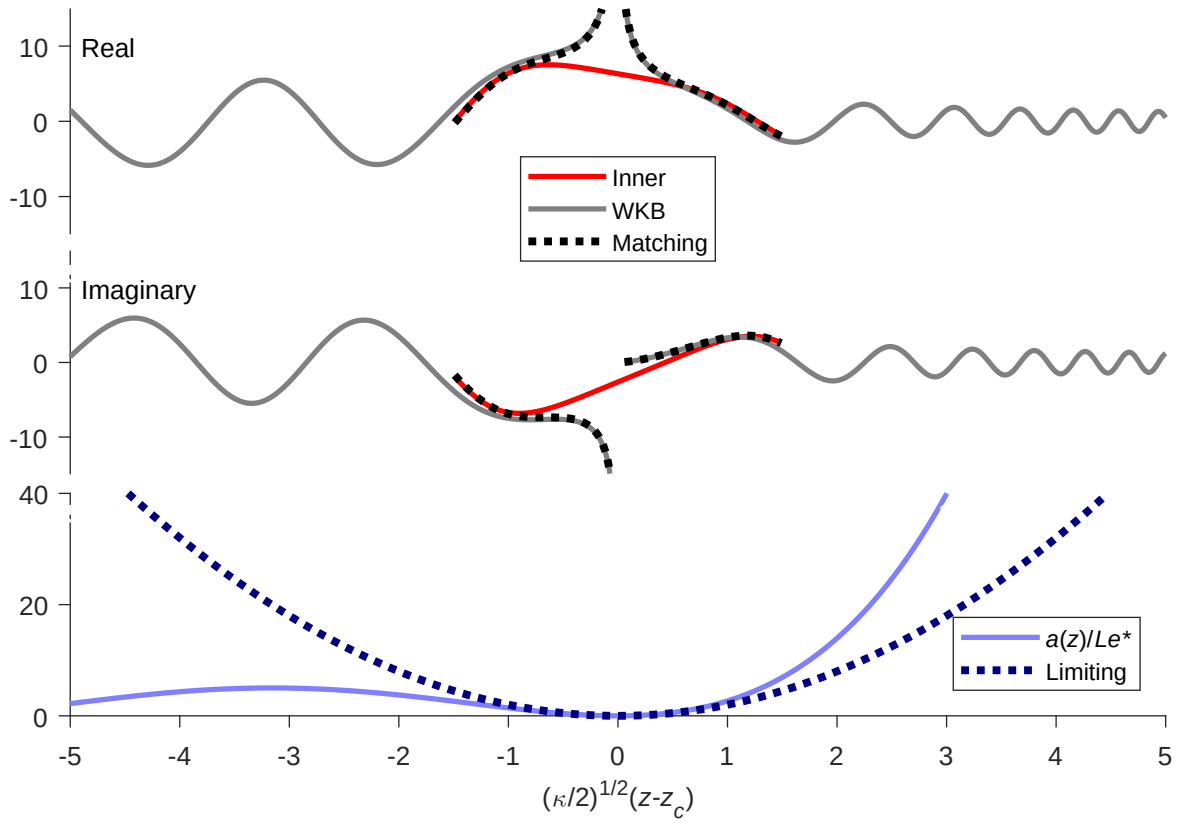

Fig. 4.4.1 Example of asymptotic matching about a turning point zero. The background field is linear in z, $\bar{\boldsymbol{B}}_\perp = (B^* z/L)\boldsymbol{e}_y$ with $Le^* = \left(B^*/\sqrt{\rho\mu}\right)/\Omega L = 5\times10^{-4}$. The frequency is $\varpi = 0.1\Omega$. The incoming wave (from the left) has $C_- = 1$ and we set $z_d = z_c$. The top two panes show the WKB solution in grey, inner solution in red, and asymptotic matching form in dashed black. The bottom pane shows $a(z)$ (solid) and its limiting form near the turning point (dashed). Note the use of inner co-ordinate scaling for z.

Reflection and transmission between two turning points

Throughout this chapter, we have paid great attention to background horizontal magnetic fields which are antisymmetric about the equator. Hence, if a critical point z_c (at which $\varpi^2 = \varpi_B^2(z_c)$) exists for positive z_c ($= z_+$, say), one will necessarily be found at $-z_c$ ($= z_-$) as well. This has two interesting consequences.

Firstly, a wave launched within the 'equatorial region' $z_- < z_0 < z_+$ (i.e. $\varpi^2 > \varpi_B^2(z_0)$) will be partially trapped in that region, with half of its energy bouncing back (and half radiating away) each time it encounters a critical level. This would provide a means by which energy may be retained in the equatorial regions — those waves with frequencies greater than the Alfvén frequency at launch (i.e. the fast roots of the MC dispersion relation) may have some of their energy returned towards the launch height z_0 by a reflection at the critical level

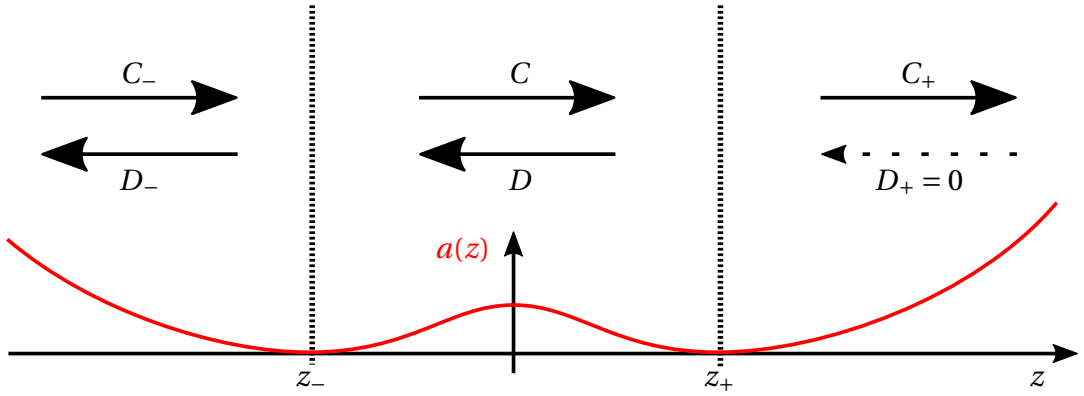

Fig. 4.4.2 Schematic showing the propagation of an incoming wave C_- through two consecutive turning point zeros at $z = z_\pm$.

caused by the matching of their frequency to the Alfvén frequency of the ambient horizontal field. The energy is not retained around the equator forever, since the reflection is only partial, but rather gradually radiates to higher latitudes; a wave which is initially propagating northward, say, will radiate $\frac{2}{3}$ of its energy to the north and $\frac{1}{3}$ south as $t \to \infty$.

A second consequence of having two critical levels concerns waves which are launched with frequencies smaller than the local Alfvén frequency, $\varpi^2 < \varpi_B^2(z_0)$, and therefore originate outside of the 'equatorial region' $[z_-, z_+]$. To fix thoughts, consider a magnetic field distribution which is linear in z, and a northward-propagating incident wave approaching z_- from below. The problem is presented schematically in figure 4.4.2 — our incident wave is given by C_- and the reflected wave by D_- in the region below z_-. Between the critical levels at $z = z_\pm$, waves may exist which travel in either direction (C and D), but above z_+ our radiation condition requires only upward-propagating solutions exist, and hence C_+ is finite but D_+ must vanish.

To approach this problem, first apply (4.4.18) at the upper critical level z_+,

$$C_+ = \frac{C}{\sqrt{2}}, \qquad D = \frac{-iC}{\sqrt{2}} e^{2i\Phi(z_+)}, \tag{4.4.20}$$

then the complete matching equation (4.4.17) at the lower critical level z_-,

$$C = \frac{\sqrt{2}C_-}{2 + \exp\{2i\,(\Phi(z_+) - \Phi(z_-))\}}, \qquad D_- = -iC\left(e^{2i\Phi(z_+)} + e^{2i\Phi(z_-)}\right). \tag{4.4.21}$$

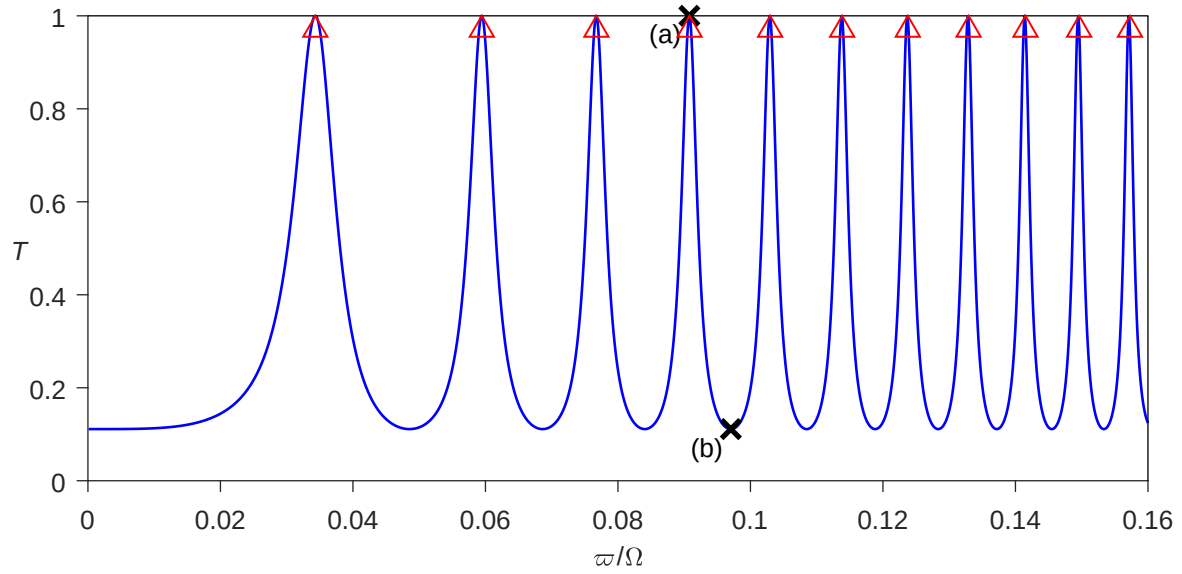

Fig. 4.4.3 The transmission coefficient T as a function of frequency for the propagation of WKB-type solutions through two consecutive turning point zeros. We have $\bar{\boldsymbol{B}}_\perp = (B^* z/L)\,\boldsymbol{e}_y$ with $Le^* = \left(B^*/\sqrt{\rho\mu}\right)/\Omega L = 5\times 10^{-4}$. Red triangles show approximate perfect transmission frequencies as per (4.4.26). The points (a) and (b) correspond to figure 4.4.4.

The net transmission and reflection relationships are hence given by the combination of these two:

$$\frac{C_+}{C_-} = \frac{1}{2+\exp\{2i\,(\Phi(z_+)-\Phi(z_-))\}}, \qquad \frac{D_-}{C_-} = \frac{-i\sqrt{2}\left(e^{2i\Phi(z_+)}+e^{2i\Phi(z_-)}\right)}{2+\exp\{2i\,(\Phi(z_+)-\Phi(z_-))\}}. \tag{4.4.22}$$

In terms of fluxes of energy, we have coefficients of transmission T and reflection R given by

$$T = \frac{|C_+|^2}{|C_-|^2} = \frac{1}{5+4\cos(2\Delta\Phi)}, \qquad R = \frac{|D_-|^2}{|C_-|^2} = 1-T, \tag{4.4.23}$$

where

$$\Delta\Phi = \Phi_+ - \Phi_- = k_\perp \int_{z_-}^{z_+} |a(\check{z})|^{\frac{1}{2}}\,\mathrm{d}\check{z}. \tag{4.4.24}$$

Note how the transmission coefficient is no longer a simple factor of $\frac{1}{2}$, but rather a function which depends upon the perpendicular wavevector, background magnetic field distribution, and wave frequency. As an example, we calculate T for the parameters used throughout this chapter, as a function of frequency, in figure 4.4.3. Note that, whatever the frequency, there is always some energy transmitted through the double critical level, and in fact we have $T \geq 1/9$. Moreover, there are certain discrete frequencies at which perfect net transmission is achieved, and therefore all of the incoming wave energy radiates from

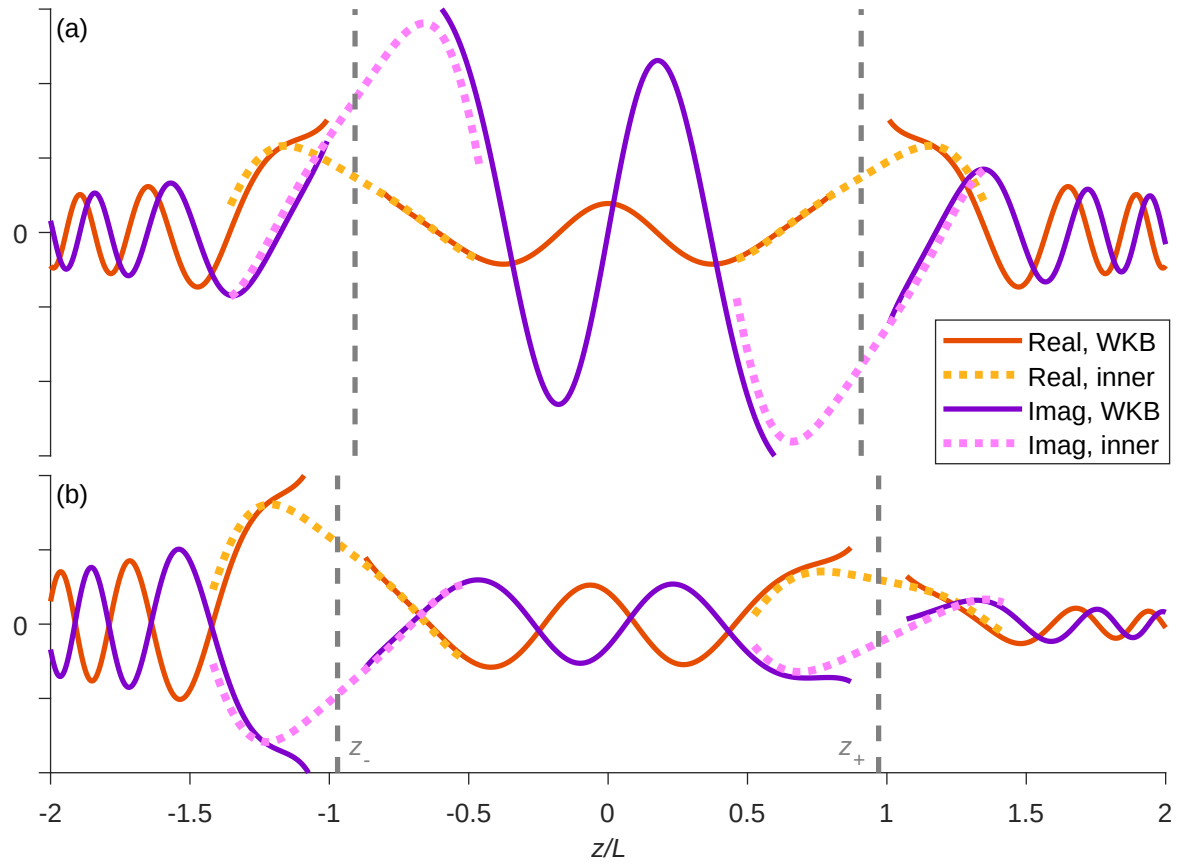

Fig. 4.4.4 Propagation of the WKB solution through two consecutive turning point zeros. The real (orange) and imaginary (purple) components of $\tilde{u}(z)$ are plotted for the WKB solution (4.4.5) as solid lines and inner solution (4.4.10) as short-dashed lines. The turning point zeros $z_\pm$ are shown as grey dashed lines. The two panes correspond to the cases marked on figure 4.4.3; (a) shows perfect transmission at $\varpi \approx 0.091\Omega$, and (b) shows maximum reflection at $\varpi \approx 0.097\Omega$.

south to north. These frequencies may be thought of as equivalent to natural resonances of the region between z_- and z_+, and are characterised by the condition $T = 1$ (or equivalently, $D_- = 0$), which leads to

$$\Delta\Phi = \frac{\pi}{2}(2n+1) \qquad \Longrightarrow \qquad \int_{z_-}^{z_+} |a(\check{z})|^{\frac{1}{2}}\,\mathrm{d}\check{z} = \frac{\pi}{2k_\perp}(2n+1)\,, \tag{4.4.25}$$

where $n \geq 0$ is some integer. If the background field is linear in z, and $\left(B^*/\sqrt{\rho\mu}\right)k_\perp/\Omega \ll 1$, these roots are very well-approximated by the frequencies

$$\frac{\varpi}{\Omega} \approx \sqrt{\frac{3\pi}{4}(2n+1)Le^*} \tag{4.4.26}$$

shown as red triangles in figure 4.4.3, in excellent agreement with the exact peaks of the transmission coefficient T.

As a demonstration of what these waveforms may look like, we plot a couple of selected solutions to this 'two turning point problem' in figure 4.4.4. The top pane (a) corresponds to a situation in which perfect transmission is obtained, and therefore the incoming travelling wave below z_- and outgoing travelling wave above z_+ have the same magnitude. The bottom pane (b) shows the contrasting case of maximum reflection at a similar, but slightly higher frequency — note how the wave amplitude decreases at both turning points due to the significant reflection of wave energy. The solution below z_- is close to being a standing wave, as the reflected solution has only a little less energy than the incident one; this energy is leaked through to the much weaker northward-travelling wave above z_+. This situation therefore appears to act in a way schematically equivalent to a simple resonator on a car exhaust pipe, in which a widened section of pipe traps acoustic waves and therefore reduces the intensity of the sound radiated downstream — but there are certain frequencies, equal to the resonances of the cavity, which are immune to this trapping and thus are transmitted downstream. Our 'resonator' is not fixed in space, but rather has ends which move as the frequency changes, since $z_\pm = \pm\varpi / (Le^*\Omega k_\perp)$, but the two systems seem equivalent in concept.

The full consequences of these findings are unfortunately not clear without resort to a complete (presumably numerical) treatment of the problem — such an approach would consider a model problem not dissimilar to those of chapter 3, but with a varying horizontal background field. It seems likely that the ray-tracing results of this chapter will hold the majority of the time, but that rays will be forced to bifurcate whenever they encounter these turning points, adding yet further to the richness of the problem. Further exploration of these ideas, however, will have to await a further study.

4.4.3 The wave ceiling

As mentioned earlier, the WKB solution also encounters difficulties at a critical point corresponding to the wave ceiling in the ray tracing of sections 4.2 and 4.3. This marks the boundary between a wave-bearing region in which the solutions will be local sinusoidal, and a non-wave region in which they will be exponentially growing or decaying. This kind of situation can lead to a discretisation of the possible frequencies the system can oscillate at, as the waves get fully trapped between two such critical levels — a classical example of this would be the approximation of the high-energy eigensolutions of Schrödinger's equation for a simple harmonic oscillator (e.g. Hinch, 1991).

However, although such a set of solutions are mathematically permissible for this system, they do not really stay honest to the physics. This is because of the presence of Ohmic dissipation — as mentioned before, this becomes particularly intense as a wave packet (or indeed, a WKB-type solution) gets close to the wave ceiling and its vertical wavenumber (i.e. z-derivative) becomes large. In fact, the Ohmic dissipation will approach infinity at the critical level, an unrealistic situation brought about by the absence of certain physics in our model. Hence one cannot expect the governing equation for an ideal fluid (4.4.1) to be valid, even approximately, close to the wave ceiling.

4.5 Discussion

4.5.1 The role of inertial-Alfvén waves

We began this chapter with the goal of assessing the value of inertial-Alfvén waves in the outer core of the Earth more generally than managed in chapter 3, which was restricted to the case of a uniform ambient magnetic field. We have shown that, in a non-uniform magnetic field, whilst the inertial-Alfvén waves are very important in the dispersal of energy from a localised source, they are in general forced to metamorphose into a more arbitrary form of MC wave as the mean magnetic field changes. That is to say, inertial-Alfvén waves are pivotal in prescribing the launch condition of a wave packet, but cease to have any special role amongst the family of MC waves once variations in $\bar{\boldsymbol{B}}$ with space begin to take effect. However, the investigation of alternative launch conditions (figure 4.2.5) suggested that the wave packets which start life as self-focussing inertial-Alfvén waves do suffer the least geometric dispersal as they propagate, even in a varying mean field.

4.5.2 Axial propagation of wave energy

In chapters 2 and 3 we looked to inertial waves, and then inertial-Alfvén waves, as arbiters of axially-elongated, 'quasi-geostrophic' flow structures. The work of this chapter now allows us to ask how this arbitration might occur in a planetary core with a spatially inhomogeneous magnetic field.

The answer appears to be very strongly dependent on the location of the initial disturbance — that is to say, the launch position z_0 in our model problems. If axially-propagating waves are fired from a position of high magnetic field strength, such that the quantity $\bar{B}(z)/\bar{B}(z_0)$ stays moderate at all times, the wave packets are permitted to continue to propagate on-axis, with only minor excursions of the dominant wavevector out of the horizontal plane. Classification of these wave types is inexact, as they flit between the inertial and

inertial-Alfvén limiting cases, plus a more general intermediate MC wave which might have $|\varpi_\Omega| \sim |\varpi_B|$; whichever type they are at a given instant, the group velocity is predominantly in the z-direction and fast by geophysical standards, though not necessarily as fast as inertial(-Alfvén) waves (i.e. core-traversal times of a few months rather than a few weeks).

If, however, MC waves are launched in a region of comparatively weak field, such that $\bar{B}(z)/\bar{B}(z_0)$ is able to get significantly larger than unity as they propagate, their ability to radiate energy on-axis is severely impaired. This is because the dominant wavevector moves out of the horizontal plane, slowing the wave packet and angling its group velocity away from $\mathbf{\Omega}$. Instead, the waves are inclined to propagate energy more and more along the horizontal magnetic field lines.

If the ambient field strength dies away again at yet higher z (figure 4.3.2), ray paths can bend back onto the axis and accelerate again. However, a ray which is not so lucky may instead be trapped beneath a *wave ceiling*, by virtue of the fact it has been refracted so acutely that it asymptotes to the horizontal, slowing down in the extreme and acquiring a wavevector aligned with – rather than perpendicular to – the rotation axis. The magnitude of this wavevector is necessarily very large, and therefore the wavelength is short and rate of dissipation rapid. Because of this, it seems likely that wave packets which approach the ceiling are victims to intense Ohmic losses before actually reaching it.

4.5.3 Variation of the magnetic field geometry

A few different arrangements of mean magnetic field have been analysed in this chapter — as well as uniform (figure 4.2.5), linear (figure 4.2.2), and sinusoidal (figure 4.3.2) one-dimensional fields, we have also looked at the effect of changing the direction as well as the magnitude of $\bar{\boldsymbol{B}}$ with z (figure 4.3.4), or applying a constant axial $\bar{B}_z$ (figure 4.3.5).

The findings in these more complicated field cases are broadly in line with the simple one-dimensional fields; the dichotomy between fast, straight, axially-propagating and slow, ceiling-restricted, curved paths is found in both situations. The addition of an x-wise magnetic field, such that $\bar{\boldsymbol{B}}$ is still in the horizontal plane but now changes direction with height, introduces some additional dispersion, with adjacent rays spreading out due to differences in the 'effective' magnetic field between them as $\bar{\boldsymbol{B}}_\perp(z)$ rotates. Alternatively, adding a constant axial field $\bar{B}_z$ (with a linear horizontal field, $\bar{B}_y \propto z$) gives mean field lines which are parabolae; for fast axial waves, there is little difference in the dispersion as a result. However, waves which asymptote along the ceiling are forced to do so whilst following one of these parabolic paths, possibly bending over backward with a packet which was initially northward-propagating (say) turning south. These waves do, however, encounter the same

hindrance as others at the ceiling, in that they are likely to be rapidly eradicated by Ohmic dissipation.

4.5.4 Limitations

It is hoped this rather idealised study, with simplified background field geometries, governing equations and launch conditions, will go some way to aiding understanding of MC wave dynamics in the context of Earth's outer core. However, it is by its very nature a primitive tool, useful for garnering intuition but not equipped to make strong quantitative predictions for the Earth. In particular, the mean magnetic field is represented poorly — its spatial variations are certainly much more complicated and three-dimensional than anything approached here, and furthermore it can also be expected to evolve significantly over time.

Violations to the assumption that the mean field varies gradually relative to the wavelength of the MC waves are also not covered here, although in section 4.4 we have identified and addressed a particular case at the turning point $|\varpi_B(z_c)| \approx |\varpi_0|$, where the vertical component of the wavevector goes to zero (infinite wavelength in the z-direction) because the wave's launch frequency matches the local Alfvén frequency. Asymptotic matching through this point between a local inner solution and an outer WKB solution showed that the MC waves may be partially reflected, opening the door to an even more complicated family of ray paths, particularly when two adjacent turning points are considered. A different type of critical point was also identified corresponding to the wave ceiling – an interface between wave-bearing and non-wave regions – though the merits of assaulting this obstacle mathematically were negated by its lack of particular physical relevance; it is believed to be more an artefact of the current formulation brought on by the absence of Ohmic dissipation.

Unfortunately, many of the limitations of chapter 3 still apply. We have, in this chapter, dexterously avoided actually specifying an initial condition, using a generic 'launch condition' instead — but if we were to have a buoyant blob (say) as a source, it would be constantly evolving and re-emitting waves with time, the complexities of which have again been avoided here. Furthermore, magnetic diffusion has been treated only heuristically, and our domain is still infinite; reflections at the CMB are thus unaccounted for.

4.5.5 Magnetic-Coriolis waves in Earth's outer core

The results of this chapter suggest that the whole spectrum of MC waves – and not just the limiting cases of inertial, magnetostrophic and inertial-Alfvén waves – are of relevance to outer core dynamics, as a given wave packet must evolve seamlessly between them as it experiences a varying background magnetic field. The inertial-Alfvén waves, which had a

very special role in promoting on-axis radiation in chapter 3, appear to be most important only at the start of a wave packet's life, determining the launch frequency which it must carry with it forever. The spatial structure of the wave (i.e. the dominant wavevector) and its propagation velocity are then forced to adapt in order to accommodate this frequency at whatever ambient magnetic field value the packet may encounter. Here is found some redemption for the 'well-separated roots' – inertial and magnetostrophic waves – spurned somewhat in chapter 3. The inertial waves are playing some part in fast on-axis radiation, particularly in regions of low magnetic field strength, and conversely wave packets which approach the ceiling and slow down as they inch along field lines are without doubt in the magnetostrophic regime.

Finally, it is worth remarking that the helical wave dynamo model is indifferent to much of this chapter's content; that is to say, because all solutions of the MC wave equation necessarily have maximal kinetic and magnetic helicity magnitude (see (3.1.22)), and their choice of whether to travel north or south is determined by its sign (negative north, positive south), all hybrid waves are equally good candidates for segregating helicity between the hemispheres, so long as they are (on average) excited in the equatorial regions. However, what this chapter does provide is some indication of how fast the various classes of waves are likely to be able to perform this duty — from core transit times of months for on-axis waves to decades (if not interminable) for magnetostrophic solutions.

Chapter 5

Hydrodynamic Rossby waves and the westward drift

Note that this chapter comprises material previously published in Bardsley, O. P. 2018, 'Could hydrodynamic Rossby waves explain the westward drift?', *Proc. R. Soc. A* **474**(2213), 20180119.

5.1 Introduction

Since its discovery over three centuries ago by Halley (1692), the westward drift of Earth's magnetic field has remained an intriguing problem in geophysics. Why should it be that many features of the observable geomagnetic field have systematically tracked west throughout 400 years of measurements? The first detailed analysis of this phenomenon was performed by Bullard et al. (1950), to be followed by many others (see Jackson & Finlay, 2015) seeking to elucidate its behaviour through interrogation of both historical data and recent satellite measurements.

The allure of westward drift can perhaps be put down to its ubiquity. Regardless of whether one looks at maps of declination at the Earth's surface or radial field at the core-mantle boundary, westward drift arises as a robust feature of geomagnetic secular variation. The apparent indifference to both spatial scale (Holme et al., 2011) and epoch (Finlay & Jackson, 2003) suggests that the westward drift is an artefact of fundamental core dynamics, and therefore its explanation may open a window onto the Earth's deep interior.

Whilst the westward drift spans many temporal and spatial scales, it also appears to be geographically localised, with secular variation being limited to low-latitude (equatorial) regions (Yukutake, 1962; Jault et al., 1988; Finlay & Jackson, 2003), and dominated by the

motion of intense flux spots with a tendency to pair north and south of the equator (Jackson, 2003). For unknown reasons, the Pacific hemisphere appears to have been relatively quiet in the modern era (Fisk, 1931), with a weaker field magnitude and lack of any convincing secular variation patterns. The dominant contribution to westward drift – centred over the equator in the Atlantic hemisphere – was found by Finlay & Jackson (2003) to be at a rate of 0.27° per year, or 17km per year at the equatorial core-mantle boundary. It is worth noting, however, that these observations face an unfortunate constraint; owing to the interference of crustal magnetism, their resolution is limited to spherical harmonic degrees below 13 — meaning there is a dearth of information at all but the largest scales of magnetic field (Roberts & King, 2013). This is a cause for concern, especially since spectra of the observable secular variation show its power increasing with harmonic degree (Holme et al., 2011), suggesting its origin is to be found at the invisible small scales. Therefore, theoretical models of the small-scale dynamics may prove useful tools for explaining the westward drift.

Motion in the outer core is thought to be stirred by vigorous convection, with thermally or compositionally buoyant material pushing radially outwards from the hot inner core. The convection is strongly-forced, meaning the distribution of density anomaly within the core is likely to be chaotic and span a vast range of scales. This raises questions for both the geodynamo as a whole, and the westward drift; how does the organised dipolar field structure emerge from this stochastic forcing, and how can it also produce the systematic drift observed at large scales?

At present, there exist two main schools of thought on the answer to this final question. Arguably the most popular model, due to Pais & Jault (2008), invokes a large-scale eccentric gyre – or westward-directed jet – which advects the mean magnetic field. An alternative hypothesis (Hide, 1966; Finlay et al., 2010; Hori et al., 2015, 2018), rests upon certain magnetohydrodynamic modes with an invariably westward phase velocity. Without remark upon the merits of either of the above models, a third possibility is here put forward, underpinned by the hydrodynamic Rossby waves produced when a rapidly-rotating fluid is forced to deviate from two-dimensionality by the presence of the container walls (in this case, the core-mantle boundary). We introduce the quasi-geostrophic theory of these waves in section 5.2, deriving their governing equation for a general container geometry, and dispersive properties in a canonical example. The waves are linked to westward drift in section 5.3, supported by initial value problems in both Cartesian and spherical geometries. The discussion of section 5.4 appraises the value of Rossby waves as a possible source of the observed westward drift.

5.2 Theory of quasi-geostrophic Rossby waves

Consider the Earth's outer core to be an inviscid, incompressible fluid in a state of rapid bulk rotation at an angular velocity $\boldsymbol{\Omega} = \Omega \boldsymbol{e}_z$, where $\boldsymbol{e}_z$ is the unit vector in the axial direction of either a Cartesian (x, y, z) or cylindrical polar (s, ϕ, z) co-ordinate system. In either case, a subscript $\perp$ denotes the component of a vector perpendicular to $\boldsymbol{e}_z$. In a reference frame rotating at $\boldsymbol{\Omega}$, the Eulerian fluid velocity is $\boldsymbol{u}(\boldsymbol{r}, t)$. The core-mantle boundary is represented by symmetric, impermeable surfaces at $z = \pm h(\boldsymbol{r}_\perp)$; for a spherical geometry of unit radius, one would have $h = \sqrt{1 - s^2}$.

5.2.1 Kinematics and the QG approximation

In a bid to simplify the analysis, the so-called *quasi-geostrophic approximation* (Cardin & Olson, 1994; Schaeffer & Cardin, 2005; Canet et al., 2014) is made. This is in deference to the fact that the rapid background rotation forces the fluid to seek steady states which are independent of the axial co-ordinate z (geostrophic). The presence of the boundaries at $\pm h$ introduces small departures from geostrophy which cause these states to evolve on a timescale much longer than the rotation period (Busse, 1970); such motions might be called *quasi-geostrophic*, though the definition of the phrase is somewhat imprecise. Here, the term quasi-geostrophic (QG) is used in a strict sense: as a label for the assumption that the velocity components perpendicular to the rotation axis ($\boldsymbol{u}_\perp$) are independent of the axial co-ordinate, an approach which has seen much success in modelling of outer core convection (Aubert et al., 2003; Gillet & Jones, 2006; Guervilly & Cardin, 2016). This is despite the fact that the assumption is only strictly valid when the boundary slope is small, a condition clearly violated in the equatorial regions of Earth's spherical core (Canet et al., 2014; Maffei et al., 2017). Moreover, the approximation remains reasonable even in the presence of a background magnetic field (Jault, 2008).

The velocity field $\boldsymbol{u}$ in this formulation is subject to three kinematic conditions:

1. Incompressibility, $\nabla \cdot \boldsymbol{u} = 0$;
2. Non-penetration at the upper and lower boundaries, $(\nabla h \mp \boldsymbol{e}_z) \cdot \boldsymbol{u}|_{\pm h} = 0$;
3. The QG approximation, $\boldsymbol{u}_\perp = \boldsymbol{u}_\perp(\boldsymbol{r}_\perp, t)$.

It can be shown that a representation of the form

$$\boldsymbol{u} = \nabla \chi \times \nabla \left(\frac{z}{h} \right) \tag{5.2.1}$$

fulfils these requirements, with the streamfunction $\chi(\boldsymbol{r}_\perp, t)$ neatly encapsulating the evolution of the vector field $\boldsymbol{u}(\boldsymbol{r}, t)$ through a scalar function of just two spatial co-ordinates. Note that this form is a generalisation of that introduced by Schaeffer & Cardin (2005), which itself improves upon the classical perturbation expansion approach (as discussed in Gillet & Jones, 2006). Restricting solutions to the form (5.2.1) offers a drastic simplification of the analysis, whilst providing a useful tool with which to probe the physics of axially-elongated structures in the core of the Earth.

5.2.2 Dynamics and governing equation

A governing equation for the streamfunction χ in this QG approach is now derived. In a reference frame rotating at the bulk angular velocity $\boldsymbol{\Omega}$, conservation of momentum for an inviscid, incompressible fluid is, from (2.2.4),

$$\frac{\partial \boldsymbol{u}}{\partial t} + \boldsymbol{u}\cdot\nabla\boldsymbol{u} + 2\boldsymbol{\Omega}\times\boldsymbol{u} = -\nabla\left(\frac{p'}{\rho}\right) \tag{5.2.2}$$

for some modified pressure p'. In the limit of small Rossby number ($U \ll \Omega L$ for some characteristic velocity U and lengthscale L), the second term (advection) may be neglected in comparison to the third (Coriolis). The curl of (5.2.2) then yields the equation

$$\frac{\partial \boldsymbol{\omega}}{\partial t} = 2\boldsymbol{\Omega}\cdot\nabla\boldsymbol{u} \tag{5.2.3}$$

for the evolution of the vorticity $\boldsymbol{\omega} = \nabla\times\boldsymbol{u}$. Evidently, steady solutions must be independent of distance along the rotation axis (i.e. geostrophic) — this is the Taylor-Proudman theorem (Proudman, 1916; Taylor, 1917). However, in order to satisfy non-penetration at $z = \pm h$, QG solutions must possess a weak z-dependence, and therefore can exhibit unsteadiness. To derive an equation for the evolution of a QG flow, one could simply substitute the representation (5.2.1) into the axial component of the vorticity equation (5.2.3), a procedure commonly employed in the literature (e.g. Aubert et al., 2003; Canet et al., 2014). However, as pointed out in Labbé et al. (2015), a more efficacious approach is to instead project the momentum equation (5.2.2) onto flows of the QG form (5.2.1), thereby obtaining a reduced model which better approximates the dynamics. This has been verified analytically in a full sphere by Maffei et al. (2017), who found remarkably good agreement with the fully three-dimensional solutions of Zhang et al. (2001).

We therefore proceed by following the derivation of Labbé et al. (2015), generalising their results in a sphere to a more arbitrary geometry. Consider a control volume V of fluid of constant horizontal cross section A, bounded at the top and bottom by the caps

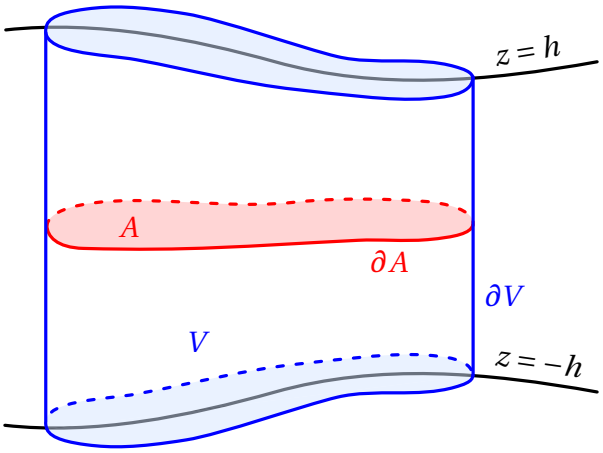

Fig. 5.2.1 Schematic of the control volume considered when deriving the governing equation for a QG flow.

$z = \pm h(\boldsymbol{r}_\perp)$. The boundaries of V and A are denoted ∂V and ∂A respectively (figure 5.2.1). After excluding advection, the momentum equation (5.2.2) is projected onto a QG trial function $\boldsymbol{u}' = \nabla\chi' \times \nabla\left(\frac{z}{h}\right)$, which by construction satisfies $\chi'\big|_{\partial A} = 0$, then integrated over V:

$$\iiint_V \boldsymbol{u}' \cdot \dot{\boldsymbol{u}}\, \mathrm{d}V + 2\Omega \iiint_V \boldsymbol{u}' \cdot (\boldsymbol{e}_z \times \boldsymbol{u})\, \mathrm{d}V = -\iiint_V \boldsymbol{u}' \cdot \nabla\left(\frac{p'}{\rho}\right) \mathrm{d}V, \tag{5.2.4}$$

with a dot over a quantity denoting a time derivative. Using the divergence theorem, the right hand side is equal to

$$\iiint_V \frac{p'}{\rho} \nabla \cdot \boldsymbol{u}'\, \mathrm{d}V - \oiint_{\partial V} \frac{p'}{\rho} \boldsymbol{u}' \cdot \mathrm{d}\boldsymbol{S} = 0 \tag{5.2.5}$$

since the choice of χ' guarantees streamlines of $\boldsymbol{u}'$ cannot pass through ∂V. The contribution from the Coriolis term simplifies to

$$2\Omega \iiint_V \boldsymbol{u}' \cdot (\boldsymbol{e}_z \times \boldsymbol{u})\, \mathrm{d}V = 2\Omega \iiint_V \left(\frac{\boldsymbol{e}_z \times \nabla\chi}{h^2}\right) \cdot \nabla\chi'\, \mathrm{d}V. \tag{5.2.6}$$

The integration from $z = -h$ to $z = h$ can be completed, thereby projecting the equations onto the horizontal plane A:

$$2\Omega \iiint_V \boldsymbol{u}' \cdot (\boldsymbol{e}_z \times \boldsymbol{u})\, \mathrm{d}V = 4\Omega \iint_A \left(\frac{\boldsymbol{e}_z \times \nabla\chi}{h}\right) \cdot \nabla\chi'\, \mathrm{d}A \tag{5.2.7a}$$

$$= 4\Omega \oint_{\partial A} \chi' \left(\frac{\boldsymbol{e}_z \times \nabla\chi}{h}\right) \cdot \boldsymbol{n}\, \mathrm{d}s - 4\Omega \iint_A \chi' \nabla \cdot \left(\frac{\boldsymbol{e}_z \times \nabla\chi}{h}\right) \mathrm{d}A \tag{5.2.7b}$$

$$= 4\boldsymbol{\Omega} \cdot \iint_A \chi' \left(\nabla\frac{1}{h} \times \nabla\chi\right) \mathrm{d}A. \tag{5.2.7c}$$

This requires use of the two-dimensional version of the divergence theorem,

$$\iint_A \nabla\cdot\boldsymbol{v}\,\mathrm{d}A = \oint_{\partial A}\boldsymbol{v}\cdot\boldsymbol{n}\,\mathrm{d}s \tag{5.2.8}$$

(where $\boldsymbol{n}$ is the in-plane unit outward normal to ∂A), then the fact that $\chi'\big|_{\partial A}=0$. A very similar procedure may be applied to the inertial term,

$$\iiint_V \boldsymbol{u}'\cdot\dot{\boldsymbol{u}}\,\mathrm{d}V = \iiint_V\left(\frac{\nabla\dot\chi}{h^2}+z^2\nabla\frac{1}{h}\times\left(\nabla\dot\chi\times\nabla\frac{1}{h}\right)\right)\cdot\nabla\chi'\,\mathrm{d}V \tag{5.2.9a}$$

$$= 2\iint_A\left(\frac{\nabla\dot\chi}{h}+\frac{h^3}{3}\nabla\frac{1}{h}\times\left(\nabla\dot\chi\times\nabla\frac{1}{h}\right)\right)\cdot\nabla\chi'\,\mathrm{d}A \tag{5.2.9b}$$

$$= -2\iint_A\chi'\nabla\cdot\left(\frac{\nabla\dot\chi+\frac{1}{3}\nabla h\times\left(\nabla\dot\chi\times\nabla h\right)}{h}\right)\mathrm{d}A, \tag{5.2.9c}$$

so equation (5.2.4) can be rewritten

$$\iint_A\chi'\left[\nabla\cdot\left(\frac{\nabla\dot\chi+\frac{1}{3}\nabla h\times\left(\nabla\dot\chi\times\nabla h\right)}{h}\right)+2\boldsymbol{\Omega}\cdot\left(\nabla\chi\times\nabla\frac{1}{h}\right)\right]\mathrm{d}A=0. \tag{5.2.10}$$

Since this must be satisfied for all possible choices of the trial function χ', the streamfunction χ must obey the governing equation

$$\nabla\cdot\left(\frac{\nabla\dot\chi+\frac{1}{3}\nabla h\times\left(\nabla\dot\chi\times\nabla h\right)}{h}\right)+2\boldsymbol{\Omega}\cdot\left(\nabla\chi\times\nabla\frac{1}{h}\right)=0. \tag{5.2.11}$$

Note that the second term inside the divergence is the sole difference between this equation and the axial vorticity formulation (i.e. plugging (5.2.1) into the z-component of (5.2.3)); for moderate values of ∇h, however, this difference becomes significant.

5.2.3 QG Rossby waves

The governing equation (5.2.11) can support oscillatory solutions known as QG Rossby waves, in analogy to their atmospheric counterparts Hide (1966); Davidson (2013), discussed in detail by Vallis (2017), for example. The theory of QG Rossby waves in Earth's interior mirrors this classical analysis — to extract their archetypal form, select Cartesian co-ordinates (x,y,z) and a linear height profile $h(y)=H+h'y$ for positive constants H and h', the domain height and slope respectively. This aims to capture the slope of the core-mantle boundary at zero order, with the x-axis oriented east and the y-axis radially inwards. Furthermore, the slope is for the moment assumed small (in comparison to the aspect ratio of the QG

structures), so (5.2.11) may be written in the linearised form

$$\frac{\partial}{\partial t}\nabla^2\chi \approx \frac{2\Omega h'}{H}\frac{\partial \chi}{\partial x}. \tag{5.2.12}$$

Note that an equivalent equation could also stem from the axial vorticity formulation, or indeed a perturbation expansion approach (Jault & Finlay, 2015). Seek travelling wave solutions of the form $\chi(x,y,t) \propto \exp\{i\,(\boldsymbol{k}_\perp \cdot \boldsymbol{r}_\perp - \varpi(\boldsymbol{k}_\perp)\,t)\}$ with frequency ϖ and wavevector $\boldsymbol{k}_\perp = [k_x, k_y, 0]^T = k_\perp[\cos\alpha, \sin\alpha, 0]^T$, where α is the angle between the wavevector and the x-axis and $k_\perp = |\boldsymbol{k}_\perp|$. This yields the dispersion relationship for QG Rossby waves,

$$\varpi = \frac{2\Omega h'}{H k_\perp}\cos\alpha. \tag{5.2.13}$$

Writing $\boldsymbol{e}_{\boldsymbol{k}_\perp}$ for the unit vector in the direction of $\boldsymbol{k}_\perp$ and $\boldsymbol{e}_\alpha$ for the unit vector in the direction of increasing α (figure 5.2.2), the phase velocity corresponding to (5.2.13) can be expressed as

$$\boldsymbol{c}_p = \frac{\varpi}{k_\perp}\boldsymbol{e}_{k_\perp} = \frac{2\Omega h'}{H k_\perp^2}\cos\alpha\ \boldsymbol{e}_{k_\perp}. \tag{5.2.14}$$

Note that the component of phase velocity in the x-direction is always positive, meaning wave crests invariably progress eastwards. However, the same is not true for the wave energy, which instead propagates at the group velocity, given by the gradient in $\boldsymbol{k}_\perp$-space of the frequency,

$$\boldsymbol{c}_g = \frac{\partial \varpi}{\partial k_\perp}\boldsymbol{e}_{k_\perp} + \frac{1}{k_\perp}\frac{\partial \varpi}{\partial \alpha}\boldsymbol{e}_\alpha = -\frac{2\Omega h'}{H k_\perp^2}\left(\cos\alpha\ \boldsymbol{e}_{k_\perp} + \sin\alpha\ \boldsymbol{e}_\alpha\right). \tag{5.2.15}$$

The relationship between the phase and group velocities is best understood diagrammatically; figure 5.2.2 is a velocity diagram relating the two, similar to the plots of Duba & McKenzie (2012). The magnitude of $\boldsymbol{c}_g$ is independent of α, so on the velocity diagram the vector $\boldsymbol{c}_g$ is the diameter of a circle of radius $\Omega h'/Hk_\perp^2$. Furthermore, $\left(\boldsymbol{c}_p + \boldsymbol{c}_g\right)\cdot\boldsymbol{c}_p = 0$, so $\boldsymbol{c}_p$ is a chord of the same circle terminating at the base of $\boldsymbol{c}_g$. Since $\boldsymbol{c}_p$ is always in the positive x direction, the circle must lie to the right of the origin as shown.

Using figure 5.2.2, it is possible to probe the effect of varying the wavevector orientation α for a given $k_\perp$ (i.e. a specified horizontal length scale). Consider only positive frequencies ($-\frac{\pi}{2} < \alpha \leq \frac{\pi}{2}$), for which figure 5.2.2 makes sense. The phase velocity vector $\boldsymbol{c}_p$ is constrained to move along the dashed circle, whereas the group velocity vector $\boldsymbol{c}_g$ starts where $\boldsymbol{c}_p$ finishes and is necessarily a diameter of the same circle. Although the phase velocity always has a positive x-component, the group velocity shows no such preference. In fact, the x-component of $\boldsymbol{c}_g$ is negative (westward) for $|\alpha| < \frac{\pi}{4}$ and positive (eastward) for $|\alpha| > \frac{\pi}{4}$. When $\alpha = 0$, $\boldsymbol{c}_p$ and $\boldsymbol{c}_g$ are exactly opposite, so an observer following a wave group moving

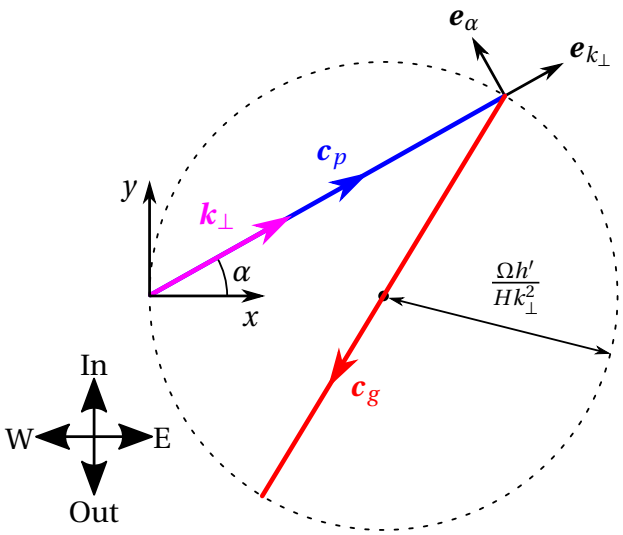

Fig. 5.2.2 Velocity diagram for QG Rossby waves when $h = H + h'y$ for small h'. Phase velocity $\boldsymbol{c}_p$ is related to group velocity $\boldsymbol{c}_g$ for a given choice of $\boldsymbol{k}_\perp$. The rotation axis is out of the page, and the labelled directions orient the figure within Earth's outer core.

westward would see wave crests heading in the opposite direction at twice the speed of the group. When $\alpha = \frac{\pi}{2}$ the group velocity remains finite (and due east) despite the fact the waves have no phase velocity. Waves with $\alpha = \frac{\pi}{4}$ propagate directly outwards and waves with $\alpha = -\frac{\pi}{4}$ inwards.

The dependence of wave velocity on $k_\perp$ is comparatively trivial; waves with longer wavelengths (smaller $k_\perp$) travel faster. As $|\boldsymbol{c}_g| \sim k_\perp^{-2}$, the waves are highly dispersive.

5.3 The westward drift

A possible explanation for the westward drift of Earth's magnetic field at the core-mantle boundary based upon this classical theory of hydrodynamic QG Rossby waves is now offered. Suppose, not unreasonably, that the fluid outer core is stirred by gravitating buoyant anomalies, which constitute localised disturbances to the system in the form of convective upwellings or plumes. Consider one such disturbance introduced at a location outside of the tangent cylinder (i.e. not directly north or south of the solid inner core). The disturbance will in general be three-dimensional, but the velocity field it instigates will rapidly become elongated along the rotation axis through the action of inertial waves (Davidson et al., 2006), and therefore quasi-geostrophic after a short transient period. It is thus useful to consider a thought experiment posed as an initial value problem in which a localised QG velocity field

is specified as an initial condition, and the flow allowed to evolve as an assemblage of QG Rossby waves, operating on a timescale much longer than the rotation period.

A generic initial condition will excite a broad spectrum of waves – that is to say, many different choices of wavevector $\boldsymbol{k}_\perp$ – which will all spread from the source according to their individual dispersive properties. A disturbance of characteristic size ℓ will have a spectrum peaked around a wavevector magnitude $k_\perp$ of order ℓ^{-1}, but will in general excite wavevectors of all possible orientations α. Therefore, consider the dependence of the group velocity on wavevector orientation by referring back to figure 5.2.2. For wavevectors with $\alpha \approx \pm\frac{\pi}{2}$, corresponding to structures elongated in the east-west direction, the group velocity is east; for wavevectors with $\alpha \approx 0$, i.e. structures elongated in the radial direction, the group velocity is west. QG Rossby waves therefore disperse in a manner which segregates different spatial structures from an arbitrary initial disturbance, with east-west extended features heading east and radially extended features west.

However, it is unreasonable to assume the excitation of these waves in the core of the Earth is arbitrary. For motions continually stirred by vigorous convection, one might expect the proliferation of sinuous radial plumes, emanating from the inner core and being much longer than they are wide. Such structures commonly arise in numerical and experimental studies of core dynamics (e.g. Olson, 2011; Schaeffer et al., 2017). Due to the constraint imposed by the rapid background rotation, such plumes would also be elongated in the axial direction, forming a series of radial sheets which are likely to be well-represented by the QG approximation (Gillet et al., 2012). In the context of our thought experiment, a radial sheet (extended in the y-direction) will possess much more energy in wavevectors pointing east-west ($\alpha \approx 0$) than radially ($\alpha \approx \pm\frac{\pi}{2}$). When the solution to such an initial value problem is evolved, the abundance of wavevectors with $\alpha \approx 0$ will dominate the picture. Since the group velocity for these solutions is in the negative x direction, a radially-extended disturbance will preferentially transmit energy to the west, making this class of QG Rossby waves an intriguing candidate for the mechanism underlying westward drift.

5.3.1 Demonstration through a simple Cartesian model problem

To support the arguments made so far, consider a simplistic model problem which demonstrates the ability of QG Rossby waves to segregate different spatial structures. The canonical equation (5.2.12) is solved in a domain which is infinite in x and y, starting from some initial condition $\chi(\boldsymbol{r}_\perp, t=0) = \chi_{\text{init}}(\boldsymbol{r}_\perp)$, by taking a two-dimensional spatial Fourier transform. Emphasis is placed upon the significance of the choice of initial condition, which is

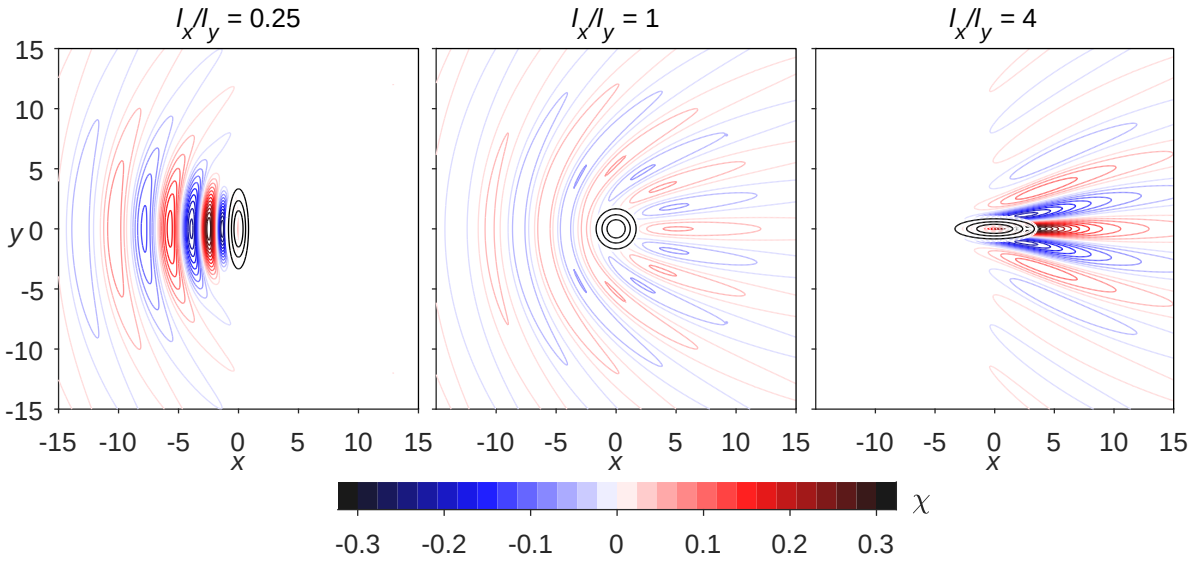

Fig. 5.3.1 Solutions to the canonical QG Rossby wave equation (5.2.12) for a simple initial value problem starting from (5.3.1). The height of the container is $h = H + h'y$. Contours of streamfunction χ are plotted at $2\Omega h' t/H = 15$ for three different choices of aspect ratio, and black contours are at quartiles of the initial condition. Lengths are in units of $\sqrt{\ell_x \ell_y}$.

constrained to be of the form

$$\chi_{\text{init}} = \exp\left\{-\frac{1}{2}\left(\frac{x^2}{\ell_x^2} + \frac{y^2}{\ell_y^2}\right)\right\}. \tag{5.3.1}$$

Since contours of χ are equivalent to streamlines in the equatorial plane, this corresponds to a columnar vortex of extent ℓ_x in the x-direction and ℓ_y in the y-direction. Using $\sqrt{\ell_x \ell_y}$ as the unit of length, the solution to the initial value problem may be written as the two-dimensional dispersion integral

$$\chi(\boldsymbol{r}_\perp, t) = \frac{2}{\pi}\int_0^{\pi/2}\int_0^{\infty} k_\perp \exp\left\{-\frac{1}{2}k_\perp^2\left(\ell_x^2\cos^2\alpha + \ell_y^2\sin^2\alpha\right)\right\} \times \cos\left(\left[k_\perp x - \frac{2\Omega h' t}{H k_\perp}\right]\cos\alpha\right)\cos\left(k_\perp y \sin\alpha\right)\, \mathrm{d}k_\perp \mathrm{d}\alpha, \tag{5.3.2}$$

wherein $k_\perp$ and α have the same interpretations as in the dispersion relation (5.2.13). This expression is evaluated numerically for three different choices of the initial condition's aspect ratio ℓ_x/ℓ_y (figure 5.3.1). The central pane shows the case of an axisymmetric initial condition, which excites waves of all orientations α equally and therefore shows no preferential direction for energy transport, although the partition of different spatial structures

is visible. The left pane shows the case of a radially-extended initial condition, four times longer in the direction of the slope than it is wide; the bias towards westward-propagating waves is self-evident. For completeness, the right pane features an initial condition which is elongated in the east-west direction, which exhibits a strong preference for eastward propagation. It is worth remarking that the aspect ratio need not be extreme for this effect to be apparent; it is very clear-cut here even for a moderate value of 4:1.

5.3.2 Westward-propagating waves in a sphere

It has been established so far that, in the case of a gentle slope, the linearised equation (5.2.12) supports wave motions which partition different spatial structures — crucially, with flows elongated in the direction of the slope going west. However, it is not obvious that the same will necessarily hold true for a more complicated geometry with an appreciable slope, such as that presented by the core-mantle boundary. Therefore, consider an initial value problem similar to that of the previous section, but in an enclosed spherical geometry reminiscent of Earth's core. A full sphere – deficient of the solid inner core – is used in order to simplify the analysis. First, mode shapes and frequencies are derived in this geometry, following Maffei et al. (2017), before the calculated modes are used to solve an illustrative initial value problem.

Despite the spherical geometry, cylindrical polar coordinates (s,ϕ,z) – with s being the radial location, ϕ the azimuthal angle, and z the distance along the rotation axis – are adopted in order to usefully apply the QG approximation. Taking lengths in units of outer core radii, the governing equation is then (5.2.11) with the axisymmetric height profile $h(s)=\sqrt{1-s^2}$:

$$\left[\frac{\partial}{\partial s}\left(\frac{s}{h}\frac{\partial}{\partial s}\right)+\frac{1}{hs}\left(1+\frac{s^2}{3h^2}\right)\frac{\partial^2}{\partial\phi^2}\right]\frac{\partial\chi}{\partial t}-\frac{2\Omega s}{h^3}\frac{\partial\chi}{\partial\phi}=0. \tag{5.3.3}$$

First, note that any solution satisfying $\partial_t\chi=\partial_\phi\chi=0$ will be a particular integral of this equation. This corresponds to the steady, strictly geostrophic motion of coaxial cylinders ($\boldsymbol{u}=u_\phi(s)\boldsymbol{e}_\phi$); hence, the axisymmetric component of any initial condition will not evolve, and one need only solve (5.3.3) for the non-axisymmetric portion of the flow. This can be done by seeking normal mode solutions of the form

$$\chi(s,\phi,t)=\mathbb{R}\left\{\tilde{\chi}(s)\exp\left(i\left[m\phi-\omega t\right]\right)\right\} \tag{5.3.4}$$

for some azimuthal wavenumber m and modal frequency ϖ. This turns (5.3.3) into an ordinary differential equation for the radial mode shape,

$$\frac{\mathrm{d}}{\mathrm{d}s}\left(\frac{s}{h}\frac{\mathrm{d}\tilde{\chi}}{\mathrm{d}s}\right)+\left[\frac{2\Omega m s}{\varpi h^3}-\frac{m^2}{hs}\left(1+\frac{s^2}{3h^2}\right)\right]\tilde{\chi}=0, \tag{5.3.5}$$

which must be solved subject to boundary conditions at the origin ($s=0$) and the equatorial boundary ($s=1$). Regularity at the origin requires $\tilde{\chi}\sim s^m$ as $s\to 0$, whereas non-penetration at the outer boundary requires

$$u_s|_{s=1}=\lim_{s\to 1}\left(\frac{1}{hs}\frac{\partial\chi}{\partial\phi}\right)=0. \tag{5.3.6}$$

Since χ is a streamfunction, its constant value at the outer boundary can be chosen, so is set at zero; more specifically, we must have $\tilde{\chi}(s\to 1)\sim h^3$ in order for $u_s=(hs)^{-1}\partial_\phi\chi$ to be zero and $u_\phi=-h^{-1}\partial_s\chi$ to be finite at the outer boundary. The solution to the eigenvalue problem posed by (5.3.5) and these boundary conditions is given in Maffei et al. (2017); the mode shapes are of the form

$$\tilde{\chi}_n^m(s)=s^m h^3 P_{n-1}^{(3/2,m)}(2s^2-1) \tag{5.3.7}$$

and the corresponding frequencies are

$$\varpi_n^m=\frac{\Omega m}{n(2n+2m+1)+m/2+m^2/6}. \tag{5.3.8}$$

Here, $n\geq 1$ is the radial mode number, equal to the number of turning points of $\tilde{\chi}_n^m$ within the domain. The mode shapes are expressed in terms of Jacobi polynomials $P_\nu^{(\alpha,\beta)}(x)$ (Abramowitz & Stegun, 1964). Note that, for all $m\geq 1$, the frequency ϖ_n^m is positive, meaning all modes revolve in a prograde (eastward) sense; this is analogous to the observation that the phase velocity in the Cartesian problem (5.2.14) is always in the positive x-direction. Just as in that problem, this does not preclude the possibility that the energy from a localised disturbance can nevertheless propagate west, as demonstrated below.

The general solution to (5.3.3) (setting aside the axisymmetric particular integral for a moment) can be written as an infinite sum of the above modes,

$$\chi(s,\phi,t)=\mathbb{R}\left\{\sum_{m=1}^{\infty}\sum_{n=1}^{\infty}C_n^m\tilde{\chi}_n^m(s)e^{i(m\phi-\varpi_n^m t)}\right\} \tag{5.3.9}$$

for some complex coefficients C_n^m to be determined by the initial condition $\chi_{\text{init}}(s,\phi)$. In fact, it can be seen from the self-adjoint equation (5.3.5) that the radial mode shapes (5.3.7)

are orthogonal with respect to the function s/h^3, i.e.

$$\int_0^1 \frac{s}{h^3}\tilde{\chi}_n^m(s)\tilde{\chi}_{n'}^m(s)\,\mathrm{d}s = 0 \quad \text{for} \quad n \neq n', \tag{5.3.10}$$

which enables the derivation of an expression for each modal coefficient as an integral over the equatorial plane,

$$C_n^m = \frac{\int_0^1 \frac{s}{h^3}\tilde{\chi}_n^m(s)\oint \chi_{\text{init}}(s,\phi)e^{-im\phi}\,\mathrm{d}\phi\mathrm{d}s}{\pi\int_0^1 \frac{s}{h^3}\left[\tilde{\chi}_n^m(s)\right]^2\,\mathrm{d}s}. \tag{5.3.11}$$

All that remains is the axisymmetric portion of the flow, given simply by

$$\chi_{\text{ax}}(s) = \frac{1}{2\pi}\oint \chi_{\text{init}}(s,\phi)\,\mathrm{d}\phi. \tag{5.3.12}$$

This analysis allows the solution of an illustrative initial value problem, similar to that of section 5.3.1, by using (5.3.11) to express the initial condition as a linear sum of modes and solving for the streamfunction at a later time by evaluating the sums in (5.3.9) truncated at finite m and n.

Choice of initial condition

If the simple Cartesian cartoon discussed in section 5.3.1 is to be believed, the choice of initial condition, and therefore distribution of energy in $\boldsymbol{k}_\perp$-space (or equivalently, between modes), will have a profound effect on the direction of net energy propagation. In fact, those modes for which the frequency ϖ_n^m in (5.3.8) is a decreasing function of m will be associated with westward propagation of energy; in the Cartesian case, $c_{g,x}$ is negative for $\partial\varpi/\partial k_x < 0$, and analogously retrograde group velocity is seen in the sphere for $\partial\varpi_n^m/\partial m < 0$, i.e.

$$m > \sqrt{6n(1+2n)}. \tag{5.3.13}$$

For a westward drift to be observed in this model problem, the harmonic content of the initial condition must be biased towards modes which satisfy this inequality. For definiteness, discussion is restricted to the form of initial condition

$$\chi_{\text{init}}(s,\phi) = h^3 s\exp\left\{-\frac{1}{2}\left(\frac{(s-s_0)^2}{\ell_s^2}+\frac{s_0^2\phi^2}{\ell_\phi^2}\right)\right\}. \tag{5.3.14}$$

This is essentially a columnar Gaussian vortex, as for the model problem of section 5.3.1, with the pre-multiplying factor $h^3 s$ ensuring the boundary conditions are satisfied at from

the outset. It is broadly unimportant exactly what form the initial condition takes, however — it is the general distribution of energy between modes which will dictate the solution's character.

There are three controlling lengths in the initial condition (5.3.14); the radial and azimuthal extents of the vortex ℓ_s and ℓ_ϕ, and the radial location of the vortex centre s_0. In search of a westward bias to energy propagation, the parameters $\ell_s = 0.1$, $\ell_\phi = 0.01$ and $s_0 = 0.7$ are selected, giving a slender radially-extended structure near the middle of the outer core region $0.35 < s < 1$ (though there is no inner core boundary in this calculation). The solution is expressed as a finite sum of modes (i.e. a truncated version of (5.3.9)) by evaluating the integrals (5.3.11) for the coefficients C_n^m numerically. Due to the narrowness of the initial condition, more modes of high azimuthal wavenumber are required; the ranges $m \leq 200$ and $n \leq 50$ are used.

Westward bias to energy propagation in a sphere

Figure 5.3.2 shows the solution to the initial value problem evaluated at $\Omega t = 2 \times 10^4$ ($t =$ 8.7yr). Streamlines in the equatorial plane are produced by plotting contours of χ, with the black contours corresponding to the initial value (5.3.14). Although this solution is many times more complicated than the Cartesian problem of figure 5.3.1, there remains a striking preference for wave propagation to the west of the initial disturbance. This is despite the fact that each individual eigenmode has an eastward phase velocity; it is the superposition of modes which creates the visible westward bias. Wave motion appears to be confined to a circular band near the initial radial location s_0, with little activity very close to the outer boundary or near the rotation axis. The dashed line is at $s = 0.35$, where the inner core would be if it were included in the model; thankfully, the vast majority of activity occurs outside of this region.

The preference for westward propagation may be understood in exactly the same way as the Cartesian problem of section 5.3.1, but with the small slope assumption now relaxed. The majority of the energy from the radially-extended initial condition is contained in modes with large azimuthal wavenumbers, which conspire to produce a westward group velocity despite individually having eastward phase velocities. To demonstrate that the former prevails, consider the distribution of energy in the sphere as a function of longitude and time. Namely, the meridionally-averaged specific kinetic energy,

$$\left\langle \tfrac{1}{2}\boldsymbol{u}^2 \right\rangle (\phi, t) = \int_0^1 \left(\int_{-h}^{h} \tfrac{1}{2}\boldsymbol{u}^2 \, \mathrm{d}z \right) s \mathrm{d}s = \int_0^1 \frac{s}{h} \left[(\nabla\chi)^2 + \frac{1}{3} (\nabla\chi \times \nabla h)^2 \right] \mathrm{d}s, \tag{5.3.15}$$

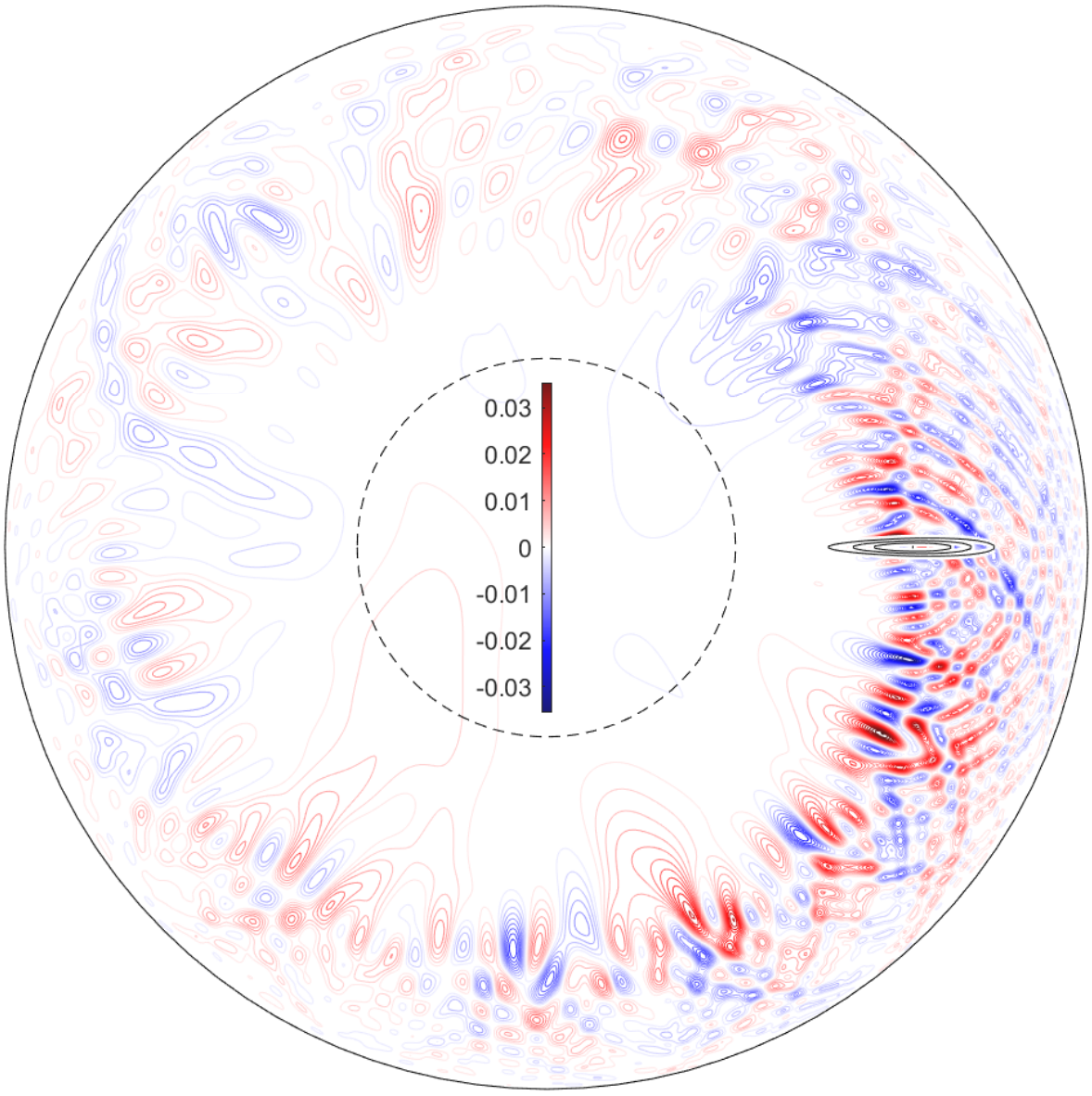

Fig. 5.3.2 Contours of χ (i.e. streamlines in the equatorial plane, viewed from the north) at $\Omega t = 2\times10^4$ for an initial value problem starting from a radially extended vortex (5.3.14) with $\ell_s = 0.1$, $\ell_\phi = 0.01$, and $s_0 = 0.7$. Solid black contours are at quartiles of the initial condition, and the dashed black line shows the would-be location of the solid inner core.

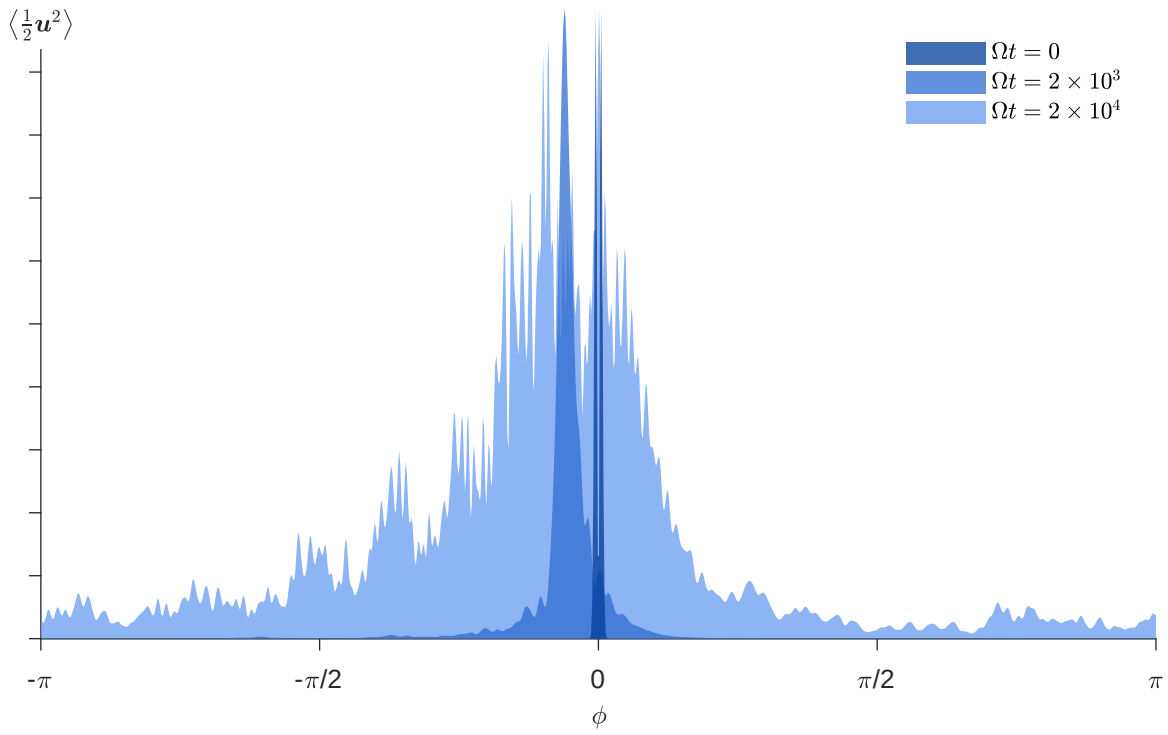

Fig. 5.3.3 Specific kinetic energy, averaged over meridional slices, as a function of longitude ϕ for the initial condition and two later times $\Omega t = 2 \times 10^3$ and $\Omega t = 2 \times 10^4$. Plots are normalised to have the same maxima, though in actuality contain equal areas.

is evaluated as a function of ϕ at a few choice times (figure 5.3.3). The energy, initially localised around $\phi = 0$, is almost all at negative ϕ when $\Omega t = 2 \times 10^3$, and is still sharply peaked as the waves have had little time to disperse. Come $\Omega t = 2 \times 10^4$, which corresponds to figure 5.3.2, the energy is much more dispersed but retains its westward bias; of course, reflections and circumnavigations mean a little energy does end up to the east of the initial disturbance.

5.4 Discussion

The model problems above successfully demonstrate the possibility for westward transport of energy by hydrodynamic QG Rossby waves, but are intended as a proof-of-concept rather than an accurate representation of core dynamics. Clearly, the flow in Earth's outer core isn't the solution to an initial value problem, but rather the result of continual convective stirring; the interplay between buoyancy and velocity fields will introduce complexity beyond the scope of this study (see Guervilly & Cardin, 2016). However, the present theory demonstrates

that westward propagation requires only the prevalence of radial plumes, which are likely to be robustly generated by the buoyant upwellings associated with strongly forced convection.

Indeed, discussions of vigorously forced convection are intrinsically linked to the relevant smallest lengthscale in the core of the Earth, which is itself pertinent to dynamo action (Davidson, 2016). The thickness of the radial plumes will have a strong bearing on the propagation speed of their associated wave packets, since the magnitude of the group velocity (5.2.15) is proportional to the square of the wavelength, meaning narrower structures propagate much slower. The most strongly-forced simulations to date (e.g. Schaeffer et al., 2017) show structures more slender than those considered in the model problem of figure (5.3.2), and it is not unreasonable to suspect that the true lengthscale is even smaller. In fact, it is possible to infer this lengthscale under the assumption that QG Rossby waves are responsible for the westward drift. From the expression for group velocity (5.2.15), the speed of a wave packet at a certain cylindrical radius s is given by

$$\left|\boldsymbol{c}_g\right| \approx \frac{2\Omega}{hk_\perp^2}\left|\frac{\mathrm{d}h}{\mathrm{d}s}\right| = \frac{2\Omega s}{(hk_\perp)^2}. \tag{5.4.1}$$

For an azimuthally-propagating wave packet, the angular velocity about the rotation axis is $\left|\boldsymbol{c}_g\right|/s$; equating this to the observed drift rate of the magnetic field D gives an expression for the dominant wavelength of the packet,

$$\lambda \approx 2\pi h\sqrt{\frac{D}{2\Omega}}. \tag{5.4.2}$$

Using a drift rate of 0.27° per year (Finlay & Jackson, 2003) and a radial location of the wave packet $s \sim 2000$km gives the estimate $\lambda \sim 18$km, a conceivable value for the prevalent scales in the Earth's core, but one which should be treated with caution. Firstly, it is within touching distance of the Rhines length $\sqrt{Uh/\Omega}$ (~ 4km for $U \sim 0.4$mm/s), at which the advection term in (5.2.2) becomes significant and mean flows may arise. Secondly, the aspect ratios of such structures would be improbably large for their coherence to be maintained over secular timescales. It seems more reasonable that in truth λ is greater, with additional factors – interactions with the buoyancy and magnetic fields, large values of boundary slope, or departures from quasi-geostrophy – acting to slow the wave groups down. Unfortunately, the machinery required to investigate these non-linear phenomena lies beyond our present scope.

Nevertheless, it seems remiss that so far no consideration has been given to the magnetic field, despite the fact that the observed westward drift of its large scale features is the motivation for this study. It is therefore necessary to ask what could link hydrodynamic

QG Rossby waves to the apparent motion of the spherical radial magnetic field B_r at the core-mantle boundary. Since the drift is observed to be mainly in the equatorial regions (Jackson, 2003), motion of the *cylindrical* radial field B_s, which will be approximately equal to B_r at low latitudes, is discussed instead. To a first approximation, magnetic field lines may be thought of as material curves, pinned into the fluid at all points (Roberts & Scott, 1965; Davidson, 2013), so there are essentially two ways of modifying the radial magnetic field: advection and stretching of an existing B_s by a mean flow, or rotation of the other components (B_ϕ, B_z) by transverse gradients in radial velocity ($\partial_\phi u_s, \partial_z u_s$ respectively); both mechanisms are discussed in the context of westward drift by Finlay (2005) and Aubert et al. (2013). Westward-propagating QG Rossby waves, which necessarily consist of radially-extended sheet-like structures, have small azimuthal velocities so are unlikely to advect B_s strongly enough to account for the westward drift. The radial velocity is much greater, but has small derivatives in s and z so stretching of an existing B_s or shearing of B_z are both unlikely mechanisms. The best candidate for generation of B_s is therefore shearing of B_ϕ by azimuthal gradients in u_s, which are large for the slender radial jets. Furthermore, the azimuthal magnetic field is likely to be relatively strong within the core (Hide & Roberts, 1979), and largest at mid- to low-latitudes – which could explain the equatorial bias to the observed drift, since a low-latitude B_ϕ swept out by a QG radial jet would produce a radial field anomaly at the core-mantle boundary in the vicinity of the equator.

At first glance, this argument appears to suffer from the deficiency that the manipulation of B_s occurs on the small scale of the wavelength λ, whereas the observed drift occurs in magnetic field features hundreds of kilometres across. However, the observations themselves are hampered by a lack of spatial resolution, so small-scale features simply aren't visible, even though they may in fact contain a significant portion of the energy (Holme et al., 2011). The observations instead feature large, westward-moving patches (Jackson, 2003) which one might compare to wave groups, with the small-scale details (wave crests and troughs) within each patch unavailable. It is therefore to be expected that, if the present theory were to explain the observations, large magnetic field features would appear to be advected at the group (rather than phase) velocity of QG Rossby wave packets.

The feedback of the magnetic field on the dynamics through the action of the Lorentz force has been ignored in this study. Indeed, for highly simplified field configurations it has been shown that its inclusion introduces additional oscillations known as *slow magnetic Rossby waves* which themselves have been suggested as a possible source of magnetic field drift since their phase velocity is always westward (Hide, 1966; Finlay et al., 2010; Hori et al., 2015, 2018). However, these slow solutions coexist with others known as *fast magnetic Rossby waves*, which are little more than a weakly-modified version of the hydrodynamic solutions

discussed at length above. The perturbation to the magnetic field does not strongly influence the dynamics of these waves, and so they remain an equally viable source of westward drift, with the magnetic field approximating a passive tracer at leading order.

Moreover, the fact that the dynamics of QG Rossby waves are independent of the magnetic field configuration and magnitude is a strength of the present theory. Slow magnetic Rossby modes have to date only been demonstrated for simple choices of background field (Canet et al., 2014; Labbé et al., 2015), and it is therefore unclear whether such solutions are meaningful in a geophysical context. Conversely, the fast (i.e. hydrodynamic) solutions are likely to persist regardless of the magnetic field structure, meaning they are an almost unavoidable feature of QG flows in Earth's outer core. This robustness tallies with the observation of westward drift as a systematic component of the geomagnetic secular variation, and the fact that the waves operate on a scale much smaller than the observed field features may explain the broad scale-independence of the observed drift rate. These advantages, along with those discussed above, lend credibility to the theory presented here – that hydrodynamic QG Rossby waves with radially-extended structures may underpin the westward drift present in geomagnetic secular variation records.

Chapter 6

Conclusions

We now briefly review the main conclusions of this thesis, drawn together by the theme of understanding the behaviour of various dispersive waves which are likely to exist in Earth's outer core. We ask what role these waves might play in the geodynamo, both in terms of maintaining the magnetic field against diffusion, and potentially explaining observable features of the secular variation. Interesting avenues for future research are then suggested.

6.1 Dispersion of waves from localised disturbances

Chapters 2 and 3, and Bardsley & Davidson (2016), inspected the dynamics of rotating and MHD waves at the smallest scales of the flow in the outer core — these are crucial in the helical wave dynamo model of Davidson (2014) for segregating the sign of helicity between the hemispheres, but in a broader context are important for our understanding of the basic physical processes occurring within the Earth.

In the rotating (non-magnetic) case, we highlighted the importance of low-frequency inertial waves in propagating energy, and therefore information, along the rotation axis, as previously reported in Davidson et al. (2006) and Davidson & Ranjan (2015). This was confirmed to be the case whether the source of waves was a turbulent eddy, a buoyant blob, or a random cloud of such objects, and hinged upon the ability of the many wave packets with their dominant wavevector perpendicular to the rotation axis ($\boldsymbol{\Omega} \cdot \boldsymbol{k} \approx 0$) to 'self-focus' energy radiation from a localised source.

This work was then extended into the situation where a mean magnetic field is present as well as the background rotation, in the limit of negligible magnetic diffusivity and small Lehnert number — which is to say, a rotation period much shorter than the Alfvén wave period. In this regime, a popular line of reasoning leads to the paradigm of *well-separated roots* to the rotating-MHD wave dispersion relation: the inertial waves from the non-magnetic

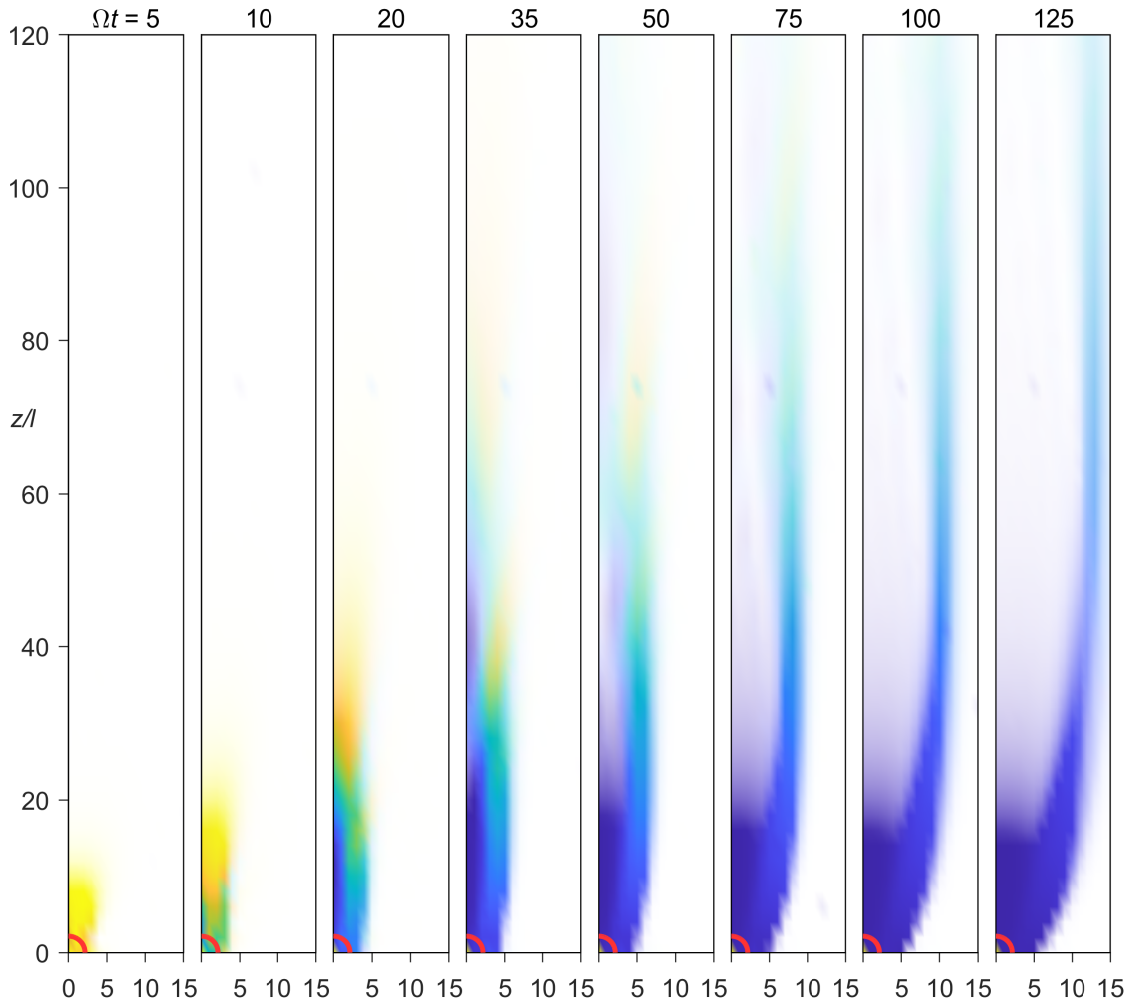

Fig. 6.1.1 Reproduction of figure 3.2.3, showing prominence of inertial-Alfvén waves.

case, plus a class of much slower magnetostrophic waves. We show that, in a situation where the magnetic field and rotation vectors are aligned (as might be the case when looking at the poloidal field near to the equatorial plane in the outer core), this mode of thinking applies very well to the radiation of waves from a buoyant blob. The fast inertial waves still possess the ability to self-focus, and shoot up along the axis, forming the same columnar vortices observed in the hydrodynamic situation. At much later times, the slow magnetostrophic waves follow in the same direction, gradually transferring energy from the velocity field to the magnetic field and balancing the buoyancy with the tension of the field lines.

However, when the background rotation and mean magnetic field are misaligned, the behaviour is changed drastically, even at a reasonably small Lehnert number. The reason is that previously-overlooked *inertial-Alfvén waves* appear to be adopting the role played by the low-frequency inertial waves in the hydrodynamic case (figure 6.1.1). This class of

wave are characterised by a wavevector which is perpendicular to the rotation axis and a group velocity which is on-axis at half the speed of low-frequency inertial waves and along magnetic field lines at the Alfvén velocity. Crucially, this group velocity is the same for all inertial-Alfvén waves of a given scale, so they still possess the ability to 'self-focus' the radiated energy density from a localised source. This was observed and quantified in a model problem, again using a buoyant blob as the wave source, and also shown for an aligned-axis vortex initial value problem and a sea of buoyant blobs.

Inertial-Alfvén waves may, therefore, be an important ingredient in the dynamics of the small, fast scales in the outer core, particularly in the creation of columnar flow structures and north-south segregation of helicity. They may even hint that a more general class of Alfvén-like waves, which counts inertial-Alfvén waves and torsional oscillations amongst its members, may be possible within the Earth. These results are tentative at the moment, being bound by the assumptions of the model problems herein, but could nevertheless be an important contribution toward a fuller understanding of the mechanisms of dynamo action.

6.2 Magnetic-Coriolis waves in a varying background field

A natural continuation of the work on radiation of MC waves from a localised source in a uniform ambient field is to consider the effects of one which varies in space, as it must do in Earth's core (chapter 4 and Bardsley & Davidson (2017)). In this situation, the inertial-Alfvén waves adopt special significance only by virtue of their dominating the radiation pattern at launch, i.e. very close to the source. We may then track how wave packets launched at the inertial-Alfvén limit propagate through a non-uniform $\bar{\boldsymbol{B}}$ using ray tracing techniques (figure 6.2.1). The outcome of this is that the wave packets are forced to develop into more generic MC waves, still on the same general dispersion relation curve, but with potentially very different propagation rates and dispersive characteristics. In particular, wave packets which are launched in a strong magnetic field tend never to deviate far off-axis, and maintain a wavevector which is approximately perpendicular to $\boldsymbol{\Omega}$ (though they may be inertial or intermediate MC waves, rather than necessarily inertial-Alfvén waves). Wave packets launched in relatively weak fields, however, are forced to follow highly refracted paths as they propagate into regions where it is stronger; their group velocity is reduced by orders of magnitude during this process, as they approach the magnetostrophic limit of the dispersion relation. In the extreme, this refraction can turn rays entirely along the horizontal magnetic field lines, a phenomenon we term the *wave ceiling*. Wave packets are severely arrested by

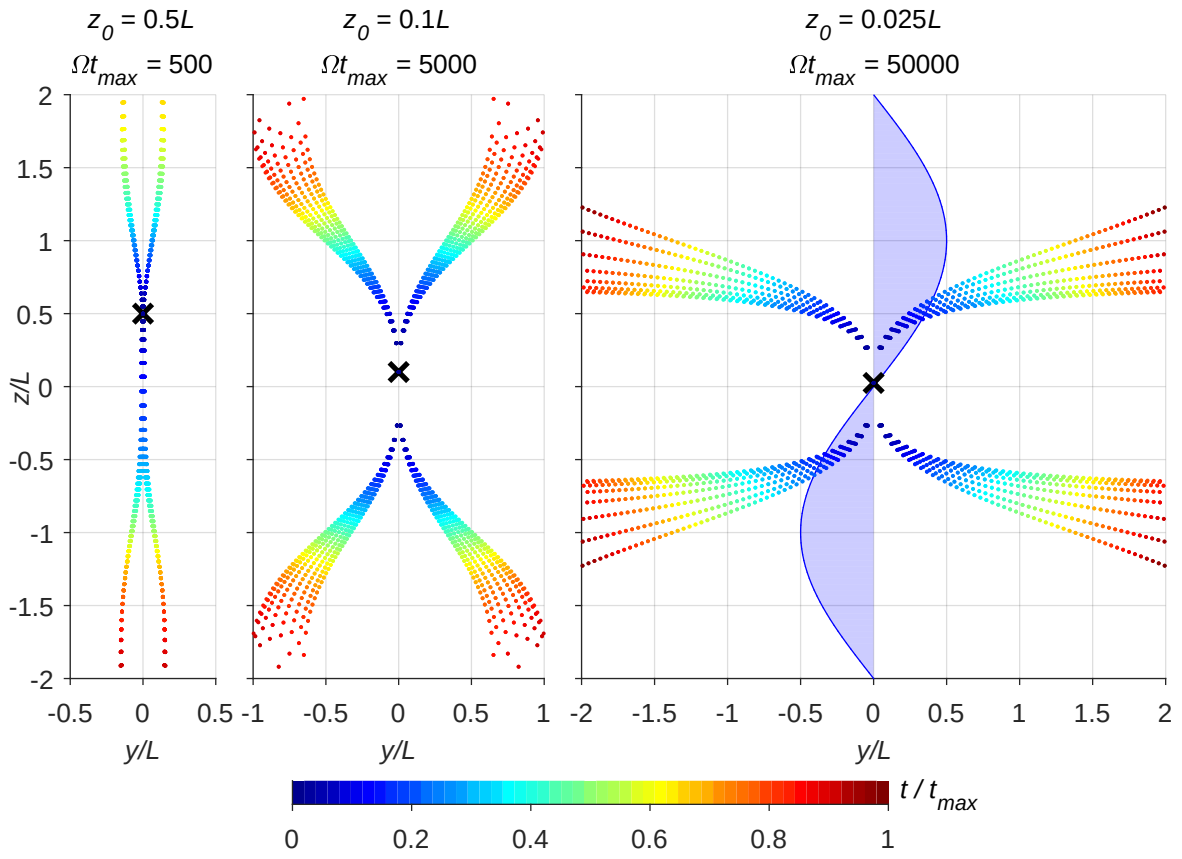

Fig. 6.2.1 Reproduction of figure 4.3.2, showing results of the ray tracing analysis.

this process, as well as being heavily damped by Ohmic diffusion due in the most part to the very short wavelengths they are forced to acquire.

Subtle alterations to the mean magnetic field, in an attempt to approximate something more geophysically relevant, appear to make little substantive change to these conclusions. A more general horizontal field might cause adjacent rays to disperse geometrically to a greater extent, but doesn't alter the propagation velocity significantly. A constant axial field changes the equation of the asymptote which constitutes the wave ceiling, introducing the curious possibility for wave packets to double back and head south (say) despite initially electing to go northward.

In summary, the results of chapter 4 imply that the whole continuum of MC waves available from the hybrid dispersion relation are in fact likely to be realised in the core of the Earth, and not just the inertial and magnetostrophic waves as the well-separated roots hypothesis might suggest, or indeed simply the inertial-Alfvén waves of chapter 3. Each may instead have its own unique role to play – inertial waves in regions of low magnetic field strength, inertial-Alfvén waves in the dispersal of energy from localised disturbances,

and magnetostrophic waves in the quenching of energy at the wave ceiling – with the more general *intermediate MC waves* connecting these limiting cases. Regardless of which class of MC wave one considers, the entire family are excellent conveyors of kinetic and magnetic helicity, and would be able to segregate it north-south from an equatorial source as required to drive a helical-wave dynamo.

6.3 Quasi-geostrophic Rossby waves and westward drift

In chapter 5 and Bardsley (2018) we outlined a new candidate theory for the westward drift of the Earth's magnetic field, as observed in records spanning the past 400 years (Jackson et al., 2000). The theory centres around *quasi-geostrophic Rossby waves*, cousins to waves of the same name ubiquitous in atmospheric dynamics. In the Earth's interior, these take the form of tall, columnar vortices aligned with the rotation axis and impinging upon the CMB at both ends; as they advect each other around the core, the vortices are squashed and stretched by the slope of the CMB, modulating their intensity accordingly and resulting in complex travelling wave possibilities (Busse, 2002). The reason these waves have not yet been proposed as a source of westward drift is obvious: their wave crests always move eastward. This is true both for an isolated wave packet in free space and any one eigenmode in an axisymmetric domain.

The key insight here is that although the *phase* velocity of QG Rossby waves is always eastward, the *group* velocity may be in any direction, and it is this which dictates where the waves will propagate energy. The direction of the group velocity is a function of the dominant wavevector of a particular wave packet, or in other words the size and spatial structure of the waves. Crucially, waves with crests running in the cylindrical radial direction (i.e. parallel to the slope of the CMB) turn out to have a westward group velocity (figure 6.3.1) — and it is exactly these waves which are most likely to be excited by the radial plumes associated with the strongly-forced convection observed in simulations of the outer core (e.g. Schaeffer et al., 2017). What's more, the observed drift rate is compatible with wavelengths in the tens of kilometres, which is a plausible estimate of dominant convective lengthscales in the outer core. Exactly how the propagation of wave packets translates into the observed westward drift has not been answered definitively, though a mechanism involving the sweeping out of a strong azimuthal field into a cylindrical radial one is presented as a possibility.

This theory has the advantage of being – in some sense – reasonably robust. This is because it depends upon small-scale waves which are likely to be reasonably insensitive to the exact nature of the forcing, beside the basic need for it to comprise of radially-extended, sheet-like convective plumes. Also – unlike the magnetic Rossby wave theory due to Hide

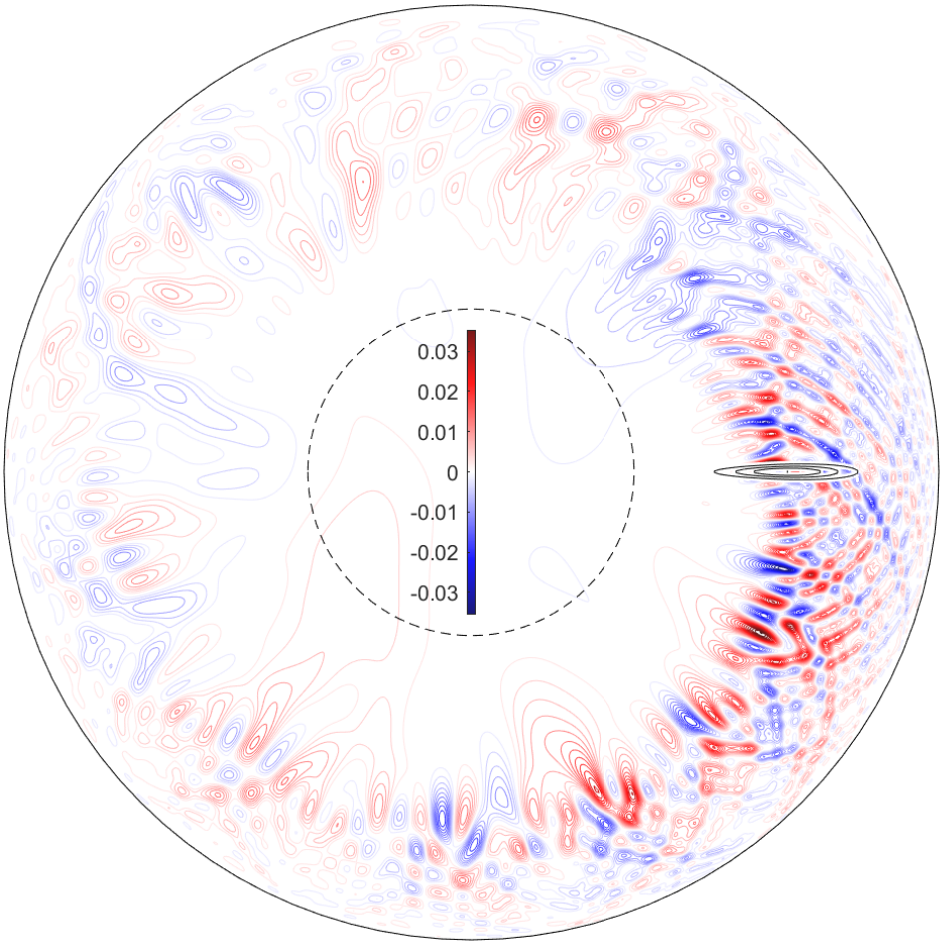

Fig. 6.3.1 Reproduction of figure 5.3.2, showing westward-propagating QG Rossby waves in a full sphere.

(1966) – it does not depend upon the particular arrangement or strength of the unknown internal magnetic field.

However, as a cohesive theory for the westward drift it unfortunately still has some way to go. It is by its very nature dependent upon the quasi-geostrophic hypothesis, with structures which span the entire outer core and therefore have rather extreme aspect ratios which are arguably unattainable in a real planet. The resolution of this discrepancy may come through an adjustment of the wave velocity because it is in container with appreciable slope, or due to slowing down of the waves by other effects, including the mean magnetic field and buoyancy distribution.

Nevertheless, the theory presented here constitutes an intriguing new possibility for explaining this aspect of the secular variation, which it is hoped will be the subject of future attention.

6.4 Future work

We close off this thesis with a look at some possible avenues for future research directly related to the ideas and model problems explored herein. As it is theoretical in nature, the limitations and therefore scope for extensions of this work are numerous — though we highlight a few of what it is hoped are the more fertile routes below.

As alluded to in chapter 3, allying the results of this thesis with numerical simulations of the geodynamo will be the most likely tool to either bolster or disprove our conclusions. Findings in Ranjan et al. (2018) and Aubert (2018) appear to be good first steps toward unlocking the secrets of inertial and inertial-Alfvén waves respectively in the small-scale behaviour of full-scale numerical models, and further reflections on the techniques which might be employed to enable more complete studies have been offered in section 3.2.4. In a related vein, an entertaining extension of the ray tracing work would be to fuse it with a numerical model — that is, to use a magnetic field configuration from a paused simulation as the mean field in a ray tracing problem and use the techniques of chapter 4 to track wave packets as they propagate through it. This could even be compared with an equivalent numerical model problem to see whether the ray tracing hypothesis is able to make reliable predictions of the energy dispersal from a localised source in a varying mean field, including effects such as a dynamic, non-linear source and a finite electrical conductivity.

The hypothesis that quasi-geostrophic Rossby waves are important for the secular variation should also be testable numerically, possibly using similar techniques to Hori et al. (2015) who searched for their magnetic cousins. The complications brought on by having a westward $\boldsymbol{c}_g$ despite an eastward $\boldsymbol{c}_p$ will require very careful treatment, however. Perhaps the most crucial part of the theory to confirm numerically will be the link between wave propagation and B_r change at the CMB — showing westward energy propagation by QG Rossby waves is not sufficient without a link to the magnetic field, and the possibility of rotation of B_ϕ by the strong radial flow is a suggested mechanism in much need of supporting evidence.

A more open-minded look into Alfvén waves in the outer core might also be prescient, incorporating torsional oscillations, inertial-Alfvén waves, and Jault (2008)'s axisymmetric intermediary between the two. This is discussed in section 3.2.4, where we speculate that Alfvén waves – likely in the form of axially-elongated flow structures – might be a more ubiquitous feature in Earth's outer core than they are currently credited with. This work could be done in a full-scale spherical simulation, but it might also be instructive to undertake the relevant DNS in a simplified domain — a periodic cube, say, akin to Davidson & Ranjan (2015) but in the limit of large magnetic Reynolds number. Note that such a study could also be equipped to answer important questions regarding deformation of the buoyant source,

losses due to Ohmic heating, and non-linear phenomena including magnetic induction through the alpha-effect. In light of the intriguing discovery of partial reflection in the WKB analysis when the background magnetic field is inhomogeneous (section 4.4), researching the dispersion of energy from a localised source in a varying $\bar{\boldsymbol{B}}$ using numerical tools would also be of considerable interest.

In our introduction (section 1.1.5) we briefly hinted that the results presented here in the context of Earth may also find application in the study of other rapidly-rotating and dynamo-harbouring planets, although – in the interests of focussing our thoughts – little has been said of this since. This topic is clearly worth some thought, in light of the apparent similarity across planetary dynamos (table 1.1.3). Perhaps the most exciting source of new data is the Juno spacecraft currently orbiting Jupiter and sending back measurements of its internal structure and magnetic field in unprecedented detail (Moore et al., 2018) — it is hoped that these readings, which don't suffer from the 'magnetic curtain' limitation found on Earth, might offer insight into planetary dynamo action in a more broadly applicable sense.

In any case, it is clear that the synthesis of mathematical theory, physical insight, computational power, careful observation and ingenious experimentation will continue to be crucial in the convergence from all sides towards a complete picture of magnetic field generation in the Earth and other planets.

References

Abramowitz, M. & Stegun, I. A. (1964), *Handbook of Mathematical Functions: With Formulas, Graphs, and Mathematical Tables*, Courier Corporation.

Acheson, D. J. (1972), 'The critical level for hydromagnetic waves in a rotating fluid', *Journal of Fluid Mechanics* **53**(03), 401–415.

Acheson, D. J. (1990), *Elementary Fluid Dynamics*, Clarendon Press.

Alfvén, H. (1942), 'Existence of Electromagnetic-Hydrodynamic Waves', *Nature* **150**(3805), 405–406.

Alfvén, H. (1950), *Cosmical Electrodynamics*, Oxford University Press.

Amit, H., Choblet, G., Olson, P., Monteux, J., Deschamps, F., Langlais, B. & Tobie, G. (2015), 'Towards more realistic core-mantle boundary heat flux patterns: a source of diversity in planetary dynamos', *Progress in Earth and Planetary Science* **2**(1), 26.

Aubert, J. (2018), 'Geomagnetic acceleration and rapid hydromagnetic wave dynamics in advanced numerical simulations of the geodynamo', *Geophysical Journal International* **214**(1), 531–547.

Aubert, J. & Finlay, C. C. (2019), Geomagnetic jerks and rapid hydromagnetic waves focusing at earth's core surface. (under review).

Aubert, J., Finlay, C. C. & Fournier, A. (2013), 'Bottom-up control of geomagnetic secular variation by the Earth's inner core', *Nature* **502**(7470), 219–223.

Aubert, J., Gillet, N. & Cardin, P. (2003), 'Quasigeostrophic models of convection in rotating spherical shells', *Geochemistry, Geophysics, Geosystems* **4**(7), 1052.

Aurnou, J. M., Calkins, M. A., Cheng, J. S., Julien, K., King, E. M., Nieves, D., Soderlund, K. M. & Stellmach, S. (2015), 'Rotating convective turbulence in Earth and planetary cores', *Physics of the Earth and Planetary Interiors* **246**, 52–71.

Backus, G. (1958), 'A class of self-sustaining dissipative spherical dynamos', *Annals of Physics* **4**(4), 372–447.

Baqui, Y. B. & Davidson, P. A. (2015), 'A phenomenological theory of rotating turbulence', *Physics of Fluids* **27**(2), 025107.

Bardsley, O. P. (2018), 'Could hydrodynamic Rossby waves explain the westward drift?', *Proc. R. Soc. A* **474**(2213), 20180119.

Bardsley, O. P. & Davidson, P. A. (2016), 'Inertial–Alfvén waves as columnar helices in planetary cores', *Journal of Fluid Mechanics* **805**.

Bardsley, O. P. & Davidson, P. A. (2017), 'The dispersion of magnetic-Coriolis waves in planetary cores', *Geophysical Journal International* **210**(1), 18–26.

Bender, C. M. & Orszag, S. A. (1999), *Advanced Mathematical Methods for Scientists and Engineers I: Asymptotic Methods and Perturbation Theory*, Springer-Verlag, New York.

Bleistein, N. & Handelsman, R. A. (1986), *Asymptotic Expansions of Integrals*, Courier Corporation.

Braginsky, S. I. (1970), 'Torsional Magnetohydrodynamic Vibrations in the Earth's Core and Variations in Day Length', *Geomagnetism and Aeronomy* **10**, 1.

Braginsky, S. I. & Roberts, P. H. (1995), 'Equations governing convection in earth's core and the geodynamo', *Geophysical & Astrophysical Fluid Dynamics* **79**(1-4), 1–97.

Brown, W. J., Mound, J. E. & Livermore, P. W. (2013), 'Jerks abound: An analysis of geomagnetic observatory data from 1957 to 2008', *Physics of the Earth and Planetary Interiors* **223**, 62–76.

Bullard, E. C., Freeman, C., Gellman, H. & Nixon, J. (1950), 'The westward drift of the Earth's magnetic field', *Phil. Trans. R. Soc. Lond. A* **243**(859), 67–92.

Busse, F. H. (1970), 'Thermal instabilities in rapidly rotating systems', *Journal of Fluid Mechanics* **44**(03), 441–460.

Busse, F. H. (2002), 'Convective flows in rapidly rotating spheres and their dynamo action', *Physics of Fluids* **14**(4), 1301–1314.

Canet, E., Finlay, C. C. & Fournier, A. (2014), 'Hydromagnetic quasi-geostrophic modes in rapidly rotating planetary cores', *Physics of the Earth and Planetary Interiors* **229**, 1–15.

Cardin, P. & Olson, P. (1992), 'An experimental approach to thermochemical convection in the Earth's core', *Geophysical Research Letters* **19**(20), 1995–1998.

Cardin, P. & Olson, P. (1994), 'Chaotic thermal convection in a rapidly rotating spherical shell: consequences for flow in the outer core', *Physics of the Earth and Planetary Interiors* **82**(3), 235–259.

Chandrasekhar, S. (1981), *Hydrodynamic and Hydromagnetic Stability*, Courier Corporation.

Chen, L., Herreman, W., Li, K., Livermore, P. W., Luo, J. W. & Jackson, A. (2018), 'The optimal kinematic dynamo driven by steady flows in a sphere', *Journal of Fluid Mechanics* **839**, 1–32.

Christensen, U. R. (2011), 'Geodynamo models: Tools for understanding properties of Earth's magnetic field', *Physics of the Earth and Planetary Interiors* **187**(3–4), 157–169.

Christensen, U. R. & Aubert, J. (2006), 'Scaling properties of convection-driven dynamos in rotating spherical shells and application to planetary magnetic fields', *Geophysical Journal International* **166**(1), 97–114.

Christensen, U. R., Aubert, J. & Hulot, G. (2010), 'Conditions for Earth-like geodynamo models', *Earth and Planetary Science Letters* **296**(3), 487–496.

Christensen, U. R. & Tilgner, A. (2004), 'Power requirement of the geodynamo from ohmic losses in numerical and laboratory dynamos', *Nature* **429**(6988), 169–171.

Christensen, U. & Wicht, J. (2007), 'Numerical Dynamo Simulations', *Core Dynamics, 245-282 (2007)* **8**.

Clement, B. M. (2004), 'Dependence of the duration of geomagnetic polarity reversals on site latitude', *Nature* **428**(6983), 637–640.

Davidson, P. A. (2012), Rapidly-rotating turbulence: an experimental perspective, *in* P. A. Davidson, Y. Kaneda & K. Sreenivasan, eds, 'Ten Chapters in Turbulence', Cambridge University Press, Cambridge, pp. 318–350.

Davidson, P. A. (2013), *Turbulence in Rotating, Stratified and Electrically Conducting Fluids*, Cambridge University Press, Cambridge.

Davidson, P. A. (2014), 'The dynamics and scaling laws of planetary dynamos driven by inertial waves', *Geophysical Journal International* **198**(3), 1832–1847.

Davidson, P. A. (2016), 'Dynamos driven by helical waves: scaling laws for numerical dynamos and for the planets', *Geophysical Journal International* **207**(2), 680–690.

Davidson, P. A. & Ranjan, A. (2015), 'Planetary dynamos driven by helical waves – II', *Geophysical Journal International* **202**(3), 1646–1662.

Davidson, P. A. & Ranjan, A. (2018*a*), 'Are planetary dynamos driven by helical waves?', *Journal of Plasma Physics* **84**(3).

Davidson, P. A. & Ranjan, A. (2018*b*), 'On the spatial segregation of helicity by inertial waves in dynamo simulations and planetary cores', *Journal of Fluid Mechanics* **851**, 268–287.

Davidson, P. A. & Siso-Nadal, F. (2002), 'On the Structure of Small-Scale Motion in the Core of the Earth', *Geophysical & Astrophysical Fluid Dynamics* **96**(1), 49–76.

Davidson, P. A., Staplehurst, P. J. & Dalziel, S. B. (2006), 'On the evolution of eddies in a rapidly rotating system', *Journal of Fluid Mechanics* **557**, 135–144.

de Wijs, G. A., Kresse, G., Vočadlo, L., Dobson, D., Alfè, D., Gillan, M. J. & Price, G. D. (1998), 'The viscosity of liquid iron at the physical conditions of the Earth's core', *Nature* **392**(6678), 805–807.

Desjardins, B., Dormy, E., Gilbert, A. & Proctor, M. (2007), Introduction to Self-Excited Dynamo Action, *in* 'Mathematical Aspects of Natural Dynamos', The Fluid Mechanics of Astrophysics and Geophysics, Chapman and Hall/CRC, pp. 1–59.

Dormy, E. (2016), 'Strong-field spherical dynamos', *Journal of Fluid Mechanics* **789**, 500–513.

Duba, C. T. & McKenzie, J. F. (2012), 'Propagation properties of Rossby waves for latitudinal beta-plane variations of f and zonal variations of the shallow water speed', *Ann. Geophys.* **30**(5), 849–855.

Dumberry, M. & Bloxham, J. (2003), 'Torque balance, Taylor's constraint and torsional oscillations in a numerical model of the geodynamo', *Physics of the Earth and Planetary Interiors* **140**(1–3), 29–51.

Dumberry, M. & Mound, J. (2010), 'Inner core–mantle gravitational locking and the super-rotation of the inner core', *Geophysical Journal International* **181**(2), 806–817.

Elsasser, W. M. (1946), 'Induction Effects in Terrestrial Magnetism Part I. Theory', *Physical Review* **69**(3-4), 106–116.

Finlay, C. (2005), Hydromagnetic waves in Earth's core and their influence on geomagnetic secular variation, PhD thesis, The University of Leeds.

Finlay, C. C., Dumberry, M., Chulliat, A. & Pais, M. A. (2010), 'Short Timescale Core Dynamics: Theory and Observations', *Space Science Reviews* **155**(1-4), 177–218.

Finlay, C. C. & Jackson, A. (2003), 'Equatorially Dominated Magnetic Field Change at the Surface of Earth's Core', *Science* **300**(5628), 2084–2086.

Finlay, C. C., Olsen, N., Kotsiaros, S., Gillet, N. & Tøffner-Clausen, L. (2016), 'Recent geomagnetic secular variation from Swarm and ground observatories as estimated in the CHAOS-6 geomagnetic field model', *Earth, Planets and Space* **68**(1), 112.

Fisk, H. W. (1931), Isopors and isoporic movements, *in* 'Terrestrial Magnetism and Electricity of the International Geodetic and Geophysical Union', Stockholm, pp. 280–292.

Galtier, S. (2016), *Introduction to Modern Magnetohydrodynamics*, Cambridge University Press.

Gilbert, W. (1600), 'De magnete', *London: Peter Short* . (English translation, Chiswick Press, London, 1900).

Gillet, N., Jault, D., Canet, E. & Fournier, A. (2010), 'Fast torsional waves and strong magnetic field within the Earth's core', *Nature* **465**(7294), 74–77.

Gillet, N. & Jones, C. A. (2006), 'The quasi-geostrophic model for rapidly rotating spherical convection outside the tangent cylinder', *Journal of Fluid Mechanics* **554**, 343–369.

Gillet, N., Schaeffer, N. & Jault, D. (2012), 'Rationale and geophysical evidence for quasi-geostrophic rapid dynamics within the earth's outer core', *Physics of the Earth and Planetary Interiors* **202-203**(Supplement C), 78 – 88.

Glatzmaier, G. A. & Roberts, P. H. (1995), 'A three-dimensional self-consistent computer simulation of a geomagnetic field reversal', *Nature* **377**(6546), 203–209.

Gradshteyn, I. S. & Ryzhik, I. M. (1980), *Table of integrals, series, and products*, 4 edn, Academic press.

Greenspan, H. P. (1968), *The theory of rotating fluids*, Cambridge University Press.

Gubbins, D. (1973), 'Numerical solutions of the kinematic dynamo problem', *Phil. Trans. R. Soc. Lond. A* **274**(1241), 493–521.

Gubbins, D. (2001), 'The Rayleigh number for convection in the Earth's core', *Physics of the Earth and Planetary Interiors* **128**(1), 3–12.

Gubbins, D. (2008), 'Implication of kinematic dynamo studies for the geodynamo', *Geophysical Journal International* **173**(1), 79–91.

Gubbins, D. (2013), Thermal Core-Mantle Interactions: Theory and Observations, *in* 'Earth's Core: Dynamics, Structure, Rotation', American Geophysical Union (AGU), pp. 163–179.

Gubbins, D. & Herrero-Bervera, E., eds (2007), *Encyclopedia of Geomagnetism and Paleomagnetism*, Encyclopedia of Earth Sciences Series, Springer Netherlands.

Guervilly, C. & Cardin, P. (2016), 'Subcritical convection of liquid metals in a rotating sphere using a quasi-geostrophic model', *Journal of Fluid Mechanics* **808**, 61–89.

Halley, E. (1692), 'An account of the cause of the change of the variation of the magnetical needle. with an hypothesis of the structure of the internal parts of the earth: as it was proposed to the Royal Society in one of their late meetings', *Philosophical Transactions* **17**(195), 563–578.

Hardy, C. M., Livermore, P. W., Niesen, J., Luo, J. & Li, K. (2018), 'Determination of the instantaneous geostrophic flow within the three-dimensional magnetostrophic regime', *Proc. R. Soc. A* **474**(2218), 20180412.

Henderson, P. & Henderson, G. M. (2009), *The Cambridge Handbook of Earth Science Data*, Cambridge University Press.

Hide, R. (1966), 'Free Hydromagnetic Oscillations of the Earth's Core and the Theory of the Geomagnetic Secular Variation', *Philosophical Transactions of the Royal Society of London A: Mathematical, Physical and Engineering Sciences* **259**(1107), 615–647.

Hide, R. & Roberts, P. H. (1979), 'How strong is the magnetic field in the Earth's liquid core?', *Physics of the Earth and Planetary Interiors* **20**(2), 124–126.

Hinch, E. J. (1991), *Perturbation Methods*, Cambridge University Press, Cambridge.

Holme, R., Olsen, N. & Bairstow, F. L. (2011), 'Mapping geomagnetic secular variation at the core–mantle boundary', *Geophysical Journal International* **186**(2), 521–528.

Hori, K., Jones, C. A. & Teed, R. J. (2015), 'Slow magnetic Rossby waves in the Earth's core', *Geophysical Research Letters* **42**(16), 2015GL064733.

Hori, K., Teed, R. J. & Jones, C. A. (2018), 'The dynamics of magnetic Rossby waves in spherical dynamo simulations: A signature of strong-field dynamos?', *Physics of the Earth and Planetary Interiors* **276**, 68–85.

Hori, K., Wicht, J. & Christensen, U. R. (2010), 'The effect of thermal boundary conditions on dynamos driven by internal heating', *Physics of the Earth and Planetary Interiors* **182**(1–2), 85–97.

Jackson, A. (2003), 'Intense equatorial flux spots on the surface of the Earth's core', *Nature* **424**(6950), 760–763.

Jackson, A. & Finlay, C. (2015), Geomagnetic Secular Variation and Its Applications to the Core, *in* G. Schubert, ed., 'Treatise on Geophysics (Second Edition)', Elsevier, Oxford, pp. 137–184.

Jackson, A., Jonkers, A. R. T. & Walker, M. R. (2000), 'Four centuries of geomagnetic secular variation from historical records', *Philosophical Transactions of the Royal Society of London. Series A: Mathematical, Physical and Engineering Sciences* **358**(1768), 957–990.

Jackson, J. D. (1998), *Classical electrodynamics*, 3 edn, John Wiley & Sons.

Jault, D. (2003), Electromagnetic and topographic coupling, and LOD variations, *in* C. A. Jones, A. M. Soward & K. Zhang, eds, 'Earth's core and lower mantle', The Fluid Mechanics of Astrophysics and Geophysics, Taylor & Francis, London, pp. 56–76.

Jault, D. (2008), 'Axial invariance of rapidly varying diffusionless motions in the Earth's core interior', *Physics of the Earth and Planetary Interiors* **166**(1–2), 67–76.

Jault, D. & Finlay, C. (2015), Waves in the core and mechanical core-mantle interactions, *in* 'Treatise on Geophysics', Vol. 8, Elsevier Science, pp. 225–245.

Jault, D., Gire, C. & Le Mouel, J. L. (1988), 'Westward drift, core motions and exchanges of angular momentum between core and mantle', *Nature* **333**(6171), 353–356.

Jones, C. A. (2011), 'Planetary Magnetic Fields and Fluid Dynamos', *Annual Review of Fluid Mechanics* **43**(1), 583–614.

Julien, K., Rubio, A. M., Grooms, I. & Knobloch, E. (2012), 'Statistical and physical balances in low Rossby number Rayleigh–Bénard convection', *Geophysical & Astrophysical Fluid Dynamics* **106**(4-5), 392–428.

Kageyama, A. & Sato, T. (1997), 'Generation mechanism of a dipole field by a magnetohydrodynamic dynamo', *Physical Review E* **55**(4), 4617–4626.

Keiling, A. (2009), 'Alfvén Waves and Their Roles in the Dynamics of the Earth's Magnetotail: A Review', *Space Science Reviews* **142**(1), 73–156.

Kivelson, M. G. & Russell, C. T. (1995), *Introduction to Space Physics*, Cambridge University Press.

Kloss, C. & Finlay, C. C. (2019), 'Time-dependent low latitude core flow and geomagnetic field acceleration pulses', *Geophysical Journal International* .

Kono, M. & Roberts, P. H. (2002), 'Recent Geodynamo Simulations and Observations of the Geomagnetic Field', *Reviews of Geophysics* **40**(4), 1013.

Kuang, W. & Bloxham, J. (1999), 'Numerical Modeling of Magnetohydrodynamic Convection in a Rapidly Rotating Spherical Shell: Weak and Strong Field Dynamo Action', *Journal of Computational Physics* **153**(1), 51–81.

Labbé, F., Jault, D. & Gillet, N. (2015), 'On magnetostrophic inertia-less waves in quasi-geostrophic models of planetary cores', *Geophysical & Astrophysical Fluid Dynamics* **109**(6), 587–610.

Larmor, J. (1919), 'How could a rotating body such as the sun become a magnet?', *Reports of the British Association* **87**, 159–160.

Lehnert, B. (1954), 'Magnetohydrodynamic Waves Under the Action of the Coriolis Force.', *The Astrophysical Journal* **119**, 647.

Li, K., Jackson, A. & Livermore, P. W. (2018), 'Taylor state dynamos found by optimal control: axisymmetric examples', *Journal of Fluid Mechanics* **853**, 647–697.

Lighthill, S. M. J. (1978), *Waves in Fluids*, Cambridge University Press.

Livermore, P. W., Hollerbach, R. & Jackson, A. (2013), 'Electromagnetically driven westward drift and inner-core superrotation in Earth's core', *Proceedings of the National Academy of Sciences* **110**(40), 15914–15918.

Livermore, P. W., Ierley, G. & Jackson, A. (2008), 'The structure of Taylor's constraint in three dimensions', *Proceedings of the Royal Society of London A: Mathematical, Physical and Engineering Sciences* **464**(2100), 3149–3174.

Loper, D. E. (2001), 'On the structure of a Taylor column driven by a buoyant parcel in an unbounded rotating fluid', *Journal of Fluid Mechanics* **427**, 131–165.

Loper, D. E. & Roberts, P. H. (1981), 'A study of conditions at the inner core boundary of the earth', *Physics of the Earth and Planetary Interiors* **24**(4), 302–307.

Maffei, S. & Jackson, A. (2016), 'Propagation and reflection of diffusionless torsional waves in a sphere', *Geophysical Journal International* **204**(3), 1477–1489.

Maffei, S., Jackson, A. & Livermore, P. W. (2017), 'Characterization of columnar inertial modes in rapidly rotating spheres and spheroids', *Proc. R. Soc. A* **473**(2204), 20170181.

Malkus, W. V. R. & Proctor, M. R. E. (1975), 'The macrodynamics of alpha-effect dynamos in rotating fluids', *Journal of Fluid Mechanics* **67**(3), 417–443.

Matsui, H., Heien, E., Aubert, J., Aurnou, J. M., Avery, M., Brown, B., Buffett, B. A., Busse, F., Christensen, U. R., Davies, C. J., Featherstone, N., Gastine, T., Glatzmaier, G. A., Gubbins, D., Guermond, J.-L., Hayashi, Y.-Y., Hollerbach, R., Hwang, L. J., Jackson, A., Jones, C. A., Jiang, W., Kellogg, L. H., Kuang, W., Landeau, M., Marti, P., Olson, P., Ribeiro, A., Sasaki, Y., Schaeffer, N., Simitev, R. D., Sheyko, A., Silva, L., Stanley, S., Takahashi, F., Takehiro, S.-i., Wicht, J. & Willis, A. P. (2016), 'Performance benchmarks for a next generation numerical dynamo model', *Geochemistry Geophysics Geosystems* **17**(5), 1586–1607.

Matsui, H., King, E. & Buffett, B. (2014), 'Multiscale convection in a geodynamo simulation with uniform heat flux along the outer boundary', *Geochemistry, Geophysics, Geosystems* **15**(8), 3212–3225.

Mitchell, A. (2018), *The Spinning Magnet: The Force That Created the Modern World – and Could Destroy It*, Oneworld Publications.

Moffatt (1978), *Magnetic Field Generation in Electrically Conducting Fluids*, Cambridge University Press.

Moffatt, H. K. & Loper, D. E. (1994), 'The Magnetostrophic Rise of A Buoyant Parcel In the Earth's Core', *Geophysical Journal International* **117**(2), 394–402.

Moore, K. M., Yadav, R. K., Kulowski, L., Cao, H., Bloxham, J., Connerney, J. E. P., Kotsiaros, S., Jørgensen, J. L., Merayo, J. M. G., Stevenson, D. J., Bolton, S. J. & Levin, S. M. (2018), 'A complex dynamo inferred from the hemispheric dichotomy of Jupiter's magnetic field', *Nature* **561**(7721), 76.

Nataf, H.-C. & Gagnière, N. (2008), 'On the peculiar nature of turbulence in planetary dynamos', *Comptes Rendus Physique* **9**(7), 702–710.

Nornberg, M. D., Ji, H., Schartman, E., Roach, A. & Goodman, J. (2010), 'Observation of magnetocoriolis waves in a liquid metal Taylor-Couette experiment', *Physical Review Letters* **104**(7). arXiv: 1002.3791.

Olsen, N. & Mandea, M. (2008), 'Rapidly changing flows in the Earth's core', *Nature Geoscience* **1**(6), 390–394.

Olson, P. (2011), 'Laboratory Experiments on the Dynamics of the Core', *Physics of the Earth and Planetary Interiors* **187**(3), 139–156.

Olson, P., Christensen, U. & Glatzmaier, G. A. (1999), 'Numerical modeling of the geodynamo: Mechanisms of field generation and equilibration', *Journal of Geophysical Research: Solid Earth* **104**(B5), 10383–10404.

Oruba, L. & Dormy, E. (2014), 'Predictive scaling laws for spherical rotating dynamos', *Geophysical Journal International* **198**(2), 828–847.

Pais, M. A. & Jault, D. (2008), 'Quasi-geostrophic flows responsible for the secular variation of the Earth's magnetic field', *Geophysical Journal International* **173**(2), 421–443.

Parker, E. N. (1955), 'Hydromagnetic Dynamo Models.', *The Astrophysical Journal* **122**, 293.

Parker, E. N. (1958), 'Dynamics of the Interplanetary Gas and Magnetic Fields.', *The Astrophysical Journal* **128**, 664.

Pavón-Carrasco, F. J. & De Santis, A. (2016), 'The south Atlantic anomaly: the key for a possible geomagnetic reversal', *Frontiers in Earth Science* **4**.

Pouquet, A. & Mininni, P. D. (2010), 'The interplay between helicity and rotation in turbulence: implications for scaling laws and small-scale dynamics', *Philosophical Transactions of the Royal Society A: Mathematical, Physical and Engineering Sciences* **368**(1916), 1635–1662.

Pozzo, M., Davies, C., Gubbins, D. & Alfè, D. (2014), 'Thermal and electrical conductivity of solid iron and iron-silicon mixtures at Earth's core conditions', *Earth and Planetary Science Letters* **393**, 159–164.

Proudman, J. (1916), 'On the motion of solids in a liquid possessing vorticity', *Proc. R. Soc. Lond. A* **92**(642), 408–424.

Ranjan, A. & Davidson, P. A. (2014), 'Evolution of a turbulent cloud under rotation', *Journal of Fluid Mechanics* **756**, 488–509.

Ranjan, A., Davidson, P. A., Christensen, U. R. & Wicht, J. (2018), 'Internally driven inertial waves in geodynamo simulations', *Geophysical Journal International* **213**(2), 1281–1295.

Roberts, B., Edwin, P. M. & Benz, A. O. (1984), 'On coronal oscillations', *The Astrophysical Journal* **279**, 857–865.

Roberts, P. H. (2007), Theory of the geodynamo, *in* P. Olson, ed., 'Core Dynamics', Elsevier, Amsterdam, pp. 67–105.

Roberts, P. H. & King, E. M. (2013), 'On the genesis of the Earth's magnetism', *Reports on Progress in Physics* **76**(9), 096801. WOS:000324171900005.

Roberts, P. H. & Scott, S. (1965), 'On analysis of the secular variation', *Journal of geomagnetism and geoelectricity* **17**(2), 137–151.

Roberts, P. H. & Wu, C.-C. (2014), 'On the modified Taylor constraint', *Geophysical & Astrophysical Fluid Dynamics* **108**(6), 696–715.

Sakuraba, A. & Roberts, P. H. (2009), 'Generation of a strong magnetic field using uniform heat flux at the surface of the core', *Nature Geoscience* **2**(11), 802–805.

Sakuraba, A. & Roberts, P. H. (2011), On Thermal Driving of the Geodynamo, *in* E. Petrovský, D. Ivers, T. Harinarayana & E. Herrero-Bervera, eds, 'The Earth's Magnetic Interior', number 1 *in* 'IAGA Special Sopron Book Series', Springer Netherlands, pp. 117–129.

Schaeffer, N. & Cardin, P. (2005), 'Quasigeostrophic model of the instabilities of the Stewartson layer in flat and depth-varying containers', *Physics of Fluids* **17**, 104111.

Schaeffer, N. & Cardin, P. (2006), 'Quasi-geostrophic kinematic dynamos at low magnetic Prandtl number', *Earth and Planetary Science Letters* **245**(3), 595–604.

Schaeffer, N., Jault, D., Cardin, P. & Drouard, M. (2012), 'On the reflection of Alfvén waves and its implication for Earth's core modelling', *Geophysical Journal International* **191**(2), 508–516.

Schaeffer, N., Jault, D., Nataf, H.-C. & Fournier, A. (2017), 'Turbulent geodynamo simulations: a leap towards Earth's core', *Geophysical Journal International* **211**(1), 1–29.

Schubert, G. (2015), *Treatise on Geophysics*, Elsevier.

Sheyko, A. (2014), Numerical investigations of rotating MHD in a spherical shell, PhD thesis, ETH-Zürich, Zürich.

Sheyko, A., Finlay, C. C. & Jackson, A. (2016), 'Magnetic reversals from planetary dynamo waves', *Nature* **539**(7630), 551–554.

Sheyko, A., Finlay, C., Favre, J. & Jackson, A. (2018), 'Scale separated low viscosity dynamos and dissipation within the Earth's core', *Scientific Reports* **8**(1), 12566.

Siso-Nadal, F. & Davidson, P. A. (2004), 'Anisotropic evolution of small isolated vortices within the core of the Earth', *Physics of Fluids* **16**(5), 1242–1254.

Siso-Nadal, F., Davidson, P. A. & Graham, W. R. (2003), 'Evolution of a vortex in a rotating conducting fluid', *Journal of Fluid Mechanics* **493**, 181–190.

Smith, P. J. & Needham, J. (1967), 'Magnetic Declination in Mediaeval China', *Nature* **214**(5094), 1213–1214.

Soderlund, K. M., Sheyko, A., King, E. M. & Aurnou, J. M. (2015), 'The competition between Lorentz and Coriolis forces in planetary dynamos', *Progress in Earth and Planetary Science* **2**(1), 24.

Sreenivasan, B. & Jones, C. A. (2006), 'The role of inertia in the evolution of spherical dynamos', *Geophysical Journal International* **164**(2), 467–476.

St Pierre, M. G. (1996), 'On the local nature of turbulence in Earth's outer core', *Geophysical & Astrophysical Fluid Dynamics* **83**(3-4), 293–306.

Staplehurst, P. J., Davidson, P. A. & Dalziel, S. B. (2008), 'Structure formation in homogeneous freely decaying rotating turbulence', *Journal of Fluid Mechanics* **598**, 81–105.

Starchenko, S. V. & Jones, C. A. (2002), 'Typical Velocities and Magnetic Field Strengths in Planetary Interiors', *Icarus* **157**(2), 426–435.

Stevenson, D. J. (1983), 'Planetary magnetic fields', *Reports on Progress in Physics* **46**(5), 555–620.

Takahashi, F., Matsushima, M. & Honkura, Y. (2008), 'Scale variability in convection-driven MHD dynamos at low Ekman number', *Physics of the Earth and Planetary Interiors* **167**(3), 168–178.

Takahashi, F. & Shimizu, H. (2012), 'A detailed analysis of a dynamo mechanism in a rapidly rotating spherical shell', *Journal of Fluid Mechanics* **701**, 228–250.

Taylor, G. I. (1917), 'Motion of solids in fluids when the flow is not irrotational', *Proc. R. Soc. Lond. A* **93**(648), 99–113.

Taylor, G. I. (1922), 'The motion of a sphere in a rotating liquid', *Proc. R. Soc. Lond. A* **102**(715), 180–189.

Taylor, G. I. (1923), 'Experiments on the motion of solid bodies in rotating fluids', *Proc. R. Soc. Lond. A* **104**(725), 213–218.

Taylor, J. B. (1963), 'The Magneto-Hydrodynamics of a Rotating Fluid and the Earth's Dynamo Problem', *Proceedings of the Royal Society of London A: Mathematical, Physical and Engineering Sciences* **274**(1357), 274–283.

Teed, R. J., Jones, C. A. & Tobias, S. M. (2014), 'The dynamics and excitation of torsional waves in geodynamo simulations', *Geophysical Journal International* **196**(2), 724–735.

Teed, R. J., Jones, C. A. & Tobias, S. M. (2015), 'The transition to Earth-like torsional oscillations in magnetoconvection simulations', *Earth and Planetary Science Letters* **419**, 22–31.

Tigrine, Z., Nataf, H.-C., Schaeffer, N., Cardin, P. & Plunian, F. (2018), Torsional Alfvén waves in a dipolar magnetic field: experiments and simulations. (hal-01949364).

Vallis, G. K. (2017), *Atmospheric and Oceanic Fluid Dynamics: Fundamentals and Large-Scale Circulation*, 2 edn, Cambridge University Press.

Walker, M. R., Barenghi, C. F. & Jones, C. A. (1998), 'A note on dynamo action at asymptotically small Ekman number', *Geophysical & Astrophysical Fluid Dynamics* **88**(1-4), 261–275.

Wang, Y.-X., Lu, X.-Y. & Zhuang, L.-X. (2004), 'Numerical analysis of the rotating viscous flow approaching a solid sphere', *International Journal for Numerical Methods in Fluids* **44**(8), 905–925.

Yadav, R. K., Gastine, T. & Christensen, U. R. (2013), 'Scaling laws in spherical shell dynamos with free-slip boundaries', *Icarus* **225**(1), 185–193.

Yadav, R. K., Gastine, T., Christensen, U. R., Wolk, S. J. & Poppenhaeger, K. (2016), 'Approaching a realistic force balance in geodynamo simulations', *Proceedings of the National Academy of Sciences* **113**(43), 12065–12070.

Yukutake, T. (1962), 'The Westward Drift of the Magnetic Field of the Earth', *Bulletin of the Earthquake Reearch Institute - University of Tokyo* **40**, 1–65.

Yukutake, T. (1979), 'Review of the geomagnetic secular variations on the historical time scale', *Physics of the Earth and Planetary Interiors* **20**(2), 83–95.

Zhang, K., Earnshaw, P., Liao, X. & Busse, F. H. (2001), 'On inertial waves in a rotating fluid sphere', *Journal of Fluid Mechanics* **437**, 103–119.

Zhang, K. & Fearn, D. R. (1993), 'How strong is the invisible component of the magnetic field in the earth's core?', *Geophysical Research Letters* **20**(19), 2083–2086.

Appendix A1

Waves at small scales I: Inertial waves

A1.1 Initial value problem: non-magnetic, vortex aligned with the rotation axis

Consider an initial value problem in a rapidly-rotating fluid, in a reference frame rotating with constant angular velocity $\boldsymbol{\Omega} = \Omega \boldsymbol{e}_z$. The initial condition on the velocity field $\boldsymbol{u}_0$ is taken to be a Gaussian-shaped vortex aligned with the rotation axis. Using cylindrical polar co-ordinates (s radial, ϕ azimuthal, z axial) with their origin at the vortex centre, this is

$$\boldsymbol{u}_0(\boldsymbol{r}) = \frac{U}{\ell}\left(\boldsymbol{e}_z \times \boldsymbol{r}\right) e^{-\boldsymbol{r}^2/2\ell^2} = \frac{Us}{\ell} e^{-\boldsymbol{r}^2/2\ell^2} \boldsymbol{e}_\phi, \tag{A1.1.1}$$

where $\boldsymbol{r}$ is the position vector, U a characteristic velocity, and ℓ a characteristic vortex size. At small Rossby number $Ro = U/\Omega\ell$, the time evolution of the flow is governed by the vorticity equation

$$\frac{\partial \boldsymbol{\omega}}{\partial t} = \left(2\boldsymbol{\Omega} \cdot \nabla\right) \boldsymbol{u}, \tag{A1.1.2}$$

where $\boldsymbol{\omega} = \nabla \times \boldsymbol{u}$ (see (2.2.7)). A further curl and time derivative gives an equation for the velocity field $\boldsymbol{u}(\boldsymbol{r}, t)$,

$$\frac{\partial^2}{\partial t^2}\nabla^2 \boldsymbol{u} + \left(2\boldsymbol{\Omega} \cdot \nabla\right)^2 \boldsymbol{u} = 0, \tag{A1.1.3}$$

which has Fourier transform

$$\frac{\partial^2 \hat{\boldsymbol{u}}}{\partial t^2} + \left(\frac{2\boldsymbol{\Omega} \cdot \boldsymbol{k}}{k}\right)^2 \hat{\boldsymbol{u}} = 0, \tag{A1.1.4}$$

where $\boldsymbol{k} = \left[k_x, k_y, k_z\right]^T$ is the wavenumber vector and k its magnitude (see (2.1.3) for definition of the transforms). This means $\hat{\boldsymbol{u}}(\boldsymbol{k}, t)$ may be expressed as the sum of harmonic

functions of time,

$$\hat{\boldsymbol{u}}(\boldsymbol{k},t) = \hat{\boldsymbol{u}}^c(\boldsymbol{k})\cos(\varpi t) + \hat{\boldsymbol{u}}^s(\boldsymbol{k})\sin(\varpi t), \tag{A1.1.5}$$

where the inertial wave frequency ϖ is given by

$$\varpi(\boldsymbol{k}) = \frac{2\boldsymbol{\Omega}\cdot\boldsymbol{k}}{k}, \tag{A1.1.6}$$

and the coefficients $\hat{\boldsymbol{u}}^{c,s}$ are supplied by the initial condition. Specifically, we have

$$\hat{\boldsymbol{u}}^c(\boldsymbol{k}) = \hat{\boldsymbol{u}}(\boldsymbol{k},0) = \hat{\boldsymbol{u}}_0 = iU\ell^4\left[k_y,\ -k_x,\ 0\right]^T e^{-\frac{1}{2}\ell^2k^2}, \tag{A1.1.7}$$

and

$$\hat{\boldsymbol{u}}^s(\boldsymbol{k}) = \frac{1}{\varpi}\left.\frac{\partial\hat{\boldsymbol{u}}}{\partial t}\right|_{t=0}. \tag{A1.1.8}$$

This second coefficient can be found from the curl of (A1.1.2), transformed and evaluated at $t=0$:

$$\hat{\boldsymbol{u}}^s(\boldsymbol{k}) = \hat{\boldsymbol{u}}_0\times\boldsymbol{e}_k = iU\ell^4k^{-1}\left[-k_xk_z,\ -k_yk_z,\ k_x^2+k_y^2\right]^T e^{-\frac{1}{2}\ell^2k^2}. \tag{A1.1.9}$$

For the purposes of evaluating the inverse transforms, we carve up $\boldsymbol{k}$-space using spherical polar co-ordinates (k radial, θ_k polar and ϕ_k azimuthal) around the rotation axis, such that

$$k_x = k\sin\theta_k\cos\phi_k, \quad k_y = k\sin\theta_k\sin\phi_k, \quad k_z = k\cos\theta_k, \tag{A1.1.10}$$

giving

$$\varpi = 2\Omega\cos\theta_k \tag{A1.1.11}$$

and

$$\hat{\boldsymbol{u}}^c = iU\ell^4k\sin\theta_k e^{-\frac{1}{2}\ell^2k^2}\left[\sin\phi_k,\ -\cos\phi_k,\ 0\right]^T, \tag{A1.1.12a}$$

$$\hat{\boldsymbol{u}}^s = iU\ell^4k\sin\theta_k e^{-\frac{1}{2}\ell^2k^2}\left[-\cos\theta_k\cos\phi_k,\ -\cos\theta_k\sin\phi_k,\ \sin\theta_k\right]^T. \tag{A1.1.12b}$$

Let $\boldsymbol{u}^{c,s}$ be the inverse Fourier transform of $\hat{\boldsymbol{u}}^{c,s}\times\frac{\cos}{\sin}(\varpi t)$, and therefore $\boldsymbol{u} = \boldsymbol{u}^c + \boldsymbol{u}^s$ can be calculated through a series of dispersion integrals:

$$\boldsymbol{u}^c = (2\pi)^{-3/2}\iiint_{-\infty}^{\infty}\hat{\boldsymbol{u}}^c\cos(\varpi t)e^{i\boldsymbol{k}\cdot\boldsymbol{r}}\mathrm{d}^3\boldsymbol{k}, \quad \boldsymbol{u}^s = (2\pi)^{-3/2}\iiint_{-\infty}^{\infty}\hat{\boldsymbol{u}}^s\sin(\varpi t)e^{i\boldsymbol{k}\cdot\boldsymbol{r}}\mathrm{d}^3\boldsymbol{k}. \tag{A1.1.13}$$

We now make use of the fact that the problem is axisymmetric, and therefore the solution will be independent of ϕ. This means we only need evaluate the solution in a single constant-ϕ plane, replacing the horizontal distance from the z-axis by the cylindrical radius s. We

choose the y-z plane ($x = 0$) and replace y with s; considering first the azimuthal velocity, we have

$$u_\phi = -\left(u_x^c + u_x^s\right)_{x=0,y\to s} \tag{A1.1.14a}$$

$$= -\left.u_x^c\right|_{x=0,y\to s} + 0 \tag{A1.1.14b}$$

$$= \frac{U\ell^4}{(2\pi)^{3/2}} \int_0^\infty k^3 e^{-\frac{1}{2}\ell^2 k^2} \int_0^\pi \sin^2\theta_k \cos\left(2\Omega t \cos\theta_k\right) \int_{-\pi}^\pi \sin\phi_k \sin\left(\boldsymbol{k}\cdot\boldsymbol{r}\right) \mathrm{d}\phi_k \mathrm{d}\theta_k \mathrm{d}k \tag{A1.1.14c}$$

$$= \frac{U\ell^4}{\sqrt{2\pi}} \sum_\pm \int_0^\infty k^3 e^{-\frac{1}{2}\ell^2 k^2} \int_0^{\pi/2} \sin^2\theta_k \cos\left(\left[2\Omega t \pm kz\right]\cos\theta_k\right) J_1(ks\sin\theta_k) \mathrm{d}\theta_k \mathrm{d}k \tag{A1.1.14d}$$

$$= \frac{U\ell^4 s}{2} \sum_\pm \int_0^\infty k^4 e^{-\frac{1}{2}\ell^2 k^2} J_{3/2}^*\left(\Pi_\pm\right) \mathrm{d}k, \tag{A1.1.14e}$$

where J_ν is the Bessel function of the first kind, $J_\nu^*(x) = x^{-\nu} J_\nu(x)$, and $\Pi_\pm^2 = k^2 s^2 + \left[2\Omega t \pm kz\right]^2$. The final step uses formula 6.688.2 from (Gradshteyn & Ryzhik, 1980). Integrations which are very similar in form, but more complicated in execution, can be performed for the other two components; the results are

$$u_s = \left.u_y^s\right|_{x=0,y\to s} = \frac{U\ell^4 s}{2} \sum_\pm \int_0^\infty k^4 e^{-\frac{1}{2}\ell^2 k^2} \left[2\Omega t \pm kz\right] J_{5/2}^*\left(\Pi_\pm\right) \mathrm{d}k \tag{A1.1.15}$$

and

$$u_z = \left.u_z^s\right|_{x=0,y\to s} = \frac{U\ell^4}{2} \sum_\pm \pm \int_0^\infty k^3 e^{-\frac{1}{2}\ell^2 k^2} \left[J_{1/2}^*\left(\Pi_\pm\right) - J_{3/2}^*\left(\Pi_\pm\right) + \left[2\Omega t \pm kz\right]^2 J_{5/2}^*\left(\Pi_\pm\right)\right] \mathrm{d}k. \tag{A1.1.16}$$

This completes the solution, and the final one-dimensional integrations over wavenumber vector magnitude must be computed numerically. Note that to solve for vorticity $\boldsymbol{\omega}$ instead of $\boldsymbol{u}$, one simply multiplies the integrands by $\pm k$.

A1.2 Initial value problem: non-magnetic, vortex axis perpendicular to the rotation axis

Here, we consider an initial value problem very similar to that of section A1.1, with a 'Gaussian-shaped' vortex as the initial condition. Here, the vortex axis is aligned perpendic-

ular to the bulk rotation axis rather than parallel to it; specifically, we choose

$$\boldsymbol{u}_0(\boldsymbol{r}) = \frac{U}{\ell}\left(\boldsymbol{e}_x \times \boldsymbol{r}\right) e^{-\boldsymbol{r}^2/2\ell^2} = \frac{U}{\ell} e^{-\boldsymbol{r}^2/2\ell^2} \left[0, -z, y\right]^T. \tag{A1.2.1}$$

Note that a weighted sum of this solution and the aligned vortex of section A1.1, plus some co-ordinate rotation about $\boldsymbol{e}_z$, allows us to solve for a vortex of arbitrary orientation as the initial condition.

The solution procedure is much the same as section A1.1, in that the Fourier transform of the solution may be written

$$\hat{\boldsymbol{u}}(\boldsymbol{k}, t) = \hat{\boldsymbol{u}}^c(\boldsymbol{k}) \cos\left(\varpi t\right) + \hat{\boldsymbol{u}}^s(\boldsymbol{k}) \sin\left(\varpi t\right), \tag{A1.2.2}$$

where $\varpi = 2\Omega\cos\theta_k$. The coefficients are now

$$\hat{\boldsymbol{u}}^c(\boldsymbol{k}) = iU\ell^4 k e^{-\frac{1}{2}\ell^2 k^2} \left[0,\ \cos\theta_k,\ -\sin\theta_k \sin\phi_k\right]^T, \tag{A1.2.3a}$$

$$\hat{\boldsymbol{u}}^s(\boldsymbol{k}) = iU\ell^4 k e^{-\frac{1}{2}\ell^2 k^2} \begin{bmatrix} \sin^2\theta_k \sin^2\phi_k + \cos^2\theta_k \\ -\sin^2\theta_k \sin\phi_k \cos\phi_k \\ -\sin\theta_k \cos\theta_k \cos\phi_k \end{bmatrix}. \tag{A1.2.3b}$$

It is most convenient to write the dispersion integrals using an amalgamation of Cartesian $[x, y, z]$ and cylindrical polar $[s, \phi, z]$ co-ordinate systems, as well as the shorthands $J^*_\nu(x) = x^{-\nu} J_\nu(x)$ and $\Pi^2_\pm = k^2 s^2 + [2\Omega t \pm kz]^2$ from section A1.1. They are

$$\begin{aligned} u_x = {} & \frac{U\ell^4 \cos^2\phi}{2} \sum_\pm \pm \int_0^\infty k^3 e^{-\frac{1}{2}\ell^2 k^2} \left[J^*_{1/2}(\Pi_\pm) - J^*_{3/2}(\Pi_\pm) + k^2 s^2 J^*_{5/2}(\Pi_\pm)\right] \mathrm{d}k \\ & + \frac{U\ell^4 \sin^2\phi}{2} \sum_\pm \pm \int_0^\infty k^3 e^{-\frac{1}{2}\ell^2 k^2} \left[2J^*_{3/2}(\Pi_\pm) - \Pi^2_\pm J^*_{5/2}(\Pi_\pm)\right] \mathrm{d}k, \end{aligned} \tag{A1.2.4a}$$

$$\begin{aligned} u_y = {} & \frac{U\ell^4}{2} \sum_\pm \pm \int_0^\infty k^3 e^{-\frac{1}{2}\ell^2 k^2} \left[2\Omega t \pm kz\right] J^*_{3/2}(\Pi_\pm) \, \mathrm{d}k \\ & + \frac{U\ell^4 xy}{2} \sum_\pm \pm \int_0^\infty k^5 e^{-\frac{1}{2}\ell^2 k^2} J^*_{5/2}(\Pi_\pm) \, \mathrm{d}k, \end{aligned} \tag{A1.2.4b}$$

$$u_z = \frac{U\ell^4 y}{2} \sum_\pm \int_0^\infty k^4 e^{-\frac{1}{2}\ell^2 k^2} J^*_{3/2}(\Pi_\pm) \, \mathrm{d}k + \frac{U\ell^4 x}{2} \sum_\pm \int_0^\infty k^4 e^{-\frac{1}{2}\ell^2 k^2} \left[2\Omega t \pm kz\right] J^*_{5/2}(\Pi_\pm) \, \mathrm{d}k. \tag{A1.2.4c}$$

A1.3 Initial value problem: non-magnetic, buoyant blob

Consider an initial value problem in which a localised region of buoyant material (or 'blob') is spontaneously introduced into a rapidly-rotating fluid. The reference frame rotates with the fluid at an angular velocity $\boldsymbol{\Omega} = \Omega \boldsymbol{e}_z$. The fluid is taken to be Boussinesq and we do not solve for the evolution of the buoyancy field, meaning the gravitational acceleration term in the momentum equation acts as a static forcing. The flow is governed by the vorticity equation (2.2.26),

$$\frac{\partial \boldsymbol{\omega}}{\partial t} = (2\boldsymbol{\Omega} \cdot \nabla)\, \boldsymbol{u} + \nabla c \times \boldsymbol{g}, \tag{A1.3.1}$$

and the continuity equation $\nabla \cdot \boldsymbol{u} = 0$. Here $c(\boldsymbol{r}) = \rho'(\boldsymbol{r})/\rho$, is the relative density perturbation and $\boldsymbol{g}$ is the (constant) acceleration due to gravity. We take $\boldsymbol{g} = -g\boldsymbol{e}_x$ to be in the negative x-direction and a localised Gaussian-shaped density perturbation,

$$c(\boldsymbol{r}) = Ce^{-\boldsymbol{r}^2/2\ell^2}. \tag{A1.3.2}$$

The magnitude C is a negative constant since the blob is buoyant.

Particular integral

The vorticity equation (A1.3.1) has a steady particular solution; namely, the velocity field $\boldsymbol{u}_{PI}(\boldsymbol{r})$ which solves

$$(2\boldsymbol{\Omega} \cdot \nabla)\, \boldsymbol{u}_{PI} = \boldsymbol{g} \times \nabla c \tag{A1.3.3a}$$

$$\frac{\partial \boldsymbol{u}_{PI}}{\partial z} = \frac{g}{2\Omega} \nabla c \times \boldsymbol{e}_x = \frac{Cg}{2\Omega\ell^2} e^{-\boldsymbol{r}^2/2\ell^2} \left[0,\ -z,\ y\right]^T, \tag{A1.3.3b}$$

which is

$$\boldsymbol{u}_{PI} = \frac{Cg}{2\Omega} e^{-r_\perp^2/2\ell^2} \begin{bmatrix} 0 \\ e^{-z^2/2\ell^2} \\ \sqrt{\frac{\pi}{2}} \frac{y}{\ell} \operatorname{erf}\left(\frac{z}{\sqrt{2}\ell}\right) \end{bmatrix} + \boldsymbol{u}_{PI}^G(\boldsymbol{r}_\perp), \tag{A1.3.4}$$

where $\boldsymbol{u}_{PI}^G$ is the as-of-yet-undetermined 'geostrophic' portion of the flow, independent of the axial co-ordinate z. This will emerge in the long-time behaviour of the time-dependent flow, so we will not consider it as belonging the particular integral.

We may also express the particular integral in Fourier space (defined by 2.1.3); the transform of (A1.3.3a) gives

$$\hat{\boldsymbol{u}}_{PI} = \frac{\boldsymbol{g} \times \boldsymbol{k}}{2\boldsymbol{\Omega} \cdot \boldsymbol{k}} \hat{c} = \frac{Cg\ell^3}{2\Omega} e^{-\frac{1}{2}\ell^2 k^2} \left[0,\ 1,\ -k_y/k_z\right]^T \tag{A1.3.5}$$

where $\boldsymbol{k} = [k_x,\ k_y,\ k_z]^T$ is the wavenumber vector, and $\hat{c} = C\ell^3 e^{-\frac{1}{2}\ell^2 k^2}$ is the transform of the buoyancy field.

Complementary function

We now seek a solution to (A1.3.1) which is time-dependent, by writing the velocity field as the sum of the just-calculated particular integral and a complementary function $\boldsymbol{u}_{CF}$,

$$\boldsymbol{u}(\boldsymbol{r},t) = \boldsymbol{u}_{PI}(\boldsymbol{r}) + \boldsymbol{u}_{CF}(\boldsymbol{r},t). \tag{A1.3.6}$$

Substituting this into (A1.3.1), we find that $\boldsymbol{u}_{CF}$ obeys the inertial wave equation (2.2.8) and therefore, akin to Appendix A1.1, its Fourier transform may be written

$$\hat{\boldsymbol{u}}_{CF} = \hat{\boldsymbol{u}}^c_{CF}(\boldsymbol{k})\cos(\varpi t) + \hat{\boldsymbol{u}}^s_{CF}(\boldsymbol{k})\sin(\varpi t), \tag{A1.3.7}$$

where $\varpi(\boldsymbol{k}) = 2\boldsymbol{\Omega}\cdot\boldsymbol{k}/k$ is the inertial wave frequency. The initial condition is that the velocity field is zero when the buoyant blob is spontaneously introduced, and therefore

$$\boldsymbol{u}(\boldsymbol{r},0) = \boldsymbol{u}_{PI}(\boldsymbol{r}) + \boldsymbol{u}_{CF}(\boldsymbol{r},0) = 0 \quad\Longrightarrow\quad \hat{\boldsymbol{u}}^c_{CF} = -\hat{\boldsymbol{u}}_{PI} = \frac{\boldsymbol{e}_k\times\boldsymbol{g}}{\varpi}\hat{c}. \tag{A1.3.8}$$

To find $\hat{\boldsymbol{u}}^s_{CF}$, we need to find the initial flow acceleration. Taking the Fourier transform of the curl of the vorticity equation (A1.3.1) at $t=0$ gives

$$\left.\frac{\partial\hat{\boldsymbol{u}}}{\partial t}\right|_{t=0} = \frac{\boldsymbol{k}\times(\boldsymbol{g}\times\boldsymbol{k})}{k^2}\hat{c} \quad\Longrightarrow\quad \hat{\boldsymbol{u}}^s_{CF} = \frac{\boldsymbol{e}_k\times(\boldsymbol{g}\times\boldsymbol{e}_k)}{\varpi}\hat{c} \tag{A1.3.9}$$

Inverse Fourier transforms

Let $\boldsymbol{u}^{c,s}_{CF}$ be the inverse Fourier transform of $\hat{\boldsymbol{u}}^{c,s}_{CF}\times\begin{matrix}\cos\\ \sin\end{matrix}(\varpi t)$, and therefore $\boldsymbol{u}_{CF} = \boldsymbol{u}^c_{CF} + \boldsymbol{u}^s_{CF}$ can be calculated through a series of dispersion integrals:

$$\boldsymbol{u}^c_{CF} = (2\pi)^{-3/2}\iiint_{-\infty}^{\infty}\hat{\boldsymbol{u}}^c_{CF}\cos(\varpi t)e^{i\boldsymbol{k}\cdot\boldsymbol{r}}\mathrm{d}^3\boldsymbol{k}, \tag{A1.3.10a}$$

$$\boldsymbol{u}^s_{CF} = (2\pi)^{-3/2}\iiint_{-\infty}^{\infty}\hat{\boldsymbol{u}}^s_{CF}\sin(\varpi t)e^{i\boldsymbol{k}\cdot\boldsymbol{r}}\mathrm{d}^3\boldsymbol{k}. \tag{A1.3.10b}$$

In component form, these reduce to

$$u^c_{CF,y} = \frac{-gC\ell^3}{4\Omega}\sum_{\pm}\int_0^{\infty}k^2 e^{-\frac{1}{2}\ell^2k^2}J^*_{1/2}(\Pi_{\pm})\,\mathrm{d}k, \tag{A1.3.11a}$$

$$\frac{\partial u^c_{CF,z}}{\partial(\Omega t)} = \frac{-gC\ell^3}{2\Omega} y \sum_{\pm} \pm \int_0^\infty k^3 e^{-\frac{1}{2}\ell^2 k^2} J^*_{3/2}(\Pi_\pm)\,\mathrm{d}k, \tag{A1.3.11b}$$

$$\frac{\partial u^s_{CF,x}}{\partial(\Omega t)} = \frac{-gC\ell^3}{2\Omega} \sum_{\pm} \int_0^\infty k^2 e^{-\frac{1}{2}\ell^2 k^2} \left[J^*_{1/2}(\Pi_\pm) - J^*_{3/2}(\Pi_\pm)\right] \mathrm{d}k$$
$$- \frac{gC\ell^3}{2\Omega} x^2 \sum_{\pm} \int_0^\infty k^4 e^{-\frac{1}{2}\ell^2 k^2} J^*_{5/2}(\Pi_\pm)\,\mathrm{d}k, \tag{A1.3.11c}$$

$$\frac{\partial u^s_{CF,y}}{\partial(\Omega t)} = \frac{-gC\ell^3}{2\Omega} xy \sum_{\pm} \int_0^\infty k^4 e^{-\frac{1}{2}\ell^2 k^2} J^*_{5/2}(\Pi_\pm)\,\mathrm{d}k, \tag{A1.3.11d}$$

$$u^s_{CF,z} = \frac{-gC\ell^3}{4\Omega} x \sum_{\pm} \mp \int_0^\infty k^3 e^{-\frac{1}{2}\ell^2 k^2} J^*_{3/2}(\Pi_\pm)\,\mathrm{d}k. \tag{A1.3.11e}$$

Here, $J^*_\nu(x) = x^{-\nu} J_\nu(x)$ where $J_\nu(x)$ is the Bessel function of the first kind, and $\Pi^2_\pm = [2\Omega t \pm kz]^2 + k^2 r^2_\perp$.

Vorticity

The vorticity can also be found in two halves; the particular integral, by differentiating (A1.3.4), is

$$\boldsymbol{\omega}_{PI} = \frac{gC}{2\Omega\ell} e^{-r^2_\perp/2\ell^2} \begin{bmatrix} \sqrt{\frac{\pi}{2}}\left[1 - \frac{y^2}{\ell^2}\right] \mathrm{erf}\left(\frac{z}{\sqrt{2}\ell}\right) + \frac{z}{\ell} e^{-z^2/2\ell^2} \\ \sqrt{\frac{\pi}{2}} \frac{xy}{\ell^2} \mathrm{erf}\left(\frac{z}{\sqrt{2}\ell}\right) \\ -\frac{x}{\ell} e^{-z^2/2\ell^2} \end{bmatrix}. \tag{A1.3.12}$$

The complementary function is given by the same integrals (A1.3.11a)–(A1.3.11e) as the velocity field, but with the integrands multiplied by $\pm k$ in each case.

Appendix A2

Waves at small scales II: Magnetic waves

A2.1 Initial value problem: magnetic, buoyant blob

Consider an initial value problem identical to that of appendix A1.3, studying the radiation of waves from a localised buoyant anomaly, but now with a constant mean magnetic field $\bar{\boldsymbol{B}}$ as well as the background rotation. The flow in governed by the linearised ideal vorticity and induction equations (3.1.27) and (3.1.26b),

$$\frac{\partial \boldsymbol{\omega}}{\partial t} = (2\boldsymbol{\Omega}\cdot\nabla)\,\boldsymbol{u} + \frac{1}{\rho\mu}\left(\bar{\boldsymbol{B}}\cdot\nabla\right)\nabla\times\boldsymbol{b} + \nabla c\times\boldsymbol{g}, \tag{A2.1.1a}$$

$$\frac{\partial \boldsymbol{b}}{\partial t} = \left(\bar{\boldsymbol{B}}\cdot\nabla\right)\boldsymbol{u}, \tag{A2.1.1b}$$

plus $\nabla\times\boldsymbol{u}=\boldsymbol{\omega}$ and $\nabla\cdot\boldsymbol{u}=\nabla\cdot\boldsymbol{b}=0$, which combine to give the hybrid wave equation (3.1.14) for $\boldsymbol{u}$:

$$\left[\frac{\partial^2}{\partial t^2} - \frac{1}{\rho\mu}\left(\bar{\boldsymbol{B}}\cdot\nabla\right)^2\right]^2 \nabla^2\boldsymbol{u} + (2\boldsymbol{\Omega}\cdot\nabla)^2\,\frac{\partial^2\boldsymbol{u}}{\partial t^2} = 0. \tag{A2.1.2}$$

Taking the three-dimensional spatial Fourier transform (2.1.3), this becomes

$$\left(\frac{\partial^2}{\partial t^2} + \varpi_B^2\right)^2 \hat{\boldsymbol{u}} + \varpi_\Omega^2\,\frac{\partial^2\hat{\boldsymbol{u}}}{\partial t^2} = 0, \tag{A2.1.3}$$

where $\varpi_B = \bar{\boldsymbol{B}}\cdot\boldsymbol{k}/\sqrt{\rho\mu}$ is the Alfvén wave frequency and $\varpi_\Omega = 2\boldsymbol{\Omega}\cdot\boldsymbol{k}/k$ is the inertial wave frequency. Seeking harmonic solutions in time, we may write $\hat{\boldsymbol{u}}$ as

$$\hat{\boldsymbol{u}}(\boldsymbol{k},t) = \hat{\boldsymbol{u}}_+ + \hat{\boldsymbol{u}}_-, \qquad \hat{\boldsymbol{u}}_\pm(\boldsymbol{k},t) = \hat{\boldsymbol{u}}_\pm^c(\boldsymbol{k})\cos(\varpi_\pm t) + \hat{\boldsymbol{u}}_\pm^s(\boldsymbol{k})\sin(\varpi_\pm t), \tag{A2.1.4}$$

wherein the frequencies are given by

$$\varpi_\pm(\boldsymbol{k}) = \frac{\varpi_\Omega}{2}\left(1 \pm \sqrt{1+\left(\frac{2\varpi_B}{\varpi_\Omega}\right)^2}\right). \tag{A2.1.5}$$

The coefficients $\hat{\boldsymbol{u}}_\pm^{c,s}$ derive from the initial condition $\boldsymbol{u} = \boldsymbol{b} = 0$, plugged into successive time derivatives of (A2.1.1a):

$$\hat{\boldsymbol{u}}|_{t=0} = 0 \qquad \Longrightarrow \qquad \hat{\boldsymbol{u}}_+^c + \hat{\boldsymbol{u}}_-^c = 0 \tag{A2.1.6a}$$

$$\left.\frac{\partial \hat{\boldsymbol{u}}}{\partial t}\right|_{t=0} = \boldsymbol{e}_k \times \left(\boldsymbol{g} \times \boldsymbol{e}_k\right)\hat{c} \qquad \Longrightarrow \qquad \varpi_+ \hat{\boldsymbol{u}}_+^s + \varpi_- \hat{\boldsymbol{u}}_-^s = \boldsymbol{e}_k \times \left(\boldsymbol{g} \times \boldsymbol{e}_k\right)\hat{c} \tag{A2.1.6b}$$

$$\left.\frac{\partial^2 \hat{\boldsymbol{u}}}{\partial t^2}\right|_{t=0} = \varpi_\Omega \left(\boldsymbol{g} \times \boldsymbol{e}_k\right)\hat{c} \qquad \Longrightarrow \qquad \varpi_+^2 \hat{\boldsymbol{u}}_+^c + \varpi_-^2 \hat{\boldsymbol{u}}_-^c = \varpi_\Omega \left(\boldsymbol{e}_k \times \boldsymbol{g}\right)\hat{c} \tag{A2.1.6c}$$

$$\left.\frac{\partial^3 \hat{\boldsymbol{u}}}{\partial t^3}\right|_{t=0} = -\left[\varpi_\Omega^2 + \varpi_B^2\right]\boldsymbol{e}_k \times \left(\boldsymbol{g} \times \boldsymbol{e}_k\right)\hat{c} \qquad \Longrightarrow \qquad \varpi_+^3 \hat{\boldsymbol{u}}_+^s + \varpi_-^3 \hat{\boldsymbol{u}}_-^s = \left[\varpi_\Omega^2 + \varpi_B^2\right]\boldsymbol{e}_k \times \left(\boldsymbol{g} \times \boldsymbol{e}_k\right)\hat{c}. \tag{A2.1.6d}$$

Eliminating for the coefficients, we get

$$\hat{\boldsymbol{u}}_\pm^c = \pm\left[1+\left(\frac{2\varpi_B}{\varpi_\Omega}\right)^2\right]^{-1/2} \frac{\left(\boldsymbol{e}_k \times \boldsymbol{g}\right)\hat{c}}{\varpi_\Omega}, \tag{A2.1.7a}$$

$$\hat{\boldsymbol{u}}_\pm^s = \pm\left[1+\left(\frac{2\varpi_B}{\varpi_\Omega}\right)^2\right]^{-1/2} \frac{\boldsymbol{e}_k \times \left(\boldsymbol{g} \times \boldsymbol{e}_k\right)\hat{c}}{\varpi_\Omega}. \tag{A2.1.7b}$$

This completes the solution for $\hat{\boldsymbol{u}}$ in Fourier space. The vorticity and perturbation magnetic fields are subsequently given by

$$\hat{\boldsymbol{\omega}} = \sum_\pm i k\left(-\hat{\boldsymbol{u}}_\pm^s \cos\left(\varpi_\pm t\right) + \hat{\boldsymbol{u}}_\pm^c \sin\left(\varpi_\pm t\right)\right), \tag{A2.1.8a}$$

$$\frac{\hat{\boldsymbol{b}}}{\sqrt{\rho\mu}} = \sum_\pm \frac{i\varpi_B}{\varpi_\pm}\left(\hat{\boldsymbol{u}}_\pm^s\left[1-\cos\left(\varpi_\pm t\right)\right] + \hat{\boldsymbol{u}}_\pm^c \sin\left(\varpi_\pm t\right)\right). \tag{A2.1.8b}$$

Note that the coefficients (A2.1.7a) and (A2.1.7b) are very similar to those in the non-magnetic case (A1.3.8) and (A1.3.9), only multiplied by $\pm\left[1+(2\varpi_B/\varpi_\Omega)^2\right]^{-1/2}$ (though the $\pm$ is not the same as that in appendix A1.3).

A2.1.1 Aligned-field case

In the case when the magnetic field is aligned with the background rotation vector, $\bar{\boldsymbol{B}} = \bar{B}\boldsymbol{e}_z$, the parameter $2\varpi_B/\varpi_\Omega$ which distinguishes this case from the non-magnetic one is a

function only of the magnitude of $\boldsymbol{k}$, and not its orientation:

$$\frac{2\varpi_B}{\varpi_\Omega} = \frac{\bar{\boldsymbol{B}}\cdot\boldsymbol{k}/\sqrt{\rho\mu}}{\boldsymbol{\Omega}\cdot\boldsymbol{k}/k} = \frac{\bar{B}k/\sqrt{\rho\mu}}{\Omega} = Le\times\ell k, \tag{A2.1.9}$$

where $Le = \bar{B}/\Omega\ell\sqrt{\rho\mu}$ is the Lehnert number (see equation 3.1.17). Hence the results (A1.3.11a)-(A1.3.11e) from appendix A1.3 carry straight over, only now being multiplied by an additional factor, with a new frequency, and summed over two sign choices:

$$u_y^c = \frac{-gC}{4\Omega}\sum_{\pm,(\pm)}(\pm)\int_0^\infty \kappa^2 e^{-\frac{1}{2}\kappa^2}\left[1+Le^2\kappa^2\right]^{-1/2} J^*_{1/2}\left(\Pi_\pm^{(\pm)}\right)\mathrm{d}\kappa, \tag{A2.1.10a}$$

$$\frac{\partial u_z^c}{\partial(\Omega t)} = \frac{-gC}{2\Omega}\frac{y}{\ell}\sum_{\pm,(\pm)}\pm(\pm)\int_0^\infty \kappa^3 e^{-\frac{1}{2}\kappa^2}\left[1+Le^2\kappa^2\right]^{-1/2} J^*_{3/2}\left(\Pi_\pm^{(\pm)}\right)\mathrm{d}\kappa, \tag{A2.1.10b}$$

$$\frac{\partial u_x^s}{\partial(\Omega t)} = \frac{-gC}{2\Omega}\sum_{\pm,(\pm)}(\pm)\int_0^\infty \kappa^2 e^{-\frac{1}{2}\kappa^2}\left[1+Le^2\kappa^2\right]^{-1/2}\left[J^*_{1/2}\left(\Pi_\pm^{(\pm)}\right) - J^*_{3/2}\left(\Pi_\pm^{(\pm)}\right)\right]\mathrm{d}\kappa$$
$$-\frac{gC}{2\Omega}\left(\frac{x}{\ell}\right)^2\sum_{\pm,(\pm)}(\pm)\int_0^\infty \kappa^4 e^{-\frac{1}{2}\kappa^2}\left[1+Le^2\kappa^2\right]^{-1/2} J^*_{5/2}\left(\Pi_\pm^{(\pm)}\right)\mathrm{d}\kappa, \tag{A2.1.10c}$$

$$\frac{\partial u_y^s}{\partial(\Omega t)} = \frac{-gC}{2\Omega}\frac{xy}{\ell^2}\sum_{\pm,(\pm)}(\pm)\int_0^\infty \kappa^4 e^{-\frac{1}{2}\kappa^2}\left[1+Le^2\kappa^2\right]^{-1/2} J^*_{5/2}\left(\Pi_\pm^{(\pm)}\right)\mathrm{d}\kappa, \tag{A2.1.10d}$$

$$u_z^s = \frac{-gC}{4\Omega}\frac{x}{\ell}\sum_{\pm,(\pm)}\mp(\pm)\int_0^\infty \kappa^3 e^{-\frac{1}{2}\kappa^2}\left[1+Le^2\kappa^2\right]^{-1/2} J^*_{3/2}\left(\Pi_\pm^{(\pm)}\right)\mathrm{d}\kappa. \tag{A2.1.10e}$$

We use $\kappa = k\ell$ for convenience, and have a new definition for $\Pi_\pm^{(\pm)}$:

$$\Pi_\pm^{(\pm)} = \sqrt{\left(\left[1(\pm)\sqrt{1+Le^2\kappa^2}\right]\Omega t \pm \frac{\kappa z}{\ell}\right)^2 + \left(\frac{\kappa r_\perp}{\ell}\right)^2}. \tag{A2.1.11}$$

A2.1.2 Perpendicular field case

In the case that the magnetic field $\bar{\boldsymbol{B}} = \bar{B}\boldsymbol{e}_y$ is at right angles to both $\boldsymbol{\Omega}$ and $\boldsymbol{g}$, calculating the solution in three dimensional space requires numerical evaluation of triple Fourier integrals; for example, the velocity field is given by

$$\boldsymbol{u} = \sum_\pm\sum_{s,c}\boldsymbol{u}_\pm^{s,c} \tag{A2.1.12}$$

where

$$\boldsymbol{u}_\pm^{s,c} = \frac{1}{(2\pi)^{3/2}}\iiint_{-\infty}^{\infty}\hat{\boldsymbol{u}}_\pm^{s,c}\begin{matrix}\sin\\\cos\end{matrix}(\varpi_\pm t)\cos(\boldsymbol{k}\cdot\boldsymbol{r})\,\mathrm{d}^3\boldsymbol{k}. \tag{A2.1.13}$$

It will prove convenient to use spherical polar co-ordinates $[k,\ \eta_k,\ \gamma_k]$ with their axis in the k_x-direction to describe $\boldsymbol{k}$-space (i.e. $k_x = k\cos\eta_k$, $k_y = k\sin\eta_k\cos\gamma_k$, and $k_z = k\sin\eta_k\sin\gamma_k$); this makes the expression $2\varpi_B/\varpi_\Omega$ a function of k and γ_k, but not η_k. Furthermore, restricting our domain of interest to the y-z plane ($x = 0$), it is possible to complete the η_k integration, leaving double integrals in Fourier space to be evaluated numerically. For the velocity field, the solution in the plane $x = 0$ is given by

$$u_x = \frac{-gC}{4\Omega\sqrt{2\pi}} \sum_{\pm,(\pm)} \pm \int_0^\infty \int_0^\pi \kappa^2 e^{-\frac{1}{2}\kappa^2} \left[1 + Le^2\kappa^2\cot^2\gamma_k\right]^{-1/2} \csc\gamma_k \, \mathsf{H}_1'\left(\alpha_\pm^{(\pm)}\right) \mathrm{d}\gamma_k \mathrm{d}\kappa, \quad \text{(A2.1.14a)}$$

$$u_y = \frac{-gC}{4\Omega\sqrt{2\pi}} \sum_{\pm,(\pm)} \mp \int_0^\infty \int_0^\pi \kappa^2 e^{-\frac{1}{2}\kappa^2} \left[1 + Le^2\kappa^2\cot^2\gamma_k\right]^{-1/2} \mathsf{H}_1\left(\alpha_\pm^{(\pm)}\right) \mathrm{d}\gamma_k \mathrm{d}\kappa, \quad \text{(A2.1.14b)}$$

$$u_z = \frac{-gC}{4\Omega\sqrt{2\pi}} \sum_{\pm,(\pm)} \pm \int_0^\infty \int_0^\pi \kappa^2 e^{-\frac{1}{2}\kappa^2} \left[1 + Le^2\kappa^2\cot^2\gamma_k\right]^{-1/2} \cot\gamma_k \, \mathsf{H}_1\left(\alpha_\pm^{(\pm)}\right) \mathrm{d}\gamma_k \mathrm{d}\kappa. \quad \text{(A2.1.14c)}$$

Here, $\mathsf{H}_\nu(x)$ is the Struve function of order ν and $\mathsf{H}_1'(x) = \mathsf{H}_0(x) - (\mathsf{H}_1(x)/x)$ is the derivative of the first-order version. The function $\alpha_\pm^{(\pm)}$ is defined as

$$\alpha_\pm^{(\pm)} = \left(\Omega t\left[1 \pm \sqrt{1 + Le^2\kappa^2\cot^2\gamma_k}\right](\pm)\frac{\kappa z}{\ell}\right)\sin\gamma_k (\pm)\left(\frac{\kappa y}{\ell}\right)\cos\gamma_k. \quad \text{(A2.1.15)}$$

The perturbation magnetic field is given by the sum of a particular integral and complementary function; the latter is given by

$$\frac{b_{x,CF}}{\sqrt{\rho\mu}} = \frac{-gC}{4\Omega\sqrt{2\pi}}\frac{1}{Le} \sum_{\pm,(\pm)} (\pm) \int_0^\infty \int_0^\pi \kappa e^{-\frac{1}{2}\kappa^2} \left(1 \mp \left[1 + Le^2\kappa^2\cot^2\gamma_k\right]^{-1/2}\right) \sec\gamma_k \mathsf{H}_1'\left(\alpha_\pm^{(\pm)}\right) \mathrm{d}\gamma_k \mathrm{d}\kappa, \quad \text{(A2.1.16a)}$$

$$\frac{b_{y,CF}}{\sqrt{\rho\mu}} = \frac{-gC}{4\Omega\sqrt{2\pi}}\frac{1}{Le} \sum_{\pm,(\pm)} (\mp) \int_0^\infty \int_0^\pi \kappa e^{-\frac{1}{2}\kappa^2} \left(1 \mp \left[1 + Le^2\kappa^2\cot^2\gamma_k\right]^{-1/2}\right) \tan\gamma_k \mathsf{H}_1\left(\alpha_\pm^{(\pm)}\right) \mathrm{d}\gamma_k \mathrm{d}\kappa, \quad \text{(A2.1.16b)}$$

$$\frac{b_{z,CF}}{\sqrt{\rho\mu}} = \frac{-gC}{4\Omega\sqrt{2\pi}}\frac{1}{Le} \sum_{\pm,(\pm)} (\pm) \int_0^\infty \int_0^\pi \kappa e^{-\frac{1}{2}\kappa^2} \left(1 \mp \left[1 + Le^2\kappa^2\cot^2\gamma_k\right]^{-1/2}\right) \mathsf{H}_1\left(\alpha_\pm^{(\pm)}\right) \mathrm{d}\gamma_k \mathrm{d}\kappa. \quad \text{(A2.1.16c)}$$

For the particular integral, we evaluate the negation of the above expressions at $t = 0$.

Also of interest are the vorticity $\boldsymbol{\omega}$ and magnetic vector potential $\boldsymbol{a}$; to find $\boldsymbol{\omega}$, multiply the integrands for $\boldsymbol{u}$ by $(\pm)k$, and for $\boldsymbol{a}$ multiply those for $\boldsymbol{b}$ by $(\pm)k^{-1}$.

A2.2 Initial value problem: magnetic, aligned-axis vortex

We now consider an initial value problem similar to appendix A2.1, only now the forcing comes from an initial condition on the velocity field $\boldsymbol{u}_0(\boldsymbol{r})$ rather than any buoyant source. The derivation is identical (with $\boldsymbol{g}=0$) up to equation (A2.1.5). Picking the thread up from there, the initial condition is enforced through

$$\hat{\boldsymbol{u}}|_{t=0} = \hat{\boldsymbol{u}}_0 \qquad \Longrightarrow \qquad \hat{\boldsymbol{u}}^c_+ + \hat{\boldsymbol{u}}^c_- = \hat{\boldsymbol{u}}_0 \tag{A2.2.1a}$$

$$\left.\frac{\partial \hat{\boldsymbol{u}}}{\partial t}\right|_{t=0} = \varpi_\Omega\,(\hat{\boldsymbol{u}}_0 \times \boldsymbol{e}_k) \qquad \Longrightarrow \qquad \varpi_+\hat{\boldsymbol{u}}^s_+ + \varpi_-\hat{\boldsymbol{u}}^s_- = \varpi_\Omega\,(\hat{\boldsymbol{u}}_0 \times \boldsymbol{e}_k) \tag{A2.2.1b}$$

$$\left.\frac{\partial^2 \hat{\boldsymbol{u}}}{\partial t^2}\right|_{t=0} = -\left(\varpi_\Omega^2 + \varpi_B^2\right)\hat{\boldsymbol{u}}_0 \qquad \Longrightarrow \qquad \varpi_+^2\hat{\boldsymbol{u}}^c_+ + \varpi_-^2\hat{\boldsymbol{u}}^c_- = \left(\varpi_\Omega^2 + \varpi_B^2\right)\hat{\boldsymbol{u}}_0 \tag{A2.2.1c}$$

$$\left.\frac{\partial^3 \hat{\boldsymbol{u}}}{\partial t^3}\right|_{t=0} = -\varpi_\Omega\left(\varpi_\Omega^2 + 2\varpi_B^2\right)\hat{\boldsymbol{u}}_0 \times \boldsymbol{e}_k \qquad \Longrightarrow \qquad \varpi_+^3\hat{\boldsymbol{u}}^s_+ + \varpi_-^3\hat{\boldsymbol{u}}^s_- = \varpi_\Omega\left(\varpi_\Omega^2 + 2\varpi_B^2\right)\hat{\boldsymbol{u}}_0 \times \boldsymbol{e}_k. \tag{A2.2.1d}$$

Eliminating for the coefficients, we get

$$\hat{\boldsymbol{u}}^c_\pm = \frac{1}{2}\left(1 \pm \left[1 + \left(\frac{2\varpi_B}{\varpi_\Omega}\right)^2\right]^{-1/2}\right)\hat{\boldsymbol{u}}_0, \tag{A2.2.2a}$$

$$\hat{\boldsymbol{u}}^s_\pm = \frac{1}{2}\left(1 \pm \left[1 + \left(\frac{2\varpi_B}{\varpi_\Omega}\right)^2\right]^{-1/2}\right)\hat{\boldsymbol{u}}_0 \times \boldsymbol{e}_k. \tag{A2.2.2b}$$

This completes the solution for $\hat{\boldsymbol{u}}$ in Fourier space.

A2.2.1 Specific case: $\boldsymbol{\Omega}$ and $\bar{\boldsymbol{B}}$ perpendicular, aligned-axis vortex

Consider the case, analogous to appendix A2.1.2, in which the background rotation and mean magnetic field vectors are perpendicular, $\boldsymbol{\Omega} = \Omega\boldsymbol{e}_z$ and $\bar{\boldsymbol{B}} = \bar{B}\boldsymbol{e}_y$. Additionally take the initial condition to be the aligned-axis vortex of the equivalent non-magnetic problem in appendix A1.1:

$$\boldsymbol{u}_0(\boldsymbol{r}) = \frac{U}{\ell}\,(\boldsymbol{e}_z \times \boldsymbol{r})\,e^{-\boldsymbol{r}^2/2\ell^2} = \tfrac{Us}{\ell}e^{-\boldsymbol{r}^2/2\ell^2}\,\boldsymbol{e}_\phi. \tag{A2.2.3}$$

We has a Fourier transform given by (A1.1.7). The evaluation of the inverse Fourier transforms for $\boldsymbol{u}(\boldsymbol{r},t)$ proceeds in much the same way as appendix A2.1.2; it is given by

$$\boldsymbol{u} = \sum_{\pm}\sum_{s,c} \boldsymbol{u}_{\pm}^{s,c} \tag{A2.2.4}$$

where

$$\boldsymbol{u}_{\pm}^{s,c} = \frac{1}{(2\pi)^{3/2}} \iiint_{-\infty}^{\infty} \hat{\boldsymbol{u}}_{\pm}^{s,c} \begin{matrix}\sin\\ \cos\end{matrix}(\varpi_{\pm} t)\cos(\boldsymbol{k}\cdot\boldsymbol{r})\,\mathrm{d}^3\boldsymbol{k}. \tag{A2.2.5}$$

Using spherical polar co-ordinates $[k,\ \eta_k,\ \gamma_k]$ with their axis in the k_x-direction to describe $\boldsymbol{k}$-space (as in appendix A2.1.2), and restricting the domain of interest to the plane $x=0$, the solution is given by

$$u_x = \frac{U}{4\sqrt{2\pi}} \sum_{\pm,(\pm)} (\mp) \int_0^{\infty}\int_0^{\pi} \kappa^3 e^{-\frac{1}{2}\kappa^2} \left(1 \pm \left[1 + Le^2\kappa^2\cot^2\gamma_k\right]^{-\frac{1}{2}}\right) \cos\gamma_k \mathsf{H}_1'\left(\alpha_{\pm}^{(\pm)}\right) \mathrm{d}\gamma_k \mathrm{d}\kappa, \tag{A2.2.6a}$$

$$u_y = \frac{U}{4\sqrt{2\pi}} \sum_{\pm,(\pm)} (\mp) \int_0^{\infty}\int_0^{\pi} \kappa^3 e^{-\frac{1}{2}\kappa^2} \left(1 \pm \left[1 + Le^2\kappa^2\cot^2\gamma_k\right]^{-\frac{1}{2}}\right) \sin\gamma_k\cos\gamma_k \mathsf{H}_1''\left(\alpha_{\pm}^{(\pm)}\right) \mathrm{d}\gamma_k \mathrm{d}\kappa, \tag{A2.2.6b}$$

$$u_z = \frac{U}{4\sqrt{2\pi}} \sum_{\pm,(\pm)} (\mp) \int_0^{\infty}\int_0^{\pi} \kappa^3 e^{-\frac{1}{2}\kappa^2} \left(1 \pm \left[1 + Le^2\kappa^2\cot^2\gamma_k\right]^{-\frac{1}{2}}\right) \times \left[\sin^2\gamma_k \mathsf{H}_1''\left(\alpha_{\pm}^{(\pm)}\right) + \mathsf{H}_1\left(\alpha_{\pm}^{(\pm)}\right) - \frac{2}{\pi}\right] \mathrm{d}\gamma_k \mathrm{d}\kappa. \tag{A2.2.6c}$$

Appendix A3

Magnetic-Coriolis waves in a non-uniform magnetic field

A3.1 Linearisation of governing equations

We show here that the linear hybrid wave equation (3.1.14) derived for a constant background magnetic field $\bar{\boldsymbol{B}}$ still applies approximately in the case of a mean field which is a gradually-varying function of space. The difference is that the non-zero spatial derivatives of $\bar{\boldsymbol{B}}(\boldsymbol{r})$ must be considered carefully. We begin by splitting $\boldsymbol{B}$ into mean and fluctuating parts,

$$\boldsymbol{B}(\boldsymbol{r},t) = \bar{\boldsymbol{B}}(\boldsymbol{r}) + \boldsymbol{b}(\boldsymbol{r},t), \tag{A3.1.1}$$

and making the assertion that $|\boldsymbol{b}| \sim b$ is much less than $|\bar{\boldsymbol{B}}| \sim B^*$. Furthermore, we say that $\bar{\boldsymbol{B}}$ varies over a lengthscale L much longer than the wavelength of the hybrid waves in question, which is of the order ℓ. The Lorentz force in the rotating-MHD momentum equation (3.1.11) then becomes

$$\boldsymbol{B}\cdot\nabla\boldsymbol{B} = \underbrace{\bar{\boldsymbol{B}}\cdot\nabla\bar{\boldsymbol{B}}}_{B^{*2}/L} + \underbrace{\bar{\boldsymbol{B}}\cdot\nabla\boldsymbol{b}}_{B^*b/\ell} + \underbrace{\boldsymbol{b}\cdot\nabla\bar{\boldsymbol{B}}}_{B^*b/L} + \underbrace{\boldsymbol{b}\cdot\nabla\boldsymbol{b}}_{b^2/\ell}, \tag{A3.1.2}$$

with the order of magnitude of each term given underneath. If the Lorentz force due to the mean field is conservative (i.e. $\nabla\times\left(\bar{\boldsymbol{B}}\cdot\nabla\bar{\boldsymbol{B}}\right)=0$, which is always the case in this thesis) the first term will never appear in the vorticity equation and therefore be lost at the first step of the hybrid wave equation derivation of section 3.1.3. The second term is larger than both the third (by a factor L/ℓ) and fourth (by a factor B^*/b) terms, and will therefore dominate in the linearised momentum equation, which may be written as in (3.1.12a).

Similarly, the induction equation (3.1.7) becomes

$$\frac{\partial \boldsymbol{b}}{\partial t} = \underbrace{\bar{\boldsymbol{B}}\cdot\nabla\boldsymbol{u}}_{B^*u/\ell} - \underbrace{\boldsymbol{u}\cdot\nabla\bar{\boldsymbol{B}}}_{B^*u/L} + \underbrace{\boldsymbol{b}\cdot\nabla\boldsymbol{u} - \boldsymbol{u}\cdot\nabla\boldsymbol{b}}_{bu/\ell}, \tag{A3.1.3}$$

where $|\boldsymbol{u}| \sim u$. The first term on the right-hand side is of the order L/ℓ greater than the second and B^*/b greater than the third and fourth, and therefore the linearisation (3.1.12b) is still applicable in the non-uniform $\bar{\boldsymbol{B}}$ case. This approximation leads to the governing hybrid wave equation (4.2.2).

A3.2 Group velocity of hybrid waves

The group velocity $\boldsymbol{c}_g$ of hybrid waves is given by (3.1.16),

$$\left(1 + \frac{\varpi_B^2}{\varpi^2}\right)\boldsymbol{c}_g = 2\frac{\varpi_B}{\varpi}\boldsymbol{c}_{gB} \pm \boldsymbol{c}_{g\Omega}, \tag{A3.2.1}$$

where $\varpi_B = \left(\bar{\boldsymbol{B}}\cdot\boldsymbol{k}\right)/\sqrt{\rho\mu}$ is the Alfvén wave frequency, ϖ is the hybrid wave frequency, $\boldsymbol{c}_{gB} = \bar{\boldsymbol{B}}/\sqrt{\rho\mu}$ is the Alfvén velocity and $\boldsymbol{c}_{g\Omega} = -\frac{2\Omega}{k}\sin\theta_k\boldsymbol{e}_{\theta_k}$ is the inertial wave group velocity. (Recall that k is the wavevector magnitude and θ_k is its polar angle from the k_z-axis.) When ray tracing (see section 4.2.1), we consider the mean magnetic field to be a function of z ($\bar{\boldsymbol{B}} = \bar{\boldsymbol{B}}(z)$), and the frequency $\varpi = \varpi_0$ and horizontal component of the wavevector $\boldsymbol{k}_\perp = \boldsymbol{k}_{\perp 0}$ are constant along a ray. We define $\boldsymbol{k}_{\perp 0}$ by its magnitude $k_{\perp 0}$ and the azimuthal wavevector angle ϕ_{k0}. Then, using $\sin\theta_k = k_{\perp 0}/k$, we can express the inertial wave group velocity in Cartesian components as

$$\boldsymbol{c}_{g\Omega} = \frac{2\Omega}{k_{\perp 0}}\sin^2\theta_k\left[-\cos\theta_k\cos\phi_{k0},\ -\cos\theta_k\sin\phi_{k0},\ \sin\theta_k\right]^T, \tag{A3.2.2}$$

i.e. just a function of θ_k. The hybrid wave group velocity (A3.2.1) therefore becomes

$$\boldsymbol{c}_g = \left(1 + \frac{\varpi_B^2}{\varpi_0^2}\right)^{-1}\left[2\frac{\varpi_B}{\varpi_0}\frac{\bar{\boldsymbol{B}}(z)}{\sqrt{\rho\mu}} \pm \frac{2\Omega}{k_{\perp 0}}\sin^2\theta_k\begin{pmatrix}-\cos\theta_k\cos\phi_{k0}\\ -\cos\theta_k\sin\phi_{k0}\\ \sin\theta_k\end{pmatrix}\right]. \tag{A3.2.3}$$

In the special case that the z-component of the mean magnetic field is zero, the wavevector polar angle θ_k is given explicitly as a function of z by the dispersion relation (4.2.14b); then,

we may write the axial group velocity of a ray as

$$c_{gz} = \frac{\mathrm{d}z}{\mathrm{d}t} = \pm\frac{2\Omega}{k_{\perp 0}}\left(1+\frac{\omega_B^2}{\omega_0^2}\right)^{-1}\left[1-\left(\frac{\omega_0}{2\Omega}\right)^2\left(1-\frac{\omega_B^2}{\omega_0^2}\right)^2\right]^{3/2}, \tag{A3.2.4}$$

and since $\omega_B = \left(\bar{\boldsymbol{B}}(z)\cdot\boldsymbol{k}_{\perp 0}\right)/\sqrt{\rho\mu}$ is an explicit function of z, this may be integrated for $t(z)$. As for the perpendicular component of the ray position, we have

$$\boldsymbol{c}_{g\perp} = \frac{\mathrm{d}\boldsymbol{r}_\perp}{\mathrm{d}t} = \left(1+\frac{\omega_B^2}{\omega_0^2}\right)^{-1}\left\{2\frac{\omega_B}{\omega_0}\frac{\bar{\boldsymbol{B}}(z)}{\sqrt{\rho\mu}} - \frac{\omega_0}{k_{\perp 0}}\left(1-\frac{\omega_B^2}{\omega_0^2}\right)\left[1-\left(\frac{\omega_0}{2\Omega}\right)^2\left(1-\frac{\omega_B^2}{\omega_0^2}\right)^2\right]\boldsymbol{e}_{k_{\perp 0}}\right\}. \tag{A3.2.5}$$

Dividing through by (A3.2.4), this becomes

$$\begin{aligned}\frac{\mathrm{d}\boldsymbol{r}_\perp}{\mathrm{d}z} = \pm\Bigg\{&\frac{k_{\perp 0}}{\Omega}\frac{\omega_B}{\omega_0}\left[1-\left(\frac{\omega_0}{2\Omega}\right)^2\left(1-\frac{\omega_B^2}{\omega_0^2}\right)^2\right]^{-3/2}\frac{\bar{\boldsymbol{B}}(z)}{\sqrt{\rho\mu}}\\ &-\frac{\omega_0}{2\Omega}\left(1-\frac{\omega_B^2}{\omega_0^2}\right)\left[1-\left(\frac{\omega_0}{2\Omega}\right)^2\left(1-\frac{\omega_B^2}{\omega_0^2}\right)^2\right]^{-1/2}\boldsymbol{e}_{k_{\perp 0}}\Bigg\},\end{aligned} \tag{A3.2.6}$$

which may again be integrated for $\boldsymbol{r}_\perp(z)$.